UNIVERSITY OF SOUTHAMPTON

Coherent Manipulation of Ultracold Rubidium

by

Matthew Himsworth

A thesis submitted in partial fulfillment for the
degree of Doctor of Philosophy

in the
Faculty of Engineering, Science and Mathematics
School of Physics and Astronomy

September 2009

UNIVERSITY OF SOUTHAMPTON

Abstract

Faculty of Engineering, Science and Mathematics
School of Physics and Astronomy

Doctor of Philosophy

by Matthew Himsworth

The production of dense samples of atoms whose translational velocity can be parameterized by temperatures in the microkelvin range has revolutionized the fields of spectroscopy, metrology, quantum computing and sensitive tests of quantum mechanics. Such ultracold temperatures may be reached by Doppler cooling which uses a velocity-sensitive scattering force. This technique relies upon atoms which have closed electronic transitions between two states so that the atoms may continuously absorb photon momenta and do not spontaneous decay into a dark state. Very few atoms fulfil this condition and attempts to cool molecules are inhibited by their extra degrees of freedom, via rotation and vibration, which add manifolds of extra states.

This thesis describes the early experimental stages of investigation into coherent laser-atom interactions which may be used as a general all-optical method to impart momentum to atoms and molecules and thus manipulate their velocity. The thesis covers the construction and operation of stable diode lasers, a magneto-optical trap to produce cold samples of the test species Rubidium and a high-power, phase and intensity, controllable laser to induce Raman transitions. Studies into the spectroscopy of Rubidium and the nature of coherent Raman interactions in multilevel atoms is also covered. Experimental results shows that coherent Raman transitions between the $5S_{1/2}$ ground states has been achieved in the form of sinc-squared lineshapes and Rabi-flopping.

Contents

Declaration of Authorship

I, Matthew David Himsworth, declare that this thesis titled, 'Coherent Manipulation of Ultracold Rubidium' and the work presented in it are my own. I confirm that:

- This work was done wholly or mainly while in candidature for a research degree at this University.
- Where any part of this thesis has previously been submitted for a degree or any other qualification at this University or any other institution, this has been clearly stated.
- Where I have consulted the published work of others, this is always clearly attributed.
- Where I have quoted from the work of others, the source is always given. With the exception of such quotations, this thesis is entirely my own work.
- I have acknowledged all main sources of help.
- Where the thesis is based on work done by myself jointly with others, I have made clear exactly what was done by others and what I have contributed myself.

Signed: _____

Date: _____

Acknowledgements

I would first like to thank my fellow experimenters; James Bateman without whose programming skills and depth of knowledge, the project would be barely off the ground, Richard Murray who took over the lab when I disappeared round the world for half a year, Sunil Patel for starting the project and built the first lasers and spectroscopy setup as well bringing Yorkshire to the south coast and finally Hamid Ohadi and André Xuereb, the newcomers, for bringing a fresh perspective and allowing us to borrow so much equipment from their Lab. Special thanks to my supervisor Tim Freegarde for allowing me to opportunity to work on such an interesting experiment and guiding my physics training. Thank you to the entire physics workshop team for building the vacuum chamber, diode lasers and making sure I didn't cut anything important off when I ventured into the workshop. Thanks to all the electronics technicians for practical advise as I taught myself circuit design from scratch in my first year. I would also like to note the help from the administrative team at the school for ensuring the smooth running of the project. Thank you to Jenny and David Wright for their meticulous proof-reading and helpful suggestions. I would like to thank the following (in no order) for advice and help; Dave Hanna, David Clark, Gareth Lewis, Peter de Groot, James Gates, Richard Hartley, Alistair Grundy, Ifan Hughes and Patrick Tierney. And last but by no means least, Joanna Millar (soon to be Joanna Himsworth) for giving me the time and space (and tidying up my space) in which to write up this thesis and for taking my away for 6 months which gave me a fresh outlook on the project on my return.

"(..) Sir Isaac Newton, renowned inventor of the milled-edge coin and the catflap!"
"The what?" said Richard.
"That catflap! A device of the utmost cunning, perspicuity and invention. It is a door within a door, you see, a ..."
"Yes" said Richard, "there was also the small matter of gravity."
"Gravity," said Dirk with a slightly dismissed shrug, "yes, there was that as well, I suppose. Though that, of course, was merely a discovery. It was there to be discovered." ...
"You see?" he said dropping his cigarette butt, "They even keep it on at weekends. Someone was bound to notice sooner or later. But the catflap ... ah, there is a very different matter. Invention, pure creative invention. It is a door within a door, you see."

Douglas Adams (1987) *Dirk Gently's Holistic Detective Agency*

Dedicated to Jo

Chapter 1

Introduction

This thesis concerns the experimental manipulation of Rubidium atoms by control over an atom's velocity, and therefore momentum, with external fields. The simplest method of manipulating an atom is via the absorption of a photon, with momentum $p = h/\lambda$, which is in resonance with a dipole transition between two atomic energy levels separated by energy $\Delta E = hc/\lambda$, where λ is the wavelength, c is the velocity of light in a vacuum and $\hbar \equiv h/2\pi$ is Planck's constant. The atom will recoil with absorption of a resonant photon by conservation of momentum and therefore we have manipulated the atom's velocity.

This simple effect has led to a powerful technique in which we may bring a collection of atoms moving at hundreds of $\mathrm{m\,s^{-1}}$ (close to the speed of sound) down to speeds of $\mathrm{cm\,s^{-1}}$. Doppler cooling utilizes a laser detuned to longer wavelengths so that an atom traveling against the beam wavevector is more likely to absorb a photon, and thus recoil and slow down, than an atom traveling with the beam. By applying counter-propagating laser beams along each cartesian axis we can cause the atoms at the beam overlap to feel a viscous-type force against any motion. This is commonly called *optical molasses* in analogy to movement within a molasses, or treacle, like substance and has allowed

the efficient cooling of atoms whose velocity distribution we may characterize by a 'kinetic temperature[1]' of millikelvin[2]. By reducing thermal effects which inhomogeneously broaden atomic resonance frequencies (Doppler effect and collisions) and obtaining a localized optically dense sample of atoms, we open up fields of high resolution spectroscopy, quantum information, measurement of subtle quantum effects, and sensitive tests of fundamental physics and constants.

Optical molasses relies upon systems with closed two-level transitions so that after an atom has absorbed a photon and been excited to some higher energy level it will spontaneously decay back to its initial energy level so that the process may be continuously repeated. If the excited level decays to a level whose transition frequency to the excited level lies outside of the laser bandwidth, the atom will no longer absorb photons and is lost from the cooling cycle. Very few atoms have such closed two-level transitions and so Doppler cooling is therefore a limited technique.

The title of this thesis refers to the *coherent* manipulation of Rubidium atoms. Coherence is encountered in physics textbooks usually in the context of the oscillator properties of laser emission: It is a measure of the correlation of a wave property (usually phase) between different points of the wave in time and space. This means that if we were to measure the phase of the laser light at one point we could accurately predict the phase at a later point, if the laser were phase-coherent.
In real lasers the coherence is not infinite and the output wave will be interrupted by sudden phase jumps so as to cause *decoherence*. We can characterize a quality of a laser emission by the length of time between dephasing events and the laser light may be deemed (temporally[3]) coherent if there is negligible decoherence on the relevant experimental timescales.

In quantum mechanics we treat the atomic structure with wave-like properties (wavefunctions) and so we may apply the measure of coherence to an atomic state (here we

[1]The thermodynamic definition of temperature is that of the equilibrium energy of closed system. As Doppler cooling involves loss of energy from the system by spontaneous emission of photons then we cannot use the above definition. Kinetic temperature refers to the 1D translational kinetic energy and the ideal gas; $Mv^2 = k_B T$, where M is the atomic mass, v is the velocity, k_B is the Boltzmann constant and T is the kinetic temperature

[2]For particles to be consider as 'ultracold' we define their kinetic temperature to be below a millikelvin.

[3]Another property of lasers is *spatial* coherence due to the phase across the wavefronts.

term an atomic 'state' as the full electronic configuration of the atom, which could be a superposition; a 'level' is a pure state, or eigenvector, of the system). During an interaction between an atom and a resonant light field the atom will *coherently* cycle between two levels via absorption and stimulated emission at a well-defined rate known as the Rabi frequency. Random spontaneous emission between the two levels cause phase jumps within the Rabi cycle and thus lead to *decoherence* of the interaction.

This thesis looks at new experimental methods to cool atoms with more complex electronic structures and possibly molecules using coherent broadband interactions. Dipole-allowed transitions will always spontaneously decay from higher to lower energy levels and so the atoms remain coherent for very short timescales (in the order of tens of nanoseconds). Two-photon, specifically Raman, transitions can couple dipole-forbidden levels which cannot spontaneously decay between each other and so remain coherent on much longer time scales. Furthermore, Raman transitions may also impart more momentum compared with single photon transitions thus enhancing the atomic manipulation (see Chapter 6). Efficient transfer of population between levels can be achieved by shaped-pulse interactions, namely adiabatic rapid passage, which can be spectrally broad and so couple numerous levels, thus we may no longer depend on closed two-level systems.

We begin the thesis by looking at the motivation behind the project and the problems involved with Doppler cooling of complex atoms and molecules, the current techniques available for creating cold molecules and how our investigation may provide an alternative all-optical route. In Chapter 3 we then study the atomic structure and light-atom interactions with our test species Rubidium. The experiments require numerous highly stable diode lasers and so in Chapter 4 we discuss the practical frequency stabilization of diode lasers using frequency modulation spectroscopy on sub-Doppler absorption features of Rubidium. To study new cooling techniques it is useful to start with a cold dense sample (10^{11} atoms cm^{-3}) of atoms as this provides a large signal to noise ratio, reduces Doppler effects which may swamp a subtle signal and provides an opportunity to gain experience in standard cooling techniques. The theory and construction of a magneto-optical trap to achieve cold atoms are described in Chapter 5. In Chapter 6 we outline the theory behind coherent interactions: especially pulsed Raman transitions

between stable ground states. We also discuss the theory behind the new cooling techniques such as amplified Doppler cooling and interferometric cooling. These experiments require multiple phase-coherent laser beams which must be amplitude-modulated and their relative detuning controlled to within Hertz accuracy; the apparatus for this is detailed in Chapter 7. In Chapter 8 we detail the experimental results of the coherent manipulation studies and we conclude this thesis in Chapter 9.

This project has involved four experimenters: Sunil Patel, James Bateman, Richard Murray and Myself. The division of labour has not been strictly divided and we have all had some input into each area although the main contributions are as follows: Sunil was involved with the initial set up of the laboratory, development of the diode lasers and construction of the MOT. James Bateman has been most closely involved with the experiments in the second half of this thesis and has been responsible for the computer automation of the data collection, development of coherent interaction theory and the initial design and construction of the manipulation laser. Richard Murray is the latest member of the group and has been increasingly involved in all aspects of the experiment. The majority of my involvement has been in diode laser stabilization, Rubidium spectroscopy, construction and operation of the MOT and theoretical modeling of decoherence sources within the MOT cloud.

Chapter 2

Motivation

2.1 Limitations of Doppler Cooling

Doppler cooling of atoms has been applied to Hydrogen [1], alkali-metal atoms: Li [2], Na [3], K [4], Rb [5], Cs [6] and Fr [7]; and the alkaline-earth atoms: Mg [8], Ca [9] and Sr [9]; as well as Cr [10], Yb [11] and metastable atoms He* [12] and Ne* [13]. The following discussion is limited to neutral particles although it must be noted that there is considerable work in the cooling and trapping of ions using electromagnetic fields [14][1] much of which pre-dated the cooling of neutral atoms.

The alkali-metal atoms have a single valence electron outside closed shells and in the absence of spin-nuclear coupling exhibit a single ground state; atoms excited to a higher energy state will always decay back down to the same ground state and therefore the transition can be approximated as a closed system. Other desirable properties are the existence of lasers at the transition frequencies and a fast, excited state, decay rate to ensure absorption of sufficient photons to slow the atoms down before they leave the laser beam cross-section. Alkaline-earth and Ytterbium atoms have two valence electrons which result in additional structure due to spin-spin interaction, these atoms require much more complicated apparatus for Doppler cooling, such as ultra-violet lasers. The metastable atoms do not have ground state transitions which are far too energetic

[1]The similarity of alkaline earth ions and alkali-metal atoms in electronic structure makes the former applicable in laser cooling

be addressed with lasers but do have metastable states which have lifetimes long enough as a ground state [13]. Chromium seems to be an isolated case[2] within complex atoms where Doppler cooling is achievable, as a reliable cooling transition has been found within its six valence-electron structure, although additional lasers are required to "plug" the spontaneous emission "leaks".

If we treat Chromium as a special case we come to the conclusion that Doppler cooling is only applicable to atoms with closed two-level systems and is therefore ineffective in atoms with complex electronic structures and molecules. This is a shame as Doppler cooling brought about a revolution in atomic physics since it was first experimentally achieved in 1985 by Chu et al. [3].

Doppler cooling has had a major influence on high-resolution spectroscopy by increased interaction times, which enhance the signal to noise ratio, and reduction of the first and second order Doppler effects to measure small energy changes such as recoil [15] and collisional shifts [16]. It has also been possible to perform spectroscopy on single atoms [17] therefore removing collisional perturbations.

Accurate frequency standards from high-resolution spectroscopy immediately lend themselves to the field of metrology (the study of measurement). Prior to Doppler cooling, atomic frequency standards were derived from the passage of state-selected thermal beams of Caesium atoms through a tuned microwave cavity. The stability of these clocks could reach 10 ns per day (1 part in 10^{13}) [18] and depends upon the measurement time of reference frequency; therefore a translationally cold sample of atoms would greatly improve the accuracy of atomic clocks. This led to the construction of atomic fountain clocks which have stabilities two orders of magnitude greater than previous atomic clocks [19], so accurate that new time references (other than Caesium) will need to be found [20].

Now that we can measure time accurately it is possible to measure the subtle changes, if any, of the so-called fundamental constants. A change of the fine-structure constant would violate the equivalence principle and thus break down the theory of gravitation [21]. The fine-structure constant determines the atomic hyperfine splitting and so any changes would appear as variations in transition frequencies.

[2]The closed transition was found because there is much interest in mono-energetic beams for surface deposition in nanofabrication

The atomic fountains of modern atomic clocks utilize pulsed laser fields to deflect atoms and place them in superpositions. This is a reversal of the standard optics where matter affects waves and has opened up a new field of *atom optics* where external fields affect atomic degrees of freedom [22]. Production of colder atoms allows the experimenter to enter the region where the de Broglie wavelength ($\lambda_{\mathrm{DB}} = h/p$) is greater than the atomic radius and so a Young's slit-type interference experiment may be performed with atoms [23]. In a sample of ultracold atoms whose density is high enough a temperature low enough (high phase space density[3]), the de Broglie wavelength may be greater than the separation between atoms and so individual atoms can no longer be resolved and a Bose-Einstein condensate forms [25].

Opening up the ultracold field to molecules would not just extend the above studies but also introduce new areas of study such as cold chemistry [26] where long interaction times during collisions increase tunneling probabilities and so introduce a new reaction pathway. Bethlem and Meijer [27] give an excellent detailed review on applications of ultracold molecules.

2.2 Molecular Structure

Molecules have a far more complex energy level structure than atoms due to their extra degrees of freedom [28]. The simplest diatomic molecules can spin, roll, tumble and vibrate; they can have extended molecular bonding orbitals and distorted atomic orbitals. Electronic transitions are split into numerous vibrational levels (typically separated by infrared wavelengths) which are, in turn, split into rotational levels (typically in the microwave region). Transitions between rotational states are governed by strict selection rules and so closed-transitions can be found [27]; however, any prepared state can be lost to numerous 'dark' energy levels via vibronic (vibrational-electronic) transitions and intramolecular vibrational-energy redistribution [29, 30]. The Franck-Condon principle states that an electronic transition can be considered instantaneous on the timescale

[3]The BEC condition is found when $N\lambda_{\mathrm{DB}}^3/V > 2.612$ where N is the number of atoms and V is the cloud volume [24].

of the vibrating mode of a molecule and the strength of a vibronic transition is proportional to the overlap of the vibrational wavefunctions of the states (the so called 'Franck-Condon factors'). This means that any transition (absorption or emission) will result in a distribution over many vibrational states which can be separated by frequencies greater than the laser bandwidth; therefore, Doppler cooling has limited application to cooling molecules.

Although Doppler cooling may be possible in some cases [31], it has been necessary to develop alternative methods to create a sample of cold molecules.

2.3 Cold Molecules

Current methods in which cold molecules may be produced generally fall into four categories:

- **Supersonic Expansion**

  A gas held under pressure inside a container with a hole smaller than the mean free path of the gas will slowly effuse out of the container, into vacuum, with velocities equal to the equilibrium distribution inside the container. However, when the hole diameter is larger than the mean free path, collisions occur at the exit which cause fast molecules to collide with slower molecules and vice versa [27]. As the majority of molecules are moving in the same direction (i.e. out of the hole) these collisions have the effect of narrowing the velocity distribution. Temperatures of the expelled gas can be reduced to around a Kelvin but only in the frame of the moving gas, which is usually supersonic in the laboratory frame, although it is possible to negate the flow velocity with a counter-rotating nozzle [27, 32].

- **Sympathetic Cooling**

  This technique, also known as buffer-gas cooling, uses pre-cooled atoms to act as a cold reservoir from which the molecular species of interest will achieve colder temperatures through thermal redistribution. This technique is useful as it can be applied to any gas of molecules (which are unreactive with the cooled atoms, usually Helium) as the cooling only relies upon elastic scattering cross-sections. It can

also lead to interesting mixtures of ultracold atoms/molecules [33]. Temperatures attained via sympathetic cooling were usually limited to that of the buffer-gas, down to millikelvin [34] (cryogenically cooled ^{3}He), until the turn of the century when ultracold temperatures (hundreds of nanokelvin) of atomic ensembles were made possible by dual-species magneto optical traps and thermalization with Bose-Einstein condensates [35].

- **Association**

  A molecule can be formed during a collision between atoms if the total kinetic energy of the collision is equal to that of a bound molecular state. Using cold atoms to form cold molecules in this manner is, by definition, limited by the low kinetic energy of the atomic ensemble. Two techniques provide a method to enhance the free-bound resonance: photoassociation and magnetoassociation. Photoassociation uses a photon to provide the additional energy for the colliding atoms to achieve an excited molecular bound state [36]. The molecules are typically formed in unstable, high vibrational, states near the continuum and so are usually short-lived. Methods exist to manipulate the decay of such molecules into stable, or metastable, lower energy bound states [37] and significant densities of various diatomic molecules (mainly alkali dimers) have been formed at sub-microkelvin temperatures [26, 27].

  Magnetoassociation uses magnetic fields to alter the energy levels of the colliding atoms to enhance the scattering cross-section of the molecular bound state [38]. As with photoassociation, a molecule left with an energy equal to, or greater than, the individual colliding atoms will be unstable and so it would be favourable to tune the interaction so that the molecule is left in a lower energy, and thus stable, state. This situation can be achieved if the Zeeman shifts cause an anti-crossing of molecular and atomic states, so that a magnetic field sweep through this crossing (the Feshbach resonance) will take the atoms from a higher energy unbound state into a lower energy bound state. As long as the magnetic field is maintained, the molecule does not have the energy to split into its constituent atoms and is therefore stable. Feshbach resonances have been successfully used to create molecular Bose-Einstein condensates from Bosonic *and* Fermionic atoms [39]. For

an excellent introduction to molecule formation via association see Hutson and Soldán [40].

- **Stark Deceleration**

  Polar molecules have asymmetric charge distributions such that one end is more positively charged and the other end negatively charged. A familiar example is the water molecule where the asymmetry of the bonds tends to distribute the negative charge over the Oxygen atom, which has a greater electronegativity.

  The interaction between a polar molecule and an electric field is known as the *Stark effect*. In a uniform electric field each pole of the molecule will experience an equal and opposite force and therefore no net effect, whereas an inhomogeneous electric field will exert a force which can be used to manipulate the molecules [41]. A linear stark decelerator consists of a number of electrode pairs, typically separated by millimeters, arranged perpendicularly along a linear path through which a beam of polar molecules (usually from a supersonic expansion source) is passed. As the molecules (in a low-field seeking state) enter the inhomogeneous field of the electrode pair (a 'stage') they gain Stark energy which is compensated by a loss of kinetic energy. If the field is turned off as the molecule reaches the strongest field point the molecule will not fully regain its kinetic energy and is slowed down. At each stage of Stark decelerator the electric fields are pulsed in such a manner to compensate for the reduction in velocity. The molecules have to keep climbing an 'energy hill' as they pass each stage and rarely experience a downhill gradient in order to regain their kinetic energy (similar to sub-Doppler cooling, Section 5.5).

  The longitudinal distribution of velocities can be compressed (or 'bunched') as the faster molecules will lose more kinetic energy than the slowest molecules, therefore one can time the pulse sequence to produce a velocity selective force which also conserves phase space. The molecules are then loaded into an electrostatic quadrupole trap in order to increase their density whilst the velocity remains low [27]. Typical temperatures reached via Stark deceleration are in the millikelvin region [26].

Although these techniques can result in samples of cold molecules and are very reliable they are limited in their applicability. Supersonic expansion only produces transversely cold molecules. Sympathetic cooling introduces unwanted species and only indirectly cools the molecules. Association is also indirect and is limited to molecules formed by atoms which can be Doppler cooled. Stark deceleration is limited to molecules with a strong dipole moment. A direct, all-optical, molecular cooling scheme which can be used with any molecule or complex atom would be very desirable.

2.4 Proposed Schemes

This thesis describes the investigation of techniques which aim to reduce the reliance on two-level, monochromatic, transitions in favour of broadband coherent techniques. One can use two-photon transitions to impart twice the momentum to an atom (or molecule) compared with single photon transitions (see Section 6.4). Such interactions are off-resonant with single photon transition and so the atom does not populate excited states which spontaneously decay. This thesis documents the early stages of the project in which we have performed simple coherent interactions, such as Rabi-flopping (Chapter 6), with cooled and trapped Rubidium atoms in a Magneto-Optical Trap.

The two long term goals of this project are amplified Doppler cooling [42, 43] and interferometric cooling [44]. The former (described in Section 6.5.1) uses coherent techniques to increase the amount of momentum imparted to each atom per spontaneous emission. This method still relies on the usual Doppler sensitive technique to selectively excite atoms according to their velocity, but reduces the number of spontaneous emissions needed; the atoms feel a stronger cooling force before they are lost to a dark state.

Interferometric Cooling (described in Section 6.5.2) uses solely coherent effects to cool atoms. The atoms are placed into a superposition of two states and are allowed to 'evolve' in this state. After a period the atom is recombined by a second pulse of light and the resulting state depends (among other factors) on the atom's velocity; the subsequent emission of photons can create a velocity dependent force and therefore cooling.

Chapter 3

Rubidium Spectroscopy

All of the experiments throughout this thesis involve Rubidium, a member of the alkali-metals group, which is commonly used for Doppler cooling because of its simple electronic structure. Natural Rubidium has two common isotopes; ^{85}Rb and ^{87}Rb with relative abundances 72.17% and 27.83% [45], respectively. For our coherence experiments we concentrate on ^{85}Rb, but also observe ^{87}Rb when performing pump-probe spectroscopy. Rubidium has two fine structure lines at 780 nm (D_2 line) and 795 nm (D_1 line). The former is close to the wavelength used for CD writers and so there has been much development in diode laser power at this wavelength. Another advantage is a high vapour pressure [46] at room temperature so that glass vapour cells are optically dense enough to obtain sufficient absorption spectra without the need of heating, and these are used for spectroscopy and frequency references. Rubidium is also available in 'getters' which allow one to pump atoms into a vacuum chamber, by ohmic heating of the getter, thus negating the need for complicated oven dispensers. One last important feature of ^{85}Rb with respect to coherence experiments is the 3.036 GHz hyperfine splitting of the ground state. This frequency is within the range of telecoms equipment so that amplifiers and frequency sources are available to modulate the lasers.

This chapter describes the electronic structure and important properties of Rubidium and introduce terms which will be referred to throughout this thesis. The second half of the chapter is devoted to Doppler-free spectroscopy which we use as a frequency reference to stabilize the diode lasers.

3.1 Rubidium Structure

The full electronic structure of Rubidium is $1s^2 2s^2 2p^6 3s^2 3p^6 3d^{10} 4s^2 4p^6 5s$ and so the single valence electron sits in a spherical S-orbital and the inner closed shells do not contribute to the orbital momentum (and thus transition probabilities) of the atom. We need an atom with a closed two-level system for Doppler cooling. In this section we discuss how the fine and hyperfine structure in Rubidium (and all alkali atoms) comes close to this ideal two-level system and how the magnetic structure leads to an added bonus of the ability to trap the atoms. The standard nomenclature used in this thesis is to label the orbitals as nL_{J}, where n denotes the shell, L denotes the orbital and J is the total orbital angular momentum discussed below.

3.1.1 Fine Structure

Fluorescence spectra of Rubidium gas exhibit narrow lines, in the near-infrared region, known as the 'fine structure' which is due to coupling between the orbital angular momentum $\vec{L}$ of the electron and its spin $\vec{S}$; this is known as the spin-orbit coupling. The total angular momentum and range of values are;

$$\vec{J} = \vec{L} + \vec{S}, \tag{3.1}$$

$$|L - S| \leq J \leq L + S. \tag{3.2}$$

The $5S_{1/2}$ orbital has the values $L = 0$ (S-orbital) and $S = 1/2$, therefore this state is not split. We shall refer to this orbital as the ground state as this is the lowest energy state to which the atom spontaneously decays. The excited $5P_{3/2}$ has the values $L = 1$ (P-orbital) and $S = 1/2$ and so this state is split into $5P_{1/2}$ and $5P_{3/2}$. Transitions between $5S_{1/2}$ and these states are known as the D_1 line (795 nm) and D_2 line (780 nm), respectively; we concentrate solely on the D_2 line.

3.1.2 Hyperfine Structure

The fine structure can be resolved into narrower lines, known as the hyperfine structure, and is due to the coupling of the spin-orbit $\vec{J}$ and nuclear $\vec{I}$ moments. The total angular momentum and range of values are;

$$\vec{F} = \vec{I} + \vec{J}, \tag{3.3}$$

$$|I - J| \leq F \leq I + J. \tag{3.4}$$

The nuclear angular moments of ^{85}Rb and ^{87}Rb are 5/2 and 3/2, respectively. For ^{85}Rb, this leads to a splitting of the $5S_{1/2}$ ground state into two levels, $F = 2, 3$, and the excited $5P_{3/2}$ state into four levels $F' = 1, 2, 3, 4$ as shown in Figure 3.1. We have denoted an excited state with a dash, F' and the ground state without, F. Note that the ground state splitting is much larger than that of the excited state due to the greater overlap of the spherical S-orbital with the nucleus compared with the lobed P-orbital, which has a node at the nuclear position.

3.1.3 Magnetic Structure

Application of an external magnetic field lifts the degeneracy of the hyperfine structure into $2F+1$ magnetic sublevels, denoted m_F. In weak magnetic fields, where the induced shift of the m_F states is less than the hyperfine splitting, this is known as the anomalous Zeeman effect and the energy shift of the m_F levels follow;

$$\Delta E_{\mathrm{Zeeman}} = \mu_{\mathrm{B}}\, g_{\mathrm{F}}\, m_{\mathrm{F}}\, B_{\mathrm{z}}, \tag{3.5}$$

where μ_{B} is the Bohr magneton, g_{F} is hyperfine Lande g-factor (see Table A.2 in Appendix A) and B_{z} is the magnetic field strength. Note that we have specified a direction to the magnetic field as this defines the quantization axis. Stronger magnetic fields lead to the normal Zeeman effect where the magnetic energy level splitting becomes dependent on the m_{J} sub-levels. In between the normal and anomalous Zeeman effects the energy splitting becomes non-linear and is known as the Paschen-Back effect.

3.1.4 Selection Rules

Whether or not given dipole transitions between levels are allowed is determined by a series of selection rules which reflect the conservation of atomic and optical angular momentum between levels [47]. For example, the selection rule $\Delta L = \pm 1$ is due to the conservation of angular momentum when an atom absorbs a photon with momentum $\pm 1\hbar$. Therefore an atom in an S-orbital can absorb a photon and be excited into a P-orbital but not into another S-orbital (or D, F etc. orbitals. This is possible with multiphoton transitions discussed in Chapter 6). The actual strength of the transition is calculated in Section 3.2.3, and here we just state the general electric dipole selection rules as to whether a transition is allowed [48];

$$\Delta L = \pm 1 \tag{3.6}$$

$$\Delta J = 0, \pm 1 \ (J = 0 \nrightarrow J' = 0) \tag{3.7}$$

$$\Delta m_{\mathrm{J}} = 0, \pm 1 \tag{3.8}$$

$$\Delta F = 0, \pm 1 \tag{3.9}$$

$$\Delta m_{\mathrm{F}} = 0, \pm 1 \tag{3.10}$$

$$\Delta S = 0 \tag{3.11}$$

From the selection rules we can see that the ^{85}Rb $F = 3 \rightarrow F' = 4$ and ^{87}Rb $F = 2 \rightarrow F' = 3$ are closed transitions as they can only decay back to the ground state from which they were excited. This means we may treat the transition as a two level system and so meet the requirement for Doppler cooling.

3.1.5 Transition Frequencies

Figure 3.1 shows the hyperfine structure for the two common isotopes of Rubidium. The hyperfine energy shift depends upon the angular momentum of each state and is calculated from Equation A.1 in Appendix A. The relative detunings of each level from $F = 3 \rightarrow F' = 4$ (Doppler cooling transition) are found in Table A.3, also in Appendix A. The isotope shift (78.095 MHz) is due to the difference between the nuclear/electron mass ratio of each isotope and is measured experimentally [49].

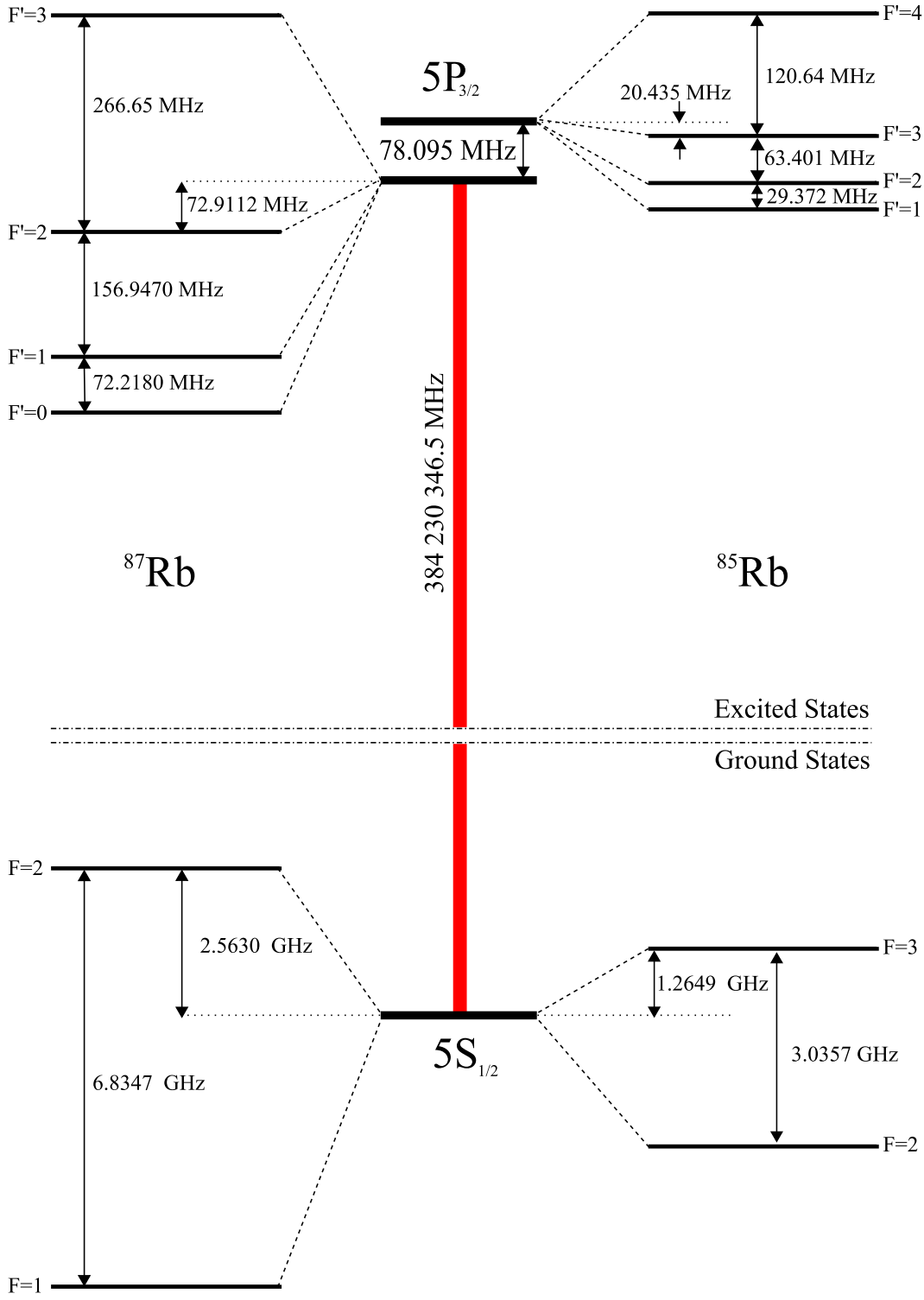

FIGURE 3.1: *Hyperfine structure of ^{85}Rb and ^{87}Rb. Hyperfine splitting calculated in Appendix A [50, 51].*

3.2 Important Properties

I mention here a few useful properties of Rubidium which will be used throughout the thesis.

3.2.1 Thermal

As this thesis is concerned with the cooling of atoms it is worth mentioning their thermal properties. We must also include the standard disclaimer when discussing temperature. So far we have discussed the temperature of ultracold atoms in which we use 'temperature' as convenient scale in discussing the translational velocity, and therefore kinetic energy, of particles via the relation $T = \frac{Mu^2}{3k_\mathrm{B}}$ (average in three dimensions, where M is the mass of the particle, u is the speed and k_B is Boltzmann's constant).

For discussions of laser spectroscopy of a gas of Rubidium atoms in a glass vapour cell, we shall assume the atoms obey the statistics of a Maxwell-Boltzmann distribution in that the atoms are at an equilibrium temperature in which collisions are the sole interaction (i.e. no quantum effects). We can verify this by calculating the mean free path $\lambda_\mathrm{mfp} = (\sigma_\mathrm{coll} N_\mathrm{V})^{-1}$ where N_V is the number density of atoms and σ_coll is the collisional cross-section $\simeq \pi R_\mathrm{A}^2$. Taking the separation between two Rubidium atoms R_A to be 470 pm [52], and a density of $\simeq 10^{15}\mathrm{m}^{-3}$ in the vapour cells from the absorption studies ($5 \times 10^{15}\mathrm{m}^{-3}$ see Section 3.3) we find a mean free path of approximately 300 m! This is much greater than the dimensions of the glass vapour cell and so the temperature must be dominated by collisions with the cell walls.

The Maxwell-Boltzmann distribution of a velocity vector component for a sample of atoms, with mass M and a mean temperature T, is

$$f_\mathrm{D}(v) = \sqrt{\frac{M}{2\pi k_\mathrm{B} T}} \exp\left[-\frac{Mv^2}{2k_\mathrm{B}T} \right]. \tag{3.12}$$

The most probable speed is

$$u_\mathrm{D} = \sqrt{\frac{2k_\mathrm{B}T}{M}} \tag{3.13}$$

and full width at half maximum (FWHM) of

$$\Delta v_{\mathrm{D}} = 2u_{\mathrm{D}}\sqrt{\ln 2} \tag{3.14}$$

The subscript 'D' refers to 'Doppler' as the inhomogeneous broadening of absorption spectra is modeled by a Maxwell-Boltzmann distribution of Doppler-shifted atoms.

3.2.2 Lifetime

Spontaneous emission of a photon by an atom placed in an excited state is due to perturbation by zero-point energy fluctuations described by quantum field theory [53]. Spontaneous emission typically occurs after a period of time dependent upon the atomic structure and available vacuum modes. If we treat the atomic electron as a classical dipole oscillator (neglecting the internal energy states) with damping equal to the decay rate[1] γ, the amplitude of oscillation is

$$\mu(t) = \mu_0 \cos(\omega_0 t) e^{-\frac{\gamma}{2}t} \tag{3.15}$$

where ω_0 is the Bohr frequency of the transition from the excited state to ground (we assume only one decay route) and μ_0 is the dipole strength. We can find the spectral properties of this decaying oscillator by taking the Fourier transform.

$$\mu(\omega) = \mu_0 \int_0^\infty \cos(\omega_0 t) e^{-\frac{\gamma}{2}t} e^{-i\omega t} dt \tag{3.16}$$

We assume that the electron was excited to the upper state at time $t = 0$ so the integration for $t < 0$ is zero. The intensity ($I(\omega) \propto \mu(\omega)^* \mu(\omega)$) of spontaneous emission is

$$I(\omega) \propto \frac{\gamma}{(\omega - \omega_0)^2 + \gamma^2/4} \tag{3.17}$$

The spectral lineshape is a Lorentzian with a FWHM of γ. The widening of this 'natural' linewidth is known as *radiative broadening* of the excited state.

[1] This is the probability of decay which is the square of the probability amplitude, hence the factor of 1/2 in the exponential in Equation 3.15.

To calculate the lifetime of the excited state requires full quantum electro-dynamical treatment and for complex atoms the value is usually found from experiment. Experimental resolution has not been fine enough to distinguish between lifetimes of the two isotopes of Rubidium and the measured value is $26.25 \pm 0.07\,\text{ns}$ [54], which results in a natural width of $\approx 2\pi \times 6\,\text{MHz}$. It is common in many texts to use two forms of the decay rate, γ and Γ. Throughout this thesis I refer to $\gamma = 1/\tau$ as the natural decay rate and shall attempt to avoid the use of Γ which refers to all homogeneous broadening mechanisms such as collisional dephasing (with rate γ_{coll}) and is defined as $\Gamma = \gamma/2 + \gamma_{coll}$. Historically γ and Γ are referred to as the *longitudinal* and *transverse* decay rates, respectively, and shall see the reason for this in Chapter 6.

3.2.3 Dipole Matrix Elements

The equation of motion for a quantum system is described by the time dependent Schrödinger equation

$$i\hbar\frac{\partial}{\partial t}\Psi(\vec{r},t) = \hat{\mathscr{H}}\Psi(\vec{r},t) \tag{3.18}$$

where $\hat{\mathscr{H}}$ is the Hamiltonian operator, which has eigenvalues corresponding to the total energy of the system, and $\Psi(\vec{r},t)$ is the wavefunction of the quantum system, which may be a superposition of basis eigenstates

$$\Psi(\vec{r},t) = \sum_{\mathrm{k}} c_{\mathrm{k}}(t)\psi_{\mathrm{k}}(\vec{r})e^{-\frac{iE_{\mathrm{k}}t}{\hbar}} = \sum_{\mathrm{k}} c_{\mathrm{k}}|k\rangle \tag{3.19}$$

where we have separated the radial, $\psi_{\mathrm{k}}(\vec{r})$, and temporal, $c_{\mathrm{k}}(t)$, components and used the Dirac Bra-Ket notation on the far right hand side for simplicity. Our idealized two-level system containing only a ground, $|g\rangle$, and excited, $|e\rangle$, state may be written

$$|\Psi\rangle = c_{\mathrm{g}}|g\rangle + c_{\mathrm{e}}|e\rangle \tag{3.20}$$

and the probability amplitudes are normalized to unity: $|c_{\mathrm{g}}|^2 + |c_{\mathrm{e}}|^2 = 1$.

The Hamiltonian of the system is composed of the unperturbed energy levels, $\hat{\mathscr{H}}_0$ with eigenvalues E_k, and the applied external field, $\hat{\mathscr{H}}_{\mathrm{F}}$, which in the case of laser beam we

shall treat as a classic oscillator with frequency ω and amplitude $\vec{E}_0$

$$\hat{\mathscr{H}}_{\mathrm{F}} = -\hat{\mu} \cdot \vec{\mathscr{E}}_0(e^{-i\omega t} + e^{i\omega t}) = -\hat{\mu} \cdot \vec{\mathscr{E}} \tag{3.21}$$

where $\hat{\mu} = -q\vec{r}$ is the dipole operator which relates the strength of an external field on the atomic electron with charge q at position $\vec{r}$ from the nucleus. In the *dipole approximation* the dimensions of the atomic wavefunction are considered smaller than the wavelength of the perturbing light so that the electric field phase across the atom is uniform.

By substituting Equations 3.20 and 3.21 into Equation 3.18 and multiplying by $\langle e|$ we can find the variation of probability amplitude of the excited state

$$\frac{\partial}{\partial t}c_{\mathrm{e}}(t) = -\frac{i}{\hbar}c_{\mathrm{g}}(t)\vec{\mathscr{E}}e^{-\frac{i(E_{\mathrm{g}}-E_{\mathrm{e}})t}{\hbar}}\left[-q\int_{-\infty}^{\infty}\psi_{\mathrm{e}}^{*}\vec{r}\psi_{\mathrm{g}}d\vec{r}\right] \tag{3.22}$$

The *dipole matrix element*, distinguished by square brackets, determines the strength of a transition by the spatial overlap of the stationary wavefunctions between the initial, i, and final, f, states [55]

$$\mu_{\mathrm{if}} = \mu_{\mathrm{fi}} = -q\int \psi_{\mathrm{i}}^{*}\vec{r}\psi_{\mathrm{f}}d\vec{r}. \tag{3.23}$$

and the square of the dipole matrix moment is proportional to the probability of a transition per unit time (Fermi's golden rule). We may find the values of the dipole matrix elements using the Wigner-Eckhart theorem [47, 51] which, in practice, means that we may separate constants of the angular momentum of the magnetic structure from the hyperfine structure and similarly the hyperfine structure from the fine structure; each step 'reduces' the dipole matrix element. These constants are known as the Clebsch-Gordan coefficients, whose calculation method and tabulated values are in Appendix A. Full calculation of the transition strength from theory is not possible for such complex atoms but we may reduce the Clebsch-Gordan coefficients to experimentally measurable values. μ_0 is the reduced dipole matrix elements and can be measured from the transition lifetime τ,

$$\mu_0 = |\langle J'||e\mathbf{r}||J\rangle| = \sqrt{\frac{1}{\tau}\frac{3\pi\epsilon_0\hbar c^3}{\omega_0^3}\frac{2J'+1}{2J+1}} \tag{3.24}$$

where the double vertical lines denote a reduced matrix element [51] and $\omega_0 = (E_e - E_g)/\hbar$ is the resonance frequency of the transition. We shall refer to the dipole matrix elements throughout this thesis in non state-specific situations as $\mu_{12} = \langle 2|q\vec{r}|1\rangle$ and for specific Rubidium transitions as $\langle F', m'_{\mathrm{F}}|q\vec{r}, p|F, m_{\mathrm{F}}\rangle$ where $p = -1, 0, +1$ is the polarization of the incident field for left circular (σ^-), linear (π) and right circular (σ^+) polarizations, respectively.

3.2.4 Rabi Frequency

The solution to the probability of the two-level atom to be in the excited state can be found from the square of the probability amplitude $|c_{\mathrm{e}}|^2$ and can be solved from Equation 3.22 by setting the boundary condition that the atom is initially in the ground state, $c_{\mathrm{g}}(0) = 1$. The derivation is lengthy and can be found in many textbooks, a thorough example is Allen and Eberly [56]. The result is

$$|c_{\mathrm{e}}|^2 = \frac{\Omega^2}{\Omega_0^2} \sin^2\left(\frac{\Omega_0 t}{2}\right) \tag{3.25}$$

where Ω_0 is the *generalised Rabi frequency*

$$\Omega_0 = \sqrt{\Omega^2 + \delta^2} \tag{3.26}$$

in which $\delta = \omega - \omega_0$ is the detuning from resonance and Ω is the (resonant) Rabi frequency

$$\Omega = \frac{\mu E_0}{\hbar}. \tag{3.27}$$

The Rabi frequency is a commonly used term to quantify the strength of the light-atom interaction and has the units of $\mathrm{rad\,s^{-1}}$. Physically this 'frequency' relates to the rate at which a two-level atom undergoes absorption and stimulated emission cycles.

Figure 3.2 shows temporal and spectral solutions to Equation 3.25 in which we see the excited state oscillating, or 'flopping', at frequency Ω_0 with a 'sinc-squared' spectral lineshape; these plots are the result of a *coherent* interaction and are the experimental focus in Chapters 6-8.

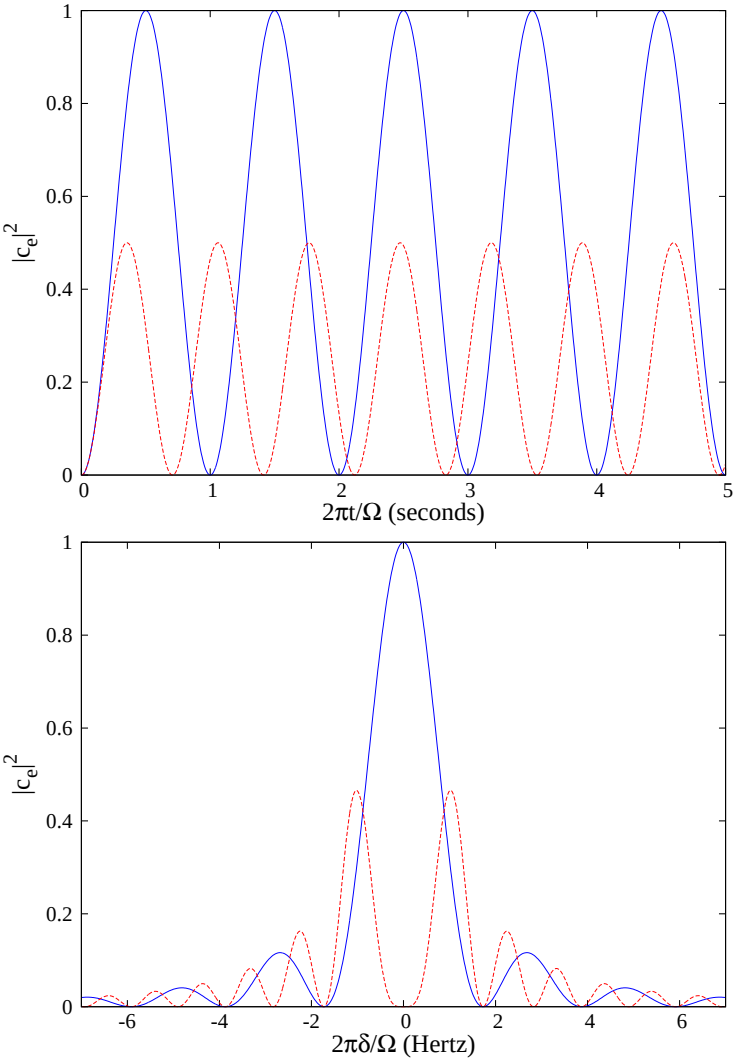

FIGURE 3.2: *Probability of excitation to the excited state with the population initially in the ground state. The top figure shows the temporal variation of the excited state population for a light beam on resonance (blue line) and off-resonance (red line) by* Ω *Hz. The lower figure shows the spectral variation of the excited state population at pulse lengths of* $0.5/\Omega$ *(blue line) and* $1/\Omega$ *seconds (red line).*

3.3 Pump-Probe Spectroscopy

As discussed earlier the atoms in a vapour cell have a Maxwell-Boltzmann distribution of velocities. The transition frequency ω_0 is Doppler shifted by $\vec{k} \cdot \vec{v}$, where $\vec{k}$ is the wavevector. Therefore the spectral resolution of a weak beam when used to probe a transition by passing through a vapour cell is limited by the Doppler width. For ^{85}Rb the Doppler width is $\sim 2\pi \times 500\,\text{MHz}$ which allows one to resolve the fine structure but not the hyperfine structure of the upper levels. To cool atoms we must stabilize

the lasers to within a few natural linewidths of a transition and so we must use sub-Doppler spectroscopic techniques. In this section we review Doppler-free pump-probe spectroscopy.

3.3.1 Method

Standard absorption studies with dilute gases involve a weak probe beam passing through a sample and the transmitted intensity is monitored as the laser frequency is scanned. By weak we mean that the intensity of the beam is low enough that most of atoms remain in the ground state. If we increase the beam intensity we promote more atoms into the excited (e) state, thus depleting the ground (g) state. The rate of change of the state populations, $N_{\rm i}$ is

$$\frac{{\rm d}N_{\rm g}}{{\rm dt}} = -B_{\rm ge}\rho(\omega)N_{\rm g} + B_{\rm eg}\rho(\omega)N_{\rm e} + A_{\rm eg}N_2 \tag{3.28}$$

$$\frac{{\rm d}N_{\rm e}}{{\rm dt}} = B_{\rm ge}\rho(\omega)N_{\rm g} - B_{\rm eg}\rho(\omega)N_{\rm e} - A_{\rm eg}N_2 \tag{3.29}$$

where $\rho(\omega)$ is the energy density per unit frequency of the incident radiation, $B_{\rm eg} = B_{\rm ge}$ are the stimulated absorption and emission Einstein coefficients (assumed to be equal, which is true for states of equal degeneracies) and $A_{\rm eg}$ is the spontaneous emission rate from the excited to ground state.

For a monochromatic laser field, it is assumed that the energy density is confined to a single mode and the stimulated pumping rate $\rho(\omega)B_{eg} = \frac{\sigma_0 I_{\rm pump}}{\hbar\omega_{ge}}$ on resonance, ω_{ge}, where $I_{\rm pump}$ is the beam intensity and σ_0 is the absorption cross-section (this form will be used in Section 3.3.3).

If we equate the steady state values ($\frac{{\rm d}N_{\rm e}}{{\rm dt}} = \frac{{\rm d}N_{\rm g}}{{\rm dt}} = 0$) and conserve total population, $N = N_{\rm e} + N_{\rm g}$, we find,

$$N_{\rm e} = N\frac{1}{2 + \frac{A_{\rm eg}}{B_{\rm eg}\rho}} \tag{3.30}$$

As we increase the beam intensity the excited state population tends to $N/2$, and the absorption and stimulated emission rates are equal and much greater than any relaxation processes. The transition is said to be *saturated* and the gas becomes transparent to

additional resonant light. The effect on the absorption spectral lines is nonlinear *power broadening.*

The trick to gain sub-Doppler resolution is to introduce a counter-propagating beam to probe the level of saturation of the transition. As with gas jet spectroscopy [57], one selects atoms with a velocity perpendicular to the probe beam to avoid Doppler effects. In pump-probe spectroscopy, one has the pump beam propagating in the +z direction and a probe beam in the -z direction. An atom moving with a velocity v_z will only be in resonance with both beams when $v_z \approx 0$, i.e. when it is moving perpendicular to the beams. The effect of a strong pump beam is to saturate the transition so that the weak counter-propagating probe beam has a reduction in absorption around the transition frequency. The recorded spectrum shows a Doppler broadened lineshape but with a narrow 'dip' at the rest-frame transition frequency; this is known as the Lamb Dip and hence this technique is also known as Lamb dip spectroscopy.

3.3.2 Apparatus

The standard apparatus for pump-probe spectroscopy involves a single laser from which a portion is split off to act as a probe. Both beams are passed through a vapour cell in opposite directions and overlapped. The frequency of the laser is then scanned across the resonance and the probe beam intensity is monitored. In order to completely remove the Doppler effects the pump and probe beams must be counter-aligned perfectly, but this may cause back-reflections into the laser. The broadening of the Lamb dip due to mis-alignment (known as Geometrical broadening) approximately follows [58].

$$\Delta\omega_{\mathrm{Geo}} \simeq k\theta\sqrt{\frac{2k_{\mathrm{B}}T}{M}} \tag{3.31}$$

where θ is the mis-alignment angle. In our system we use a beam splitting cube to overlap the pump and probe beams to remove any geometrical broadening, although this method does produce polarization effects.

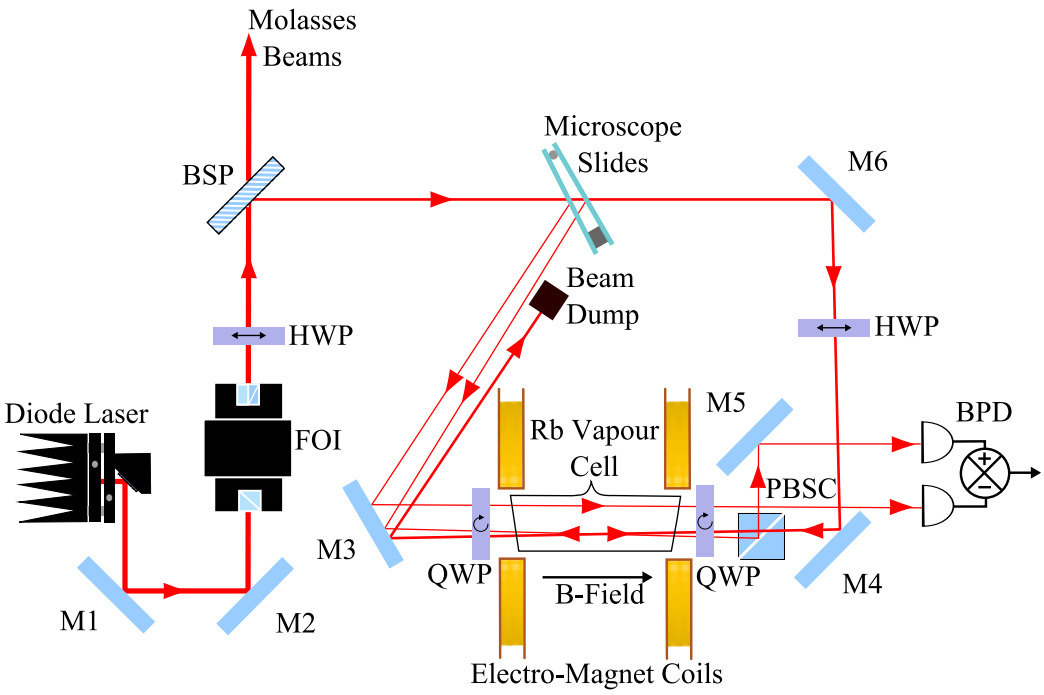

FIGURE 3.3: *Optical layout for Doppler-free spectroscopy. M; mirror, FOI; Faraday optical isolator, HWP; half waveplate, BSP; (polarizing in this case) beam splitter plate, QWP; quarter waveplate, PBSC; polarizing beam splitter cube and BPD; balanced photo-detector.*

Figure 3.3 shows the optical layout for the spectroscopy of the trapping laser[2]. The diode laser is protected from back reflections with a Faraday optical isolator with an aperture of 8 mm diameter. This is important due the retro-reflected beams from the magneto optical trap (MOT, Chapter 5). The first half waveplate rotates the polarization so that approximately 1 mW is picked off with a polarizing beam-splitter plate for the spectroscopy; the remaining 50 mW goes to the MOT optics. Two weak probe beams are picked off with two microscope slides. One probe is overlapped with the counter-propagating pump beam whilst the second probe monitors the Doppler background. The transmitted beam from the microscope slides is sent through a half waveplate to control the intensity of the pump beam through the polarizing beam splitting cube. After the polarizing beam splitting cube the pump beam goes through a quarter waveplate to create circular polarization. The probe beam from the opposite direction passes through another quarter waveplate to complete a half-wave rotation so that the probe

[2]We use two lasers for Doppler cooling designated trapping and repump

is reflected by the polarizing beam splitting cube and measured with a balanced photo-detector. The Doppler probe beam allows one to subtract the Doppler background and common mode noise with a balanced photo-detector. The use of a polarizing beam splitting cube allows the pump and probe beams to be overlapped completely thus reducing geometrical broadening, but with the increase of resolution one suffers the loss of control of the polarizations of each beam.

The DC magnetic field applied with Helmholtz coils along the beam axis allows one to shift the resonance of the transitions with the Zeeman effect (Section 5.6.8). The choice of circularly polarized beams through the vapour cell is for this Zeeman shifting technique but is not mandatory for pump-probe spectroscopy.

3.3.3 Theoretical Model

Before discussing the spectra it is helpful to derive the shape of the Lamb-dip and compare features of the calculated spectra with the measured data. This model treats the laser field as a monochromatic light source, but neglects the coherence effects between the field and atom [59], which are usually negligible a low intensities (less than tens of $\mathrm{mW\,cm^{-2}}$ for Rb).
A laser beam with intensity $I(0)$ passes through an absorbing medium in the z-direction. The intensity decreases according to Beer's law:

$$\frac{\mathrm{d}I(z)}{\mathrm{dz}} = -\alpha(\omega, v)I(z) \tag{3.32}$$

The absorption coefficient $\alpha(\omega, v)$ is proportional to the density of absorbers (atoms) N_V and the absorption cross-section $\sigma(\omega)$:

$$\alpha(\omega, v) = N_\mathrm{V}\sigma(\omega, v) \tag{3.33}$$

The absorption cross-section depends upon the homogeneous broadening due to the transition lifetime $L(\omega, v)$ and the inhomogeneous broadening $f(v)$ due to the Doppler shift of the atoms within the vapour cell. The homogeneous broadening has a Lorentzian

line shape[3] [48]

$$L(\omega, v) = \frac{\sigma_0}{2\pi} \frac{\gamma^2/4}{(\omega - \omega_{ge} - kv)^2 + \gamma^2/4} \tag{3.34}$$

where ω_{ge} is the transition frequency, $\gamma = 1/\tau$ is the linewidth of the transition lifetime τ, k is the wavevector and v is the atomic velocity. As we are dealing with exactly counter-propagating beams we have dropped the vector notation. The absorption cross-section at zero detuning is

$$\sigma_0 = \frac{2\omega_{\mathrm{ge}}\mu_{12}^2}{hc\epsilon_0\gamma} \tag{3.35}$$

where μ_{ge} is the dipole moment and c, ϵ_0 and h are the speed of light, permittivity in vacuum and Planck's constant, respectively. We can treat the atomic velocity distribution by Maxwell-Boltzmann statistics (Equation 3.12).

$$f_{\mathrm{D}}(v) = \sqrt{\frac{M}{2\pi k_{\mathrm{B}} T}} \exp\left[- \frac{Mv^2}{2k_{\mathrm{B}}T} \right] \tag{3.36}$$

For ^{85}Rb, the FWHM of the Doppler broadened D_2 line is $2\pi \sim 500\,\mathrm{MHz}$. To calculate the absorption of the weak probe beam we must integrate over the all velocities.

$$\alpha(\omega) = N_{\mathrm{V}} \int_{-\infty}^{\infty} \frac{f_{\mathrm{D}}(v)\sigma_0\gamma^2/4}{(\omega - \omega_{ge} - kv)^2 + \gamma^2/4} \mathrm{dv} \tag{3.37}$$

This equation cannot be solved analytically but can be written in terms of tabulated functions [46]. The resulting shape is known as a Voigt profile.

Now we must include the effects of the strong counter-propagating pump beam which significantly affects the population of the ground state. We calculate the ground (N_{g}) and excited state (N_{e}) populations using the rate equations;

$$\frac{\mathrm{d}N_{\mathrm{e}}}{\mathrm{dt}} = -\gamma N_{\mathrm{e}} + \frac{L(\omega, v) I_{\mathrm{pump}}}{\hbar\omega_{\mathrm{ge}}} (N_{\mathrm{g}} - N_{\mathrm{e}}) \tag{3.38}$$

$$\frac{\mathrm{d}N_g}{\mathrm{dt}} = \gamma N_{\mathrm{e}} - \frac{L(\omega, v) I_{\mathrm{pump}}}{\hbar\omega_{\mathrm{ge}}} (N_{\mathrm{g}} - N_{\mathrm{e}}) \tag{3.39}$$

where I_{pump} is the pump intensity along the +z direction and γ is the decay rate from the excited state. As the total population in a closed system must be conserved we can

[3] This is derived by solving the steady state density matrix equations in Appendix C

consider only the excited state population, N_e, and find the steady state value

$$\gamma N_\mathrm{e} = \frac{L(\omega, v) I_\mathrm{pump}}{\hbar \omega_\mathrm{ge}} (N_\mathrm{g} - N_\mathrm{e}). \tag{3.40}$$

By using $N = N_\mathrm{g} + N_\mathrm{e}$ we can solve for N_e in terms of N.

$$N_\mathrm{e} = \frac{N}{2 + \frac{\hbar \omega_\mathrm{ge} \gamma}{L(\omega, v) I_\mathrm{pump}}} \tag{3.41}$$

Inserting this into Equation 3.37 and accounting for the number density of atoms $N \rightarrow N_\mathrm{V}$, we arrive at the lineshape of pump-probe spectrum (note the opposite sign of the wavevector to denote the counter-propagating beam):

$$\alpha(\omega) = N_\mathrm{V} \int_{-\infty}^{\infty} \frac{f(v)\sigma_0}{1 + \frac{I_\mathrm{pump}}{I_S} \frac{\gamma^2/4}{(\omega - \omega_\mathrm{ge} + kv)^2 + \gamma^2/4}} \frac{\gamma^2/4}{(\omega - \omega_\mathrm{ge} - kv)^2 + \gamma^2/4} \mathrm{dv} \tag{3.42}$$

Here we have introduced the *saturation intensity*:

$$I_\mathrm{S} = \frac{\hbar \omega_\mathrm{ge} \gamma}{2\sigma_0} \tag{3.43}$$

This represents the intensity required for the pump rate to be equal to the decay rate. We can rearrange Equation 3.42 to make the effect clearer:

$$\alpha(\omega) = \frac{N_\mathrm{V} \sigma_0 \gamma^2}{4 \bar{v}_\mathrm{D} \sqrt{\pi}} \int_{-\infty}^{\infty} \frac{\exp^{-\frac{v^2}{\bar{v}_\mathrm{D}^2}}}{(\delta - kv)^2 + \gamma^2/4} \left[1 - \frac{I_\mathrm{pump}}{I_\mathrm{S}} \frac{\gamma^2/4}{(\delta + kv)^2 + \frac{\gamma^2}{4}\left(1 + \frac{I_\mathrm{pump}}{I_\mathrm{S}}\right)} \right] \mathrm{dv} \tag{3.44}$$

where $\delta = \omega - \omega_\mathrm{ge}$. We can see, even before integration, that the function is a Voigt profile with a reduction in absorption around ω_{12} (square bracketed part). Figure 3.4 shows the effect of the strong pump beam saturating the transition for pump intensity at and above saturation. The linewidth of the Lamb dip is $\gamma_\mathrm{LD} = \gamma_\mathrm{pump} + \gamma_\mathrm{probe} = \gamma(1 + \sqrt{1 + I_\mathrm{pump}/I_\mathrm{S}})$ and so is *power broadened* by the beams. The exact lineshape is also altered by coherence effects which reduce the height of the Lamb dip and increase the width; exact calculations for these effects have been carried out by Haroche and Hartman [59].

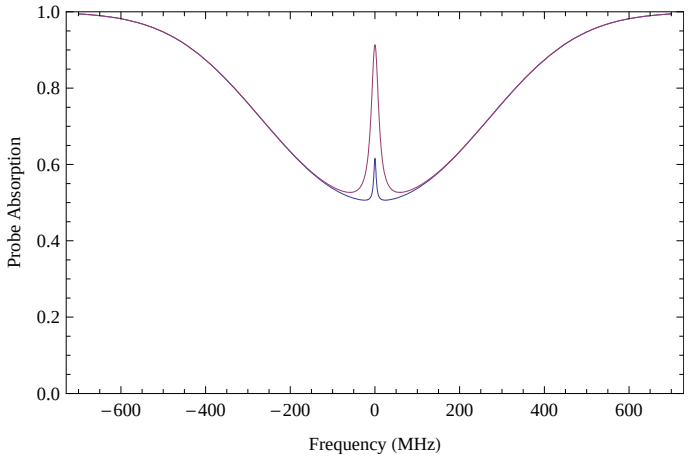

FIGURE 3.4: *Theoretical prediction of pump-probe spectrum. The Doppler-free Lamb dip at zero detuning can be seen within the Doppler broadened Voigt profile. The blue line is for a pump beam with an intensity equal to the saturation intensity. The red line depicts the spectrum for a pump intensity 50 times the saturation intensity.*

3.3.3.1 Saturation Intensity

At high pump powers, the transition rate decreases due to saturation at zero detuning but broadens due to the increased pumping at non-zero detunings. Substituting Equation 3.35 into Equation 3.43 and using the relation for the Rabi frequency, Equation 3.27, we can write the saturation intensity in terms of the Rabi frequency and state relaxation.

$$2\frac{\Omega^2}{\gamma^2} = \frac{I_{\text{pump}}}{I_{\text{S}}} \tag{3.45}$$

At saturation the Rabi frequency is equal to the decay rate, and from Equation 3.41 we see that the excited state population tends to $N/4$. In a two state system this value is easy to calculate but when various decay routes exist for different photon polarizations the saturation intensity will be altered correspondingly (see Reference [55]). A common quoted value for ^{85}Rb is the saturation for the closed transition, $|F = 3, m_F = 3\rangle \rightarrow |F' = 4, m'_F = 4\rangle$, as this can be assumed to be a two level system, at $1.6\,\text{mWcm}^{-2}$.

3.3.3.2 Crossover Resonances

We shall see in the pump-probe spectra, in the next section, that there exist twice as many Lamb dips as expected. The extra peaks are known as *crossover resonances* and appear at exactly half the separation between 'real' absorption pairs; this results

from the counter-propagating arrangement of the laser beams. Figure 3.5 shows the atomic velocity along the vertical axis and resonance frequency on the horizontal axis. The plotted lines are the Doppler shifts of atoms which are in resonance with the two beams for two separate transitions. As long as the Doppler width is greater than the hyperfine splitting, there exists two points (above and below the horizontal axis) at half the resonance splitting with which both beams interact. With two transitions, ω_1 and ω_2 , the pump beam (in the +z direction) will saturate the transitions with velocities

$$v_1 = \frac{\omega_{\text{pump}} - \omega_1}{k} \tag{3.46}$$

$$v_2 = \frac{\omega_{\text{pump}} - \omega_2}{k} \tag{3.47}$$

The counter-propagating probe will see a change in absorption when the Doppler shifts of each beam are equal, $v_1 = v_2 = 0$. This is the Lamb dip on resonance. There is another velocity class for which both beams are resonant if the frequency difference between the two beams is less than the Doppler width, at $v_1 = -v_2$. Therefore

$$\omega_{\text{pump}} - \omega_1 = -(\omega_{\text{pump}} - \omega_2) \tag{3.48}$$

$$\omega_{\text{pump}} = \frac{1}{2}(\omega_2 - \omega_1) \tag{3.49}$$

The crossover resonance is centered at exactly half the transition splitting. Although the extra peaks may complicate the spectra they are useful for relating excited states to a common ground state. Crossover peaks also appear for transitions with a common excited state, but with an increase of beam absorption due to optical pumping.

3.3.3.3 Optical Pumping

In a multi-level atom an excited state may decay into numerous ground states. The probability of decay into a specific level depends upon the ratio of coupling strengths (Clebsch-Gordan coefficients) of the excited state to dipole allowed ground states. For example, an ^{85}Rb atom in the $F' = 3$ excited state can decay into either the $F = 3$ or $F = 2$ ground states with approximately equal probabilities. If the incident radiation is tuned to the $F = 3 \rightarrow F' = 3$ transition, any atom decaying into the $F = 2$ ground

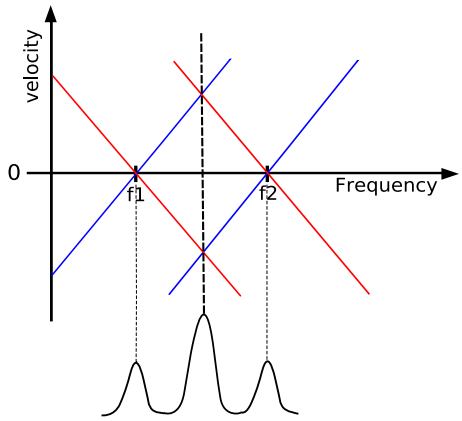

FIGURE 3.5: *Crossover resonances. The coloured lines are the Doppler shifted resonance. The red line is the Doppler shift with respect to the pump beam and the blue line likewise w.r.t. the probe beam. The crossover resonance appears half way between the two 'real' resonances,* $\omega_1 = 2\pi f_1$ *and* $\omega_2 = 2\pi f_2$

state is transparent (or 'dark') to the laser and has been *optically pumped*. We may use optical pumping to our advantage with polarized light to pump atoms into a specific magnetic sublevel. If an ensemble of atoms is in the $|F = 3, m_{\mathrm{F}} = 0\rangle$ ground state and we pump with a σ^+ polarized beam, the atoms will be excited to the $|F' = 4, m_{\mathrm{F}} = 1\rangle$ level and decay with all polarizations into the $|F = 3, m_{\mathrm{F}} = 0, 1, 2\rangle$ levels. Subsequent excitation will populate the $|F = 3, m_{\mathrm{F}} = 0, 1, 2, 3\rangle$ levels and after many cycles the atoms will be optically pumped entirely into the $|F = 3, m_{\mathrm{F}} = 3\rangle$ level.

3.3.4 Spectra

Figures 3.6, 3.7 and 3.8 show the pump-probe spectra for all of the D_2 transitions using the apparatus outlined in Section 3.3.2 with a 7.5 cm long vapour cell at room temperature (290 K). The pump and probe powers have been adjusted to maximize the Lamb dip height without significantly saturating the transitions. The frequency separations of the transitions from the cooling transition ^{85}Rb $F = 3 \rightarrow F' = 4$ can be found in Table A.3 in Appendix A and have been used to calibrate the horizontal axis; each peak has been labeled for identification and reference. The Doppler background has not been removed in order to show how the Doppler-broadened profiles vary in depth.

In each Doppler broadened absorption we can see 6 peaks corresponding to three allowed transitions and the three corresponding crossover peaks. As noted in the theoretical

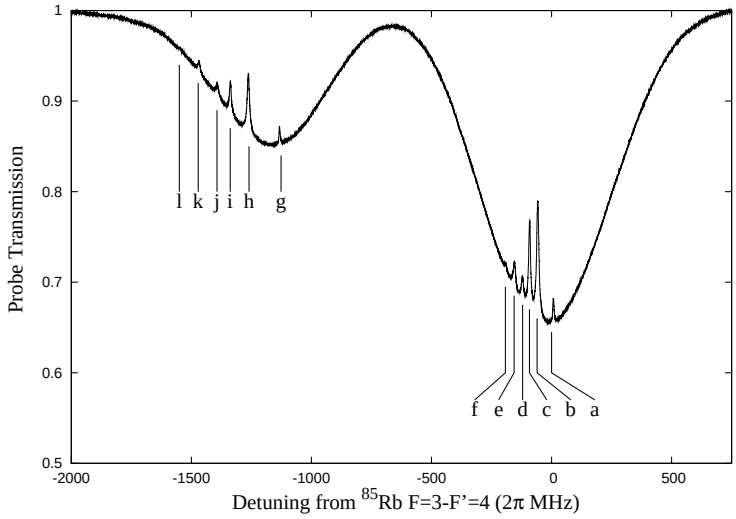

FIGURE 3.6: *Pump-probe transmission spectrum of ^{85}Rb $F = 3$ (right a-f) and ^{87}Rb $F = 2$ (left g-l).*

calculation earlier, the height and width of the Lamb dip depends upon the transition strength and decay routes. From equation 3.45 we see that the saturation intensity is inversely proportional to the dipole moment; therefore a stronger transition will have a reduced saturation intensity and show a stronger, narrower, Lamb dip. We would expect the strongest transition in ^{85}Rb to be $F = 3 \rightarrow F' = 4$ (peak a, Figure 3.6) as the $F' = 4$ state does not couple to the $F = 2$ ground state. However, peak *a* in Figure 3.6 is overshadowed by the crossover peaks (b, c and e) and is not significantly larger than the $F = 3 \rightarrow F' = 3$ transition (peak d). This is due to optical pumping of the $F = 3$ populations into the $F = 2$ ground state, via $F' = 3$ and $F' = 2$, as atoms pumped into this state are transparent to the probe beam and thus exhibit larger than expected Lamb dips.

If we use σ^+ circularly polarized beams and apply a DC magnetic field along the vapour cell axis to remove degeneracy the atoms will be optically pumped into the $|F' = 4, m'_{\mathrm{F}} = 4\rangle$ state and therefore become trapped in a closed state; such a setup shows a significant $F = 3 \rightarrow F' = 4$ Lamb dip (peak a). This closed transition is important in Doppler cooling as atoms decaying from the excited $|F' = 4, m'_{\mathrm{F}} = \pm 4\rangle$ will always decay back into the $|F = 3, m_{\mathrm{F}} = \pm 3\rangle$ ground state and therefore be cycled efficiently without loss.

Other notable features of the spectra are the relative depths of the Doppler broadened background, which is due to the relative isotopic abundances and hyperfine degeneracy,

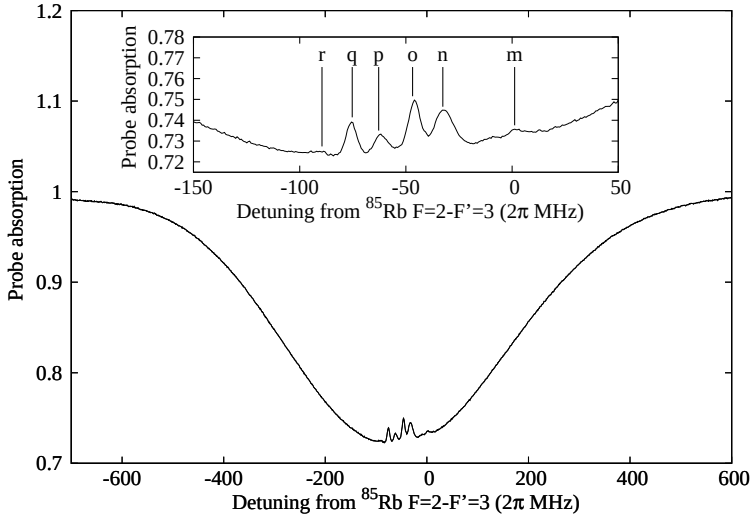

FIGURE 3.7: *Pump-probe transmission spectrum of ^{85}Rb $F = 2$. The inset is a magnified portion of the Lamb dips in order to clearly show each peak.*

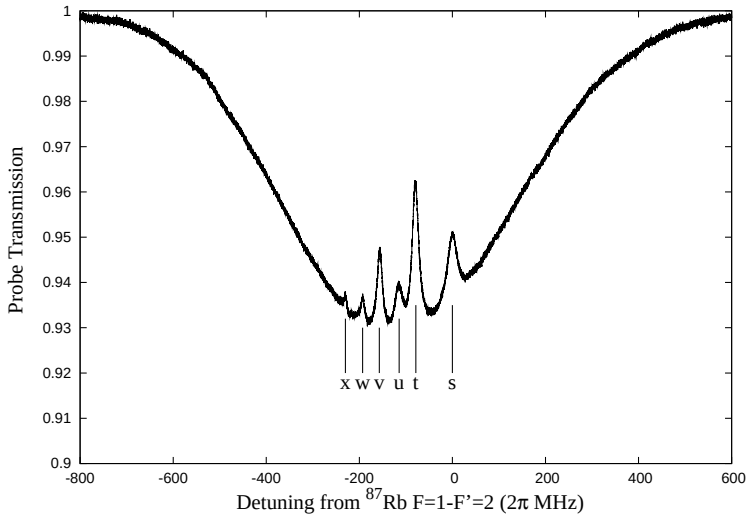

FIGURE 3.8: *Pump-probe transmission spectrum of ^{87}Rb $F = 1$.*

and the apparently weak transitions from ^{85}Rb $F = 2$ (Figure 3.7) ground state which are, in fact, due to experimental considerations; the small frequency separation of the hyperfine excited states makes them unresolvable even at low saturation and so very weak pump powers were used to record this spectrum.

3.3.4.1 Optical Pumping Model

The effect of optical pumping on multilevel atoms has been studied and modelled by Smith & Hughes [60] using the rate equations, Nakayama [61] with a four level model and Maguire et al. [62] using the density matrix. Using the rate equation approach, we

can solve for the steady state populations for a degenerate ground state coupled to three excited states with loss into a dark state. The derivation is lengthy and the result does not provide any more insight but is outlined in Appendix B. The model approximates Rubidium as a four level system with one ground state and four excited states. Atoms pumped into the other real ground state are assumed to be transparent and therefore not involved in the interaction. The fraction of atoms excited to the upper states which decay back into the initial ground state are determined by the ratio of dipole matrix elements. As the sweep of frequency of the pump and probe beams are slow compared to any relaxation processes, the interaction is assumed to come to a steady state at each frequency. The model also includes effects of finite transit time of the atoms across the beam and saturation due to the pump *and* probe beams.

Figure 3.9 shows the modelled and experimentally measured data for pump powers of $20\,\mu$W, $100\,\mu$W, $500\,\mu$W and $2500\,\mu$W with linear polarized beams with a diameter of 2 mm ($1/e^2$). We see that the model matches the data reasonably well especially at higher powers. No adjustment has been made to fit the model to the data. The model assumes that the pump intensity does not significantly decrease as it passes through the vapour cell which is true for high powers but less so at low power and so the experimental data show weaker Lamb dips for the $20\,\mu$W and $100\,\mu$W plots. Another feature in the $500\,\mu$W and $2500\,\mu$W experimental plots is the wider and stronger ^{85}Rb $F = 3 \rightarrow F' = 4$ and ^{87}Rb $F = 2 \rightarrow F' = 3$ peaks. As discussed earlier, these peaks are the only real saturating transitions in which optical pumping has no effect. The measured peaks are stronger and broader than the model, probably due to the Gaussian cross-section of the beams resulting in a variation of pumping intensities. The pump power was measured using a broad area optical power meter (Newport 818) and so only the total power over the active detector region was used for the pump intensity in the model.

These sub-Doppler spectra are used as a frequency reference to which we stabilize our diode lasers. The next chapter discusses the stability of diode lasers and the measures undertaken to achieve it.

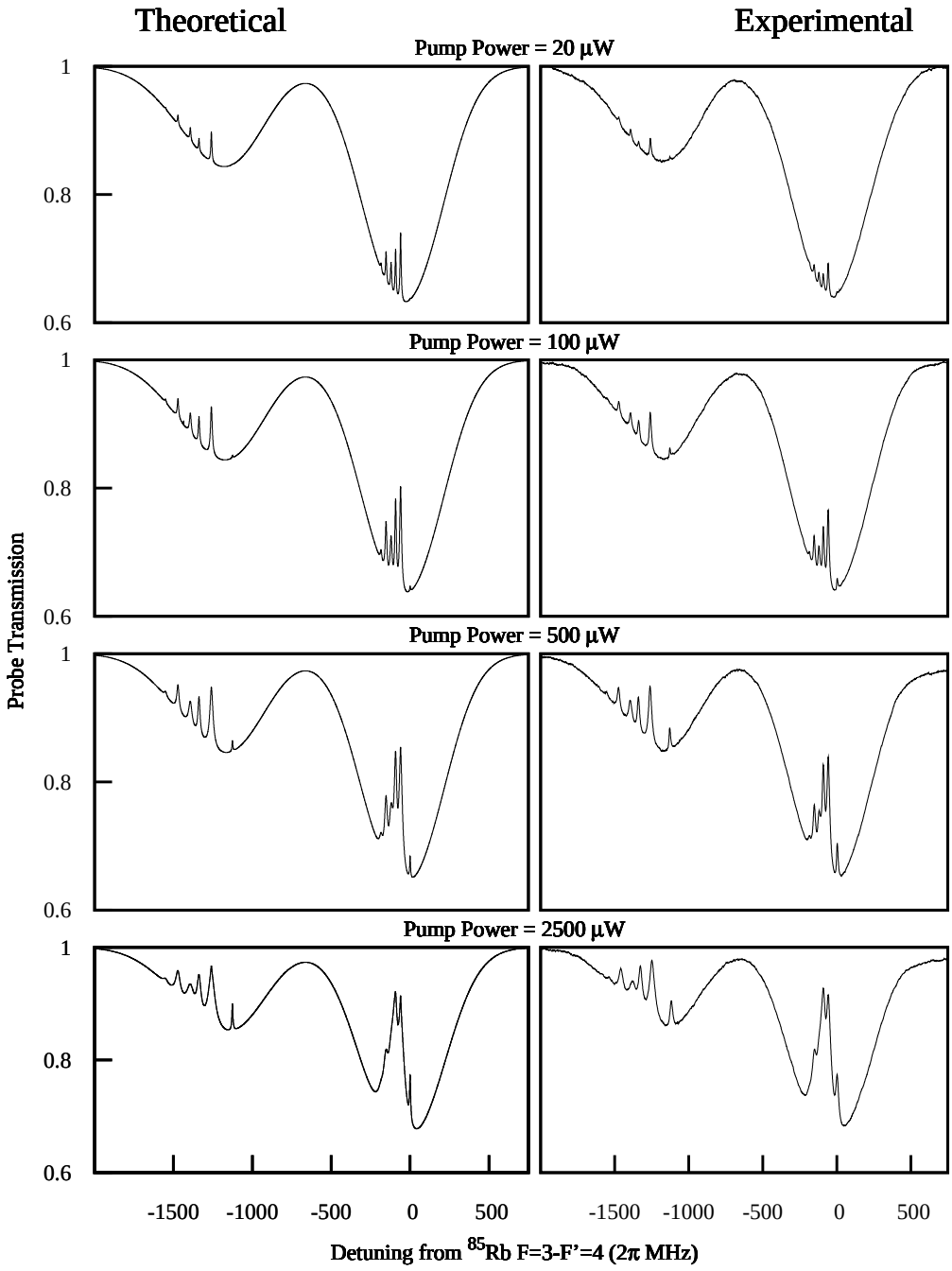

FIGURE 3.9: *Comparison between theoretical (left column) and experimental (right column) pump-probe spectra for increasing (top to bottom) pump powers.*

Chapter 4

Laser Stabilization

In metrology, the quality of an oscillator can be defined in terms of *accuracy* and *precision*: if the measured frequency does not drift from the expected value it is 'accurate' and the reproducibility of the measurement is its 'precision'.

In the coherent manipulation experiments, the laser must have a phase coherence better than, or equal to, the atomic system under investigation. We shall see in Chapter 6 that the coherent interactions are performed with two-photon Raman transitions in which the state populations do not decay spontaneously and so the coherence of the atomic system may exist for fractions of a second. Practically this limits the laser accuracy and precision to within *Hertz*. This level of stability is near the state of the art and we achieve it by modulating a single laser so that the various spectral components are phase coherent relative to each other, but the laser itself need only be stable to tens of megahertz.

In Doppler cooling the laser must be stable to within a megahertz with respect to the atomic resonance, but equally accurate to attain the coldest temperatures, and so we shall concentrate in this chapter on stabilizing this laser.

The first section of this chapter outlines the basic properties of diode lasers before describing the operation of our own laser design. The subsequent sections discuss methods to provide frequency references onto which lasers are stabilized and the electronics used to achieve it.

4.1 Diode Lasers

Diode lasers are popular tools in a number of research fields, such as atomic physics [63], spectroscopy [64], metrology [65] and quantum measurement [66]. This is due to the wide range of wavelengths (from NIR to far blue), tunability (GHz), single mode operation, small size, relatively low power and ease of modulation. Unfortunately much effort needs to be expended in order to control noise and stability of their wavelengths [67].

The high gain and short cavity lengths in diode lasers result in free-running instantaneous linewidths of tens to hundreds of MHz and the centre wavelength can also drift by tens of MHz over timescales of minutes. Even though many diode lasers may operate on a single longitudinal mode, random fluctuations between modes ('modehopping') can occur. These modehops must be controlled as the typical longitudinal mode spacing of diode lasers is in the order of tens of gigahertz.

To understand the characteristics of diode lasers and the methods employed to control them, we must first appreciate how they work. The following is a brief and simplified overview and also an opportunity to introduce relevant terms; a number of books and papers are available for a deeper understanding [63, 68, 69].

4.1.1 Principle of Operation

A diode laser is formed from a p-n junction in which a layer of p-doped semiconductor (electron deficit) next to a n-doped semiconductor (electron excess). Electrons in the n-doped region will recombine with regions of electron deficit (holes) in the p-doped region, emitting light in the case of direct bandgap semiconductors. The recombined electrons will leave fixed positively-charged donor sites in the n-doped region and the corresponding holes will form fixed negatively-charged acceptor sites in the p-doped region; thus creating an electric field between the acceptors and donors which prevents further recombination. At this point the p-n junction will have reached equilibrium and a depletion region will have formed between the p and n doped regions. Figure 4.1 shows a band diagram of this process. In terms of the Fermi energy (or more correctly:

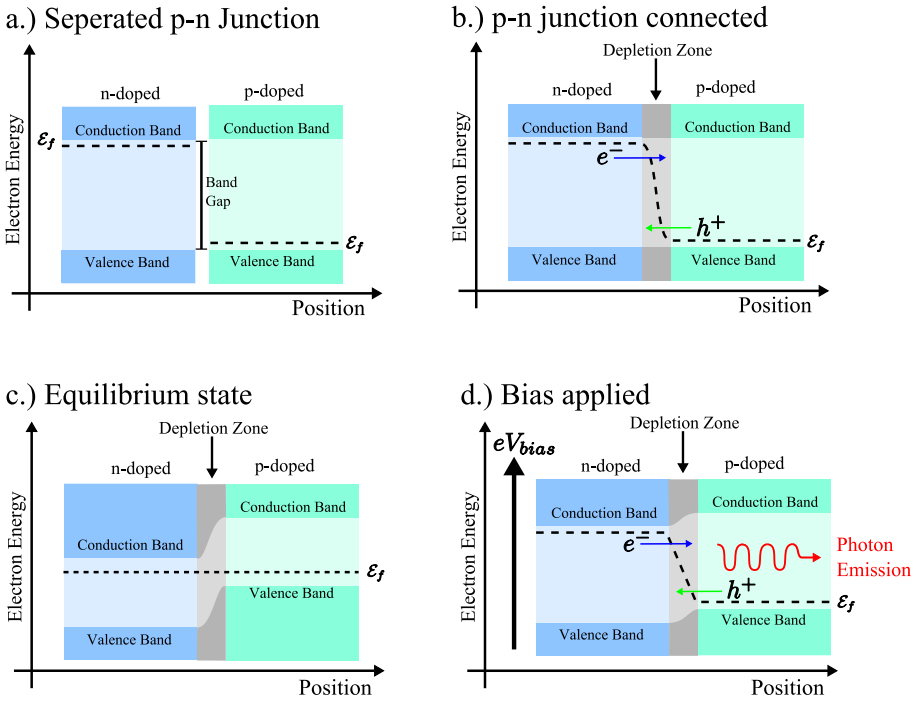

FIGURE 4.1: *Band-bending diagram of p-n junction operation. a.) Separated p-doped and n-doped semiconductor material. The band gap is the energy separating the filled valence band and the empty conduction band. The Fermi energy $\mathcal{E}_f$ (or more correctly, the chemical potential) is raised for a n-doped material due to the increase of electron states and is correspondingly decreased for p-doped material. b.) The p-n junction is formed, electrons recombine with holes, and a depleted region is formed. c.) When the Fermi energy has equalized, the electrons and holes no longer have the energy to traverse the depletion zone. d.) The application of a bias voltage provides electrons and holes the energy to overcome the potential barrier of the depletion region and recombine and emit light.*

the chemical potential) the thermal equilibrium is reached when the Fermi energy is constant across the junction.

Application of a reverse bias voltage (negative terminal to the n-doped side) increases the electric field across the depletion region and no current can flow. A forward bias voltage (negative terminal to the p-doped side) provides the energy for the electrons to cross the depletion region thus causing more annihilation by recombination and light emission; the induced current is called the *injection current*. The directionality of current flow means the p-n junction acts as a diode.

Lasing occurs when an electron has recombined with a hole, but has yet to annihilate, and is forced to undergo stimulated emission by another photon. Thus creating an identical photon which may be reflected from the cleaved facets of the semiconductor chip and go on to cause more stimulated emission. This process provides the coherent

amplification and oscillation to overcome loss processes and laser light. The point at which injection current produces amplification above any loss processes is called the *threshold current*.

The wavelength of the laser emission depends upon the band-gap of the semiconductor, usually in the region of 1-3 eV ($400 \rightarrow 1250$ nm), and the dimensions of the cavity. The difference in refractive index of the depletion region and the doped regions creates a waveguide to channel the laser light along the plane of the p-n junction. The smaller dimension perpendicular to the junction plane creates a highly-diverging elliptical output beam which must be collimated with a lens.

In reality, the layer structure of diode lasers is more complex. Additional layers confine the gain region to increase carrier density and amplification. The transverse (spatial) modes can be confined to a single mode by a thin channel formed by spatial variations in the injection current density or refractive index [63]. The longitudinal (spectral) modes depend upon the length of the Fabry-Perot cavity, created by the cleaved facets of the semiconductor chip. The range of wavelengths a diode laser can operate on depends upon the dopant concentrations and the gain bandwidth, which is usually ~ 10 nm. A typical distance between the cleaved facets of diode laser is $L = 500\,\mu$m with a semiconductor refractive index of $\eta \simeq 3.3$; therefore the longitudinal mode spacing (free spectral range) is $\Delta\nu = \frac{c}{2\eta L} \simeq 90$ GHz. We see that within the gain bandwidth there exist several longitudinal modes on which to lase. The relatively flat gain profile across neighbouring modes means a diode laser will frequently jump between modes (modehopping) if left uncontrolled.

Before we look at passive and active methods to control the spectral properties of diode lasers we must understand the theoretical limit and the causes of linewidth broadening.

4.1.2 Fundamental Linewidth

Before the invention of the first laser in 1960, Schawlow and Townes had calculated the fundamental spectral properties of 'Maser' light sources. The Schawlow-Townes [70] formula predicts a fundamental linewidth (FWHM) of a laser resonator caused by

random phase noise of spontaneous emission (quantum limited)[1];

$$\Delta\nu_{\text{fund}} = \frac{2\pi h\nu}{P}\gamma_c^2 \tag{4.1}$$

where ν is the oscillation frequency (lasing mode), P is the power in the cavity and γ_c is the cavity loss rate. For a 780 nm diode laser with an output power of 1 mW and a cavity loss rate of 30 GHz[2] we find a fundamental linewidth of 1.4 MHz.

Early diode laser experimental measurements [71] showed linewidths two orders of magnitude greater than this value. A linewidth enhancement factor, α was derived (also known as Henry's α parameter after the discoverer Charles Henry [72]), modifying Equation 4.1 to become

$$\Delta\nu_{\text{DL}} = \frac{2\pi h\nu}{P}\gamma_c^2(1+\alpha^2). \tag{4.2}$$

The α parameter is difficult to calculate and depends upon the difference of the real and imaginary parts of the refractive index of the gain medium, but it is found to range from 1.5 to 6. It is due to phase-amplitude coupling in which a change in amplitude, possibly by spontaneous emission, affects the refractive index and thus phase of laser output.

This is the theoretical linewidth of a semiconductor laser and we should expect values greater than this due to noise sources in the laboratory and imperfections in the diode construction which we discuss in the following section.

4.1.3 Noise

The effective cavity length, and thus wavelength, of diode lasers is affected mainly by two inter-related factors; temperature and current. Variations in the injection current[3] create variations in the refractive index of the semiconductor and thus change the effective path length. Temperature can physically change the cavity length (expansion/contraction), but can also affect the permittivity of the semiconductor and thus alter the refractive index and vice versa. Temperature also has a strong effect upon the threshold current

[1] This formula does not consider parasitic losses and so is the linewidth of an 'ideal' laser

[2] The FWHM of a Fabry-Perot cavity mode $\Delta\nu_{\text{FP}} = \frac{c}{2\eta L}\frac{1-R}{\pi\sqrt{R}}$, where $\frac{c}{2\eta L}$ is the FSR and R is the reflectivity of the facets. The refractive index of AlGaAs semiconductor is $\eta_{\text{SC}} \simeq 3.3$, so $R = \left[(\eta_{\text{air}} - \eta_{\text{SC}})/(\eta_{\text{air}} + \eta_{\text{SC}})\right]^2 \simeq 0.3$.

[3] The effect of the current change on wavelength is mainly due to heat produced by resistance to electron flow (Joule heating) on normal tuning timescales ($< 1\,\mu s$) [63]

and thus the current to power characteristics. The amplitude and timescales of temperature and current variations depend upon their source, such as the control electronics or environment. Mechanical disturbances also exist, which affect alignment and optical feedback to which laser diodes are exceptionally sensitive. The sources of such unwanted disturbances (noise) fall into three categories:

Fundamental Noise

These sources of noise are due to the material properties laser diode semiconductor such as shot noise, caused by random spontaneous emission which can couple into the lasing mode causing a small variations in phase and amplitude, and Johnson noise caused by thermal excitation of charge carriers. Fundamental noise is also known as the quantum noise and phase jitter and is the mechanism behind the Schawlow-Townes fundamental linewidth. The spectral distribution of this noise is flat (i.e. white noise).

Environmental Noise

This noise source is the most probable source of large disturbances of the laser, such as modehopping. The most obvious source of environmental noise is the experimenter, whether through mechanical vibration of the optical bench or by thermal air currents. Other significant sources include 50Hz mains power 'ripple', air turbulence, mechanical vibration of mounts and high frequency noise from RF sources and switch-mode power supplies.

Normally small noise sources may be amplified via mechanical resonances or optical coupling back into the diode as these lasers are very sensitive to optical feedback due to the short cavity response times and high gain. This can be a serious problem especially with magneto-optical traps where retro-reflected beams are required. If uncontrolled this will result in large (GHz) variations in wavelength and modehopping.

The majority of environmental noise (excluding specific) sources are low frequency, usually less than 1 kHz. Technically, this type of noise is known as drift or random walk and generally obeys a f^{-2} dependence upon frequency [73].

Artificial Noise

Artificial noise is similar to environmental noise in the majority of its sources, but it is intentionally added (usually unavoidably) to the laser in an attempt to control the laser output. It is common practice to modulate, or dither, the laser output either directly by applying an RF signal to the injection current or by the use of an external electro-optical modulator (EOM, Section 7.1.3). These sources add sidebands onto the laser spectrum, the number of which depends on the modulation depth (Section 4.3.3). When stabilizing the laser to some frequency discriminator, such an an atomic absorption, the detector will introduce shot and Johnson noise, although this noise can be reduced by the use of a phase sensitive detector (or lock -in amplifier), which is discussed in Section 4.3.

Other detection noise would be that of the frequency discriminator itself, such as mechanical instabilities in Fabry-Perot reference cavities or fluctuating magnetic fields shifting an absorption resonance. Another source of artificial noise is that of the control electronics; this can be fundamental noise of components, such as resistor noise, or noise from power sources, amplifiers and pickup. In the case of injection current noise, the artificial noise is difficult to distinguish from the fundamental laser diode noise. Artificial noise generally follows a f^1 power law and is known as pink or flicker noise.

4.1.4 External Cavity

The very short cavity length ($\sim 0.5\,\mathrm{mm}$) and high broadband gain of the semiconductor chip allows significant gain to short-lived fluctuations in wavelength, this property also makes diode lasers very sensitive to feedback from external optics. One can use this to reduce the linewidth and control the drift of the lasing wavelength via an external cavity.

The external cavity can limit the laser oscillation to a single mode and, if the external cavity has a narrower mode linewidth, one may also reduce the laser linewidth. The linewidth of a cavity is proportional to the energy loss per round trip therefore by increasing the cavity length one can reduce the cavity linewidth. The addition of a frequency selective cavity reflector, such as a diffraction grating, can further reduce the

cavity linewidth.

Various schemes have been presented for optical feedback via gratings [74] or Fabry-Perot cavities [75]. The method we employ is known as the 'Littrow' configuration and involves a grating placed after the collimating lens so that the first order couples around 10-15% back into the laser cavity whilst the zeroth order is used as the output beam (Figure 4.2). The spectral resolution of the grating $\Delta\lambda = \lambda/N_G$ for the first mode depends upon the wavelength λ and the number of illuminated grooves N_G. In our system, a 2mm diameter 780 nm beam illuminates a holographic grating with 1800 grooves/mm, the grating resolution is 100 GHz. This nearly limits the laser to a single internal mode of the semiconductor cavity, whilst the extended outer cavity formed by the grating and back facet of the chip creates sharper (<MHz width, mode spacing 4 GHz) modes, see Figure 4.3.

An external grating also allows fine control over wavelength tuning when a piezo electric transducer is used to change the tuning angle. The lasing wavelength can be controlled via current (-3 GHz mA^{-1}) and temperature (-20 GHz K^{-1}), but not with the fine control (100 MHz V^{-1}) of grating tuning. Genty et al [76] analysed the linewidth of a 780 nm ECDL with an external cavity length of 12 cm (much greater than ours) and found linewidths down to 8 kHz. Our ECDL configuration is based on a design by Arnold et al, who measured a linewidth of 350 kHz over 200 ms [77].

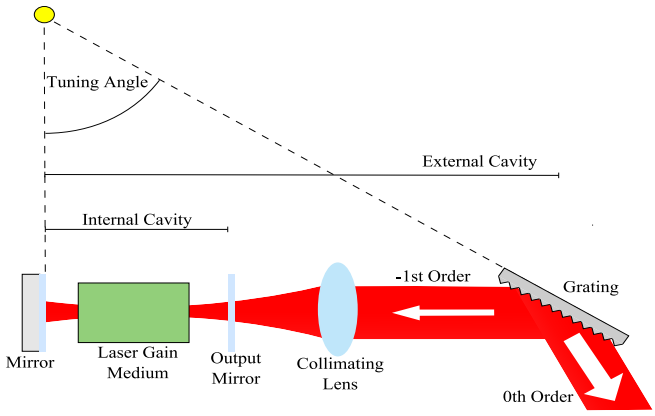

FIGURE 4.2: *Schematic of an External Cavity Diode Laser (ECDL) in the Littrow configuration. The output from the internal cavity is collimated and diffracted from an external grating, the spectral response of which can be adjusted by rotation of the tuning angle (this is equivalent to rotating the grating around the central axis) or changing the external cavity path length. In the Littrow regime the -1st order is reflected back along the incident direction (about 10-15% of the output is in this order) and the 0th order is used as the laser output.*

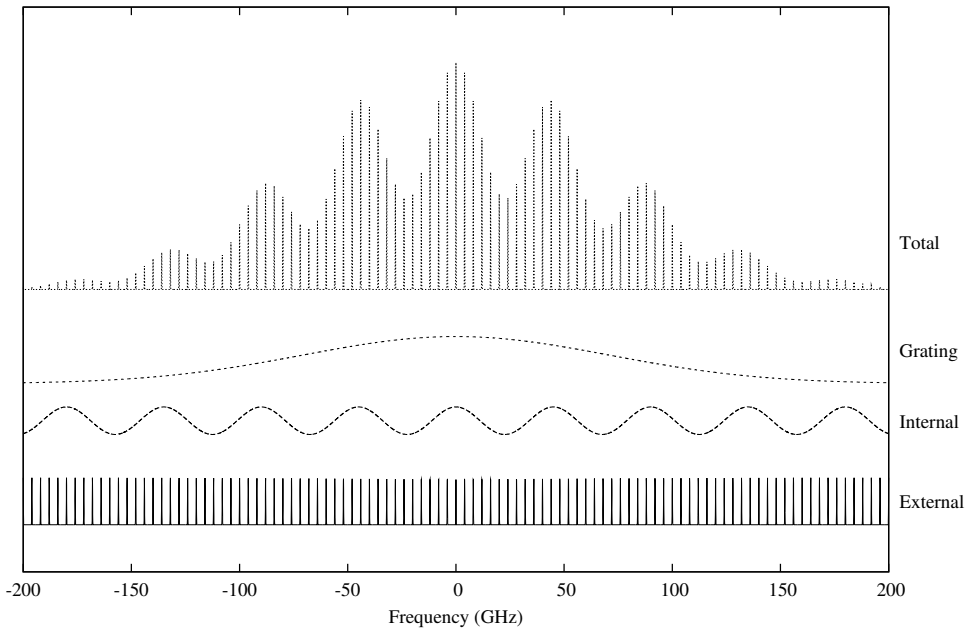

FIGURE 4.3: *External cavity diode laser mode structure using realistic and measured cavity values from Section 4.2. The narrow, closely spaced lines at the bottom are the external modes formed by the cavity between the grating and diode back-facet. The modes directly above are due to the semiconductor cavity and above those is the grating spectral response. The (magnified) combined structure is shown at the top. This figure represents the possible modes in which the diode may lase. During lasing, the strongest mode will be amplified and neighbouring modes suppressed.*

4.2 Southampton Diode Lasers

4.2.1 Design

The Southampton diode lasers are based on a design[4] by Arnold et al [77] in which a standard optical mirror mount is converted into an ECDL with only a few simple mount additions. The final refined ECDL (designed within our group) was machined in the Southampton physics workshop of which Figure 4.4 shows an exploded-type schematic view.

Two types of single-mode diode laser are used in the project: Sanyo DL-7401-201S and Sharp GH07895A6C. The latter is slightly higher power (Sharp max. 95 mW, c.f. Sanyo max. 80 mW) but is no longer produced. Apart from the power, these two diodes are practically identical.

[4]Commonly known as the 'Boshier design' after the group leader.

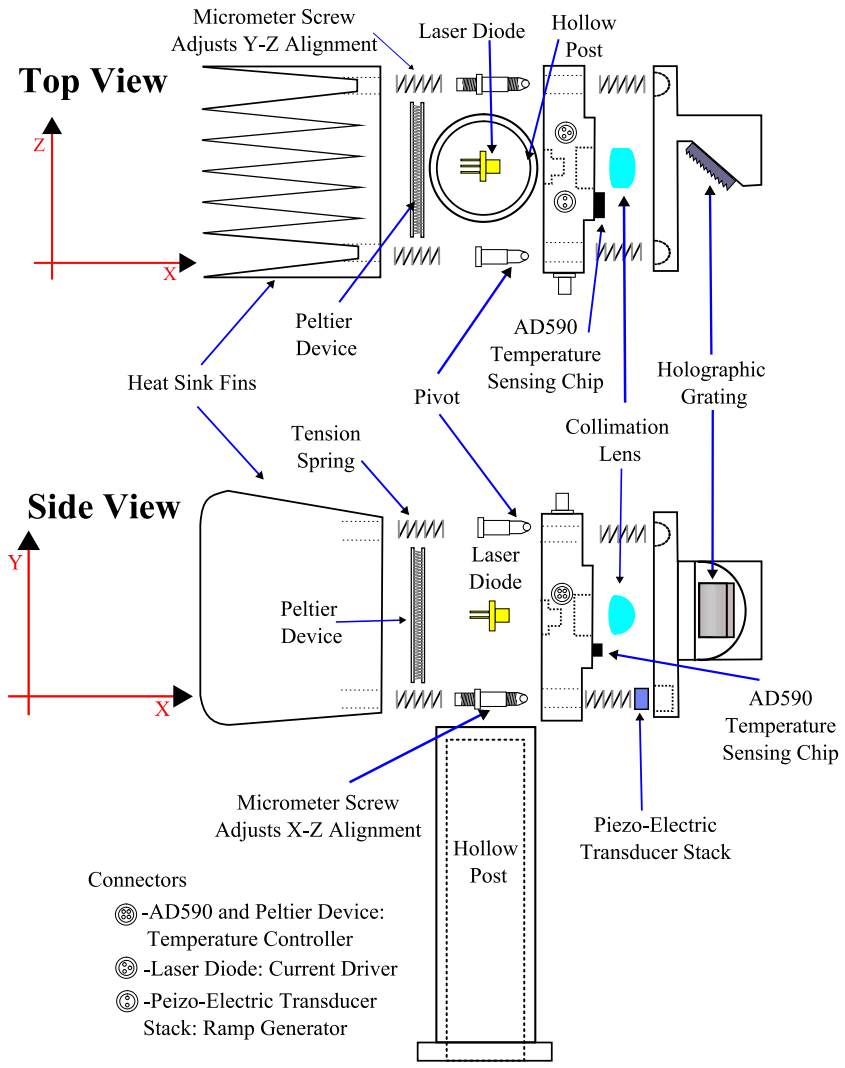

FIGURE 4.4: *Exploded schematic of the Southampton diode laser. The centre piece contains the diode, lens, temperature-sensing chip and connectors. The finned heat sink is tightly pulled against the Peltier device and the centre mount with springs. The micrometer screws push against the front grating mount (tensioned with springs) to allow coarse grating wavelength ($X-Z$ angle) and feedback ($Y-Z$ angle) alignment. The piezo-electic transducer (PZT) stack provides fine adjustment of the wavelength tuning ($X-Z$ angle). The laser diode polarization must be rotated to match the grating plane. Not to scale.*

The design uses heat sink 'fins' to remove heat produced by the Peltier device; a semiconductor p-n junction which causes heat to flow across the junction when a current is applied. The polarity and level of current dictates the rate and direction of heat flow. The temperature of the diode mount is measured by an AD590 temperature sensing chip which is read by a Newport 300B temperature controller. The 300B checks the temperature against a set value and adjusts the current to the Peltier device so as to stabilize the temperature to the set point. The specifications quote a temperature stability of

0.005℃ (long term) but this figure depends upon the efficiency of the heat sink.

The laser current is controlled by a Newport 505B current driver with a control resolution of 0.01 mA. The current noise is mainly due to 50 Hz ripple at a quoted value of (0.2 − 2 mA r.m.s). The current can be externally modulated up to 10 kHz (Low BW) or 500 kHz (High BW). The higher bandwidth introduces ten times more current noise.

The diode laser output is collimated by a Thorlabs C240TME-B lens (focal length=8mm, 0.50 NA) and the external cavity uses an Edmund Optics holographic diffraction grating with 1800 lines/mm. The angle of the diffraction grating is controlled by a Thorlabs AE0203D04F low voltage PZT stack. This allows fine tuning of the laser frequency (330 MHz V^{-1}). Coarse wavelength tuning and cavity alignment is adjusted with micrometer screws. The laser is mounted on a hollow 3 inch post, this is to cut down on thermal contact with the optical bench so that the Peltier device only removes heat from the diode mount and not the table.

4.2.2 Power Characteristics

Figure 4.5 displays the dependence of optical output power on injection current for the Sanyo diodes in the ECDL. The maximum output power is around 60 mW, which is lower than the diode specification due to power reflected back into the diode in the first order of the diffraction grating. The threshold current, at which gain mechanisms in the semiconductor overcome loss, is measured to be 30.72±0.02 mA. The gradient of the curve after this point is the external differential efficiency (or power extraction efficiency [78]) which can be used to calculate the loss mechanisms of the laser semiconductor.

4.2.3 Tuning Characteristics

Figure 4.6 shows the variation in wavelength of the lasing modes as the drive current is increased. The graph shows a series of widely spaced diagonal lines which are made up of smaller steps.

The wide spaced lines are the modes of the semiconductor internal cavity separated by the free spectral range. The length of the cavity can be calculated from the FSR of a

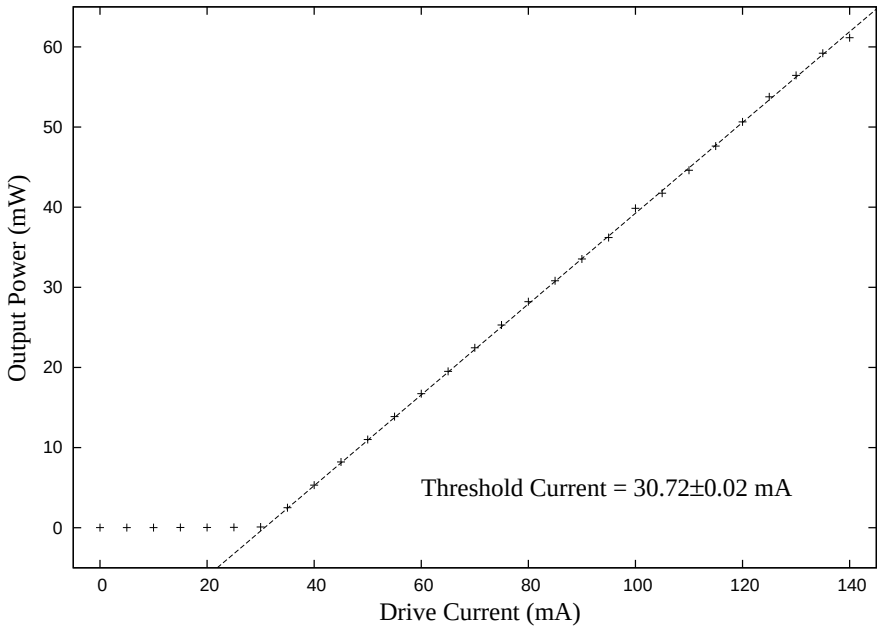

FIGURE 4.5: *Dependence of the output optical power upon injection current of the Sanyo DL7140-201S laser diodes. Power measured using a Newport 840 optical power meter.*

Fabry-Perot resonator. The separation between modes, in units of nm, is

$$L_{\mathrm{SC}} = \frac{\lambda^2}{2\eta_{\mathrm{SC}}\Delta\lambda} \tag{4.3}$$

The Sanyo semiconductor is AlGaAs which has a refractive index $\eta_{\mathrm{SC}} \simeq 3.3$. The difference in wavelength between modes in Figure 4.6 is $\Delta\lambda = 0.09\,\mathrm{nm}$ (90 GHz) leading to a cavity length of $L = 1\,\mathrm{mm}$. The manufacturer would not supply figures for the chip sizes, but the literature [63, 68] quotes typical semiconductor lengths of $\simeq 300 - 500\mu\mathrm{m}$. The larger measured size for the Sanyo diodes could be for greater heat dissipation as these diode lasers output more power than the norm ($\simeq 5 - 15\,\mathrm{mW}$) or the cavity length measurement is inaccurate as the p-n junction architecture is more complicated[5]. The wide spaced lines appear to be split into two or more sections which may indicate the linewidth of internal modes, but the splittings are inconsistent and very wide (in the order of, or greater than, the free spectral range).

The smaller steps in Figure 4.6 are the modes of the external cavity. Using Equation 4.3, the external cavity modes are separated by 0.009 nm (4.5 GHz) from which we calculate

[5]Commercial diode lasers use strained multiple quantum well structures. This structure results in lower threshold currents and thus higher powers due to reduced electron states in the conduction band [68]

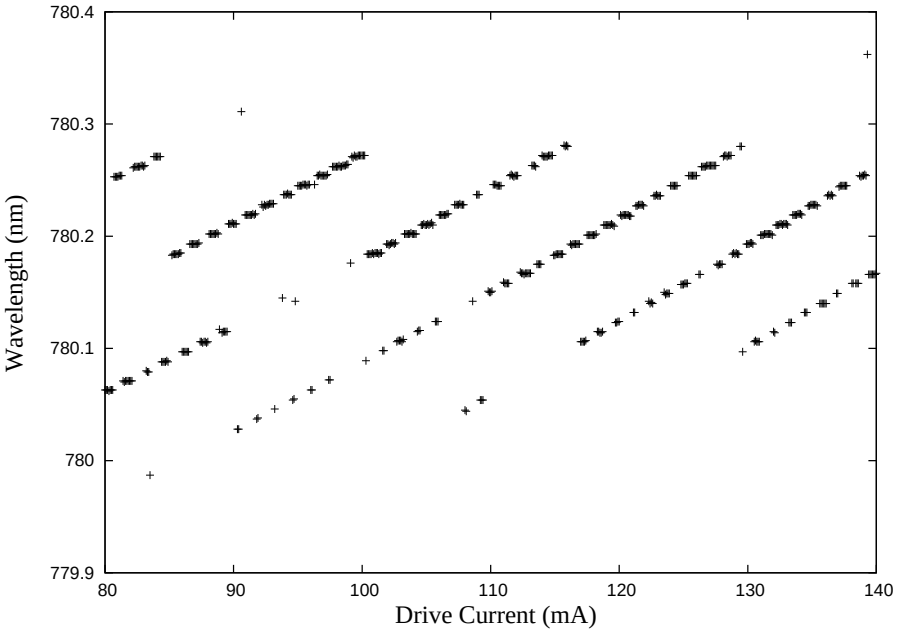

FIGURE 4.6: *Lasing modes of the Southampton lasers with respect to drive current*

the cavity length as 33 mm, which agrees with the mount design. The lasing modes are confined to a region from 780.0 nm to 780.3 nm. We calculated the resolution of the grating as $\sim$ 100 GHz in Section 4.1.4 which leads to a wavelength range of 0.2 nm at 780 nm which is reasonably close to the measured value.

4.3 Frequency Stabilization

From the specifications of the equipment outlined above, we can at best expect the laser to be stable to within several megahertz over a time span of seconds. This is far from the stability required to carry out efficient cooling of Rubidium atoms, and furthermore we have no absolute wavelength reference to tune the diode laser. We must consider more active methods to stabilize the laser frequency. To achieve the lowest temperatures in the magneto-optical trap, the trapping laser needs to be stabilized to a fraction of the atomic linewidth of the the cooled species. Rubidium has a linewidth of 6 MHz, Doppler cooling theory shows that the lowest temperature is achieved for a laser detuned by half the transition linewidth (see Section 5.1). Thus the laser should ideally be stabilized to less than a MHz for as long as possible. In this section we discuss methods in which to actively stabilize the laser to a reference frequency.

4.3.1 Active Stabilization

To control the laser frequency over long timescales to within a MHz, we need a feedback system which continually monitors the laser output and adjusts the wavelength according to its deviation from a specified point. In this state we refer to the laser as 'locked'. An electronic correction signal (known as the 'error signal') which is related to the direction and amount by which the laser deviates from a desired 'set point', feeds back to the laser driver, piezo transducer or an external modulator.

The preferable qualities of a frequency reference would be a function with a zero at the required frequency and an amplitude with opposite polarities either side extending in frequency to infinity; the most simple function (but not technically ideal) to this is a linear function. In such a situation the error signal will always correct the laser frequency no matter the deviation. In reality, no stable ideal frequency reference exists and we would always be limited by the finite gain of the control electronics. A close approximation to an ideal frequency reference is the change of refractive index of an atomic vapour across a resonance, known as an atomic dispersion curve, in which there is a zero on resonance, opposite polarity lobes on either side and a nearly linear gradient

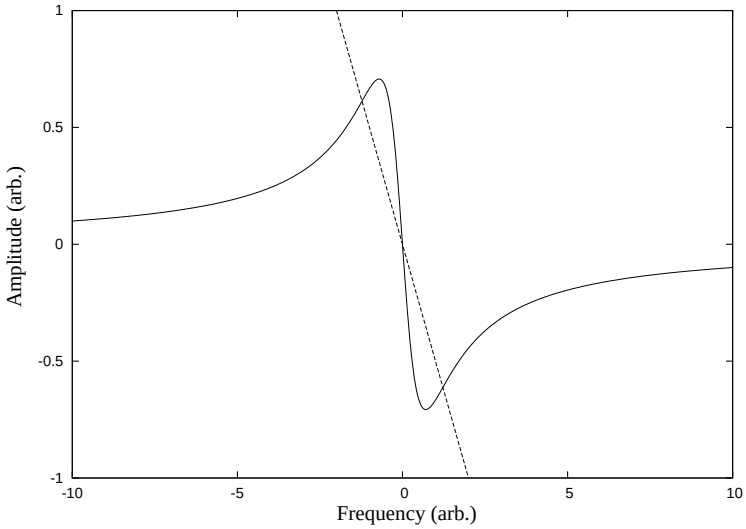

FIGURE 4.7: *Two types of error signal. The dashed linear curve is the most simple error signal with a zero at the lock point and an increasing amplitude either side with opposite polarities. The solid curve, which is equal to the real part of an atomic susceptibility (dispersion curve), is a more practical error discriminator as its does not result in an infinite response. The exact gradients are unimportant in this figure.*

across resonance (Figure 4.7). The frequencies in which a reference supplies an adequate error signal is known as the capture region.

Spectroscopy performed with glass vapour cells containing a dilute sample of low vapour pressure gas are ideal for frequency discriminators [79, 80]. One can use the side of an absorption peak to provide an error signal so that changes in the laser frequency lead to an increase or decrease in detected signal [81]. Doppler broadened lines offer a large capture region, but the gradient is very shallow resulting in a small error signal for large deviations. The Doppler-free spectra outlined in Chapter 3 have narrow resonances and so make very sensitive frequency discriminators, but the capture region is small. Locking a laser to the side of a feature works well, but one would like to lock to the centre of the transition to know the exact frequency and for symmetric capture regions around the resonance. In the next section we discuss the three most popular methods for producing an atomic dispersion shaped feature.

4.3.2 Review of Techniques

In Chapter 3 we discussed pump-probe spectroscopy which used counter-propagating pump and probe beams to resolve sub-Doppler absorption features and is fundamental

to all of the following techniques. We are primarily interested in methods to convert the Lorentzian absorption curve into a dispersion-shaped feature. The final choice was Frequency Modulation Spectroscopy (FMS), but we shall first review the main contenders and discuss their suitability to our setup.

4.3.2.1 Dichroic Atomic Vapour Laser Lock

Dichroic atomic vapour laser locking (DAVLL) has been used with Doppler broadened [82] and Doppler-free [83] spectroscopy. A small DC magnetic field (tens of Gauss for sub-Doppler features to hundreds of Gauss for Doppler broadened features) is applied parallel to the laser beams, see Figure 4.8, so that the magnetic sub-levels lose their degeneracy. The linearly polarized probe beam, composed of σ^+ and σ^- polarizations,

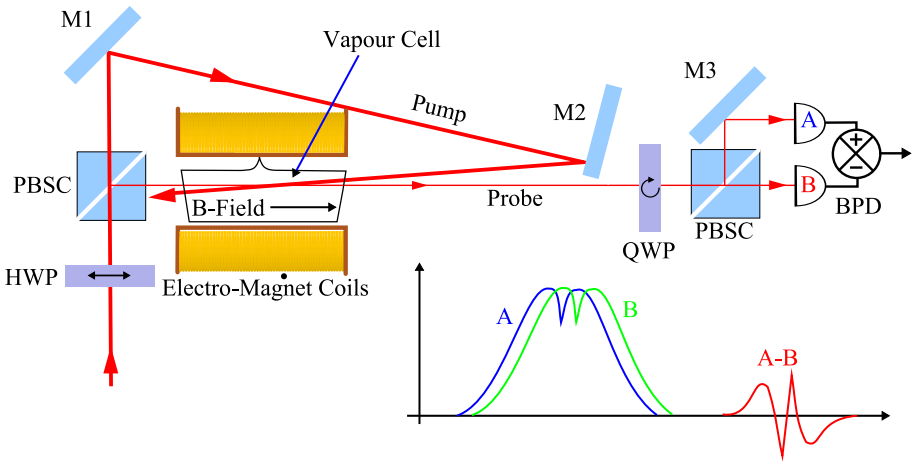

FIGURE 4.8: *Basic setup for DAVLL [83]. The laser beam is split into a probe and pump beam by a polarizing beam splitter cube, the intensity of each beam is controlled by a half wave plate. The atoms in the vapour cell experience a uniform magnetic field parallel to the beam propagation. The m_F states are Zeeman shifted by an amount proportional to the applied field. $+m_F$ and $-m_F$ levels are shifted in opposite directions. The σ^+ and σ^- components of the probe beam will see absorption lines shifted relative to one another. Each polarization component is separately detected and subtracted from one another.*

is passed through the vapour cell counter-propagating to the pump beam (as in pump probe spectroscopy). The selection rules dictate that the σ^+ (σ^-) causes a transition between the $|F, m_\mathrm{F}\rangle \rightarrow |F', m'_\mathrm{F} = m_\mathrm{F} + 1\rangle$ ($|F, m_\mathrm{F}\rangle \rightarrow |F', m'_\mathrm{F} = m_\mathrm{F} - 1\rangle$) levels. One then uses a polarizing beam-splitter to separate the components, each of which are monitored separately. The Zeeman effect causes the m_F and $-m_\mathrm{F}$ states to be shifted from degeneracy in opposite directions, therefore the σ^+ will be absorbed at a different

frequency than the σ^- component. The two detectors hence record Lorentzian profiles (Voigt profiles in the Doppler broadened setup) which are separated in frequency from one another by an amount dependent on the applied magnetic field. One then subtracts one trace from the other and a dispersion-like signal is produced.

4.3.2.2 Polarization Spectroscopy

C. Wieman and T. Hänsch, in 1976, demonstrated a Doppler-free spectroscopic technique that relied upon an induced birefringence in atomic vapour [84]. They also noted that a dispersion-like signal could be generated that was ideal for laser 'locking' without the need for modulation.

The pump-probe set up is very similar to Chapter 3: the pump beam is circularly polarized but the probe beam is linearly polarized at 45 degrees to a polarizing beam splitter cube which samples the beam after the vapour cell (see Figure 4.9). If no polarization effects occur through the vapour cell, each detector will record equal intensities which are subtracted from one another by the balanced detector and so no net signal is recorded.

Birefringence is induced by the pump beam due to the anisotropy in ground state populations is produced when σ^+ circularly polarized light optically pumps atoms into

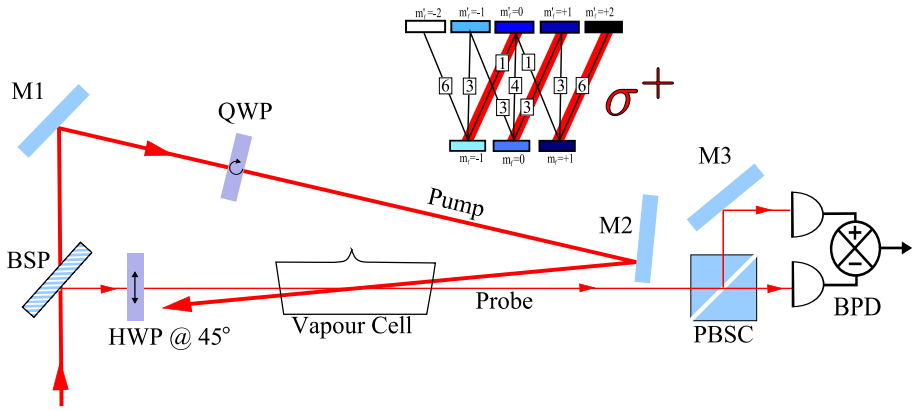

FIGURE 4.9: *Basic setup for polarization spectroscopy [80]. The energy level diagram at the top shows the transitions between m_F levels with the relative strengths of each transition labeled (the magnitude of each transition is relative to the weakest). One can see that the populations are moved to more positive m_F levels as they are pumped with σ^+ polarized light. The difference in population between the lower and upper F states affects the absorption of the probe beam. Negative m_F states absorb less photons than the positive m_F states due to lower ground state populations. The difference in absorption of the probe beam components is monitored with a polarizing beam splitter cube and a balanced photodetector.*

the positive m_F states. As before, the probe beam can be decomposed into σ^+ and σ^- components. The σ^+ component of the probe beam will experience enhanced absorption due to the greater ground state populations, whereas the σ^- will experience a reduction in absorption. The relation between absorption and refractive index, quantified by the Kramers-Kronig relation, means that changes in absorption also affect the refractive properties of the medium. Near resonance, the σ^+ and σ^- probe components travel at different speeds through the vapour which results in a relative phase difference. Reconstructing the net polarization from the circular components results in a polarization which changes from elliptical near resonance, to linear on resonance. The major axis of the elliptical polarization rotates through the resonance and so a dispersion shaped signal is mapped out by the balanced detector. The signal has a good S/N ratio, insensitivity to laser intensity noise and does not require modulation electronics which may involve extra noise sources and complexity. A similar technique which uses a 'bow-tie' cavity, instead of atomic vapour, was developed by Hänsch and Couillaud [85]. In this case the birefringence was induced by reflection from angled mirrors.

The two techniques outlined above are very popular for stabilizing lasers for magneto-optical traps, and it will be shown in Chapter 5 that the lasers need to be offset from resonance in order to cool and trap the atoms. The detuning is commonly done with acousto-optical modulators, but these are costly and one sacrifices a fraction of beam power. We detune the lasers from resonance by applying a uniform magnetic field along the vapour cell and Zeeman shift the absorption line. DAVLL also uses a magnetic field to shift the atomic resonances but relies on the difference in Zeeman shift of the m_F states to create the desired signal, hence the zero-crossing is always at the zero magnetic field frequency (an offset can be applied by reducing one of the balanced detector inputs, but this results in an asymmetrical feature and is limited by the spectral width of the absorption feature). Polarization spectroscopy relies upon optical pumping between degenerate m_F states and although the dispersion shape should remain under applied magnetic field it is severely distorted by the neighbouring m_F states. The largest S/N ratio is found when the earth's magnetic field is nulled [80].

Another technique called 'Frequency Modulation Spectroscopy' modulates the laser frequency to produce dispersion-shaped spectral features. Application of a magnetic field

can shift the absorption features without adversely deforming their shape and so we have used this to lock our lasers.

4.3.3 Frequency Modulation Spectroscopy

One can use lock-in detection techniques to achieve both high S/N and an ideal error signal. Laser diodes have very little frequency noise above 1 MHz, so by modulating the probe (or pump or both) beam at frequencies above this region and demodulating the signal after the detector one can gain a high S/N ratio by filtering out most of noise outside of the frequency of interest.

Modulation techniques fall into two camps: either the modulation frequency is less than the width of the feature of interest, or vice versa. These two areas are called wavelength modulation (WM) and frequency modulation (FM) respectively [86]. WM is technically easier to implement when the features of interest are in the MHz region, but FM contains more information as both the amplitude *and* refractive index of absorption features can be measured. Frequency modulation spectroscopy was first developed in the microwave region [87] and the technique was brought into the optical regime by Bjorklund [88] in 1980. A comparable technique using optical cavities was developed by Drever et al [89] as a sensitive detector for gravity wave interferometers. This technique was shown to be theoretically able to resolve absorption features down to the quantum noise level [90].

FM spectroscopy works as follows (Figure 4.10): The laser frequency is modulated either directly via the drive current or via the phase of the optical field with an electro-optic modulator. This modulation produces sidebands onto the central carrier; the number and strength of the sidebands depends upon the modulation index[6]. Ideal FM spectroscopy requires only two sidebands which are separated from the carrier by a modulation frequency larger than the feature of interest. In this regime only one sideband or carrier interacts with the absorption feature. The signal is then detected and demodulated, using a technique known as Heterodyne or Phase-Sensitive detection, by multiplying the detected signal with the modulation frequency. The resulting output

[6]Modulation index $\beta = \Delta f / f_{\mathrm{m}}$. f_{m} is the modulation frequency and Δf is the maximum frequency deviation of the sidebands, i.e. the highest significant harmonic of f_{m}. FM requires $\beta \ll 1$ so that there are just two sidebands

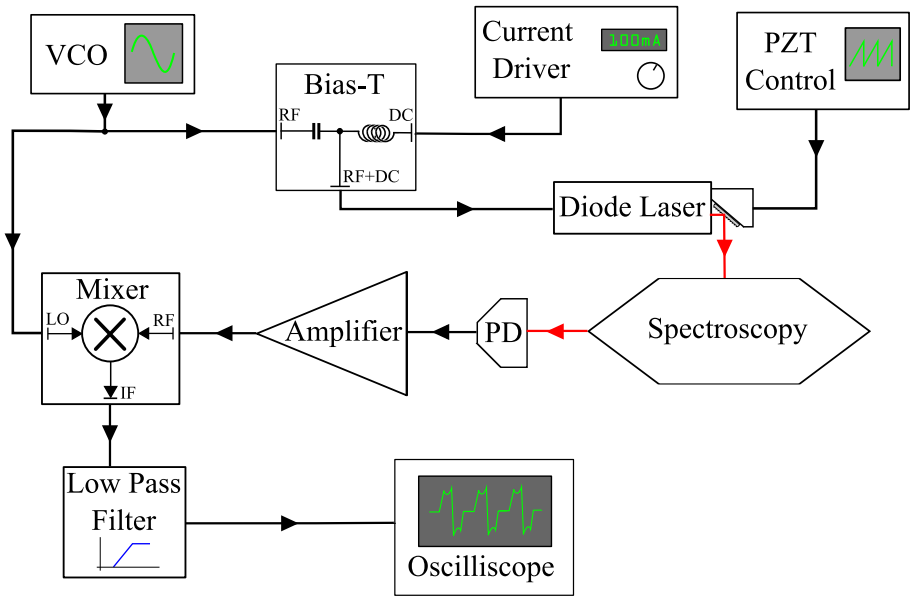

FIGURE 4.10: *Setup for modulation/demodulation of FM spectroscopy. Abbreviations; VCO - voltage controlled oscillator, PZT - piezo-electric transducer, PD - photodiode, LO - local oscillator, IF - intermodulation frequency. (RF and DC as usual). The PZT control applies a ramping voltage to scan the grating across the resonance. The Bias-T applies an RF modulation onto the DC drive current. The signal from the PD is amplified and fed to the mixer which multiplies the input signal (RF) with a local oscillator reference (LO). The mixer output (IF) consists of a DC signal (proportional to the FMS signal) and a high frequency term at twice the VCO frequency. The low pass filter removes the high frequency term leaving the spectroscopy signal. This signal is then used to stabilize the laser.*

has a component at twice the modulation frequency with may be removed with a low pass filter and a DC offset proportional to the difference in absorption of the carrier frequency and sidebands. The demodulation process can be thought of as each sideband, with relative phase π, beating against the carrier. If there is no absorbing feature then perfect cancellation between the two beats is found. When one sideband is absorbed, the magnitude *and* the phase (via the refractive index) of the beat are altered and a signal is seen. To understand and model how the signal changes with respect to the atomic absorption and refractive index, we shall examine mathematically the FM lineshape below.

4.3.4 Frequency Modulation Spectroscopy Theory

Following the derivation by Bjorklund [88], the modulated laser spectrum can be modeled as the sum of fields separated from the original laser frequency ω_c at harmonics of the modulation frequency ω_M with amplitudes weighted by Bessel functions $J_n(\beta)$ of

modulation index β (Jacobi-Anger expansion),

$$E_{\mathrm{M}}(t) = \frac{E_0}{2} \sum_{n=-\infty}^{\infty} J_{\mathrm{n}}(\beta) e^{-i(\omega_{\mathrm{c}} + n\omega_{\mathrm{M}})t} + c.c \tag{4.4}$$

When the modulation index is much less than unity, one can treat the spectrum as a central carrier frequency with two sidebands at $\pm\omega_M$. The absorption of the beam after passing through the vapour cell of length L is hence

$$E_{\mathrm{M}}(t) = \frac{E_0}{2}\Big\{T_0 J_0(\beta) e^{i\omega_{\mathrm{c}}t} + T_1 J_1(\beta) e^{i(\omega_{\mathrm{c}}+\omega_{\mathrm{M}})t} + T_{-1} J_{-1}(\beta) e^{i(\omega_{\mathrm{c}}-\omega_{\mathrm{M}})t}\Big\} \tag{4.5}$$

where

$$T_{\mathrm{n}} = \exp\big[-L\big(\alpha_{\mathrm{n}}/2 + i\eta_{\mathrm{n}}(\omega_{\mathrm{c}} + n\omega_{\mathrm{M}})\big)\big] = \exp[-\theta_{\mathrm{n}} - i\sigma_{\mathrm{n}}] \tag{4.6}$$

$$n = (-1, 0, 1) \tag{4.7}$$

and α_{n} and η_{n} are the absorption and refractive index of each frequency component (which are calculated in Appendix C). The photodetector measures the intensity of this beam which is proportional to the square of the field $I_{\mathrm{M}}(t) = \frac{1}{2}\epsilon_0 c|E_{\mathrm{M}}(t)|^2$. Substituting Equation 4.5 into the measured intensity and neglecting the $J_1^2(\beta)$ terms,

$$I_{\mathrm{M}}(t) = \frac{1}{2}\epsilon_0 c E_0^2 e^{-2\theta_0}\Big[1 + \Big\{\Big(e^w\cos(x) - e^y\cos(z)\Big)J_1(\beta)\cos(\omega_{\mathrm{M}}t) + \Big(e^w\sin(x) - e^y\sin(z)\Big)J_1(\beta)\sin(\omega_{\mathrm{M}}t)\Big\}\Big] \tag{4.8}$$

where $w = |\theta_0 - \theta_1|$, $x = |\sigma_1 - \sigma_0|$, $y = |\theta_0 - \theta_{-1}|$, $z = |\sigma_0 - \sigma_{-1}|$ are the differences in phase (σ_n) and amplitude (θ_n) between the sidebands and carrier. Using $e^a \simeq 1 + a$, $\cos(a) \simeq 1$ and $\sin(a) \simeq a$ and neglecting the product of small terms we can assume w, x, y, z to be small and reduce Equation 4.8 to;

$$I_{\mathrm{M}}(t) = \frac{1}{2}\epsilon_0 c E_0^2 e^{-2\theta_0}\Big[1 + \big(\theta_{-1} - \theta_1\big)J_1(\beta)\cos(\omega_{\mathrm{M}}t) + \big(\sigma_{-1} + \sigma_1 - 2\sigma_0\big)J_1(\beta)\sin(\omega_{\mathrm{M}}t)\Big] \tag{4.9}$$

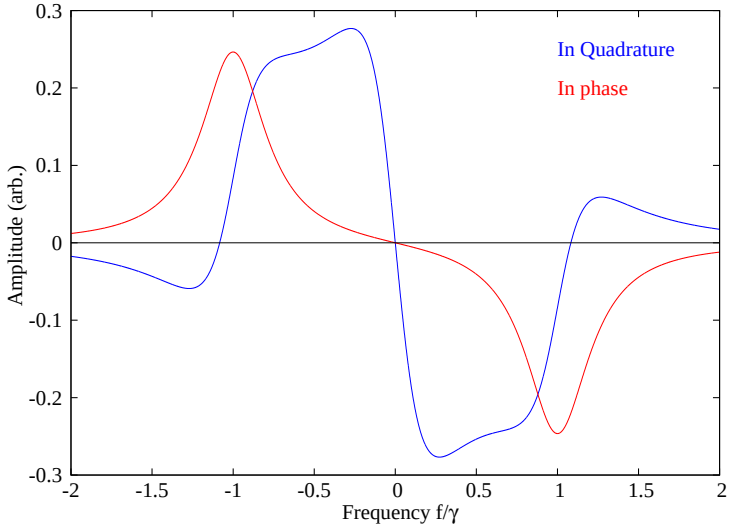

FIGURE 4.11: *Theoretical lineshapes of frequency modulation spectroscopy.*

We can now see how the phase and amplitude can be obtained; the in-phase (cosine) component is equal to the difference in absorption between the two sidebands, whereas the in-quadrature (sine) component is the difference in phase between the two sidebands and the carrier. In the FM regime, the sidebands are separated enough that any change of one component by the absorption feature does not affect any other component. i.e. if the component affected is the +1 sideband, then $\theta_{-1} = \theta_0 = \theta$ is the constant absorption offset and $\sigma_{-1} = \sigma_0 = \sigma$ is the constant dispersion offset. We can now define the changes of the +1 sideband with respect to these constants, $\Delta\theta = \theta_1 - \theta$ and $\Delta\sigma = \sigma_0 - \sigma$. We arrive at a simple expression for the FM lineshape,

$$I_{\mathrm{M}}(t) = \frac{\epsilon_0 c E_0^2 e^{-2\theta_0}}{2}(1 - \Delta\theta J_1(\beta)\cos(\omega_{\mathrm{M}}t) + \Delta\sigma J_1(\beta)\sin(\omega_{\mathrm{M}}t)) \tag{4.10}$$

Figure 4.11 shows the lineshape as calculated with Equation 4.10. The in-quadrature feature has a nearly ideal lineshape for use as a frequency reference. There is a nearly linear gradient around the resonance frequency and by using higher modulation frequencies the lobes of the in-quadrature feature can be broadened thus increasing the capture range. We will be limited in modulation frequency to 30 MHz by the separation between absorption features.

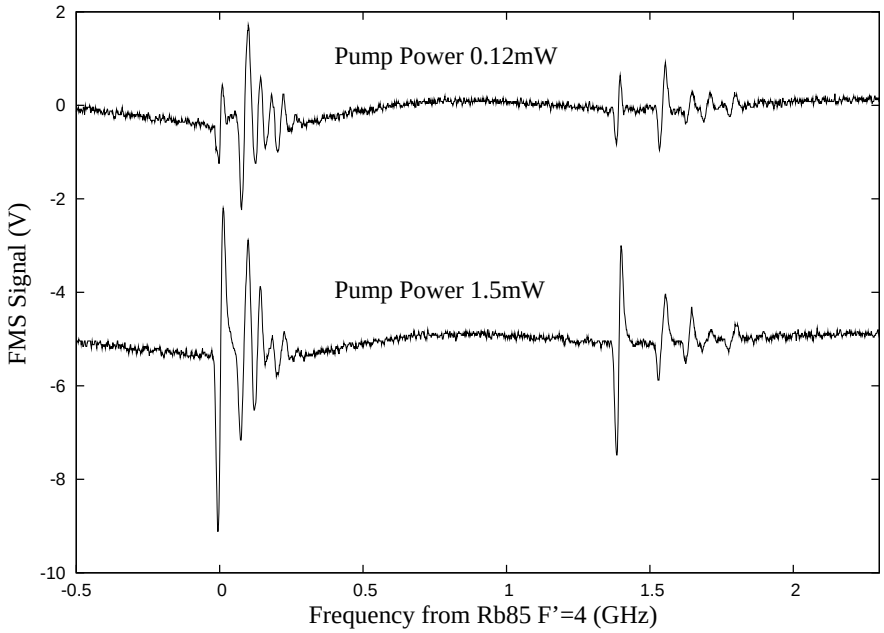

FIGURE 4.12: *The frequency modulation spectrum of ^{85}Rb (Left) and ^{87}Rb (Right). The upper trace shows an unsaturated (*$0.6\times$ *saturation intensity) FM spectra whereas the lower trace (offset for clarity) shows the saturated (*$7.5\times$ *saturation intensity) case. The probe beam power is* $10\,\mu W$ *with a diameter* $4mm$.

4.3.5 Rubidium Frequency Modulation Spectra

Figure 4.12 shows the measured FM spectrum for Rubidium 85 and 87 for the $F = 3 \rightarrow F'$ and $F = 2 \rightarrow F'$ transitions, respectively. The modulation frequency is 25MHz and modulation index $\beta = 0.6$. The detector is a Thorlabs PDB110 Balanced detector (using only one input in this case), the output of which is sent to the demodulation circuit (see Appendix D). The output is then amplified with Stanford Research Systems SR570 pre-amplifier with a 10 kHz 12 dB low pass filter. The upper trace is the unsaturated spectrum, the lower is the saturated case. The height of the FMS peaks depends upon the gradient of the pump-probe peaks. As the $F = 3 \rightarrow F' = 4$ transition is closed and is not optically pumped into the lower ground state, the transition is weaker but also less broadened and so has a larger FMS peak at higher powers. This is ideal for Doppler cooling which also relies upon this 'closed' transition for exactly that reason. An added bonus of FM spectroscopy is the (near) removal of the Doppler background as the change in absorption between the sidebands is very small due to the large Doppler width. In Figure 4.12 we can see a small residual Doppler background (this reduction is even greater in WM spectroscopy due to the lower sideband separation).

4.4 Control Electronics

Now that we have a frequency discriminator signal we may feed it back into the laser control elements such as drive current, temperature controller or the grating piezo control so as to stabilize the laser frequency. One would be fortunate if the error signal could be fed directly into a control element and result in a perfect response, therefore the error signal must be conditioned so as to tailor the response to the control element. For example, a sharp sudden deviation would be ineffective when sent to a temperature controller which has a large time constant due to slow propagation of thermal waves. Luckily in this case there would be no negative results, but neither would there be a benefit. One must tailor the frequency spectrum of the error signal via filters and amplifiers to the control elements, such a device is known as a *servomechanism*, or just 'servo'.

The following analysis assumes the principles of control theory and the use of Laplace transforms, which are described explicitly in Appendix D.

4.4.1 PID Servo

The most popular type of servo controller is the PID which stands for Proportional, Integral and Differential. The simplest control law is proportional: The (Laplace Transformed) correction signal $w(s)$ is equal to the error signal $e(s)$ multiplied by a gain factor, C_{P},

$$w(s) = C_{\mathrm{P}}\, e(s) \tag{4.11}$$

There is no frequency dependence in the response. If we examine the closed-loop response of the proportional term we find,

$$w(s) = \frac{C_{\mathrm{P}}}{1 + C_{\mathrm{P}}} p(s) \tag{4.12}$$

The correction signal will faithfully follow the error signal and return the system to the set point p(s). This is generally true, but if we were to take the steady state values ($s \to 0$), we find $w(0) \neq p(0)$ as there will always be a difference $\frac{C_{\mathrm{P}}}{1+C_{\mathrm{P}}}$. The physical cause of this difference is the requirement for the signal to deviate from the set point in

order for proportional controller to respond, so there must always be some 'sag' in the system. This is known as 'proportional droop' and can only be overcome with infinite gain which is unrealistic and unstable.

Fortunately there is a cure in the integral control which continually sums the offset from the set point produced by the proportional droop. Practically the integrator cannot sum indefinitely as this would require infinite gain and the accumulated signal may be too great for the system to respond accurately. The error signal is summed over a set period (integration time, τ_{I}) and builds up a large signal which counters slow deviations from the set point. The control law for the integrator is

$$x(s) = C_{\mathrm{I}} \frac{e(s)}{\tau_{\mathrm{I}} s} \tag{4.13}$$

If we close the loop as we did before with the proportional control we find that the integral control will always return the system to the setpoint if $s \to 0$ (or $\tau_{\mathrm{I}} \to \infty$)

$$w(s) = \frac{C_{\mathrm{I}}}{C_{\mathrm{I}} + \tau_{\mathrm{I}} s} p(s) \tag{4.14}$$

$$w(i\omega) \frac{C_{\mathrm{I}}}{C_{\mathrm{I}} + i\omega/\omega_{\mathrm{I}}} p(i\omega) \tag{4.15}$$

$$w(0) = p(0) \tag{4.16}$$

For most purposes a PI servo is adequate.

A differential control can be added to allow the servo to 'predict' a fast deviation. The control law for the differential control is;

$$x(s) = C_{\mathrm{D}} \tau_{\mathrm{D}} \, s \, e(s) \tag{4.17}$$

This control responds to the rate of change of the error signal so that it can correct a potentially large deviation before the event becomes uncontrollable. A differential control can be hard to use as the gain increases with frequency and can easily put the system into oscillation. The bandwidth and gain for this control must be considered carefully and a low pass filter included to roll-off the gain to retain a suitable phase margin. From a design point of view, it pays to use the signal before it is compared with

the set point for the differential control as it monitors the rate of change of the signal therefore the set point has no meaning, this allows one to adjust the set point whilst the system is locked without the unwanted response of the differential control.

4.4.2 Southampton PID Servo

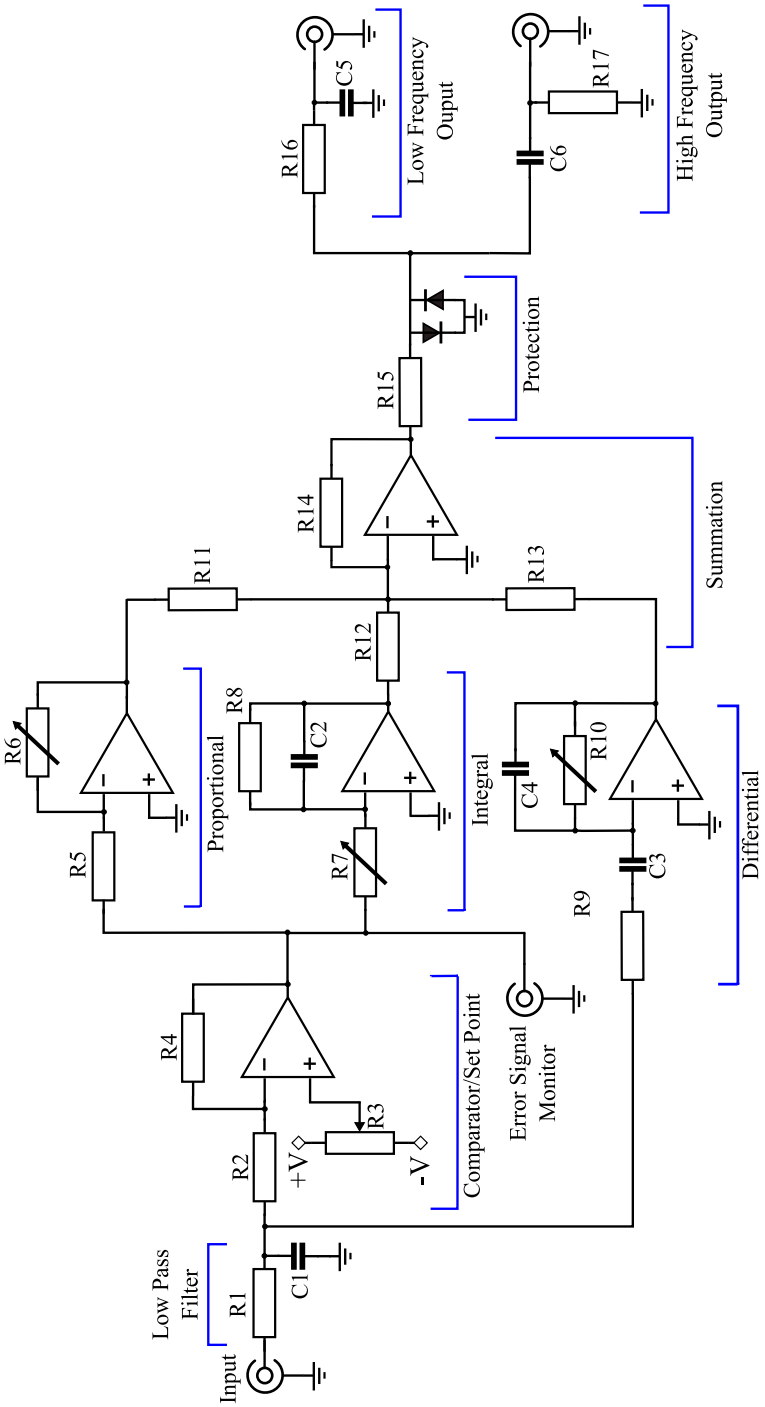

FIGURE 4.13: *Simplified circuit diagram of the Southampton PID Circuit. See Appendix A for full circuit details.*

The PID Servo used to stabilize the trapping and repump lasers is based around the the design by Bowring et al [79]. Figure 4.13 shows a simplified circuit diagram of the actual circuit for discussion purposes, the full design can be found in Appendix D. The output from the demodulator is sent to the input where it is first filtered to remove high frequency pickup and also limit the bandwidth of the servo to retain a large phase margin. The low pass filter is set to 300 kHz (-3 dB point) as this is the bandwidth of the laser driver to which the error is fed back. The input to the differential stage is routed from here to avoid a large response if the set point changes while the laser is locked. The signal is then compared with a set point voltage using a unity gain inverting amplifier circuit. The output from this stage is the error signal which can be monitored.

The error signal is now separated into the proportional and integral stages. The proportional stage is a simple inverting amplifier ($-R_6/R_5$) with gain variable from 0 to 2. The integral gain is

$$\frac{1}{R_7}\frac{R_8}{1+2\pi f R_8 C_2} \tag{4.18}$$

The integral stage acts as a low frequency amplifier in which the low frequency error is accumulated as charge across capacitor C_2. R_8 is known as a drain resistor and is added to limit the gain at very low frequencies, which may lead to the infinite gain instability discussed earlier. Other designs may use a switch instead to reset the capacitor. It must be noted that as the integrator only responds to errors in the past it may overshoot the set point and so must be used together with a proportional control.

The differentiator has a gain

$$\frac{R_{10}}{R_9}\frac{2\pi f C_3}{(1+2\pi R_{10} C_4 f)(1+2\pi f C_3)} \tag{4.19}$$

where R_{10} and C_3 actively differentiate the signal, working as a high frequency amplifier. At very high frequencies the phase of the differential stage can invert, so R_9 and C_4 are used as a low pass filter to roll off the gain.

The signals from the P, I and D stages are summed together. Their respective amplitudes governed by the ratios of R_{14} with R_{11}, R_{12} & R_{13}. Bowring et al [79] suggest a ratio $\frac{1}{2}$:$\frac{1}{2}$:$\frac{1}{33}$ whereas, due to the higher gain required to reduce 50 Hz mains ripple via the PZT, the summation ratios in the Southampton circuits are $\frac{1}{2}$:3:$\frac{1}{33}$. It was found that

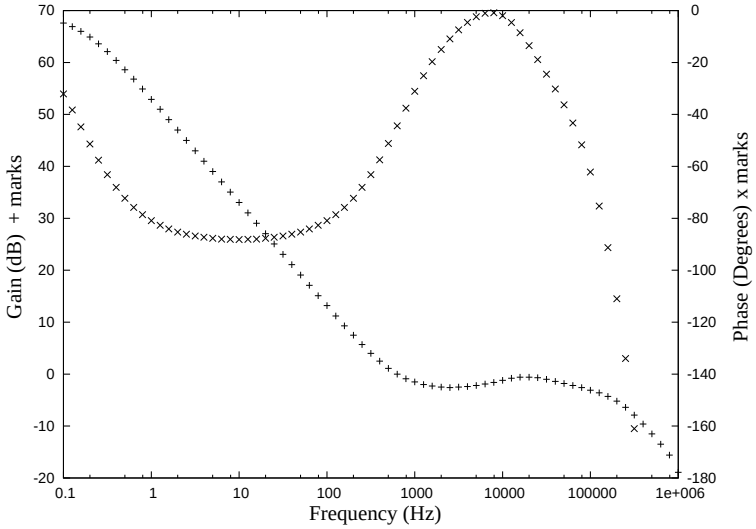

FIGURE 4.14: *Bode plot of the Southampton PID for a typical lock setting calculated by OrCAD. The gain (+ marks) is overwhelmed by the integral in order to reduce 50 Hz noise. The proportional response is barely visible until 1 kHz. The lump centered around 30 kHz is the differential response. The phase (x marks) is mainly due to the integrator at -90°. The low frequency tendency to 0° is due to the drain resistor. At higher frequencies the proportional (0°) response increases. The differential phase shift of +90° is not noticeable due to the low gain. The bandwidth is limited by the input filter at 300 kHz.*

having an increase the gain was more stable than using a longer time constant, which sent the laser into oscillation.

The next stage uses two diodes to restrict the output of the PID to ± 0.7 V (the diode drop voltage) to prevent large currents being supplied to the laser diode (in the actual design an inverter stage is included here to correct the signal polarity) . The output is split into a low frequency (< 1 kHz) and high frequency (>1 kHz) output. The low frequency correction signal is sent to the piezo transducer stack which controls the external cavity grating, and the high frequency correction goes to the drive current controller to avoid heating effects associated with large low frequency corrections to the drive current, which was found to cause the laser to modehop.

The Bode plot is useful in control theory and for understanding the gain and phase response, with frequency, of any electronic component and helps visualize how the circuit will react. For example, the differentiator should respond at high frequencies but also to the rate of change of the signal, hence a 90° phase shift (the case for a perfect sine wave input). The Bode plot can also warn of instabilities as unwanted oscillation may arise when the phase of the response reaches 180° when the there is still gain

above unity (negative phase margin). Figure 4.14 shows the open-loop Bode plot for the Southampton circuit from the diagram in Appendix D, calculated using the PSpice circuit simulator in OrCAD [91]. The performance of this circuit is discussed in the next section, as well as possible improvements.

4.5 Locking Analysis

There are several methods to measure the stability of the laser, most of which rely upon measuring the beat note produced when two beams are incident on a detector. The linewidth can then be measured using a radio frequency spectrum analyser. The most accurate method is self-homodyne detection [92] which involves splitting the beam with an AOM, delaying one path with a optical fibre then detecting the beat note of the two beams using a photodetector. The AOM is required so that the beat note is shifted away from the low frequency noise of the detector and the fibre path must be longer than the phase coherence of the laser: if the linewidth is 1 MHz the fibre must be greater than 0.5 km therefore the technique can be very expensive.
A similar technique is to beat the laser with a more stable laser, but this of course requires one to have a more stable laser at the right wavelength. For the MOT beams we require two stable lasers and thus have two nearly identical pump-probe setups[7]. The linewidth of the beat note of two identical lasers is the quadrature sum of the individual linewidths if the lasers have a Gaussian spectral shape, and twice the individual linewidths if they have a Lorentzian shape [93]. If the noise is pure frequency noise we should expect a Lorentzian shape, any residual amplitude or white phase noise will produce a more Gaussian shape. From the beam note we may perform a fast Fourier transform to find the linewidth and we may also measure the temporal stability with the Allan variance.

4.5.1 Beat Note

When two optical fields are incident on a fast photodetector, a beat note is produced equal to the difference in frequency of the two fields. The requirements for the setup of

[7]The lasers and electronics are identical, but the pump-probe setup is slightly different

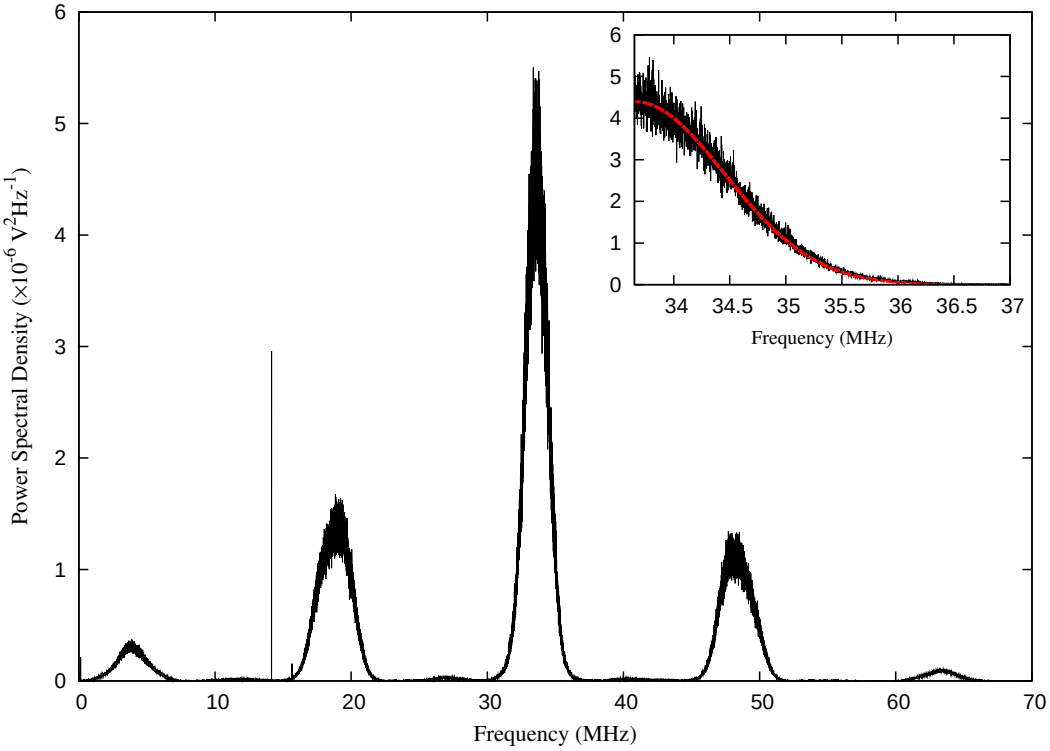

FIGURE 4.15: *Power spectrum of the measured beat note between the trapping and repump lasers with 200 samples of 1 ms length. We see a central Gaussian-shaped peak around 33 MHz which has a FWHM of* $\simeq 1.89 \pm 0.2$ *MHz. The two lobes either side of the central peak are due to the modulation frequency, these are wider than the central feature because the modulation frequencies of each laser are slightly different to avoid cross-coupling. The thin peak around 14 MHz is the pickup of one of the laser modulation drivers. The inset in the top right shows the fit of the central peak to a Gaussian lineshape (red).*

this experiment are:

- The photodetector and subsequent electronics should have a greater bandwidth than the detuning between lasers. Silicon PIN photodiodes can have bandwidths up to a GHz.
- The beat frequency should be higher than the spectral width of the lasers. As mentioned earlier, diode lasers can have linewidths of tens of MHz, whereas ECDLs can be as small as hundreds of kHz.
- The polarizations of the two beams cannot be orthogonal.
- The two beams must be as close to copropagating as possible to prevent spatial fringes.

The last requirement relates to differences in the wavevectors of the two beams producing spatial fringes such as that found in Michelson interferometers. If the fringe spacing is smaller than the detection region, no beat note will be found. This can be achieved 'by eye' and optimized by monitoring the amplitude of the beat note.

Our setup picks off a portion of the beam close to the laser with a securely mounted microscope slide to limit the path length of the beams to the detector, to reduce fluctuations caused by pressure changes and piezo scanning. The beams are aligned using mirror pairs and combined with a polarizing beam splitter cube, the polarizations being adjusted with half waveplates beforehand. The beams are sent through an iris (to aid alignment), a linear polarizer to combine the beam polarizations and a neutral density filter (to reduce intensity below damage threshold of the PD) before finally being focused onto the detector (MenloSystems FPD 510) . With the output of the photodiode AC coupled into the oscilloscope, the beatnote is significant (S/N $\simeq$ 50). Figure 4.15 shows the beat note between the trapping and repump lasers with exactly the same electronics[8]. One laser is locked to the crossover of ^{85}Rb $F' = 3, 4$ whereas the other is locked to the crossover of ^{85}Rb $F' = 2, 4$. The linewidth of the central carrier is $\simeq 1.89 \pm 0.2$ MHz and has a Gaussian shape (see inset in figure 4.15). This leads to individual linewidths of 1.33$\pm$ 0.14 MHz for a sample period of 1 ms, although this value does not change within the uncertainty over timescales of 100 μs$\rightarrow$10 ms. The Gaussian shape indicates residual amplitude noise probably due to amplifier noise in the control electronics or motion of the grating due to PZT correction and mechanical instabilities. The modulation depth can also be measured from this plot. The apparent decrease in sideband power at higher frequencies is due to the fall off of detector response (-3 dB at 200 MHz). Using the lower two sidebands we find a modulation depth of $\simeq 0.6$.

[8]The only difference between the setups is the spectroscopy configuration, although the lineshapes of the error signal should be nearly identical

4.5.2 Allan Variance

The measurement of the stability of oscillators recommended by the IEEE is the Allan variance [94]. It is defined as;

$$\sigma_\nu^2(\tau) = \frac{1}{2}\left\langle [\nu_\tau(t+\tau) - \nu_\tau(t)]^2 \right\rangle \tag{4.20}$$

where $\langle\rangle$ denotes a time average and

$$\nu_\tau(t) = \frac{\Delta\nu(t)}{\nu_0 \tau} \tag{4.21}$$

is the average normalised (with respect to the carrier frequency ν_0) frequency deviation $\Delta\nu$ over the sampling period τ. The Allan variance is also known as the 'two sample zero dead-time variance'. We can see that this means that the variance is measured between two consecutive sampling periods (i.e. no 'dead time' between the two sample points). This value is used instead of the normal variance (or standard deviation) as the power-law spectral characteristics of some types of common noise sources can cause the normal variance to diverge rapidly as the number of samples increases [95, 73].

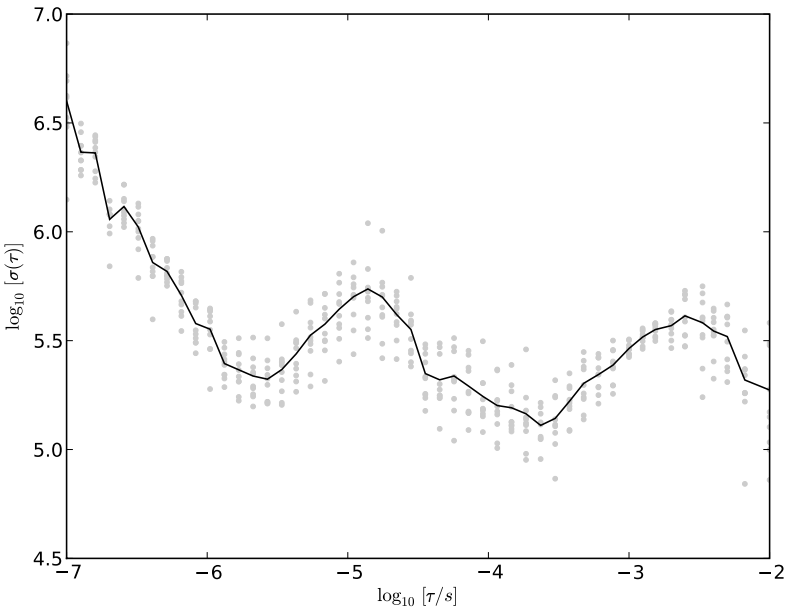

FIGURE 4.16: *Logarithmic plot of the Allan variance of the beam note between two similarly locked diode lasers. Plot calculated by James Bateman.*

To measure the Allan variance, the beat note was recorded, as before, with a Tektronix DPO4104 digital scope. The record length was 10 mega samples (MS) at a sampling rate of 500 MS s^{-1}. Hence the longest time period was $\simeq$20 ms. To calculate the Allan variance, the number of zero-crossings of the beat note was measured for a sample period and divided by the sample time. The average frequency deviation from consecutive sampling periods was then plotted. Instead of plotting the normalized Allan variance $\sigma_\nu^2(\tau)$ it is more common to plot the un-normalized square-root of the Allan variance $\sigma(\tau)$ as it may be directly read as a frequency variation.

The power law dependence of the Allan variance to the sample time is not a direct relation to standard spectral power laws but a useful conversion table can be found in Reference [95] which is summarized in Table 4.1.

The average of Allan variance of 10 runs is shown in Figure 4.16. The variance between 100 ns and 1 μs is white phase noise which is amplifier and fundamental noise of the laser diode. From 1 μs to 10 ms is flat flicker-frequency noise, due to noisy electronics, with lumps at 10 μs and 3 ms which are attributed to 'servo bumps' caused by the tail-off of the servo response: the low frequency bump is the piezo servo response and the high frequency is the current servo response. We did not measure to lower frequencies but would expect the Allan variance to drop to much lower values as the lasers are very stable over tens of minutes. If we take the amplitude of the flicker frequency noise, we find the stability between the two lasers to be 220 ± 130 kHz over 1 μs$\rightarrow$10 ms. The

Slope on a log-log $\sigma(\tau)$ plot	Spectral power law $S_\nu(f) = H_\alpha f^\alpha$	Type of noise	Source of noise
-1	$H_2 f^2$	White phase noise	External additive white noise sources, such as amplifier stages.
$\approx$-1	$H_1 f^1$	Flicker phase noise	Not fully understood, possibly due to physical properties of the resonator, electronics or environment
-0.5	$H_0 f^0$	White frequency noise	Shot noise of Johnson noise
0	$H_{-1} f^{-1}$	Flicker frequency noise	Noisy electronics
+0.5	$H_{-2} f^{-2}$	Random walk frequency noise	Oscillator environment, i.e. temperature, vibration.

TABLE 4.1: *Conversion between the spectral power law function of different noise sources and the slope of a log-log Allan variance plot.*

majority of noise appears to be white noise which has a Gaussian spectrum which agrees with the beat note spectrum in Figure 4.15.

4.5.3 Room for Improvement

In terms of metrology, the lasers are accurate to 220 ± 130 kHz over 10ms and precise to 1.33 ± 0.14 MHz over 1ms which is acceptably near to the required level for the magneto-optical trap of < 1 MHz. Even so, improvements can been made, and the main area for improvement is the lock lifetime. This can vary from minutes up to an hour and mode-hops are the main culprit for lock instabilities. Time lags between the temperature stabilizer and frequency stabilizer responses may cause such large jumps. When mode hops are not to blame the laser may unlock due to limitations in the gain (integral wind-up). In this section we briefly outline where and why improvements can be made to the ECDLs and electronics.

4.5.3.1 ECDL

The ECDLs used in this project are the real work-horses and rarely fail. There are only a few minor improvements which can improve stability and make the ECDLs easier to work with for the experimenter. The first improvement is to correct the change in pointing direction. Any change of the PZT and coarse alignment screw results in a change of beam direction which affects the MOT alignment further down the optical bench. This problem can be overcome by simply adding a mirror onto the grating mount. Temperature drifts of the laser can be large enough that the gain of the PID cannot correct and the laser modehops; a larger heatsink would help, as would placing the external cavity within a draft-proof enclosure. The aforementioned improvements have been implemented in a new design currently under construction. Another improvement, though unlikely to be applied in the new design, is the use of anti-reflection coated laser diodes which results in larger tuning ranges and therefore a reduction in modehopping [96].

4.5.3.2 PID

The largest problems with the PID are noise and lock timescales. The error signal output from the PID adds much noise to the monitor signal. The data collected for the FM spectra (Figure. 4.12) were amplified with a very low noise SR570 amplifier and not the monitor in the PID circuit. A new design for the PID was developed for use in another experiment (cavity stabilization via a PZT) and there was a possible need to stabilize the manipulation laser. The previous PID was specifically designed for the one laser system. It also had a few design errors which required expedient, non-optimized 'fixes' (such as requiring separate LF and HF output). An improved design with better noise reduction and separate HF and LF outputs is in the initial testing stage at the time of writing. Other electronic improvements are power supply filtering of the PZT scanning & offset voltage and a DC-DC voltage converter to attain a larger scanning range, which is believed to be a common source of unlocking.

Chapter 5

Magneto-Optical Trap

To investigate coherence effects on atoms it is advantageous to confine and cool the atoms to prevent decohering events, such as interacting with the walls of the chamber and collisions between atoms. A cold dense ensemble of atoms allows one to increase the intensity of the manipulation beams by interacting with a smaller target; therefore a larger force can be applied to the atoms. As we are exploring subtle velocity dependent forces, reducing the initial distribution of velocities one can work with increases the signal to noise ratio. Finally, creating cold atoms via Doppler cooling provides experience of standard cooling techniques. In the first half of this chapter we review the basic techniques for Doppler cooling atoms and the operation of a magneto-optical trap (MOT) which cools and compresses the atomic gas. We devote the second half to the construction and characteristics of the MOT built in Southampton.

5.1 Cooling Force

When an atom absorbs a photon it will recoil in the same direction as the photon momentum $\hbar\vec{k}$. This is known as radiation pressure and can been seen in the deflection of comet tails caused by the sun's radiation. If the atom is in motion then its resonance frequency is Doppler shifted. In the laboratory frame, a red-detuned (lower frequency) laser will be scattered more by an atom moving toward rather than away from the beam, thus resulting in a force against its direction of travel. This method of slowing atoms

is known as Doppler cooling and was first proposed by Hänsch and Schawlow in 1975 [97]. The addition of a second laser propagating in the opposite direction (equally red-detuned) will result in a viscous-like force on the atom thus reducing its 1D velocity and its kinetic 'temperature' along the beam axis. This viscous force is called *Optical Molasses* [98] and was first demonstrated by Chu in 1985 [3].

After an atom has absorbed a photon it may spontaneously emit a photon and recoil in any direction and so undergo a random walk as a result of multiple events. At room temperature an atom's average velocity is around $250\,\mathrm{ms}^{-1}$, so in order to bring it nearly to a halt it must absorb several tens of thousands of photons. After many absorption-emission cycles the net recoil due to spontaneous emission sums to zero whereas the absorption recoil is non-zero.

To gain a quantitative value of this force on an atom we can write it in terms of the rate of change of momentum,

$$F = \frac{\Delta P}{\Delta t} = \hbar\vec{k}\gamma\rho_{\mathrm{gg}} \tag{5.1}$$

The rate at which the atom can absorb photons from the beam is equal to the spontaneous decay rate γ times the population of the absorbing ground state ρ_{gg}, i.e. the atom must return to the ground state before another $\hbar\vec{k}$ of momentum can be absorbed. We can derive the population of the ground state via the density matrix derived in Appendix C. The force on the atom from each beam can then be written,

$$F(\pm k) = \pm\frac{1}{4}\hbar k\gamma\frac{\Omega^2}{(\delta \mp kv)^2 + \gamma^2/4 + \Omega^2/2} \tag{5.2}$$

where δ is the detuning of the laser from resonance, kv is the Doppler shift[1] of the resonance of an atom with velocity v and Ω is the Rabi frequency. It is useful to rewrite this equation with the substitution for the saturation intensity, I_{S},

$$\Omega^2 = \frac{\gamma^2}{2}\frac{I}{I_{\mathrm{S}}} \tag{5.3}$$

[1] as we are dealing with beams in one dimension we have dropped the vector notation

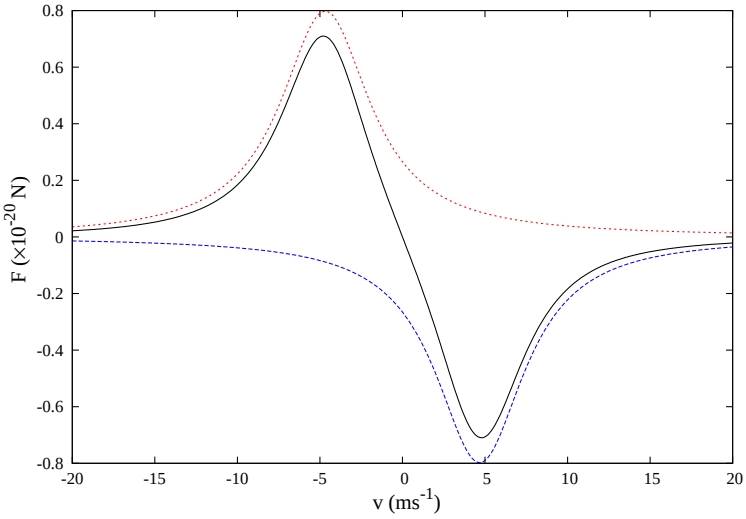

FIGURE 5.1: *1D scattering force curve from two counter-propagating beams on an atom's c.o.m. velocity. The laser frequency is detuned $-\gamma$ from resonance. The Red and Blue curves are the force from individual lasers and the black curve is the sum of the two.*

So the scattering force now becomes,

$$F(\pm k) = \pm\frac{1}{2}\hbar k\gamma\frac{I/I_{\mathrm{S}}}{\frac{4}{\gamma^2}(\delta \mp kv)^2 + 2I/I_{\mathrm{S}} + 1}. \tag{5.4}$$

The total force on an atom versus its velocity is shown in Figure 5.1. We can find an approximate relation for this force by performing a Taylor series expansion of the total force, $F = F(+k) + F(-k)$, and assuming the Doppler shift is small compared with δ and γ [99],

$$F \simeq 4\hbar k^2\frac{I}{I_{\mathrm{S}}}\frac{2v\delta/\gamma}{(\frac{4}{\gamma^2}(\delta)^2 + 2I/I_{\mathrm{S}} + 1)^2} \tag{5.5}$$

As qualitatively predicted earlier, in order to produce a force to counter the atom's velocity ($F \propto -v$), the laser must be detuned to longer wavelengths ($\delta < 0$). The force is proportional to beam power for low intensities but becomes limited by the saturation intensity at which the scattering rate is maximum. The optical molasses cooling force is limited to the extent where the inhomogeneous broadening of the resonance coincides with the homogeneous widths of the resonance lifetime. One can see that the minimum velocity an atom can reach is limited by the final recoil of a spontaneous emission. In an ensemble of atoms the spectral width of the spontaneous decay (Section 3.2.2) will result in a distribution of velocities.

This is a hand-waving description of the Doppler temperature limit and does not take

into account diffusion and drift of the cold atom cloud and heating from re-absorption of scattered photons. An exact derivation can be found in Reference [100]. We shall just quote the result here,

$$T_{\text{Doppler}} = \frac{\hbar}{2k_{\text{B}}\tau} \tag{5.6}$$

For Rubidium, the Doppler limit is $145\,\mu$K.

5.2 Repump beams

So far in this chapter we have assumed that we are dealing with a two-level atom. In reality we could approximate the Rb D_2 line as a 6 level system in the absence of external fields. Due to the selection rules the upper ground state $F = 3$ has dipole-allowed transitions to the excited $F' = 2, 3, 4$ levels and the lower ground state $F = 2$ is likewise connected to the $F' = 1, 2, 3$ excited levels. The cooling transition $F = 3 \rightarrow F' = 4$ is chosen as it is closed from spontaneous decay into the lower ground state. Unfortunately, there is a small but finite probability of exciting an atom from $F = 3 \rightarrow F' = 3$ due to the Lorentzian nature of the absorption probability. We can estimate the fraction of atoms excited to this state by comparing transition cross-sections (Eqn.3.35),

$$\Delta\sigma = \frac{\sigma(F = 3 \rightarrow F' = 3, \delta_{3\rightarrow 3})}{\sigma(F = 3 \rightarrow F' = 3, \delta_{3\rightarrow 3}) + \sigma(F = 3 \rightarrow F' = 4, \delta_{3\rightarrow 4})} \simeq 1.4\% \tag{5.7}$$

where we have assumed a detuning of -3 linewidths from the cooling transition, a beam intensity equal to the saturation intensity (for simplicity we have used the same saturation intensity for both transitions) and neglected the $F = 3 \rightarrow F' = 2$ transition.

The $\sim$1% excited to the $F' = 3$ excited state then has nearly equal probabilities of decaying into the dark lower ground state (see Tables A.4 and A.5 in Appendix A). As mentioned at the beginning of this section in order to cool the atoms to near stationary, we required absorption of tens of thousands of photons so this small fraction of dark state decay becomes significant. A simple remedy to this problem is to use a 'repump' beam connecting the $F = 2 \rightarrow F' = 3$ transition to optically pump the dark state population back into the cooling cycle. Optical pumping or spontaneous redistribution

of populations into dark states, as mentioned earlier, is the reason why Doppler cooling is applicable to only a small fraction of the periodic table.

5.3 Trapping Force

Although optical molasses can confine the atom's random walk to within the beam regions [98, 3], the optical scattering force cannot create a trapping potential alone because it cannot not converge onto a single point in free space, as encompassed in the optical form of the Earnshaw theorem[2] [102]. The theorem does not include the influence of the optical field upon the internal degrees of freedom of the atoms and how they affect the centre of mass motion [103]. The addition of a magnetic field gradient and the resulting Zeeman shifts of the hyperfine structure provide a spatial dependence of the resonance frequencies [104], permitting the trapping force which is the basis of the magneto-optical trap.

The shift of the energy levels depends upon the hyperfine gyromagnetic ratio, g_{F} (Table A.2, Appendix A), the projection of the state vector, m_{F}, along the magnetic field on the z axis B_{z}, and the Bohr magneton, μ_{B}.

$$E_{\mathrm{Zeeman}} = \mu_{\mathrm{B}} g_{\mathrm{F}} m_{\mathrm{F}} B_{\mathrm{z}}. \tag{5.8}$$

To produce a trapping force the atoms must absorb photons from beams which oppose the atom's velocity when the atom moves away from the centre of the trap. A quadrupole magnetic field is applied using two coils in the anti-Helmholtz condition so that the magnetic field in the centre of the trap is zero and increases approximately linearly away from the centre. To ensure the atom only interacts with the beams that oppose its velocity we must clarify the notation of circular polarization and dipole transition selection rules [22].

Circular polarization is produced when a linearly polarized beam traveling in the (for example) positive z direction passes through a quarter waveplate so that the x and y

[2]Earnshaw theorem; No charged body can be in static stable equilibrium under the influence of electric forces alone [101]

components are delayed from one another by π radians. The electric field vector rotates in the $x-y$ plane and, if observed toward the beam source, a clockwise rotation is termed *right circularly polarized*, σ^R, and an anticlockwise rotation is *left circularly polarized*, σ^L. Of course, if viewed from the source the electric field vector rotates in the opposite sense and we use *positive circularly polarized*, σ^+, for clockwise rotation and *negative circularly polarized*, σ^-, for anti-clockwise rotation. We can see that $\sigma^L = \sigma^+$ and $\sigma^R = \sigma^-$. The positive/negative nomenclature has an additional meaning in dipole transitions. For an atom which have a quantization axis along the positive z axis (formed in our case by an

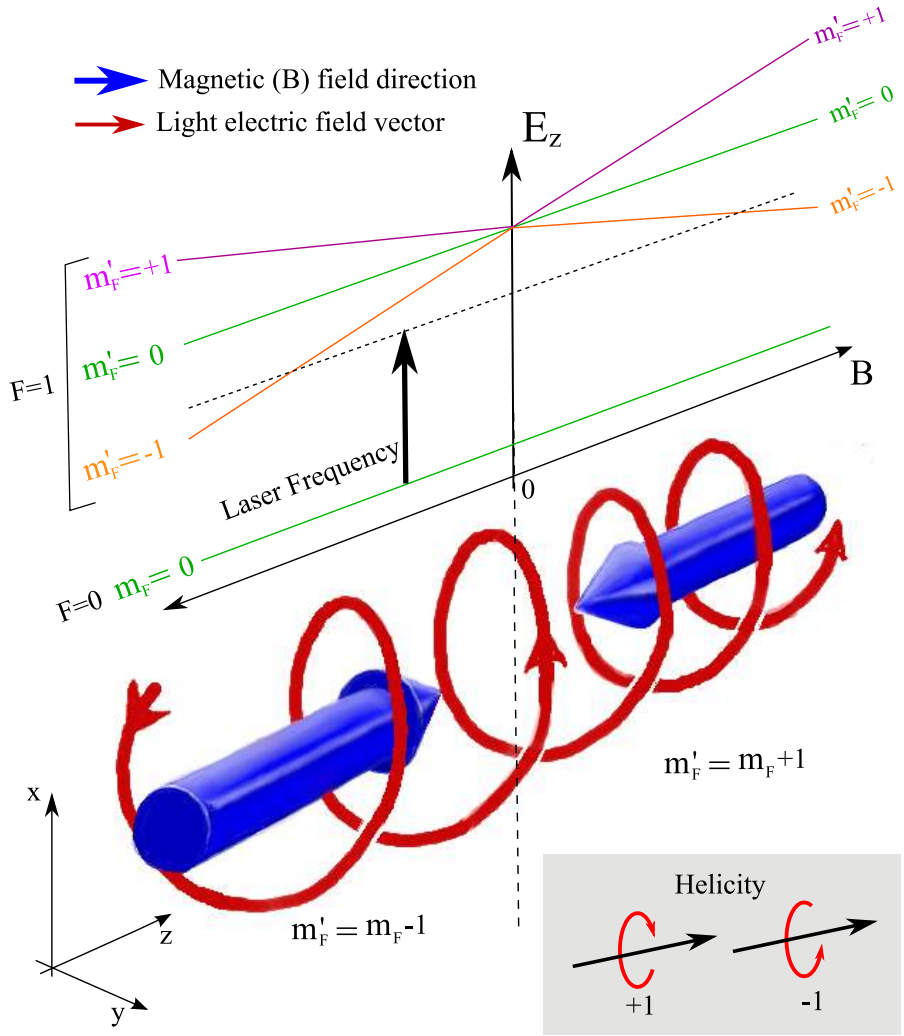

FIGURE 5.2: *Origin of the trapping force in a MOT. The upper graph shows the Zeeman shift of the magnetic sublevels of a atom with an simplified hyperfine structure with an F=0 ground state and F=1 excited state (the effect is still valid for similar J states). The diagram below the graph shows the trace of the tip of the electric field vector (red arrow) of a beam traveling in the z direction. The transitions induced by the beam on either side of the trap centre depends upon the helicity (grey box) of the beams with respect to the local magnetic field (blue arrow). See text for more details.*

external magnetic field), a σ^+ resonant beam will impart $+1\hbar$ of angular momentum to the atom and cause a transition from $m_{\mathrm{F}} \rightarrow m'_{\mathrm{F}} = m_{\mathrm{F}} + 1$ and similarly a σ^- beam will induce a $m_{\mathrm{F}} \rightarrow m'_{\mathrm{F}} = m_{\mathrm{F}} - 1$ transition. If the quantization axis is reversed then the polarizations and transitions are swapped. The important feature of the polarization in the *helicity* of the electric field vector as shown in the grey box in Figure 5.2, which also demonstrates the origin of the trapping force in a MOT[3].

The blue arrows indicate the direction of the magnetic field which reverses as one crosses the centre of the trap. The diagram shows a snapshot of the trace of a the tip of the electric field vector for a single σ^- polarized beam traveling in the positive z direction. On the left hand side the beam has -1 helicity with respect to the magnetic field and therefore causes a transition to $m'_{\mathrm{F}} = m_{\mathrm{F}} - 1$, on the right hand side the helicity is $+1$ and causes $m'_{\mathrm{F}} = m_{\mathrm{F}} + 1$ transitions. As the beams are red-detuned for cooling of the atoms, the polarization of the beam must be σ^- so that the atoms are more likely to absorb the photons which return them to the trap centre.

The spatial dependence of the force can be included in Equation 5.4 by including another detuning factor,

$$F(\pm k) = \pm\frac{1}{2}\hbar k\gamma \frac{I/I_{\mathrm{S}}}{\frac{4}{\gamma^2}(\delta \mp kv \pm \frac{\Delta\omega}{\Delta B}\frac{\Delta B}{\Delta z}z)^2 + I/I_{\mathrm{S}} + 1} \tag{5.9}$$

where $\frac{\Delta\omega}{\Delta B} = \frac{\mu_{\mathrm{B}} g_{\mathrm{F}} m_{\mathrm{F}}}{\hbar}$. With a static detuning the fraction of atoms interacting with the optical field will be limited to a small fraction of the Maxwell-Boltzmann distribution of velocities. In a relatively high background pressure, such as a vapour cell, this technique can nonetheless result in a significant number of cooled atoms [105]. To achieve higher loading rates, the optical field can be 'chirped' or a gradient magnetic field can be placed along the atomic loading path to bring a larger fraction of atoms into resonance to a counter-propagating laser beam [105, 106].

[3] A useful guide to helicity is the 'right hand grip rule'. When using a screwdriver with your thumb pointing along the shaft, a clockwise rotation should tighten a screw and move the screwdriver forward, an anticlockwise rotation loosens the screw and moves the screwdriver backward. These correspond to +1 and -1 helicity, respectively. The thumb can be thought of as the wavevector direction, the rotation as the electric field vector rotation (clockwise/anticlockwise) and the movement of the screwdriver (forward and back) as the quantization direction. Hence if one goes to tighten a screw by a clockwise rotation but finds the screwdriver moving backwards and loosening the screw (wavevector antiparallel to quantization axis) then the helicity is -1.

5.4 Magneto-Optical Trap

We can extend the two-dimensional models presented of the cooling and trapping forces into 3 dimensions by using 6 laser beams along each axis and applying a quadrupole magnetic field with the zero at the overlap point of the beams. Figure 5.3 shows the MOT configuration with the correct polarization and field directions as outlined in the previous section. This type of trap is the most common type of cold atom source, although other configurations exist [107, 108]. It is remarkably robust to alignment errors and the lasers can be detuned (to the red) across several linewidths [109] with imperfect polarizations and a cold atom cloud may still form. The development of laser cooling and trapping won the originators Steve Chu, Claude Cohen-Tannoudji and William Phillips, the Nobel prize for physics in 1997 [110].

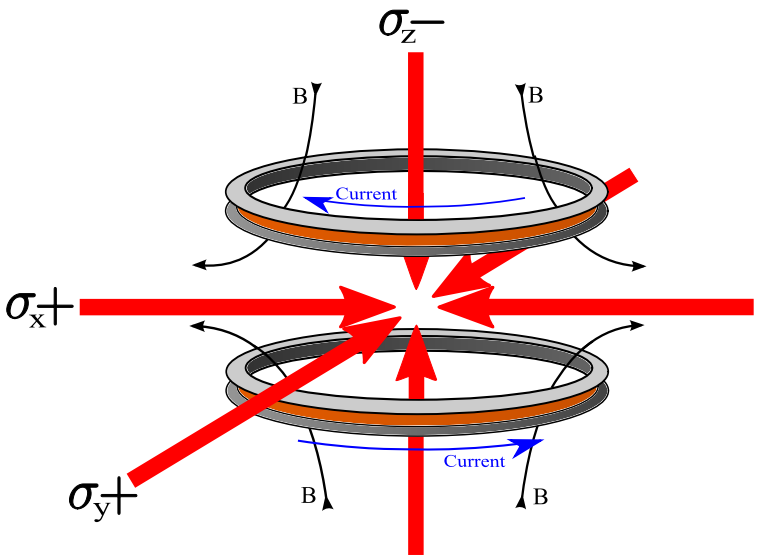

FIGURE 5.3: *Polarizations and magnetic fields in a 3D MOT.*

5.5 Sub-Doppler Temperatures

The first measurements of the temperature of cold atoms in a MOT were close to predictions of the Doppler Limit [3, 111]. However, researchers soon noticed temperatures below this limit and careful measurements with a variety of methods confirmed this [109]. This sub-Doppler cooling was named 'supermolasses'. Standard Doppler cooling

theory neglects any effects due to multi-level structure of real atoms and so a new theoretical mechanism called *Polarization Gradient cooling* was proposed by two separate groups [112, 113]. Due to optical molasses the atoms now move slowly enough that variations in the light field due to the polarization of two counter-propagating beams can have a significant effect upon the hyperfine sub-levels. The main process of this sub-Doppler cooling is non-adiabatic optical pumping of ground state populations during motion through a light field with a changing intensity and/or polarization. The exact mechanism depends upon the polarizations used and the specific atomic energy levels.

We briefly describe the linear polarized beams setup for a $J = 1/2$ ground state as it most clearly illustrates the important mechanisms [24]. From Figure 5.4 we can see that the field from two counter-propagating beams with orthogonal linear polarizations changes from σ^+ to π^{-45} to σ^- to π^{45} in $\lambda/8$ increments (using π^θ, where θ is the rotation of the linear polarization with respect to the parallel linear polarization, i.e. $\pi^{\parallel} = \pi^0$ and $\pi^{\perp} = \pi^{90}$). An atom originally in a region of σ^+ will be optically pumped

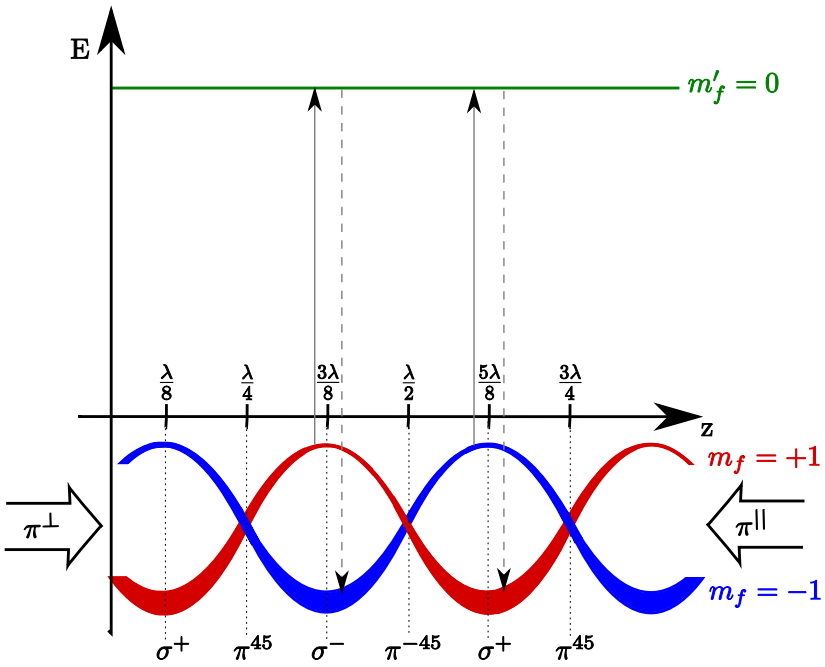

FIGURE 5.4: *The Sysiphus effect of Sub-Doppler cooling. See text for details. The width of the lower m_F states (red and blue) representative of the state populations.*

into the $m_J = +1/2$ state. The light shift[4] of this state is 3 times more negative than the $m_J = -1/2$ state [24]. As the atoms move into a region of σ^- light the state is shifted to higher energies. The atoms will then be pumped into the $m_J = -1/2$ state and find themselves at a lower energy. The atoms are always climbing potential energy 'hills' and releasing the energy as kinetic energy by spontaneous emission. The 'forever climbing a hill' analogy gives the effect its name as 'Sisyphus Cooling'. The effect is maximum when the transit time from $\sigma^+ \rightarrow \sigma^-$ is equal to the optical pumping time.

This is just one example of a sub-Doppler cooling mechanism and the actual mechanism in a 3D MOT with 6 beams with various polarizations is complicated to analyze, although the basic principle outlined above is fundamental. The limit of sub-Doppler cooling is constrained by the single photon recoil limit, although other methods such as Raman cooling exist to cool below the photon recoil [114, 115].

As one cools atoms to lower temperatures and with higher densities we enter the Bose-Einstein Condensate (BEC) regime, which is a quantum mechanical effect underlined by the Heisenburg uncertainty principle. As an atom's velocity is reduced, we may accurately know its momentum and therefore we must surrender accurate knowledge of the atom's position. In a dense sample of atoms the uncertainty in position may become larger than the inter-atomic distance so that the atoms form into a single wavefunction: a 'Macro-atom' on millimeter scales. This fundamental work won the first experimenters Eric Cornell, Wolfgang Ketterle and Carl Wieman, the Nobel prize in physics 2001. For a good review of BEC theory see Reference [116].

[4]The light shift is a perturbation of the state energy due to a strong off-resonance electric field which distorts the wavefunction (albeit negligibly compared with Zeeman shifts). The shift tends to oppose the sign of the detuning

5.6 Southampton MOT

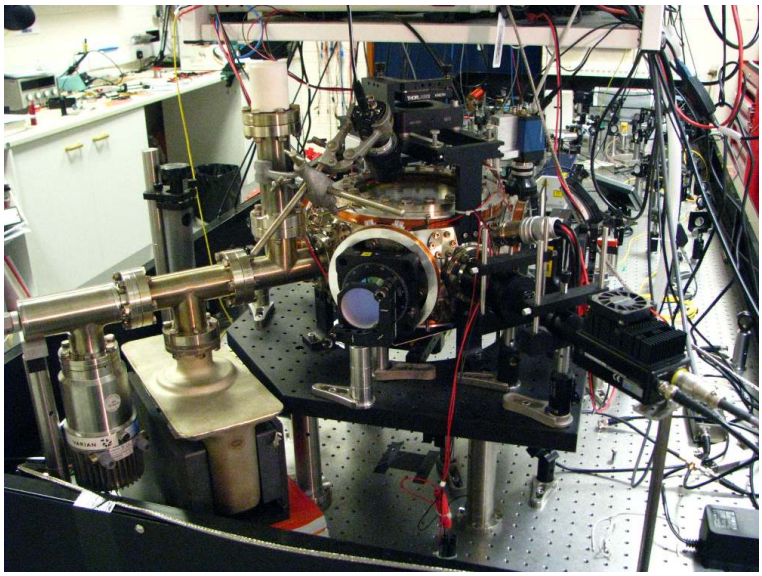

FIGURE 5.5: *Photograph of the Southampton magneto-optical trap.*

This section outlines the layout and operation of the Southampton MOT and examines the characteristics of the cooled Rubidium cloud formed within it. A more detailed description on how the MOT was built is given in Sunil Patel's PhD Thesis [117] .

5.6.1 Chamber and Layout

The chamber was machined by the in-house workshop from a single piece of 316 stainless steel, chosen for its low magnetic susceptibility. The chamber has 22 ports as shown in Figure 5.6. Four perpendicular 65 mm diameter windows facing in the x and y plane are used for the x and y MOT beams. Two large 135 mm diameter windows facing along the z-axis are for the remaining MOT beams and the quadrupole-field coils are wound round these windows. Four 38 mm diameter (diagonal to the $x-y$ arms) and sixteen 16 mm diameter subsidiary ports allow access for the vacuum system, CCD cameras and manipulation beams (thirteen of the 16 mm ports are blanked).

The chamber was cleaned with a three stage process: first, the machining oil and debris were cleaned off in an ultrasonic bath with deionized water and household washing-up liquid. Secondly, every component was cleaned with high purity acetone to remove grease and thirdly everything was cleaned with ultra-pure methanol which evaporates leaving

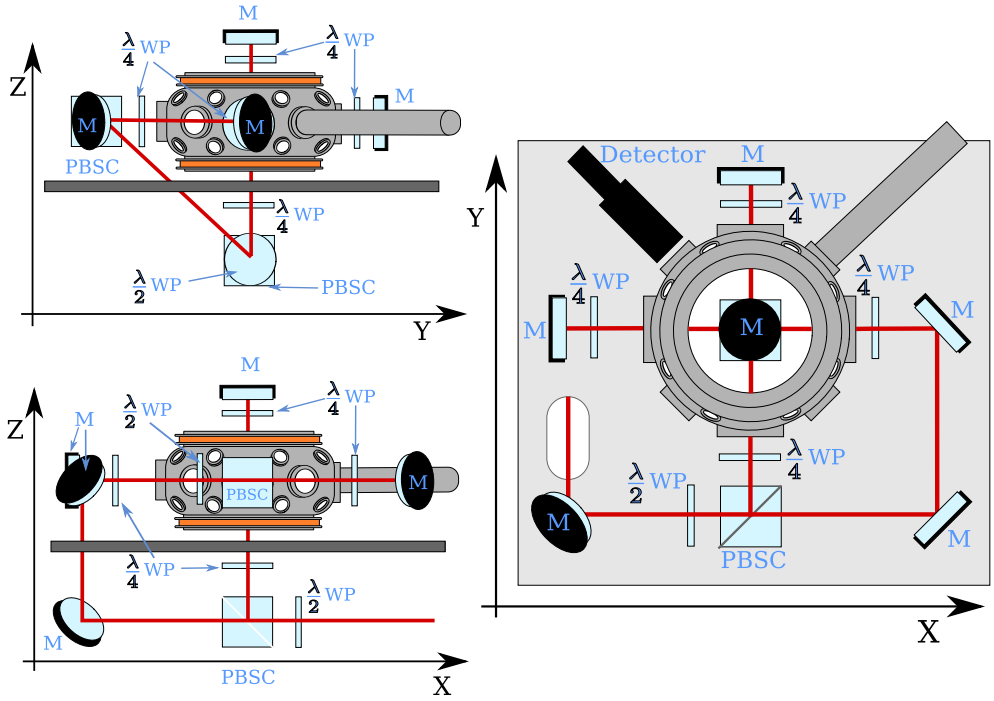

FIGURE 5.6: *Schematic of the beam path and MOT optics. WP: waveplate, PBSC: polarizing beam splitter cube. The grey tube off the side of the chamber leads to the vacuum system.*

minimal residue. An initial pump down with a scroll-pump and turbo-pump checked for leaks. The chamber was then refilled to atmospheric pressure with dry Nitrogen to reduce moisture intake. The chamber was then baked[5] at 220℃ for 3-4 days to remove any absorbed gases and moisture in the chamber walls.

5.6.2 Vacuum System

The MOT was evacuated using a 4 stage pump system. The initial scroll-pump takes the pressure down from atmospheric pressure to 10^{-2} mbar. The second system is a turbo-pump to reduce the pressure down to 10^{-6} mbar. The scroll-pump is still required to help evacuate the output of the turbo-pump. These pumps were kept on during the entire bake out. A passive sorption pump was activated during the bake by the passage of a current of 2.5 Amps. The fourth pump is an ion-pump which was baked out with the chamber but not activated. Once the bake out was complete the main valve was sealed leaving only the sorption and ion-pump evacuating the chamber. These pumps

[5]The chamber was baked several times over a period of a month in the laboratory of D. Segal at Imperial College, London. The multiple bake-outs were due to a faulty scroll pump, incorrect window coatings (manufacturer's mistake) and sheared valve

are left working for the lifetime of the chamber to clean out the slow desorption from the walls and to remove any of the test species added to the chamber. The final ultra high vacuum achieved is estimated from the current through the ion-pump created by ionized gas particles. The current measured is within the current noise level (10^{-7} A) implying a vacuum better than 10^{-9} mbar. Due to saturation of the ion-pump and a leak, the chamber was re-baked in-situ in winter 2008 using heater tape.

5.6.3 Rubidium Source

Rubidium is introduced into the vacuum chamber via an alkali-metal dispenser comprising of a resistively-heated getter. These are alkali salts (in our case Rb_2CrO_4) mixed with a reducing agent (Zr-Al mix) and release Rubidium vapour when heated above 400℃ by passing a current above ∼3A. Five getters (SAES Rb/NF/xx/25/FT 10+10) are spot-welded onto a six-terminal feedthrough, the remaining terminal acting as a common ground. Before the rebake in 2008, the chamber walls were coated in enough Rb that the background vapour pressure was sufficient to load the MOT cloud. After the rebake a single getter has been used during the entire experiment, usually with 3.0 A applied approximately five minutes to fill the chamber before each experiment.

5.6.4 Magnetic Field

The quadrupole magnetic field required for the MOT was created by two coils in the anti-Helmholtz condition (current flow is anti-parallel between each coil). The coils are fitted around the large 135 mm diameter windows and wound on an Aluminium former built in the departmental workshop. Each coil consists of 432 turns of 22 SWG insulated copper wire and is supplied with a current of 2 A; the central axial field gradient is measured to be ∼5 $\mathrm{G\,cm^{-1}}$. This figure is approximate because the measurement was taken with the coils separate from the chamber and aligned with the coil planes vertical whereas they are horizontal in the MOT[6]. During the MOT operation the (air-cooled) coils reach a steady state temperature of $\simeq$ 70℃ and require a current of 2.0 A in the lower coil and 1.93 A in the upper coil in order to compensate for the earth's magnetic field. These

[6]The chamber was excavated before the coils were built so in-situ measurements were not possible

values were found experimentally by moving the atom cloud to the centre of the MOT beams. Due to the anti-Helmholtz configuration, the horizontal field gradient ($x - y$ plane) is half the vertical gradient (through the coils) so, with equal beam intensities, one should expect an oblate-spheroid shaped MOT cloud.

5.6.5 MOT Beams and Polarization

The MOT requires two beams along each axis, each circularly polarized according to Figure 5.3. We achieve this by splitting a single beam using polarizing beam splitting cubes and waveplates, see Figure 5.6. Each beam is retro-reflected in order to ensure co-propagation and to reuse beam power. This retro-reflection is useful for alignment but can interfere with the laser diodes so suitable isolation is important. Both the trapping and repump beams are sent through 110 MHz acousto-optic modulators (AOMs) for fast switching. The operation and performance of the AOMs is discussed in Section 7.1.3. The trapping beam is tuned to the correct wavelength via Zeeman shifting, detailed in Section 5.6.8. The exact detuning of the repump laser is less important than that of the trapping laser, so a simplified pump-probe setup is used (Figure 5.7, c.f. Figure 3.3). In fact the MOT can be formed with the repump laser unlocked and drifting by tens of megahertz.

Initially the trapping and repump beams were combined using a polarizing beam splitting cube, then focused through a pin hole to clean up the beam profile, expanded with a telescope and aligned into the MOT optics. The resulting MOT cloud did not have a uniform shape and flickering interference fringes appeared across it. Also, any realignment of the lasers would also lead to realignment of a majority of the MOT optics. The layout now utilizes a single-mode optical fibre cable into which the two lasers are coupled via a beam-splitting cube after the AOMs. This setup greatly improves the beam quality and the MOT optics rarely need to be adjusted. Various output collimators can be purchased to adjust the beam diameter. The current collimator provides 7.1 mm diameter beams with powers of $\approx$10 mW, in each of the trapping and repump beams. The ends of the fibres are cleaved to prevent strong back reflections.

Alignment of the correct polarizations into the chamber via quarter-waveplates is not trivial if the slow and fast axes of the waveplates are unknown. One may notice from Figure 5.3 that the symmetry in the $x-y$ plane means that as long one ensures correct polarization pairs (σ^+ counter to σ^-) along each axis then the relative polarization between axes does not matter. The polarization pairs may be found by analysing linear polarized light through both a quarter-waveplate and a polarizing beam-splitter cube. In the case of retro-reflected beams this is not required because the polarization reflected back is always perpendicular to the incident beams no matter the quarter-waveplate axis. This statement is mathematically proved in reference [118], but we can understand it qualitatively by noting the double pass through the same quarter-waveplate has the same effect as a single pass through a half-waveplate such that it delays the orthogonal field axes by $\lambda/2$. The components of σ polarized light are $\lambda/4$ out of phase so that no matter the axes of the half-waveplate, the input polarization will always be orthogonal to the output polarization. As long as the first quarter-waveplate is aligned at 45° to the incident linear polarized light we are now left with 2 possible configurations which can be tested by reversing the magnetic field direction through each coil.

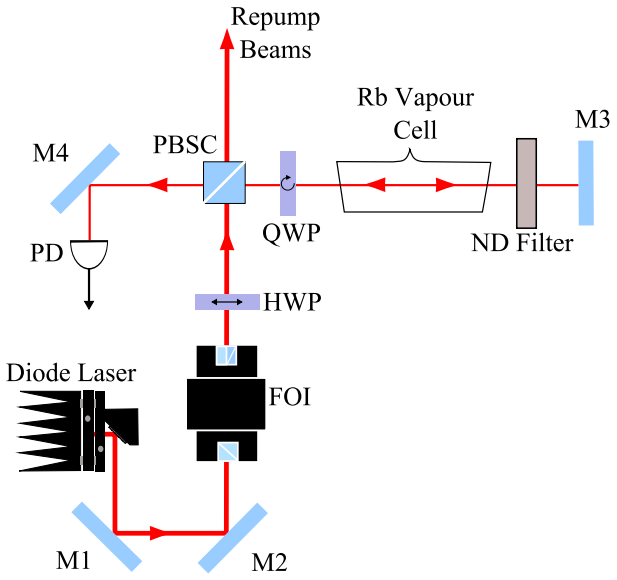

FIGURE 5.7: *Setup of the repump laser spectroscopy. After passing through the Faraday isolator the HWP allows the control of the beam power picked off at the PBSC. The beam passes through the vapour cell to pump the atoms then retro-reflected through a ND filter and QWP twice to reduce the probe power and correct the polarization so that the probe passes through the PBSC and onto the detector.*

5.6.6 UV enhanced loading

Due to the large chamber volume, a large amount of Rubidium needs to be released in order to have a sufficient background pressure for trap loading. It was found that after a long operating period the increased MOT chamber temperature (due to heating by the quadrupole coils) caused desorption of atoms from the chamber walls, reducing or eliminating the need for the getters. The downside of this is a lack of control of the vapour pressure and long waiting periods (up to an hour) for the MOT to reach a stable temperature. Colleagues mentioned the use of UV light to increase chamber wall desorption via the photoelectric effect, a technique which can increase loading rates by two orders of magnitude [119], previously described by [120]. The studies used high power UV LEDs ($\mathrm{W\,cm^{-2}}$ in Ref. [120] and tens of $\mathrm{mW\,cm^{-2}}$ in Ref. [119]), but we found ordinary off-the-shelf UV diodes to be equally useful (intensity $\sim 1\,\mathrm{mW\,cm^{-2}}$). We use 10 LEDs powered via a 10 V signal from one of the Tabor waveform generators. This allows one to switch the UV off during data collection to reduce background scatter.

The effect, named light induced atom desorption (LIAD), is thought to be related to the photoelectric effect where electrons are released from a surface when the incident light has the correct frequency above a threshold and the rate of desorption is proportional to the intensity. Once the light is turned off the background pressure is seen to reduce more rapidly than turning off the getters. As mentioned in Reference [119], a general theoretical description of this effect for all types of surfaces is still needed.

5.6.7 Detectors

The MOT cloud is monitored by three separate detectors.

- A Watec CCD camera (WAT-902DM) is used for general monitoring of the MOT cloud and for beam alignment. We also use this camera in the coherence experiments to check that the MOT cloud remains during long experimental runs by the cloud fluorescence (in case the trapping and repump beams have become unlocked and drifted) and to confirm alignment of the photo-multiplier tube. The output from the CCD camera is sent to a monitor and to a TV Card on the computer.

We also use this camera to take some spatial measurements of the MOT cloud in conjunction with the telescope system (Figure 5.8 and Section 5.7). In Figure 5.12 we see a typical image of the trapped cloud (left). Misalignment of the trapping beams can impose a torque on the atoms and form them into a ring [121].

- We also employ a second CCD camera (Prosilica GE680) with a high frame rate (up to 1000 fps for short exposures) for experiments involving spatially dependent forces [122] and for cloud expansion measurements [117]. The output of the camera is connected to a computer via USB. The computer can control all aspects of the CCD sensor (frame size, frame rate, exposure, binning, etc) as well as trigger recording, which is important to limit the large amount of data when using a high frame rate.

- The third is a photo-multiplier tube (PMT) for low light levels and fast response time. We use a Hamamatsu H7422-50 PMT module with integral bias voltage and fan-assisted cooling. Fluorescence from the MOT cloud is collected and focused on the PMT with a 1:1 telescope, see Figure 5.8. The lens system has a large (2 inch diameter) objective lens in order to maximize light collection. Nearly all of the coherence data have been collected with the PMT due to its fast response and high S/N. The CCD camera can also be connected to this telescope system for cloud shape measurements and a silicon PIN detector was used before the PMT arrived. The output from the PMT is passed through a SR570 low noise current amplifier to improve response.

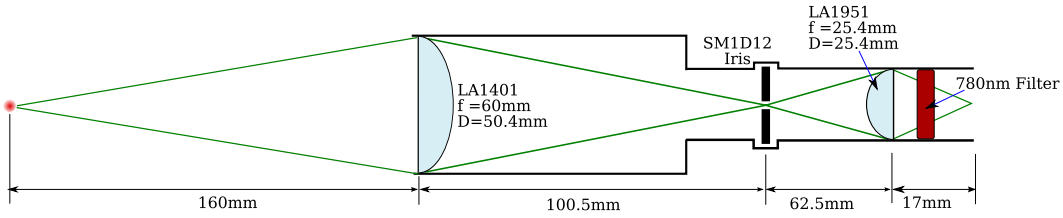

FIGURE 5.8: *Detection optics (not to scale). All components from Thorlabs. The lenses are AR-coated, dimensions; D=diameter, f=focal length.*

5.6.8 Zeeman Shifting

In some cases, such as Doppler cooling or laser beat-note measurement, it may be useful to shift the laser set point off resonance. Small shifts (several MHz) can be achieved by simply moving the set point off the centre of the error signal, but this is limited by the linewidth of error signal. One can use optoelectronic components such as acousto-optical modulators or electro-optical modulators to shift the frequency but one usually suffers loss of power or extra frequency components. We use the Zeeman effect to shift the pump-probe lineshape with the use of a DC magnetic field applied along the beam axis [123]. The magnetic field is formed with a Helmholtz pair to give a uniform field across the vapour cell, optical access to the Rubidium fluorescence and small footprint.

The ideal Helmholtz configuration assumes an infinitely thin current loop. Of course, the copper wire has finite width and the coils have a limited packing efficiency. Numerical modelling established that, of the various possible configurations, the most uniform field would be achieved by coils with the wider dimension along the radius of the coil-form. This can be qualitatively explained by the longitudinally thinner coils tending toward the Helmholtz condition of a single coil.

In order to reduce broadening of the lineshape at high field strengths the field must

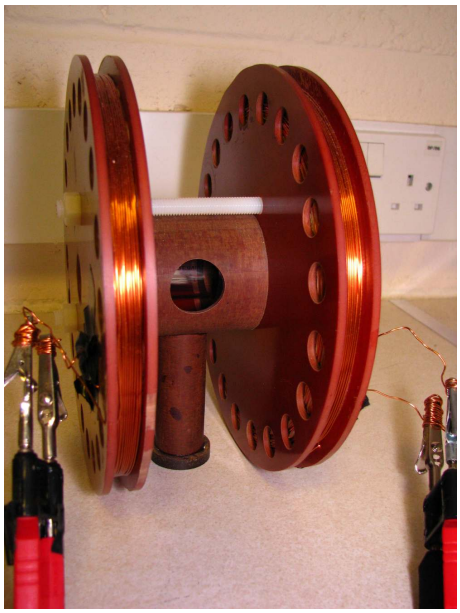

FIGURE 5.9: *Photograph of the Zeeman shift coils.*

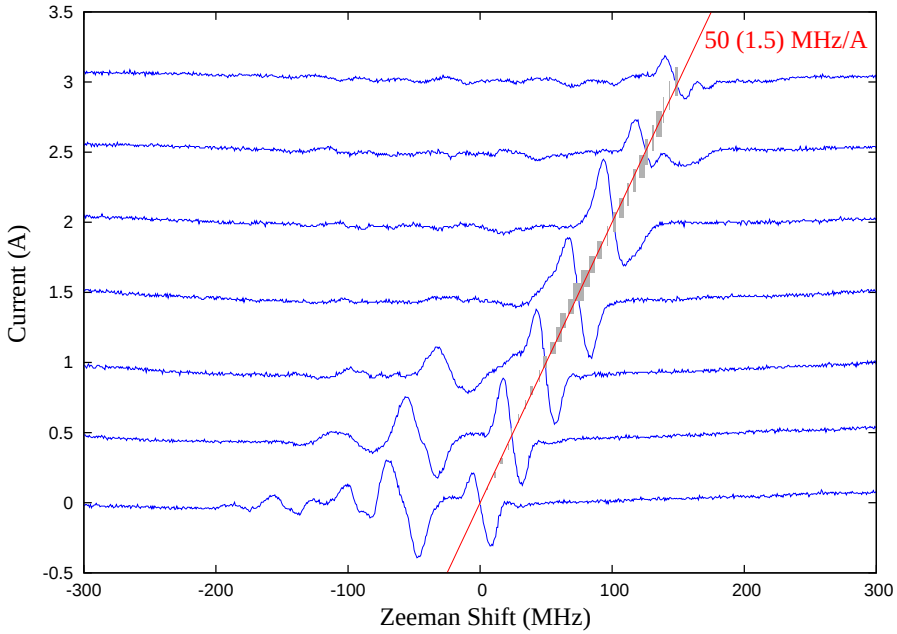

FIGURE 5.10: *Doppler free FMS spectra of* ^{85}*RbF* $= 3$ *with increasing field strength. The shift of the lock point has been calibrated by the beat frequency with an unshifted laser locked to the same transition. Only 6 spectra (offset by coil current) are shown but the Zeeman shifts at other currents is shown by grey rectangles, the size of which is the error. The shift of the beat note with coil current is* $50.0 \pm 1.5\,\mathrm{MHz\,G^{-1}}$. *(red line)*

be uniform to within 1% along the vapour cell. For ^{85}Rb on the $|F = 3, m_F = 3\rangle \rightarrow |F' = 4, m'_F = 4\rangle$ transition with a field of 100 G, the resulting shift is 140 MHz with a non-uniformity of 1.4 MHz (From Eqn. 3.5). A secondary requirement of the coils is that they must fit on the optical table with the vapour cell at 10 cm from the table. The coils were made from Tufnol, which is a resin-based composite which can withstand the high temperatures produced by the air-cooled coils.

A photograph of the coils can be seen in Figure 5.9. Each coil has 300 turns (25 deep by 12 wide) made from 0.71 mm diameter insulated copper wire. After every 2 layers of turns a layer of masking-tape was used to stop unwarranted cross-winding overlap. The center radius of the coils is 8 cm and their separation is also 8cm (Helmholtz condition). The dependence of the magnetic field upon DC current was measured using a Hall probe as $33.0 \pm 0.2\,\mathrm{G\,A^{-1}}$. Modelling the magnetic field with the above coil dimensions predicts a field of $36\,\mathrm{G\,Amp^{-1}}$ with a uniformity of 0.8% across the vapour cell. The discrepencies could be due to an uncalibrated Hall probe as the calcuated resistance in the coils was 12.7 Ohms and measured at 12.8 ± 0.5 Ohms.

Figure 5.10 shows the shift of the lock point with increasing coil current. The points are shown as grey rectangles, the dimensions of which are the uncertainty in measurement. The Zeeman shifted spectra for the major y-axis ticks are shown in blue. The best fit of the Zeeman shift of the ^{85}Rb $|F = 3, m_F = 3\rangle \rightarrow |F' = 4, m_{F'} = 4\rangle$ transition is $50.0 \pm 1.5\,\mathrm{MHz\,A^{-1}}$. The change in FMS lineshape at high magnetic fields is possibly due to the Paschen-Back effect in which m_F is no longer a good quantum number at high fields, when the Zeeman shift is greater than the hyperfine splitting. This hypothesis is supported by the observation that no change is seen in ^{87}Rb lineshape which has a larger hyperfine splitting. The laser remains in lock even with fast detuning ($\mathrm{MHz\,ms^{-1}}$) and this may be a useful way of scanning the laser detuning in a calibrated manner.

5.7 Characterization

This section covers typical measured properties of the atom cloud in a MOT: the cloud size and density, the loading rate, the trap lifetime and the temperature of the Rubidium cloud.

5.7.1 Loading/Loss rates

The steady state atomic density in a MOT is a function of loading and loss rates. By monitoring the fluorescence of the trapped atoms as the magnetic field is switched on, one can gain information about these rates and useful quantities such as background vapour pressure and capture velocity. The rate of change on the number of trapped atoms, $N(t)$, is

$$\frac{\mathrm{d}N(t)}{\mathrm{dt}} = R_f - \gamma_\mathrm{L} N(t) \tag{5.10}$$

where R_f is the loading rate and γ_L is the loss rate [6]. The loading rate is dependent on the background atom density, n_v, the trapping volume, V (which is defined by the beam size and Zeeman detuning), the average velocity of the background vapour, u, atoms and the critical capture velocity, v_c:

$$R_\mathrm{f} = \frac{n_\mathrm{v} V^{2/3} v_\mathrm{c}^4}{2u^3}\,\mathrm{s}^{-1} \tag{5.11}$$

The solution of Equation 5.10 for $t \geq 0$ is,

$$N(t) = \frac{R_\mathrm{f}}{\gamma_\mathrm{L}}(1 - e^{-\gamma_\mathrm{L} t}). \tag{5.12}$$

One can see that the steady state fluorescence is given by $\frac{R_\mathrm{f}}{\gamma_\mathrm{L}}$ and the initial slope of the trap loading is governed by γ_L. The background vapour pressure can be calculated from the loading rate curves, but the equation is strongly influenced by the fourth power of the capture velocity which is difficult to calculate accurately.

The conversion between the signal measured by the PMT and trapped atom number is calculated by Equation 5.13. We have taken into account the solid angle of the fluorescence collection area of the lens system, the quantum efficiency and gain of the

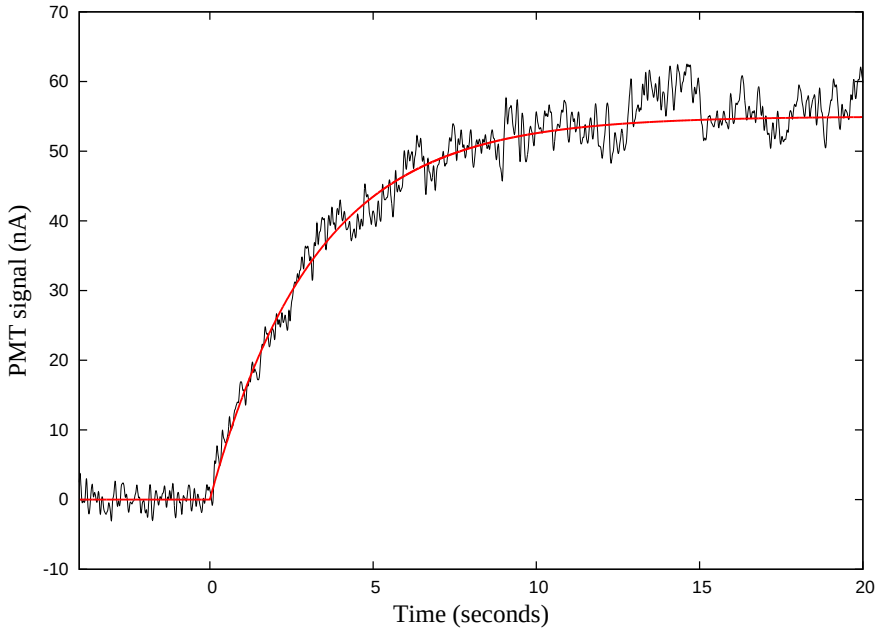

FIGURE 5.11: *Fluorescence of the MOT cloud measured by the PMT as the magnetic field is switched on at t=0. The current from the PMT is directly measured via an SR570 current amplifier with a sensitivity of 90 mA/W and a gain of* 10^4*. The data have been smoothed with a 100 ms Gaussian filter (see Section 8.3). The red curve is modeled using Equation 5.12 with* $\gamma_L = 312 \pm 2$ *mHz and a steady state current of 55nA (see Equation 5.13). Fluctuations of the loaded MOT are due to interference fringes created by the retro-reflected beams.*

PMT, and scattering rate of the atoms.

$$N(\infty) = \frac{4D^2 i_{\mathrm{PMT}}}{\eta_{\mathrm{D}} \eta_O \hbar\omega_0 L^2} \frac{1}{R_{\mathrm{SC}}} \simeq \frac{7.7 \times 10^{17} i_{\mathrm{PMT}}}{R_{\mathrm{SC}}} \tag{5.13}$$

where $i_{\mathrm{PMT}} = 55 \pm 4 \times 10^{-9}$A, $D = 160$ mm is the distance from the cloud to the objective lens which has a radius $L = 25.4$ mm, $\hbar\omega_0$ is the photon energy and $\eta_{\mathrm{D}} = 900\,\mathrm{A\,W^{-1}}$ (1×10^4 gain) and $\eta_O = 0.9$ are the efficiencies of the PMT and optics (the main loss is from the 780nm filter), respectively. R_{SC} is the scattering rate of each atom and can be estimated by dividing the steady state population of the ground state (Equation C.34) by the lifetime (Section 3.2.2.). For the closed $|F = 3, m_{\mathrm{F}} = 3\rangle \rightarrow |F' = 4, m_{\mathrm{F'}} = 4\rangle$ transition at a detuning -3γ and intensity of $3\,\mathrm{mWcm^{-2}}$, we have a steady state population of $\sim \frac{1}{40}$, and hence the steady state number of atoms in the cloud is $4.5 \pm 0.5 \times 10^4$. From Figure 5.11 we can then calculate the loss rate $\gamma_{\mathrm{L}} = 312 \pm 2$ mHz and the loading rate $R_{\mathrm{f}} = N(\infty) \times \gamma_{\mathrm{L}} = 14 \pm 1.5 \times 10^4$ atoms per second.

5.7.2 Cloud Size and Density

The MOT cloud size was measured using the Watec CCD cameras through the PMT optical system. The pixel to length scale was calibrated by imaging calipers placed at the distance of the MOT cloud. The MOT cloud is imaged at the centre of the CCD array and is small enough that we may neglect any image aberrations. The exact shape of the MOT cloud is a convolution between a hard edged sphere, due to the balancing of the forces due to the beams and the photon re-absorption pressure, and the Maxwell-Boltzmann distribution of velocities of the atoms within the cloud. For simplicity we have fitted, via least squares, the measured fluorescence to a Gaussian function (Figure 5.13). The FWHM in the vertical y axis is $350\,\mu$m and $330\,\mu$m in the horizontal x plane. The exact shape of the cloud is not uniform, as can be seen in Figure 5.12, as misalignments and intensity imbalances can have a strong effect. An impressive example of this is misaligning one arm so that the atoms feel a torque. This produces ring shapes, sometimes orbiting a central cloud. A few experimental [124] and theoretical papers have been presented in relation to this effect [125].

Assuming a spherical and isotropic distribution of atoms (not strictly true, see reference [125]) with a diameter of $350\,\mu$m, results in a density in the MOT of $\sim 2\times10^9$ atoms per cm^3. The density is a results of the equilibrium between the attractive trapping force and the repulsive force produced the absorption of scattered photons. An approximation to the theoretical density which can be obtained in the trap has been calculated in Reference

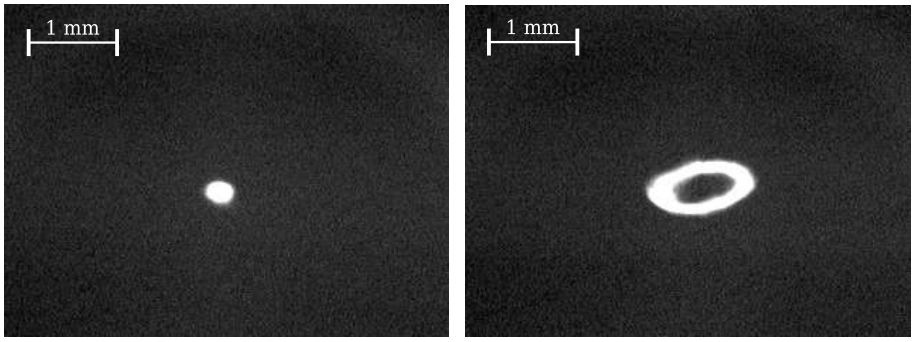

FIGURE 5.12: *Images of the MOT cloud taken with the Watec Camera. Near perfect alignment of the trapping beam results in a spherical cloud (left). A slight misalignment of the beams can create doughnut shaped clouds.*

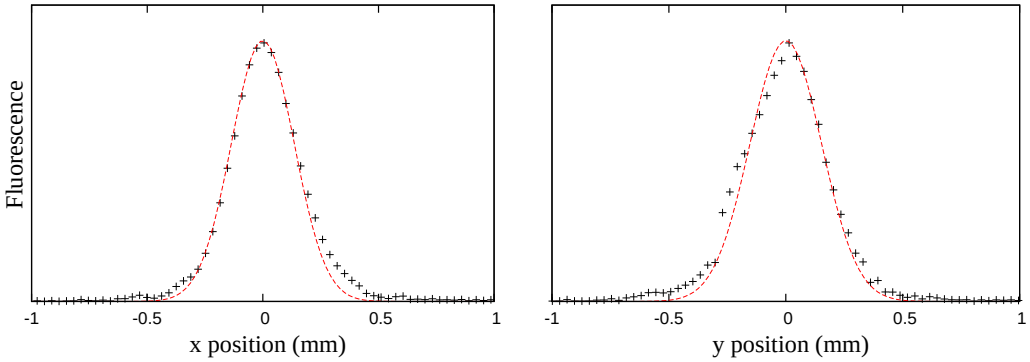

FIGURE 5.13: *Plot of the CCD pixel count (dots) for each axis across the center of the image with Gaussian fitted curves (dashed line). The x axis FWHM is 330μm and the y axis FWHM is 350 μm.*

[126] (Equation 59) and predicts a density of $\sim 10^9$ atoms per cm^{-3} for parameters outlined above, which agrees with our measured value.

5.7.3 Temperature

The temperature of the atoms within a MOT can be measured either in situ [127] or by ballistic methods [109]. In this section we address the destructive ballistic methods which fall into two categories, time of flight or release and recapture (R&R). The time of flight technique requires a thin probe beam placed underneath the cloud to measure the distribution of fall times and thus the temperature of the atoms. This technique is more technically demanding than release and recapture, but is less affected by systematic errors such as the cloud shape. The release & recapture method only requires the MOT beams and is easy to implement, although it can be less accurate and more time consuming [109].

5.7.3.1 Release and Recapture

Cold atoms are collected in the trap and are allowed to come to a steady state (as measured by the fluorescence) over a period of ten seconds. The trapping and repump beams are then extinguished within 10 ns by AOMs and the atoms leave the trap centre with their instantaneous velocity, the magnetic field remains on during experiment. The trapping beams are pulsed after a variable delay and the fluorescence from the remaining

atoms is measured using the lens system in Figure 5.8 and a PMT. The beams start to cool the atoms again, but the fluorescence is measured over $5\,\mu$s so that the cooling effects are negligible.
The difference in the fluorescence measured between the pulse and initially loaded MOT is fitted to a theoretical model and the temperature derived.

Theoretical Analysis

The common method [109] for modeling the R&R decay rate is to convolve the Maxwell Boltzmann distribution of velocities with the cold atom cloud shape and measure the loss of atoms as they expand away from the fluorescence measurement volume. We assume that the cloud dimensions are smaller than the detector area and originate from a single point; this is generally true if the dimensions of the cloud are much smaller than the measurement volume so that any initial shape information will be negligible by the time the atoms reach the edge of the detection region. We also assume that any atoms heading along the axis of the imaging optics (z axis) will have a constant fluorescence (i.e. they do not leave the detection region) and so only consider atoms leaving in the plane perpendicular ($x-y$) to the optical axis. The distance traveled in the time t by a symmetrically expanding cloud is $\sqrt{a_y + a_x} = \sqrt{2}a$, where $a_x = a_y$, if they have a mean temperature T. The decay of fluorescence due to atoms leaving is

$$g(w,t,T) = \frac{1}{t}\sqrt{\frac{M}{\pi k_{\mathrm{B}} T}} \int_{-w}^{+w} \exp\Big(-\frac{Ma^2}{t^2 k_B T}\Big)\mathrm{da} \tag{5.14}$$

For each time t we can integrate over the radius of detection area w and find the percentage of atoms remaining. One will notice that we have two variables, the temperature and the width of the detection region. To find the best fit to measured data in Figure 5.14, the sum of the squared differences (least squares) between the model and data was calculated and the minimum value found by inspection. A rough fit for $d = 400 \pm 200\,\mu$m (half the photodetector area) results in a temperature of $T = 100 \pm 50\,\mu$K, but the least squares minimum varied little over various temperature/detection region values and is therefore unreliable.

The previous, simplistic, model is too reliant on unknown factors so a numerical model was devised by J. Bateman [118] to account for effects due to imaging optics, expansion in

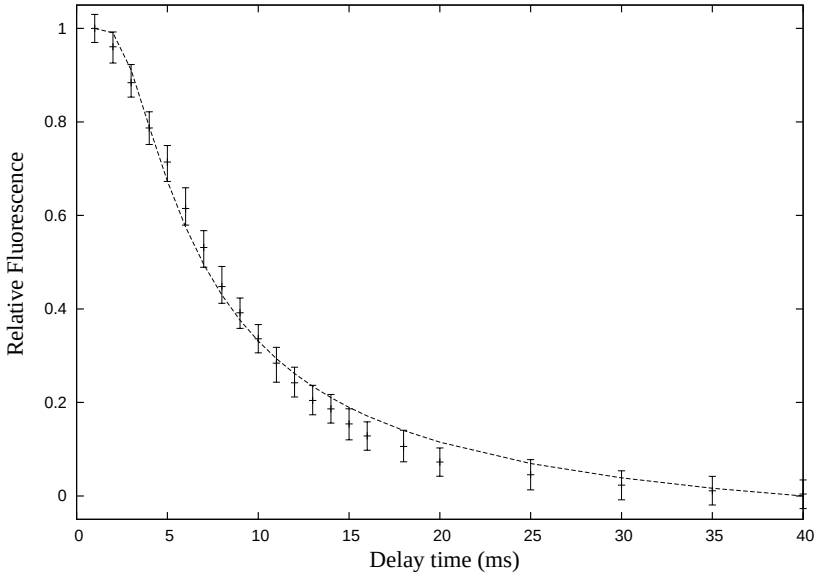

FIGURE 5.14: *Release & recapture model from Equation 5.14 using a Silicon photo detector instead of the PMT before the rebake (see text). The crosses are data-points and the dashed line is the best fit model for a temperature of* $T = 100 \pm 50\,\mu K$ *and sample region* $d = 400 \pm 200\,\mu m$*. The error in the data is the standard deviation from 5 separate runs, the heights of the fluorescence peaks were measured by hand. The heights of the data were scaled so that 100% fluoresence occured at time* $t = 0\,ms$ *and the constant fluorescence at* $t = 45ms$*. The model was scaled likewise. As noted in the text, the data fits a number of temperature/sample region configurations and so this fit is very tenuous.*

3 dimensions under the influence of gravity and finite beam size. In the numerical model, we had an initially uniform density sphere of cold atoms with a diameter smaller than the detection region (with the same approximation as above). The atoms expand ballistically with instantaneous velocities according to the Maxwell Boltzmann distribution and fall under gravity. After a variable delay each atom emits a photon in a random direction; those photons which fall into the lens system, placed at the experimentally measured distance, and also hit the active area of the detector are recorded (via a ray tracing algorithm).

Figure 5.16 shows data collected using the PMT in winter 2008 and Figure 5.15 shows the data collected with a Silicon PIN photodetector in spring 2007. The latter plot shows many theoretical curves for possible temperatures as the numerical model takes several hours to compute so using a fitting algorithm is impractical. The closest fit to the Silicon detector data (no getters) is $80 \pm 20\,\mu$K whereas the PMT data (with getters) shows a much increased temperature of $220 \pm 50\,\mu$K. The dimensions and response of

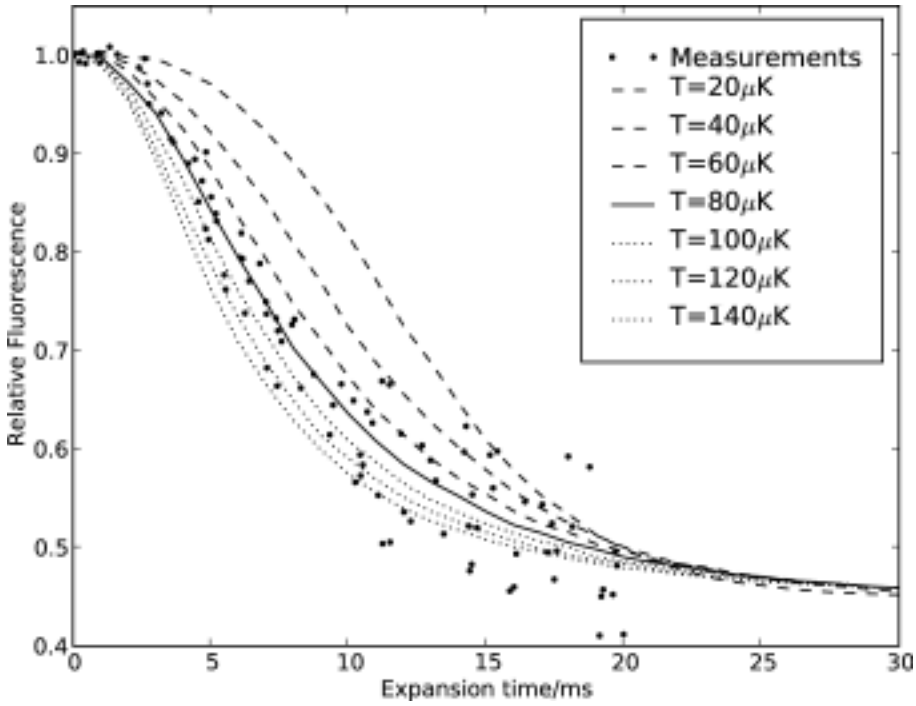

FIGURE 5.15: *Release & recapture data and numerically modeled curves for various temperature of the MOT cloud. This data was taken before the chamber was re-baked and so was loaded from background gas released from the walls of the 'warmed up' chamber, therefore no getter was required. The best fit is* $80 \pm 20\,\mu K$*. Data and plot by James Bateman*

each detector have been accounted for in the model and so we do not think the different detectors are responsible for the large differences in the measured temperature. As noted earlier the data sets are taken a year apart and so direct comparisons should not be made as the MOT setup has changed within this time.

The temperature appears related to the accuracy of the beam alignment with perfect alignment resulting in the coldest temperature, but this also introduced fringes across the MOT cloud. The higher temperature measured above is most likely due to a beam misalignment. The MOT beam require re-allignment usually once a week due to thermal drifts of the optics and so we can assume the temperature is nominally of the order $\sim 10^{-5}\,\mathrm{K}$

If we assume a MOT temperature of $100\,\mu$K and density of 10^9 atoms per cm^3 to estimate the coherence properties of the cold atoms. In the next chapters we see that we need to turn off the MOT trapping beams in order to perform coherence experiments and so the temperatures during free expansion are most important. Using the mean free path calculations from Section 3.2.1, the average distance an atom will travel between

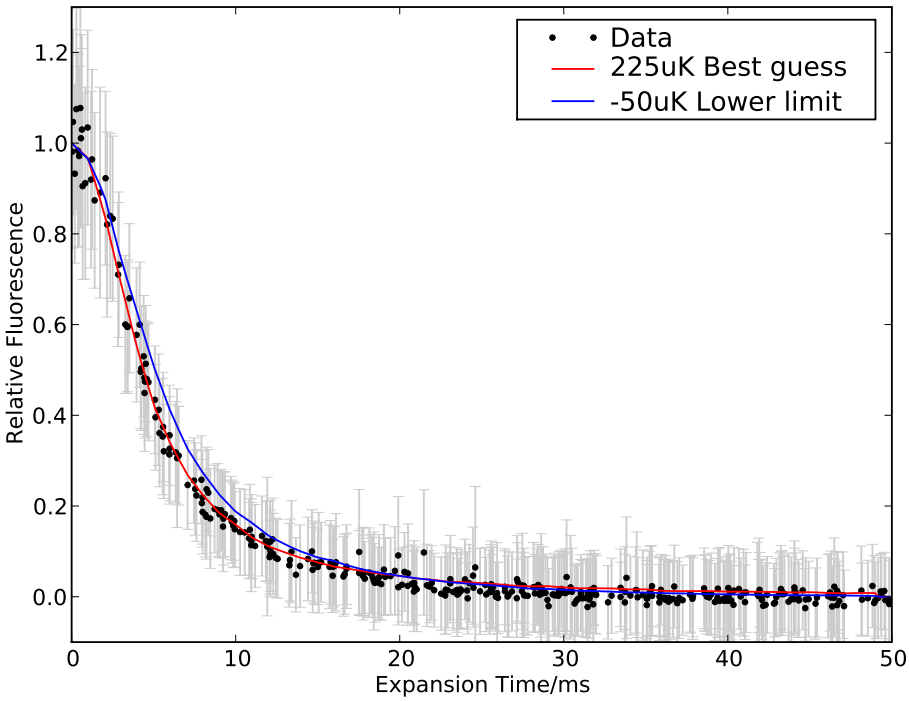

FIGURE 5.16: *Release and recapture data and numerical model for data collected with the PMT and with the getters on. The closest fit to the data is* $220 \pm 50\,\mu K$*. Data and plot by James Bateman*

collisions, which cause decoherence, is ∼1.4 km and using Equation 3.14 the time between collisions is over 2 hours, so we can consider collisions to be negligible. The constraining timescale is the cloud expansion loss (Figure 5.15) and so we must perform the coherent manipulations within a few milliseconds.

Chapter 6

Coherent Manipulation

6.1 Coherent Control

The aim of the work described in this thesis was to investigate techniques which allow one to control atomic momentum using coherent laser fields. We are especially interested in cooling methods that rely upon coherent atom-optical interactions. Raman transitions will be the work-horses of the experiments outlined in the next two chapters because they allow one to transfer populations between two states of equal spin-nuclear momentum states, which are forbidden in single photon transitions. These states cannot spontaneously decay between each other through electric dipole radiation because angular momentum is not conserved.

In this chapter we begin by deriving the optical Bloch vector which provides an intuitive understanding of atom-light interactions. From this picture we can find schemes which allow efficient transfer of populations, and therefore momentum, between atomic states. We end the chapter by outlining the proposed cooling schemes using pulsed coherent interactions.

6.2 Theoretical Tools

To discuss the methods used for coherent control of atomic momentum we shall use the semi-classical picture of quantum-atom/classical-field interaction. This is because we wish to describe effects upon ensembles of atoms which may spontaneously emit, therefore a closed basis set in terms of wavefunctions becomes incalculable. We shall use the density matrix formalism and calculate the statistical properties of the ensemble. The derivation of the density matrix can be found in most graduate quantum physics textbooks, (for example [99]), and has been included in the Appendix C so that we may dip into any relevant results. We first derive the optical Bloch vector (OBV) formalism which provides an intuitive picture of coherent interaction of a field and a two level atom. We then discuss how we may approximate a real atom as a two level system by the use of Raman transitions and identify regions where this approximation breaks down.

6.2.1 Optical Bloch Vector

In Appendix C we derive the density matrix equations for a two level system which describes the probability, ρ_{gg} or ρ_{ee}, of finding an atom in either the ground or the excited state, respectively, and the off-diagonal *coherences* $\rho_{\mathrm{eg}} = \rho^*_{\mathrm{ge}}$ which represent the coupling (or more accurately, the interference) between states caused by external fields and decay mechanisms.

$$\dot{\tilde{\rho}}_{\mathrm{gg}} = -\frac{i\Omega}{2}(\tilde{\rho}_{\mathrm{eg}} - \tilde{\rho}_{\mathrm{ge}}) + \gamma\tilde{\rho}_{\mathrm{ee}} \tag{6.1}$$

$$\dot{\tilde{\rho}}_{\mathrm{ee}} = \frac{i\Omega}{2}(\tilde{\rho}_{\mathrm{eg}} - \tilde{\rho}_{\mathrm{ge}}) - \gamma\tilde{\rho}_{\mathrm{ee}} \tag{6.2}$$

$$\dot{\tilde{\rho}}_{\mathrm{ge}} = -i\tilde{\rho}_{\mathrm{ge}}\delta - \frac{i\Omega}{2}(\tilde{\rho}_{\mathrm{ee}} - \tilde{\rho}_{\mathrm{gg}}) - \frac{\gamma}{2}\tilde{\rho}_{\mathrm{ge}} \tag{6.3}$$

$$\dot{\tilde{\rho}}_{\mathrm{eg}} = i\tilde{\rho}_{\mathrm{eg}}\delta + \frac{i\Omega}{2}(\tilde{\rho}_{\mathrm{ee}} - \tilde{\rho}_{\mathrm{gg}}) - \frac{\gamma}{2}\tilde{\rho}_{\mathrm{eg}} \tag{6.4}$$

where $\delta = \omega - \omega_{eg}$ is the detuning of the laser frequency ω from the atom rest-frame resonance ω_{eg} and Ω is the (real valued) resonant Rabi frequency introduced in Chapter

3. We may rearrange the density matrix equations in terms of the Pauli spin matrices.

$$u = \begin{pmatrix} 0 & 1 \\ 1 & 0 \end{pmatrix} \rho \quad = \rho_{\mathrm{ge}} + \rho_{\mathrm{eg}} \tag{6.5}$$

$$v = \begin{pmatrix} 0 & -i \\ i & 0 \end{pmatrix} \rho \quad = -i(\rho_{\mathrm{ge}} - \rho_{\mathrm{eg}}) \tag{6.6}$$

$$w = \begin{pmatrix} 1 & 0 \\ 0 & -1 \end{pmatrix} \rho \quad = \rho_{\mathrm{gg}} - \rho_{\mathrm{ee}} \tag{6.7}$$

Substituting Equations 6.5, 6.6 and 6.7 into density matrix equations, we find

$$\dot{u} = \delta v - \frac{\gamma}{2} u \tag{6.8}$$

$$\dot{v} = -\delta u + \Omega w - \frac{\gamma}{2} v \tag{6.9}$$

$$\dot{w} = -\Omega v + \gamma(1 - w) \tag{6.10}$$

these equations are known as the Optical Bloch Equations (OBEs). If we neglect the relaxation terms for the moment (i.e. set $\gamma \approx 0$), we may construct a vector using this formulation.

$$\vec{R} = u\hat{\mathbf{x}} + v\hat{\mathbf{y}} + w\hat{\mathbf{z}} \tag{6.11}$$

The application of an external field then acts like a torque on vector $\vec{R}$

$$\frac{\mathrm{d}\vec{R}}{\mathrm{dt}} = \vec{R} \times \vec{\Omega} \tag{6.12}$$

where

$$\vec{\Omega} = \Omega\hat{x} + \delta\hat{z} \tag{6.13}$$

with a magnitude

$$|\vec{\Omega}| = \sqrt{\Omega^2 + \delta^2} \tag{6.14}$$

We can see that the 'state vector' $\vec{R}$ has a constant length, as $\frac{\mathrm{d}\vec{R}}{\mathrm{dt}}$ is orthogonal to both $\vec{R}$ and the 'field vector' $\vec{\Omega}$. Therefore $\vec{R}$ describes the surface of a unit-radius sphere. This is known as the Optical Bloch Vector (OBV) picture and was developed by Feynman, Vernon and Hellwarth [128]. Its construct is analogous to the Poincaré sphere

describing optical polarization. We will predominantly use the relaxation-free OBV but spontaneous emission can be included phenomenologically causing the state vector to no longer have a constant length, and therefore decay toward the centre of the OBV sphere during the interaction and toward the ρ_{gg} ($w \rightarrow -1$) with no applied field.
As mentioned in Section 3.2.2, the decay rates are commonly separated into 'longitudinal' and 'transverse' decay. Phase interruptions, such as collisions will cause decay of the coherences and hence decay toward zero in the $x-y$, or *transverse* plane. Depopulating will cause decay along the z-axis or *longitudinal* axis.

6.2.2 Rabi Oscillations

Using the OBV we can visualize the effect of a strong resonant field interacting with an atom, or ensemble of atoms. From Equations 6.11 and 6.12, at zero detuning ($\delta = 0$) the field vector $\vec{\Omega}$ will point along the x-axis and the state vector $\vec{R}$ will draw out a great circle in the $y-z$ plane with a frequency equal to the resonant Rabi frequency Ω, as previously shown in Figure 3.2. If the atom was initially in the lower state, the population would oscillate between the two levels; this is known as Rabi-flopping[1] and can be seen in the OBV picture in Figure 6.1. If we include spontaneous decay from the excited state into the ground state (i.e. a closed two level system), the coherences are damped out and the population in each state tends to 1/2 as predicted in the rate equation derivation in Section 3.3.1.

6.2.3 π Pulses

In Figure 6.1 we see that during a Rabi 'flop' on resonance, the population in a state is transferred with nearly 100% efficiency into the opposite state if the laser is pulsed with a time equal to $\tau_{\text{Int}} = n\pi/\Omega$, where n is an odd positive integer and $\tau_{\text{Int}} \ll 1/\gamma$. This inversion interaction is called a π pulse. We may also finish the pulse a quarter way through a Rabi cycle so that the pulse area $\Omega\tau_{\text{Int}} = \pi/2$ and the atom is left in a superposition of the two states. This is known as a $\pi/2$ pulse and is a key tool in atom

[1] We distinguish between the Rabi Frequency Ω and the Rabi flopping - or Generalized Rabi - frequency $\sqrt{\Omega^2 + \delta^2}$. The former defines the strength of an interaction whereas the latter defines the rate of population cycling. Only at resonance are these two parameters equal

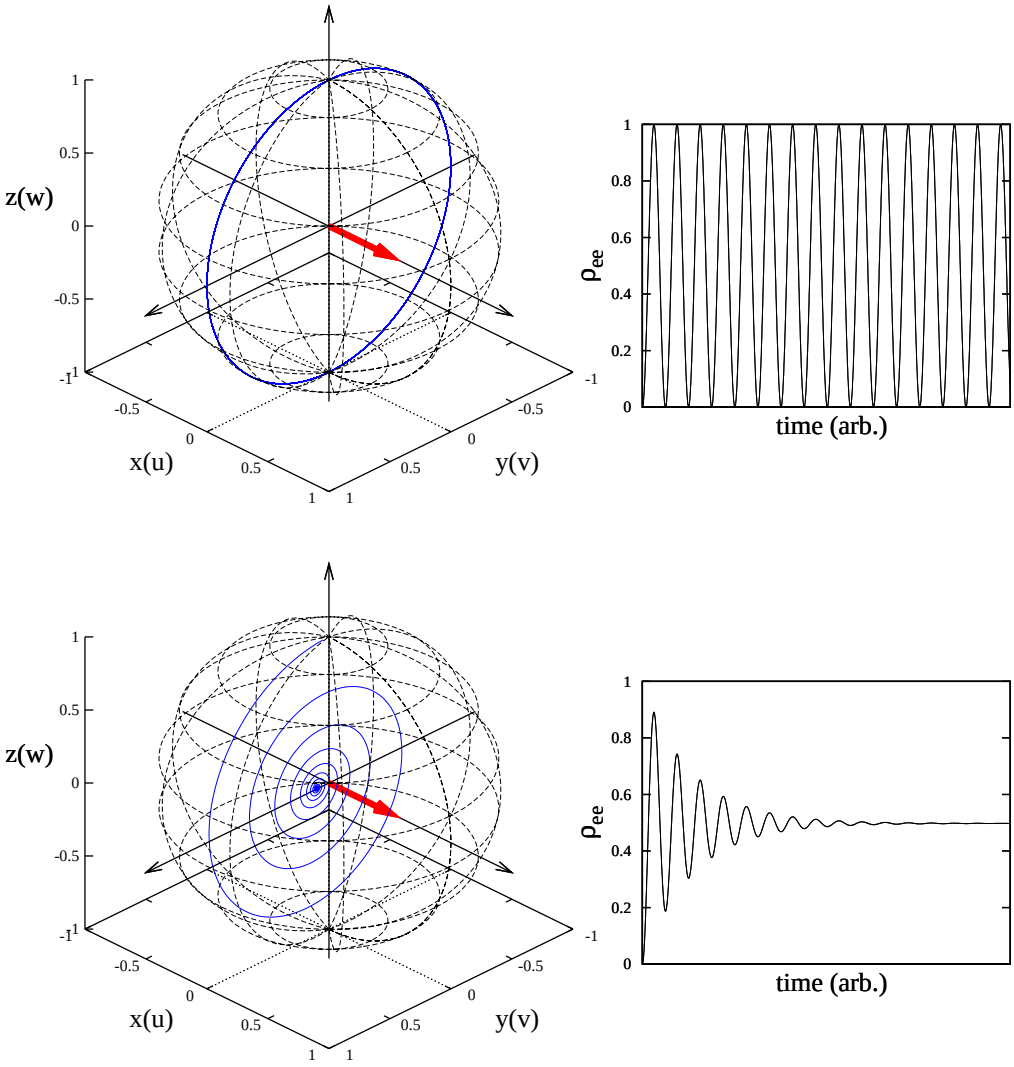

FIGURE 6.1: *Numerical simulation of Rabi flopping on the optical Bloch sphere. Top; The field vector (red) on resonance points along the x-axis and the state vector traces out the blue circle as the populations oscillate between states at a frequency* Ω *(see state populations in the top right graph). Bottom; Rabi-flopping with decay, the populations tend toward 1/2.*

interferometry [15]: as with most pulse shaping techniques the technique was transferred to the optical region from NMR techniques [129]. As we have been dealing with atomic ensembles throughout this thesis it is worth mentioning that the superposition state occurs for a *single atom*, but the inclusion of *gamma* is a statistical property of the ensemble.

6.2.4 Adiabatic Rapid Passage

Achieving population inversion or superposition experimentally using fractional π-pulses is wrought with technical difficulties such as extinguishing the beam sharply at the correct time, and motional effects in a spatially dependent optical and magnetic field, which causes the atomic resonance frequency to be shifted so that the detuning and coupling strengths will vary. After applying a π-pulse to such an ensemble, one would find the atoms in a distribution of states and superpositions. This does not mean that π-pulses are impossible, but one cannot expect the theoretical 100% inversion [130, 131, 132].

Fortunately we may use pulse shaping techniques (in both frequency and intensity) to produce more robust state control. The general term for one such technique is *adiabatic rapid passage*. In describing adiabatic rapid passage (ARP), the OBV really shows its true worth as an intuitive picture. In Figure 6.2 we start with the atom in the ground state ($w = 1$). We introduce a laser field far off resonance ($\delta = -\infty$) with a constant intensity: the state vector $\vec{R}$ rotates around the field vector $\vec{\Omega}$ at a frequency $|\vec{\Omega}|$. We term this small rotation as a *nutation*. If the driving field is brought to resonance at a rate which is slower than the generalised Rabi frequency, but faster than spontaneous decay (this is the 'rapid' part) then the state vector will 'adiabatically' follow the field vector. As the driving field passes through resonance and heads off to distant positive detuning ($\delta = \infty$) the atom is left in the inverted state. The conditions for this adiabatic passage are [132]

$$\gamma^3 \ll \frac{1}{2}\left|\Delta\frac{\mathrm{d}\Omega}{\mathrm{dt}} - \Omega\frac{\mathrm{d}\Delta}{\mathrm{dt}}\right| \ll (\Omega^2 + \Delta^2)^{3/2} \tag{6.15}$$

The simple process of constant intensity but linearly varying detuning does not leave the state vector completely in the inverted state as can be seen from the remaining nutations, but with careful consideration of both frequency and intensity pulse shapes, we may transfer all populations with a high probability. Pulse shapes also exist for $\frac{\pi}{2}$-pulses using ARP. Our group has addressed the theory behind adiabatic state inversion and superpositions [133]. The Mathematica code for the numerical simulations of the Bloch sphere can be found in Appendix D.

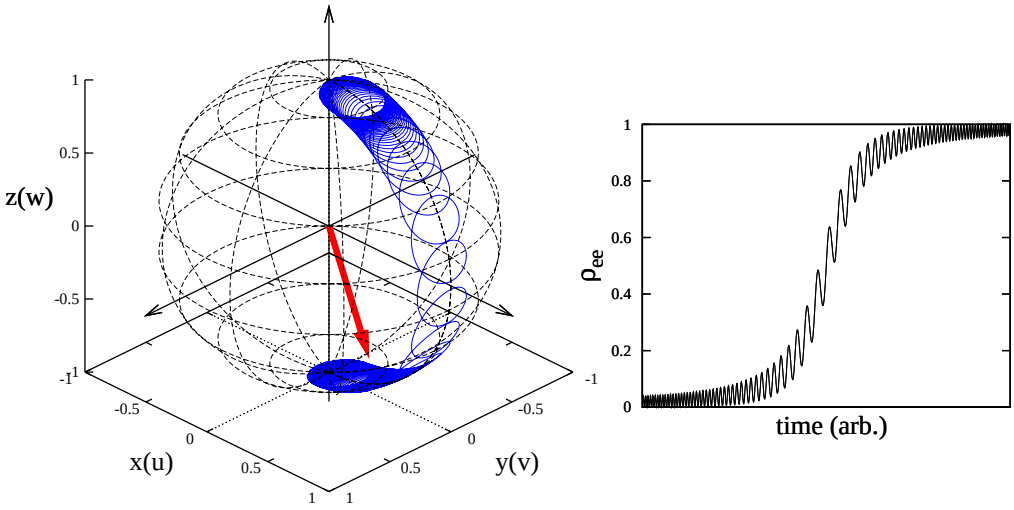

FIGURE 6.2: *Numerical simulation of adiabatic rapid passage on the optical Bloch sphere. The beam intensity is constant but the frequency is chirped from far below to far above resonance. We see nutation of the state vector (blue) around the field vector (red, shown at an arbitrary position as it rotates in the $x-y$ plane). The resulting state populations are shown on the right.*

6.3 Raman Transitions

One may ask why we are spending so much time describing the interaction of a two-level system with a laser when we have already seen in Chapter 3 that Rubidium is certainly not a two-level system. The above Rabi oscillations do indeed occur in any transition but the lifetime of the state is usually too short to interact coherently with the atom before decay. As hinted at the beginning of this chapter, we are interested in transitions between the two $5S_{1/2}$ *ground* states of Rubidium which do not spontaneously decay. The electric dipole transition between these states is forbidden but we may use two photons mediated by a 'virtual' dipole-allowed state.

To understand the dynamics of a three-level system interacting with a bi-chromatic field we shall solve the time-dependent Schrödinger equation (TDSE) [134, 135]. The level diagram and detunings are shown in Figure 6.3; it is a Λ-type configuration with two ground states ($|1\rangle$ and $|3\rangle$) between which electric dipole transitions are forbidden. Both ground states are radiatively coupled to the excited $|2\rangle$ state (which may spontaneously decay) with state energies $E_2 > E_3 > E_1$. We assume a large detuning from the radiative state $|2\rangle$ so that we may neglect spontaneous emission and single photon transitions.

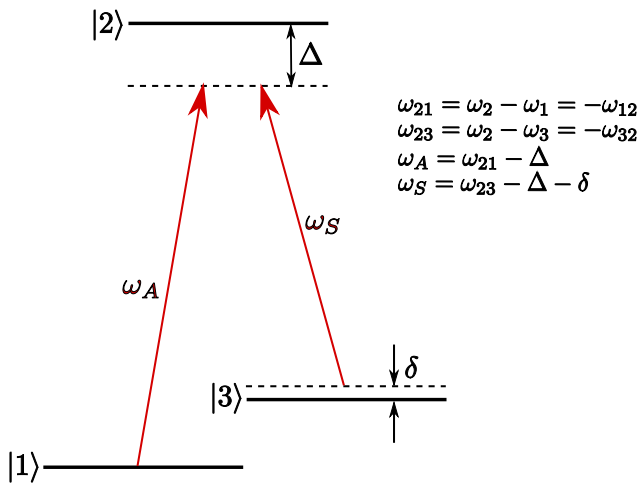

FIGURE 6.3: *Lambda-type 3 level system and relative detunings*

This assumption will be justified by the result of the derivation. The wavefunction of the atoms is

$$\Psi(\vec{r},t) = C_1(t)\psi_1(\vec{r})e^{-i\frac{E_1}{\hbar}t} + C_2(t)\psi_2(\vec{r})e^{-i\frac{E_2}{\hbar}t} + C_3(t)\psi_3(\vec{r})e^{-i\frac{E_3}{\hbar}t} \tag{6.16}$$

where $E_k = \hbar\omega_k$ and we have separated the wavefunction into time-dependent probability amplitudes ($C_n(t)$) and the spatially-dependent radial ($\psi_n(\vec{r})$) parts under the dipole approximation. The atoms interact with a bi-chromatic field.

$$E(t) = \frac{\mathscr{E}_{\mathrm{S}}}{2}(e^{-i\omega_{\mathrm{S}}t} + e^{i\omega_{\mathrm{S}}t}) + \frac{\mathscr{E}_{\mathrm{A}}}{2}(e^{-i\omega_{\mathrm{A}}t} + e^{i\omega_{\mathrm{A}}t}) \tag{6.17}$$

where we have defined the higher and lower frequency beams, Stokes (S) and anti-Stokes (A) respectively[2]. The Hamiltonian of the system is

$$\mathbf{H} = \begin{pmatrix} E_1 & \mu_{12}\cdot\mathscr{E}(t) & 0 \\ \mu_{21}\cdot\mathscr{E}(t) & E_2 & \mu_{23}\cdot\mathscr{E}(t) \\ 0 & \mu_{32}\cdot\mathscr{E}(t) & E_3 \end{pmatrix} \tag{6.18}$$

[2]In the literature, the anti-Stokes beam is commonly called the 'pump' beam. In previous section of this thesis we have termed the pump beam as the 'stronger' beam, as we are here dealing with nearly equal strength couplings in our Raman system, the pump nomenclature is misleading.

where $\mu_{ij} = \mu_{ji}$ is real. Substituting Equations 6.18 and 6.16 into the TDSE then multiplying by $\psi_i^*(\vec{r})e^{i\omega_i t}$ we find the rate of change of the state probability amplitudes

$$i\dot{C}_1 = \frac{C_2\mu_{12}\mathscr{E}_A}{2\hbar}e^{-i\Delta t} \tag{6.19}$$

$$i\dot{C}_2 = \frac{C_1\mu_{12}\mathscr{E}_A}{2\hbar}e^{i\Delta t} + \frac{C_3\mu_{23}\mathscr{E}_S}{2\hbar}e^{i(\delta+\Delta)t} \tag{6.20}$$

$$i\dot{C}_3 = \frac{C_2\mu_{23}\mathscr{E}_S}{2\hbar}e^{-i(\delta+\Delta)t} \tag{6.21}$$

As previously assumed in the derivation of the two-level density matrix, we may remove the exponential terms by substituting the following 'slow variables'[3].

$$C_1 = \tilde{C}_1, \quad C_2 = \tilde{C}_2 e^{i\Delta t}, \quad C_3 = \tilde{C}_3 e^{-i\delta t} \tag{6.22}$$

We define the resonant Rabi frequencies.

$$\Omega_A = \frac{\mu_{12}|\mathscr{E}_A|}{\hbar} \tag{6.23}$$

$$\Omega_S = \frac{\mu_{23}|\mathscr{E}_S|}{\hbar} \tag{6.24}$$

We arrive at our final form for the rate of change of the state probabilities.

$$i\dot{\tilde{C}}_1 = \frac{\Omega_A}{2}\tilde{C}_2 \tag{6.25}$$

$$i\dot{\tilde{C}}_2 = \Delta\tilde{C}_2 + \frac{\Omega_A}{2}\tilde{C}_1 + \frac{\Omega_S}{2}\tilde{C}_3 \tag{6.26}$$

$$i\dot{\tilde{C}}_3 = \frac{\Omega_S}{2}\tilde{C}_2 - \delta\tilde{C}_3 \tag{6.27}$$

We can see that if the two beams are in the Raman condition ($\delta = 0$) there is a constant motion between states $\tilde{C}_1$ and $\tilde{C}_3$ dependent only upon the coupling strength of each beam with no population in the radiative $\tilde{C}_2$ state. This may be seen as a dark state in the 'dressed' picture of the atom-photon interaction [136].

A common approach to solving these equations, known as 'adiabatic elimination', is to note that the radiative $\tilde{C}_2$ state undergoes fast changes of population, compared with the ground states, and therefore averages to zero over many oscillations. Exact derivation of the three-level system without this approximation yields the same results for all

[3]This is equivalent to a rotation into the frame of the detunings

detunings [137]. By setting Equation 6.26 to zero and substituting it into Equations 6.25 and 6.27 we find the new evolution of the Raman system as

$$-i\hbar\frac{\partial}{\partial t}\begin{pmatrix}\tilde{C}_1\\ \tilde{C}_3\end{pmatrix} = \hbar\begin{pmatrix}\frac{\Omega_{\mathrm{A}}^2}{4\Delta} & \frac{\Omega_{\mathrm{S}}\Omega_{\mathrm{A}}}{4\Delta}\\ \frac{\Omega_{\mathrm{S}}\Omega_{\mathrm{A}}}{4\Delta} & \frac{\Omega_{\mathrm{S}}^2}{4\Delta}-\delta\end{pmatrix}\begin{pmatrix}\tilde{C}_1\\ \tilde{C}_3\end{pmatrix} \tag{6.28}$$

where the result is in the format of the TDSE to expose the Hamiltonian. Comparison with Equation 6.18 shows that the Raman two-photon Rabi frequency is

$$\Omega_{\mathrm{R}} = \frac{\Omega_{\mathrm{A}}\Omega_{\mathrm{S}}}{2\Delta} \tag{6.29}$$

Comparison of this result with the single photon scattering rate from Equation 3.34 reveals that at large detunings the single photon scattering rate is proportional to the square of the detuning, whereas the two-photon scattering rate scales linearly with detuning. We now justify our assumption of negligible spontaneous emission at large detuning as the two photon transition rate is larger than the single photon scattering.

In Chapter 3 we did not discuss the perturbation of the state energies due to the incident beams, as we were dealing with weak beams in which the resulting shift in energy (AC Stark shift, light-shift or Autler-Townes effect [138, 139]) is much smaller (kHz) than the linewidth of the saturated transition (tens of MHz), although light shifts were briefly mentioned in Chapter 5 as they are a fundamental element of sub-Doppler cooling.
As the lifetime of the ground states does not depend upon spontaneous emission and as we are dealing with a cold sample we may also neglect collisional spin-exchange transitions, the linewidth of the ground state is now defined by power broadening ($\frac{\Gamma_{\mathrm{Power}}}{2} = \Omega_{\mathrm{R}}$) and interaction times ($\Gamma_{\mathrm{I}} \simeq 2\pi/\tau_{\mathrm{I}}$). These mechanisms broaden the ground states far less than radiative broadening, therefore the light shifts have a more significant effect on the Raman tuning δ. From the eigenvalues of the Hamiltonian in Equation 6.28, the light shifts of the ground states are

$$\Delta E_1 = \hbar\frac{\Omega_{\mathrm{S}}^2}{4(\omega_{21}-\omega_{\mathrm{A}})} \tag{6.30}$$

$$\Delta E_3 = \hbar\frac{\Omega_{\mathrm{A}}^2}{4(\omega_{23}-\omega_{\mathrm{S}})} \tag{6.31}$$

where we have assumed that the light shift of state $|1\rangle$ due to Ω_S is much smaller than Ω_A and vice versa. We see that the states are 'repelled' by the incident beams, i.e. if $\omega_A > \omega_{21}$ the state $|1\rangle$ is shifted to lower energies and if $\omega_A < \omega_{21}$ the state $|1\rangle$ is shifted to higher energies.

6.3.1 Coherent Population Trapping

We have shown that we can prepare a nearly ideal two state system via off resonance Raman transitions. We briefly examine the situation where the single photon detuning is near resonance $\Delta \to 0$ within the Raman resonance condition $\delta = 0$, as such situations occur within the parameter space of the experiment. From Equations 6.25, 6.26 and 6.27 we noted that there was a dark eigenstate of the coupled system in which the radiative $|2\rangle$ state is not populated [135]. This dark state does not depend upon the detuning from resonance and so will still exist at $\Delta = 0$. In our derivation of this equation we neglected spontaneous emission as we were far detuned from the single photon resonance. We may no longer use this assumption but careful derivation including spontaneous emission terms shows that the atom is optically pumped into this dark state after a few cycles and so the atom becomes transparent to the pumping beams [140]. This effect is known as coherent population trapping (CPT, in the regime $\Omega_A \simeq \Omega_S$) or electromagnetically induced transparency (EIT, in the regime $\Omega_A \gg \Omega_S$ or vice versa).

The first experiments by Alzetta [141] showed narrow 'dark' resonances in Sodium vapour when both Raman beams were resonant with transitions to a common state. The 'dark' state we refer to here is that there is a reduction in the spontaneous emission from a normally radiative state. The widths of these dark states were narrower than the natural homogeneous width and depended upon the intensity of the coupling beams. Along with the 'adiabatic elimination' explanation discussed before, we may also think of the effect as deconstructive interference between decay paths [142]. In this condition, with initially equal populations in both ground states, there is no change after application of the Raman beams. When there exists an unequal distribution between the states, the fast Rabi cycling will equalize the distributions. Another effect of

on-resonance Raman transitions is the absence of the light shift of the ground states, therefore the narrow CPT resonance is used as a clock transition [143].

Another closely related technique for adiabatic transfer between two ground states in a Raman-type configuration is stimulated Raman adiabatic passage (STIRAP) [132]. Referring to Figure 6.3, we set $\delta = \Delta = 0$ so that each beam are resonant. With the population initially in state $|1\rangle$ we apply Ω_S but keep $\Omega_A = 0$. We may call state $|1\rangle$ the dark state as it is not coupled to $|2\rangle$. We then increase Ω_A and decrease Ω_S toward zero. When $\Omega_A = \Omega_S$, we are in the CPT condition and have equal population in levels $|1\rangle$ and $|3\rangle$ but the atoms remains in the dark dressed state. As Ω_S tends to zero and Ω_A remains constant, the populations are completely transferred to $|3\rangle$ with no single photon effects (in a pure 3 level system). This is a very popular technique for atom interferometry but is not suited to our situation as it is not symmetric for both states, i.e. we cannot transfer populations between $|1\rangle$ and $|3\rangle$ simultaneously.

One may ask why, when we detune from resonance there exists a stable dark state on-resonance? The reason is that there will always been some spontaneous decay and therefore loss of population. By detuning far from resonance we can ensure that the single photon scattering rate is far outweighed by the two photon transition rate.

6.3.2 Raman Transitions with Rubidium

We now turn to achieving Raman transitions in an atom with a more complicated structure, namely ^{85}Rb. From our discussion of the structure of Rubidium in Chapter 3 we have two $5S_{1/2}$ ground states F=2 & 3, and four $5P_{3/2}$ excited states F′=1, 2, 3 & 4, each of which is separated into $2F + 1$ magnetic sub-states. Raman transitions can only occur between states which have a common dipole-allowed 'virtual' state. This means we have two Raman pathways via the F′=2 & 3 excited states. Figure 6.4 shows the Raman pathways for $\sigma^+ - \sigma^+$ polarized beams.

In order to calculate the two-photon transition rate we must sum over all possible Raman routes when far detuned from the excited state as the hyperfine splitting is much less

than the detuning[4]. Some pathways result in a two-photon transition probability that

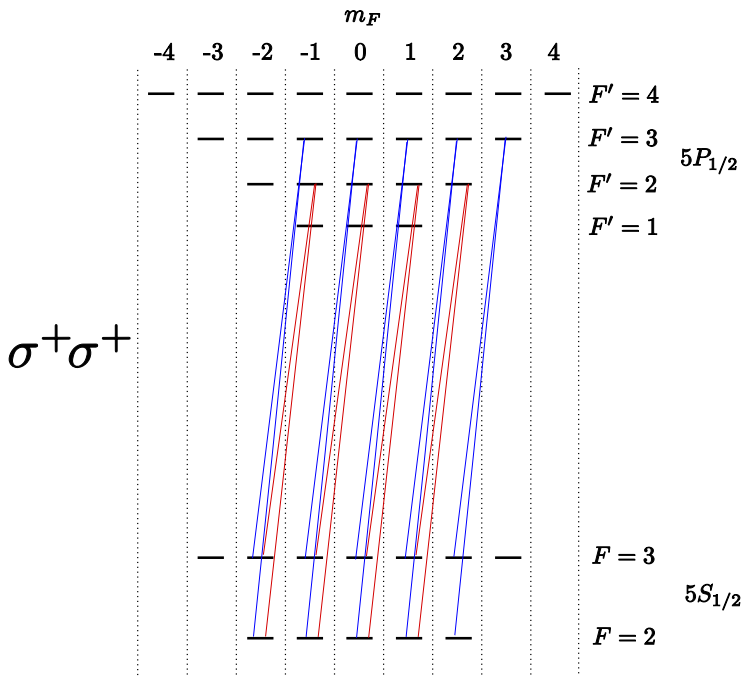

FIGURE 6.4: *Allowed Raman pathways in ^{85}Rb with $\sigma^+ - \sigma^+$ polarized beams. The different coloured couplings are merely an aid to the eye.*

is identically zero. An example of this is a Raman transition $|F = 2, m_\mathrm{F} = 0\rangle \rightarrow |F' = 3, m'_\mathrm{F} = 0\rangle$ with $\pi - \pi$ polarized beams (we assume a quantization axis is applied). From the dipole matrix moments in Appendix A we see that both the $|F = 2, m_\mathrm{F} = 0\rangle \rightarrow |F' = 2, m'_\mathrm{F} = 0\rangle$ and $|F = 3, m_\mathrm{F} = 0\rangle \rightarrow |F' = 3, m'_\mathrm{F} = 0\rangle$ transition have zero dipole matrix elements and so a Raman transition cannot occur.

We can use this argument to impose a quantization axis to the interaction. Atoms in zero magnetic field (as they tend toward in a MOT) have no quantization axis so that there is no distinction between, say, $\pi - \pi$ transitions or $\sigma - \sigma$ transitions; therefore the two-photon transition probability, when summed over all possible routes with all polarizations, may be greatly reduced or zero. For efficient population transfer we must use a definite Raman Rabi frequency and therefore distinct polarizations and quantization axis. This also lifts the degeneracy of the magnetic sub-levels.

[4]Technically we must find the eigenvalues for the multilevel system, not merely summing each Raman pathway.

James Bateman has numerically calculated the two-photon transition frequencies and transfer efficiencies for various polarization couplings for ^{85}Rb. We shall just quote the results here, but refer the reader to his PhD thesis [118] for details of the derivation. The two photon Rabi frequency is

$$\Omega_R = \chi \frac{|\langle J||\mu||J'\rangle|^2}{c\epsilon_0\hbar^2}\frac{I}{\Delta} \tag{6.32}$$

where $|\langle J||\mu||J'\rangle|$ is the reduced dipole moment ($4.227qa_0$ for ^{85}Rb, where q is the electron charge and a_0 is the Bohr radius), I is the total beam intensity (the sum of the two Raman beams which are assumed to have equal intensity) and χ is the numerically calculated factor which accounts for each individual Raman route. It has been assumed that $\Omega_\mathrm{A} = \Omega_\mathrm{S}$ at large detunings. The results show that the only polarization couplings which result in non-zero Raman probabilities for the $|F = 2, m_\mathrm{F}+\epsilon1-\epsilon2\rangle \rightarrow |F' = 3, m'_\mathrm{F}\rangle$ transition are in Table 6.1.

Polarizations ϵ1-ϵ2	Quantization axis
$\sigma^\pm - \sigma^\pm$	parallel to each beam
$\sigma^- - \pi^0$	parallel to σ beam and the electric field of the π beam
$\pi^0 - \sigma^+$	parallel to σ beam and the electric field of the π beam
$\pi^\perp - \pi^{||}$	parallel to each beam

TABLE 6.1: *Polarizations of the Raman beams which result in non-zero transition probability between $F = 2$ and $F = 3$.*

As we cannot currently separate the polarization in each beam in the current configuration (as they are formed from a single laser) we concentrate on the $\sigma^\pm - \sigma^\pm$ polarized beams and the $m_F = 0$ states due to their insensitivity to magnetic fields. Using Equation 6.32 we find the two-photon Rabi frequency between the $|F = 2, m_\mathrm{F} = 0\rangle \rightarrow |F' = 3, m'_\mathrm{F} = 0\rangle$ states as

$$\Omega_\mathrm{R}|_{m_\mathrm{F}=0} = 0.197\frac{I}{\Delta} \tag{6.33}$$

where Ω_R and Δ are in MHz, I is in Wm^{-2}.

It must be noted that the Rabi frequency has a dependence on the intensity of the Raman beams and so one must ensure the intensity noise of the beams is low or one may see significant decoherence, as shown in Chapter 8. Diode lasers are suited to such experiments as their amplitude noise is usually smaller than other tunable lasers and

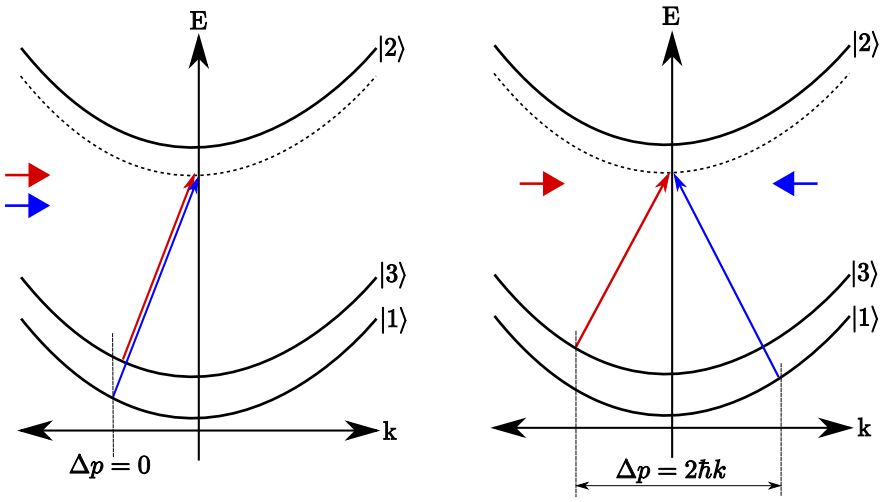

FIGURE 6.5: *Dispersion plots of a lambda system with Doppler shifts. The co-propagating beams (left) are Doppler insensitive whereas the counter propagating beams (right) are highly Doppler sensitive.*

decreases with increasing injection current [63]. One must also ensure that the variation in intensity of the beam's Gaussian profile is negligible over the atomic cloud to avoid a distribution of Rabi frequencies.

6.4 Momentum Transfer

We have seen how the transfer of momentum from single photons to atoms can lead to Doppler cooling and trapping. We now turn our attention to the momentum imparted via Raman transitions. We have chosen to use Raman transitions not only to simulate a two level system but also due to the greater momentum imparted to an atom compared to a direct RF transition between ground states (magnetic dipole allowed). Figure 6.5 shows the Doppler shift of the state energies for the counter- and co-propagating Raman beam setups. As with sub-Doppler spectroscopy the atom will absorb energy from both beams when the detunings and Doppler shifts cancel to result in resonance.

$$\begin{aligned}
\omega_{12} - \omega_{23} \equiv \omega_{13} &= (\omega_{\mathrm{A}} + \vec{k}_{\mathrm{A}} v) - (\omega_{\mathrm{S}} + \vec{k}_{\mathrm{S}} v) \\
&= \omega_{\mathrm{S}} - \omega_{\mathrm{A}} && [\vec{k}_{\mathrm{A}} = \vec{k}_{\mathrm{S}} = k] \\
&= \omega_{\mathrm{S}} - \omega_{\mathrm{A}} + 2kv && [\vec{k}_{\mathrm{A}} = -\vec{k}_{\mathrm{S}} = k]
\end{aligned}$$

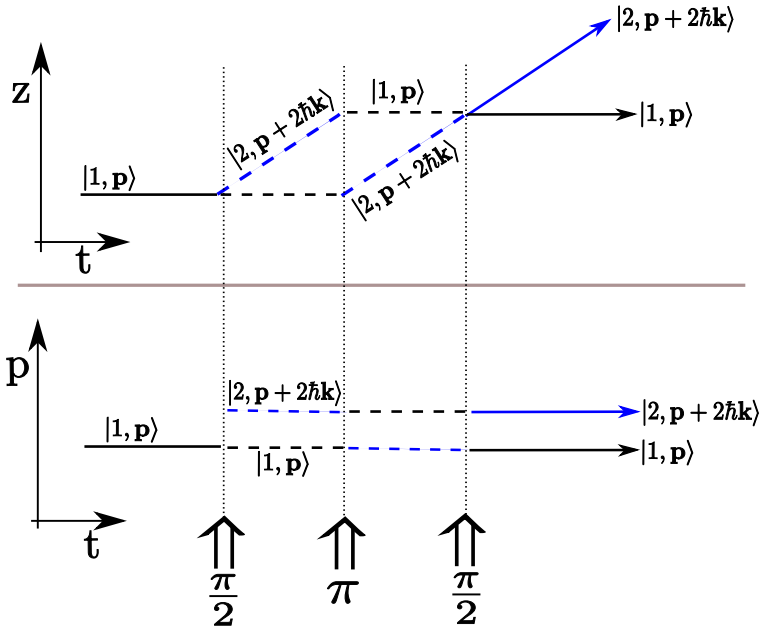

FIGURE 6.6: *Position (top) and momentum (bottom) versus time for a simple atom interferometer [149]. At the first $\pi/2$ pulse the atom is placed in a superposition and the atomic wavepacket is coherently separated in momentum and real space. The π pulse alters the atom's trajectory so that the atoms are recombined at the same position with the second $\pi/2$. This interferometer is used for very sensitive gravity measurements. In a uniform gravity field the phase shift of both arms of the interferometer is the same. Any changes in the gravitational field during the superposition can be measured by the phase change at recombination.*

We see that the co-propagating setup is Doppler insensitive whereas the counterpropagating setup is highly Doppler sensitive.

Our initial experiments into achieving Rabi flopping involve the co-propagating setup so as to maximize signal but this cannot be used to impart momentum. Once we have achieved large Raman Rabi frequency (larger than the Doppler width within the MOT cloud, $\sim$100 kHz) we shall be able to impart $2\hbar k$ to the atoms for each Rabi cycle. Applying $\pi/2$ pulses via Raman transitions allows us to place the atoms into a superposition so that we can build an *atom interferometer*. We can see that π-pulses act as 'mirrors' and $\pi/2$ are beam splitters [144]. Atom interferometry has been used for cooling atoms below the recoil limit [115], extremely sensitive measurements of gravity [145, 146] and the fine-structure constant measurements [147] (see Reference [148] for a good review of atom interferometers). The first such atom interferometer using Raman π-pulses was achieved by Kasevich and Chu [149]; a schematic and description of their experiment is shown in Figure 6.6.

6.5 Long-Term Experimental Objectives

The motivation of this thesis as outlined in Chapter 2 is to investigate experimentally new methods of cooling atoms and possibly molecules by coherent manipulation of the momentum states. The first half of this chapter discussed the methods in which this momentum manipulation can be achieved via pulsed Raman interactions. The second half is devoted to the specific experiments we plan to investigate. Within the description of each technique we shall, for simplicity, use π and $\pi/2$ pulses to describe the effect upon the state populations, whereas eventually the transfer will be achieved via tailored ARP pulses. In this section we discuss two novel cooling techniques, amplified Doppler cooling and interferometric cooling, and also include a third experiment, vapour cell interferometry, which does not cool atoms, but is an interesting application of the same setup.

6.5.1 Amplified Doppler Cooling

Amplified Doppler cooling [42, 43] relies on coherently imparting many $\hbar k$ of photon momenta to an atom before spontaneous emission occurs to amplify the effective force per spontaneous emission, which must occur in order to remove entropy from the system. Figure 6.7 shows the pulse scheme for amplified Doppler cooling. It is also useful to visualise the velocity distribution of the atoms as we show with the smaller graphs at the bottom.

The first pulse splits the velocity distribution into two groups: the red velocity group is excited to state $|b\rangle$, the blue group remains in state $|a\rangle$. Experimentally this velocity selective pulse can be a broadband chirp from far above to exactly on-resonance or a velocity sensitive Raman transition. The following pulses are population inverting π-pulses and we shall treat a one dimensional example along the vertical z axis. The first pulse is directed -z. The blue atoms in state $|a\rangle$ absorb a photon and recoil in the -z direction. The state $|b\rangle$ atoms (red) emit a stimulated photon and recoil in the $+z$ direction. We now have the blue atoms in state $|b\rangle$ and red atoms in $|a\rangle$. The second pulse, in direction $+z$, causes the red atoms to gain momentum in the $+z$ direction

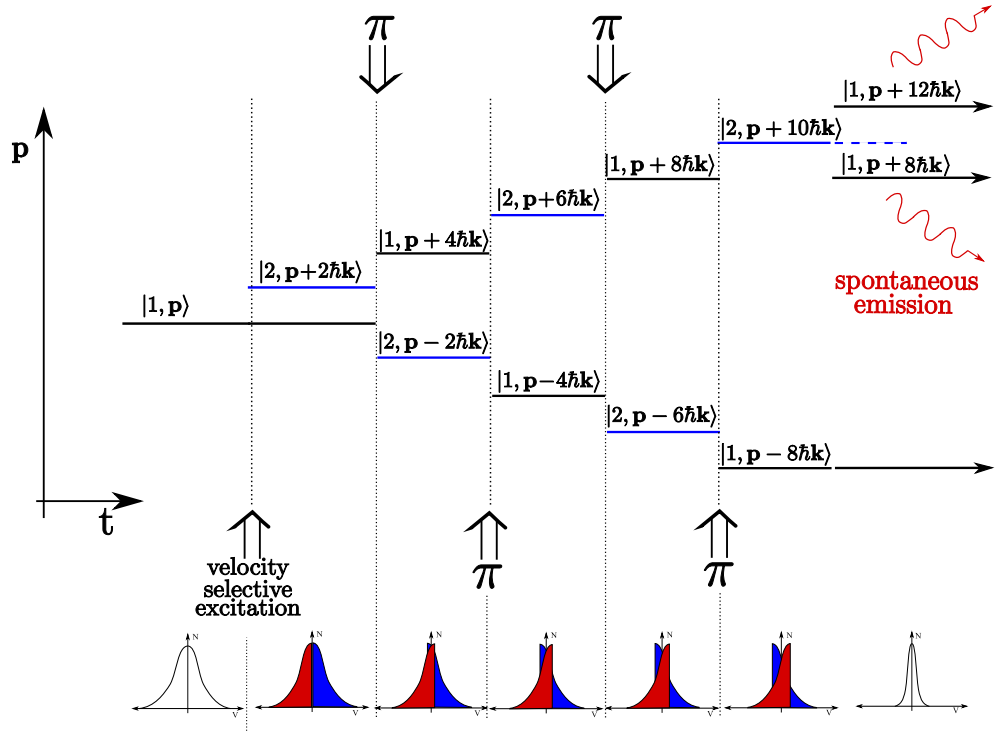

FIGURE 6.7: *Pulse sequence for amplified Doppler cooling. The top figure shows the momentum of the atoms during the pulse sequence. The initial velocity-selective interaction splits the velocity distributions into two groups which we show in the small graphs at the bottom. During the pulse sequences the two velocity groups are overlapped and when optimal overlap is achieved spontaneous emission mixes the two groups back together and we are left with a narrower, colder, distribution of atomic velocities.*

(again) and the blue atoms to -z (again). The two atom groups thus continually gain momentum in opposite directions. Once the optimum overlap of the two groups is reached, spontaneous emission is 'allowed' to occur. This means the pulse sequence is completed well before the natural lifetime of the state. In our Raman setup, we apply a single pump beam to the excited state. This thermalizes the two groups and results in a non-reversible force which is required in order to cool the atoms. One can image this technique as 'folding' the velocity distribution, whereas standard Doppler cooling is 'squeezing' the distribution. Each fold narrows the distribution far more than compressing by $\hbar k$ per spontaneous emission cycle because both atoms in the excited *and* ground state absorb momentum.

Of course, in reality atoms have a probability of decay during the pulse sequence and this can result in a heating mechanism. There is an optimum ratio of pulse sequences to heating that results in an efficient cooling mechanism; the reduction of spontaneous emissions required to cool atoms can be as much as three orders of magnitude as the

force scales as 2^n, where n is the number of spontaneous emissions [42]. If we begin the sequence with a position dependent excitation (such as in the Zeeman trapping in a MOT) we can move the atoms, similar experiments have been investigated by Bakos et al [150].

6.5.2 Interferometric Cooling

Atomic interferometry uses $\pi/2$ pulses to place the atoms into a superposition of two states [44] as shown in Figure 6.8. In the case of counter-propagating Raman beams, the interaction is Doppler-sensitive so that the wavepackets of the states $|1, p\rangle$ and $|2, p + 2\hbar k\rangle$, placed in a superposition, are separated in both momentum and real space. The superposition remains as long as the separation between wavepackets is less than the coherence length $l_{coh} = \hbar/2\Delta p$, where Δp is the momentum spread.

The difference in energy of the two wavepackets is proportional to the phase difference $\Delta\phi$ of the two arms of the interferometer,

$$\Delta\phi \propto \left(E_2 + \frac{(p + 2\hbar k)^2}{2M}\right) - \left(E_1 + \frac{p^2}{2M}\right) = E_2 - E_1 + \frac{2\hbar pk}{2M} + \frac{4(\hbar k)^2}{2M} \qquad (6.34)$$

where p is the momentum, k is the wavenumber, M is the atomic mass and E_1 & E_2 are the rest frame energies of the two states. In a two level system $E_2 - E_1$ remains constant and neglecting the small $(\hbar k)^2$ term we find the phase of the superposition is proportional to the momentum $\Delta\phi \propto p$. The two arms of the interferometer are recombined with a second $\pi/2$, and the resulting probability of leaving the atom in an excited state is a sinusoidal function of the delay between $\pi/2$ pulses. One can then adjust the delay so as to ensure atoms which are in the excited state, and therefore have absorbed the photon momentum, feel a force against their motion. The two additional π-pulses are applied to increase the sensitivity of the interferometer and, in the case of multilevel atoms, making sure each wavepacket spends equal time in each internal energy state.

In the optical Bloch vector picture, during the superposition, the state vector will rotate in the $x-y$ plane at a frequency equal to the Bohr frequency between the coupled states,

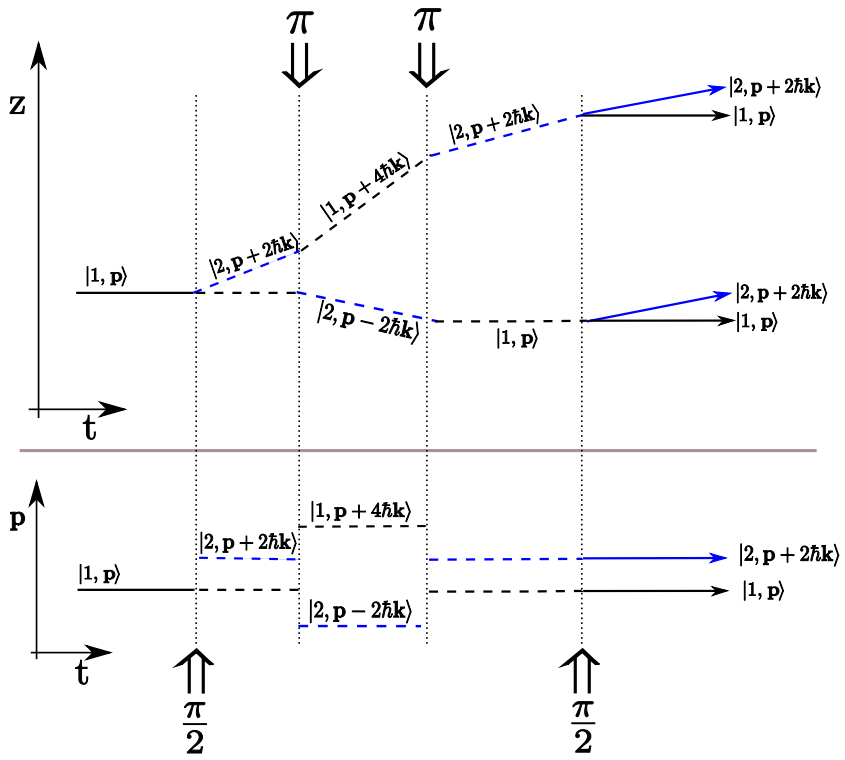

FIGURE 6.8: *Pulse sequence for interferometric cooling. Atoms are placed in a superposition the phase evolution of which depends upon the atomic velocity [44].*

which depends upon the velocity of the atom via the Doppler shift. At the application of the second $\pi/2$, an atom with a state vector is aligned along the $y = +1$ direction will be rotated into $w = -1$ state whereas if the state vector is pointing in the $y = -1$ direction it will rotated to the $w = +1$ state. If the state points in $x = \pm 1$ direction the atom remains in a superposition.

The cooling force depends only upon the atomic velocity and not the specific transition frequency, therefore by using chirped ARP pulses, superpositions may be generated amongst many states and so we may apply this technique to complex atoms and molecules.

6.5.3 Vapour Cell Interferometry

This experiment does not lead to a cooling technique, but is presented here as it uses the same methodology as interferometric cooling. Ramsey fringes are a result of putting the atoms into a superposition of two states, allowing the state vector to precess, then completing the beamsplitter by applying another $\pi/2$ pulse. The resulting state depends

upon the time delay between pulses and will show an oscillatory fluorescence, hence fringes, as a function of delay. This effect has been experimentally investigated for decades but always by *temporal/frequency* measurement of the fringes [148]. We propose, and hope shortly to try, a technique to spatially map these fringes on a visible scale in a vapour cell.

Using a long Rubidium vapour cell (20cm), one initially prepares the atoms in one ground state using optical pumping. A $\pi/2$ pulse is then applied along the z-direction (axially along the cell). The atoms will begin to precess in this superposed state until a second $\pi/2$ pulse is applied in the -z direction a time T later, which must be shorter than the diffusion time of the atoms out of the beam. The free evolution precession period of the atoms is equal to the Bohr frequency of the two states. In Rubidium 85, a Raman transition coupling the two ground states results in a frequency splitting of $\sim 3\,\mathrm{GHz}$, therefore the distance between atoms with the same precession angle is $\sim 4\,\mathrm{cm}$. The second $\pi/2$ pulse will interact with the atoms at different times, and so the fluorescence of each atom will depend upon it position along the cell, thus Ramsey-type fringes will appear along the cell.

Chapter 7

Manipulation Laser

To achieve stimulated Raman transitions in our cold sample of Rubidium atoms we require an intense bi-chromatic laser source consisting of two phase coherent beams separated in frequency around the ground state hyperfine splitting of 3.036 GHz. We must be able to control the amplitude, relative frequency and direction of each beam on a microsecond timescale. We must also be able to prepare our atomic sample in a particular state, provide a 'quantization axis' and detect fluorescence from the sample with good time resolution and signal to noise. This chapter begins with the description of our laser source followed by the various beam path components to generate the required control. We then address the computer control and synchronization of each component, detection methods and the practical intricacies of Raman transitions in Rubidium.

7.1 Raman Fields

This section describes the significant optical components and their function along the beam path for the manipulation-laser layout as set up in the winter of 2008[1].

[1]The layout has undergone numerous redesigns in recent months in order to counter previously unexpected and undesirable effects, changes are still underway at the time of writing.

7.1.1 Laser Source

The achievement of high two-photon Rabi frequencies at large detunings requires high intensity CW single-mode laser sources. A suitable candidate is a Ti:Sapphire laser in CW mode which may produce several Watts at 780nm with a very narrow linewidth, but the price of such devices makes them prohibitive. Semiconductor lasers are susceptible to damage at high powers due to their small mode volume, the highest power standard single-mode diode lasers are limited to around 100 mW. Designs based upon master-oscillator power amplifiers (MOPA) utilize tapered gain regions so that the beam is amplified as it passes through the semiconductor. The width of the gain region increases to spread the power density and thus avoid damage or thermal lensing, see Figure 7.1 [151, 152]. Such devices can be used to amplify a lower power laser (as we shall see in Section 7.1.5) or be integrated into a single monolithic device.

We employ a Sacher Tiger laser which has a tapered amplifier chip with open anti-reflection coated facets on both sides. The output from the 'narrow' facet is fed back to the diode by a rotatable grating in the Littrow configuration. Spontaneous emission from the tapered chip is dispersed by the grating and a narrow frequency range is amplified by a single pass through the gain region, therefore avoiding the beam direction dependence on grating tuning which we find in the MOT lasers. The output from the 'wide' facet is collimated and passed through a Faraday isolator as back reflections may damage the semiconductor due to its high gain. The specified output power from the 'Tiger' is up to 1 W. We have found this laser to be unreliable and after many returns to the manufacturers for various malfunctions we obtained up to 350 mW on a 'good' mode

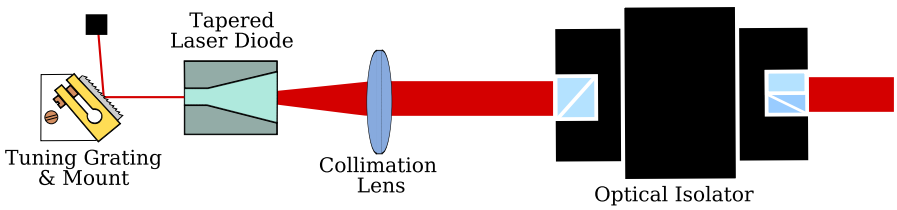

FIGURE 7.1: *Internal layout of the Sacher Tiger laser. The tapered diode design produces large amplification of up to 1 W in a single pass. The grating filters the output via back reflection on the 1st order (Littrow). High isolation (> 40 dB) is mandatory as small back-reflections can damage the diode due to high amplification into a small gain region.*

but still with poor beam shape. This is sufficient for the current experiments but we require amplification further down the beam path.

To increase the two-photon transition probability above that of a single photon transition we must detune the laser from resonance by tens to hundreds of GHz. There exist no spectral features on to which to lock in this region, and the unavailability of such high bandwidth photodetectors rules out beat-note locking [153]. As the two-photon transition rate does not change rapidly with a drift of tens of MHz, at tens of GHz detuning, we use the Advantest Q8326 wavelength meter which has a resolution of 50 MHz as a reference. The accuracy of its measurement has been tested against the Rb locked MOT lasers and found to be offset by only +100 MHz (0.3 ppm). The wavelength is read by a computer in which a simple software PI control is fed back to the Tiger current, piezo and temperature controller (Sacher Pilot). As long as the Tiger does not mode-hop it remains stable to approximately ±100 MHz over a day.

7.1.2 Beam Path

As shown in Figure 7.2, the output of the Tiger laser is passed through a second Faraday isolator (Linos > 40 dB isolation) as the laser is still affected by backscatter even with the internal isolator. The beam is focused through a +310 MHz acousto-optic modulator (AOM, see Section 7.1.3) which spatially divides the beam by a ratio 1:4; the weaker beam forms one of the Raman fields and the stronger beam is focused through an Electro-Optical Modulator to apply sidebands of $\simeq \pm 2.725$ GHz. The exact frequency of the sidebands can be tuned via the frequency generator or an I&Q modulator (see Section 7.1.3). The lower frequency sideband forms the second Raman field.

It is possible to create both Raman fields using the EOM but this can cause cancellation of the Raman transition. The EOM is phase modulated which results in sidebands which have a constant π phase difference with respect to the carrier. The Raman transition is a coherent interaction so the phase relationship between the state populations and incident field is important. As with the FM spectroscopy, each sideband beats with the carrier with the modulation frequency but opposite phase which causes deconstructive interference between the Raman transition pathways [134, 154].

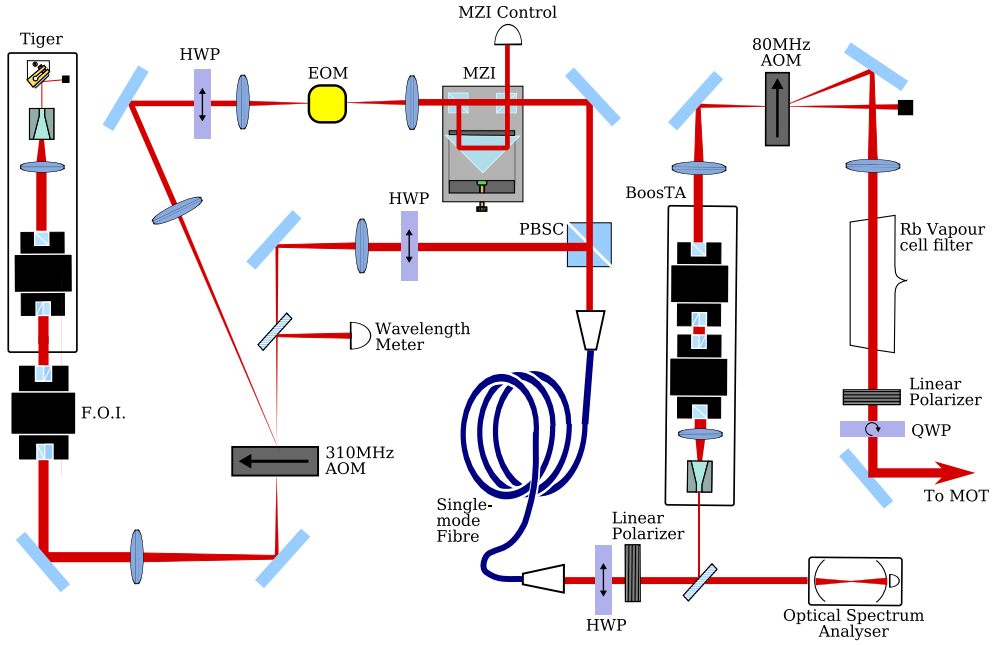

FIGURE 7.2: *Manipulation laser beam path. Abbreviations; H/QWP - half/quarter waveplate, PBSC - Polarizing beam splitting cube, FOI - Faraday optical isolator, EOM - Electro-optical modulator, AOM - Acousto-optical modulator, MZI - Mach Zehnder interferometer, BoosTA - Toptica tapered amplifer. This is a simplified layout, for clarity, omitting some steering mirrors and lenses.*

The strong carrier frequency can introduce light shifts and single photon effects and so is removed by a Mach-Zehnder interferometer (see section 7.1.4); the other upper sideband is retained as the power is much lower than the carrier. The beams are combined using a polarizing beam splitter cube (PBSC), collimated and coupled into a single mode-fibre in order to clean up the beam profile. The output from the fibre is collimated and passed through a linear polarizer to align the polarizations of the two Raman beams so that they are equally amplified by a tapered amplifier (Toptica BoosTA, Section 7.1.5). Output from the BoosTA is focused through a 80 MHz AOM which acts as an intensity modulator. The diffracted order is collimated and passed through a long (20 cm) Rubidium vapour cell to filter any resonant amplified spontaneous emission (see Section 7.1.5) and then through a second linear polarizer and quarter-waveplate to create the $\sigma - \sigma$ polarized Raman beams required from Section 6.3.2. The Raman beams are then directed into the MOT alongside the y-arm of the MOT beams.

The reader may note that in the current layout we cannot produce counter-propagating Raman beams due to the BoosTA, or switch the propagation direction the beams. The switching will be achieved with a Pockels Cell which rotates the input polarization by

90 degrees by application of a high DC voltage across a crystal whose birefringence is proportional to applied electric field. The separation of the Raman beams may be achieved by a second Mach-Zehnder interferometer after the BoosTA or by using a second BooSTA (or getting the Tiger to work at full power!) to amplify each beam separately.

7.1.3 Optical Modulators

In order to produce and control the Raman beams we employ several optical modulators which are controlled via either acoustic-waves or AC electric fields. This section describes the physics behind these components and their operation.

7.1.3.1 Acousto-Optical Modulator

The main manipulation beam path utilises two Acousto-Optical Modulators (AOMs) as well as two more AOMs to control the Trapping and Repump beams. AOMs operate by passing a travelling sound wave through a crystal so as to alter the refractive index through density variations in the sound wave. The variations form a type of moving grating to deflect an incoming optical beam. For this reason AOMs are occasionally called Bragg deflectors. As the sound waves are travelling, the grating is moving and so the deflected beams are 'Doppler shifted' from the incident beam. This is a result of conservation of energy and momentum and the frequency shift and deflection angles are quite small since $|\vec{k}_{\mathrm{ac}}| \ll |\vec{k}_{\mathrm{op}}|$, where $\vec{k}_{\mathrm{ac}}$ and $\vec{k}_{\mathrm{op}}$ are the wavevectors of the acoustic and optical waves, respectively.

The response time for an AOM depends upon the transit time of the sound wave across the beam so the narrower the beam the better; typical transit times are several nanoseconds. The diffraction efficiency of the incident beam into the first order (Bragg regime) can be as high as 80% of the zeroeth order output and can be controlled by the amplitude of the sound wave.

7.1.3.2 Electro-Optical Modulator

The operation of the electro-optical modulator (EOM) is based upon the Pockels effect where the birefringence of a crystal depends upon the applied electric field. We have already mentioned Pockel's cells where a DC electric field induces a birefringence so that one of the polarization components of incoming light is delayed with respect to the other component thus creating a controllable waveplate. An EOM works on the same principle but with varying electric fields so as to modulate the phase of the incoming beam, with the polarization of the incoming beam aligned to the crystal axis to avoid such waveplate effects. The phase modulation introduces sidebands in the same manner as current modulating the diode lasers in FM spectroscopy.

We use a New Focus 4431M EOM which consists of a Magnesium Oxide Doped Lithium Niobate ($MgO:LiNbO_3$) crystal in a microwave cavity that is resonant around 2725 MHz (the resonant frequency may be adjusted with a tuning screw by ± 1 GHz). The wavefronts of the input beams must be as flat as possible across the crystal so that one does not produce varying phase-modulation across the beam profile. The EOM is driven by an Agilent 8648C frequency synthesiser and amplified by a Miteq AMF-6B-027029-40-37P power amplifier (5 W max output). Control of the frequency and phase of the EOM during pulses (for ARP) is achieved with an I&Q modulator as described in the next section.

Full characterisation of the EOM and RF power components can be found in James Bateman's thesis [118] though we shall quote the important results. The specified bandwidth of the EOM resonance is 0.5% of the applied RF (BW $\simeq$ 13 MHz) although we find the FWHM of the response to be twice this value (22 MHz) and not symmetric around the centre frequency. We also measured the power in each sideband and thus the modulation depth of the EOM. We find only $\simeq$ 44% of the expected power into the sidebands and, along with the response and recollection of larger sidebands previously, we suspect damage to the EOM crystal. Even so, the power in each sideband is acceptable for initial experiments.

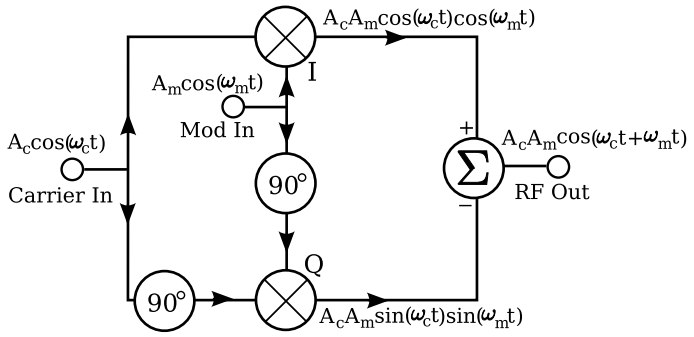

FIGURE 7.3: *Single sideband - suppressed carrier (SSB-SC) with an I&Q modulator. The carrier (ω_c) and modulation (ω_m) inputs are split into two paths, one of which is phase shifted by 90 °. The in-phase (I) components are mixed together and the quadrature-phase (Q) components are mixed together and the I and Q parts are then summed together. Depending upon the relative signs of the I and Q parts, either the upper (shown) or lower sideband is derived with the carrier and other opposite suppressed. In our system the I and Q inputs are synthesized separately.*

7.1.3.3 I&Q Modulator

The EOM frequency is fixed for the experimental results described in Chapter 8. Future experiments require modulation of this frequency and the method is outlined here for future reference.

To shape the frequency chirp of the manipulation laser to achieve efficient Adiabatic Rapid Passage we must adjust one of the Raman frequencies. The 310 MHz AOM has a limited bandwidth and the beam direction will change with frequency so we instead modulate the EOM. Modulation of the EOM drive frequency will add extra sidebands onto each EOM component resulting in at least 9 frequencies, each of which will introduce extra lightshifts and single photon scattering. We may use some tricks from the RF communication industry and suppress the RF carrier and redundant modulation sideband. One obvious method is to include a filter which removes the carrier and redundant modulation sideband but the filter response roll-off would need to be impractically steep. Another technique is known as 'single sideband suppressed carrier' (SSB-SC) or a Hartley Modulator: Figure 7.3 describes the principle of operation. We use an I&Q Modulator ('I' refers to In-phase and 'Q' to Quadrature-phase) from Miteq, the local oscillator is provided by an Agilent 8648C and the I and Q inputs are from the Tabor 3362 which can synthesize 300 M samples per second with a waveform memory of 16 Mb.

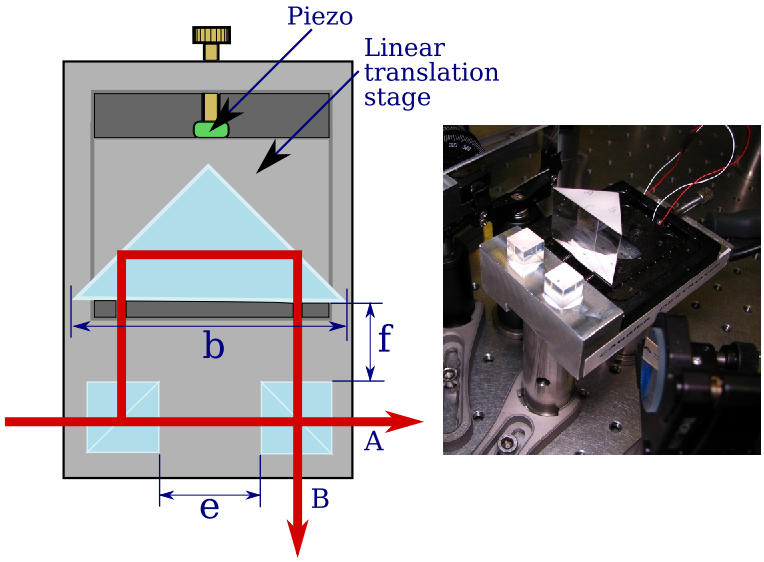

FIGURE 7.4: *Mach-Zehnder 'Carrier Destroyer'. The input beam is split along two paths and interfered at the second beamsplitter cube (non-polarizing). By tuning length f we can cause deconstructive interference of the carrier at port A thus separating out the sidebands. The actual device carefully constructed by André Xeureb is shown on the right.*

7.1.4 Mach-Zehnder Interferometer

The output from the EOM consists of the central carrier with two sidebands separated from it by around 2725 MHz. The strong carrier may cause single photon effects, such as light shifts, which can overwhelm and detune the Raman signal. We would therefore like to remove any optical fields which do not take part in the Raman process. Dotsenko et al [154] used a Mach-Zehnder interferometer (MZI) to remove the central carrier in a similar experiment[2], in which this stage was even more important as they used the two unshifted sidebands of the EOM as the Raman fields: the opposite phase of the sidebands resulted in a complete cancellation of the Raman transition. We do not have this problem as we shift the carrier by +310 MHz using the beam-splitting AOM. Figure 7.4 shows a schematic and photograph of our interferometer.

By adjusting the separation of the prism and beamsplitting cubes (i.e. changing distance f) the difference in optical path length between the two paths can be made to constructively interfere for one frequency and deconstructively interfere for another frequency, so that they exit by different ports. We will not go into the derivation for path difference

[2]Another method utilises a Fabry-Perot cavity [155]

but we shall quote the result from Reference [156] [3];

$$f = \frac{1}{2}\left[\left(N_2 - N_1 - \frac{1}{2}\right)\frac{c}{\Delta\nu} - \eta b + e\right] \tag{7.1}$$

where N_1 and N_2 are integers relating to the order of the phase delay (multiples of 2π), $\Delta\nu$ is the frequency difference of the components we wish to separate, c is the speed of light in a vacuum, η is the refractive index of the prism and f, b and e are lengths defined in Figure 7.4. With off-the-shelf components, Haubrich et al [156] found a fringe contrast of up to 96% with only 2% loss of input power.

In our initial setup (shown in Figure 7.4) the values are $\Delta\nu = 2.725\,\text{GHz}$, $\eta = 1.5$, b=35 mm, e=11 mm, f=9 mm, this leads to a difference in phase order of $N_2 - N_1$=0.5 which is not a whole number therefore the device does not achieve the best efficiency. The difference in path length necessary to cancel the carrier output from port A, f, is adjustable with piezo-electric transducers. Due to the limited translation of the linear stage we cannot achieve the optimum fringe contrast and, although we can reduce the carrier to negligible levels, we lose power in the sidebands. A new MZI is currently being built which will have improved efficiency and will combine the 310 MHz AOM shifted beam with the sidebands as well.

7.1.4.1 Stabilization

The performance of the MZI depends upon the stability of the MZI itself via thermal expansion of the mount and by the stability of the Tiger laser wavelength. The thermal expansion coefficient of stainless steel, from which the linear translator is made, is $\sim 20 \times 10^{-6}\,\text{K}^{-1}$. A change in temperature of 1 K of the path difference, $2f$, will lead to a phase shift of $\sim \pi$. A shift in the Tiger laser frequency by 10 GHz will result in a similar phase shift.

Stabilization of the MZI for maximal cancellation of the carrier frequency may be achieved by dithering the piezo voltage to produce an error signal similar to the FMS locking scheme in Chapter 4. Dithering will introduce extra frequency components on

[3] The reference describes the device for use in beam combination and the equation is derived for that purpose. It still applies in our situation as we are merely performing the time reversal.

similar timescales to the experimental pulse periods which is undesirable. The drift of the MZI is very slow, in the order of minutes and negligible compared with the drift of the Tiger laser, so we use computer control to adjust the piezo voltage between sampling periods. The output of the MZI is monitored by a photodiode (see Figure 7.7) and the voltage is read by the computer via a digital-to-analogue converter (DAC) interface board. A program written by James Bateman iteratively adjusts the piezo voltage (via another output on same DAC board) so as to minimize the carrier intensity. This process takes approximately 2 seconds during the trap loading period.

7.1.5 Optical Amplifer

The two-photon Rabi frequency, given by Equation 6.32, is proportional to the intensity of the applied field and inversely proportional to the detuning from excited state resonance. After passing through the beam path elements outlined in the previous section, the 300 mW output from the Tiger laser is reduced to approximately 20 mW, most of the loss being from inefficient coupling into the fibre due to poor beam shape and unavoidable power loss from polarization correction. To avoid single photon effects we detune by tens to hundreds of GHz and so require intense Raman beams to achieve a sufficiently high Rabi frequency.

We are limited in how tightly we may focus the beam by the size of the MOT cloud. The beams have a Gaussian profile and for a uniform Rabi-flopping rate for all atoms the change of intensity across the cloud must be minimal. To amplify the Raman beams before entering the MOT we pass the beam into a Toptica BoosTA which consists of a tapered amplifier chip of similar design to the Sacher Tiger [152]. A single pass through the BoosTA can amplify the input beam power by greater than 20db whilst retaining the spectral properties of the input beam. The system works well apart from amplified spontaneous emission (ASE) produced even with no 'seed' laser.

7.1.5.1 Amplified Spontaneous Emission

Incoherent amplified spontaneous emission (ASE) from the BoosTA results in a broad spectrum which overlaps with the mode of the Raman beams projected on to the MOT

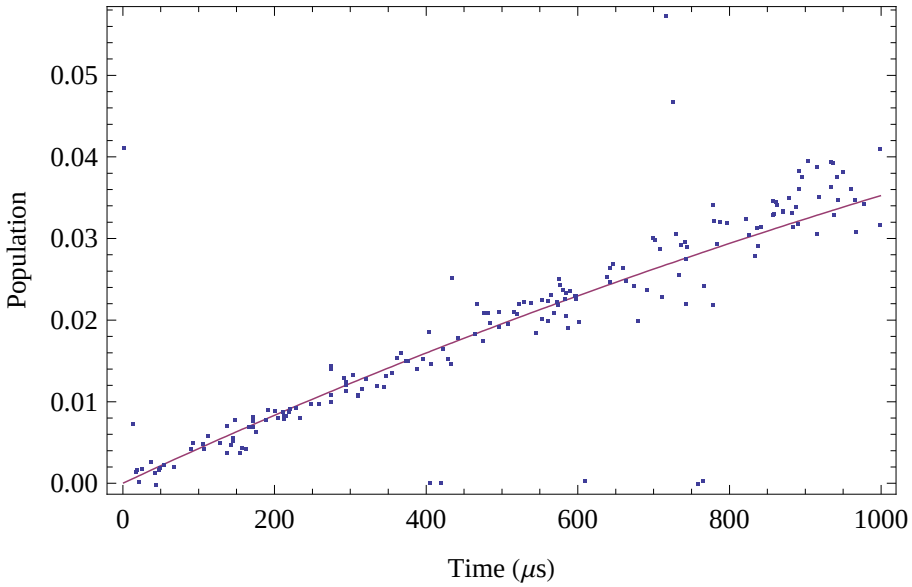

FIGURE 7.5: *Population transfer from $5S_{1/2}$ F3 to F2 via amplified spontaneous emission from the unseeded BoosTA*

cloud. The manufacturer's specifications state that the ASE is less than 40dB of the amplified mode and is reduced at higher gain. Even at this level, however, resonant photons can cause single photon scattering rates around hundreds of Hz at a detuning from resonance of hundreds of GHz, which would dampen out the coherent Rabi flopping. Of course only a fraction of the resonant ASE photons are scattered along the beam but at large detuning where the Rabi frequency is small, the ASE decoherence is still significant. To check whether the dephasing is due to ASE or collisions with the surrounding gas we measured the transfer from state $F = 3$ to $F = 2$ after initially pumping all atoms into $F = 3$ with various pulse times but with no laser seeding the BoosTA. Figure 7.5 shows that the scatter increases with time due to ASE photons. The zero pulse time is equivalent to the BoosTA blocked and so we can assume there is no dephasing due to collisions with the surrounding gas. We can estimate the scattering rate for $t \geq 0$ by assuming an exponential repopulation with

$$P(t) = P(\infty)(1 - e^{-\gamma_{Deph}t}) \tag{7.2}$$

where P is the population, $P(\infty)$ is the population at steady state which we assume to be 0.1 (half the total population in the $m_F = 0$ state when shared amongst 4 other m_F levels) and γ_{Deph} is the depopulation rate from $F' = 3$ which we fit to $\simeq 2\pi \times 80\,\text{Hz}$; this

value is the decoherence due to scattering from the $F' = 2$ and $F' = 3$ excited states (the Raman states). There will also be scattering from the non-Raman states which are dipole forbidden to scatter into the opposite ground state ($F = 2 \rightarrow F' = 1$ and $F = 3 \rightarrow F' = 4$). If the relaxation rate of the excited state is much less than the two photon Rabi frequency we can consider scattering to non-Raman states as a decohering, but not depopulating, rate. As the ASE is reduced when the gain of the BoosTA is increased [157], the measured decohering rate is a large overestimate.

A simple remedy is to filter the resonant photons using a heated Rubidium vapour cell as shown in Figure 7.2. We heat a 20 cm long vapour cell to 200°C which results in no observable population transfer ($< 1\%$) between states when repeating the measurement in Figure 7.5. The vapour cell should not be placed too close to the optical fibre input to avoid coupling of vapour cell fluorescence.

7.1.6 GPS calibration

All of the RF electronics are synchronised to the 10 MHz reference from the Agilent 8648C. This ensures that all pulse timings are accurate and the frequency between the Raman beams is stable for maximum coherence. The jitter (or high frequency noise) of the 10MHz reference is well within experimental constraints (see next section) but we must be more concerned with the drift of the reference frequency. Agilent specify a total uncertainty of the frequency to be approximately 20 kHz, the largest contributor to this drift being the ageing (other drifts are power line noise and thermal expansion).

To measure the reference we use a global positioning system (GPS) derived signal which includes a pulse every second in which the pulse edge is correct to 0.1 μs [158]. This method can be very cheap and the GPS system is referenced to coordinated universal time[4]. By using the GPS pulse edge to trigger a counter we count the number of oscillations of the reference over a second and measure the uncertainty. We require the frequency measurement to be accurate to 1 Hz (≈300 Hz at 2.7 GHz) and so with a clock trigger uncertainty of 1 μs we must measure for 10 seconds (for a 10 MHz signal). We use a Garmin OEM 18x LVC GPS receiver and an Acces I/O Products USB-CTR-15

[4]The averaged time of 20 or so atomic clocks around the world

counter, details of the operation of which can be found in reference [118]. We find that the Agilent 10 MHz stability is to within 30 mHz over 200 seconds, which is more than adequate.

7.2 Manipulation Laser Coherence

For maximum coherence of the Raman transition and thus fringe contrast of the Rabi-flopping, the two Raman beams must be phase coherent to one another for the duration of the manipulation pulses (10 μs to 10 ms). This requires the relative phase stability between the two Raman beams to be much less than 100 Hz. We have used the beat note method described in Chapter 4 to measure the stability of the Tiger laser and the EOM sidebands relative to the stable Trapping laser. As mentioned in Section 4.5 we are limited by the stability of our reference laser but we may measure the beat of the unmodulated carrier (which we assume is related to the 310 MHz AOM shifted beam) and the beat of one of the EOM sidebands and take the difference to measure the relative stability and thus the relative phase stability of the Raman fields. Figure 7.6 shows the Allan variance for the beat note between the Rb stabilized trapped laser and the Tiger carrier and one EOM sideband.

We first note that at longer timescales the drift of the unlocked Tiger laser dominates. The increased white noise noise (see Table 4.1) at short timescales on the sideband plot can be attributed to noise introduced by the RF amplifier. As the RF noise and Tiger stability can be assumed to be uncorrelated we can subtract the squares of the carrier and sideband noise to find the relative RF noise and thus the phase coherence between the Raman beams (dotted line). We see the RF noise at longer times to be negligible and extrapolation into the experimental timescales leads to an relative phase stability of less than 10 Hz.

7.3 Computer Control

Figure 7.7 outlines the connections between the various manipulation components along the beam path and their connection to the computer and Agilent reference frequency. The computer relays information to each component through either USB, GPIB or Ethernet connections. The computer communicates using VISA (Virtual Instruments Software Architecture) which is an interface language that treats the external hardware as an internal piece of software therefore removing the need to explicitly communicate with individual external apparatus within the programming code. The language chosen to program the VISA components is Python due to its ease of coding and large available libraries of functions. For each different pulse sequence the Tabor arbitrary function generators require 16 bit encoded amplitude and offset waveform data which are generated by a Python function from a table of real voltages. The waveform may be complex frequency chirps or simple square pulses in which to trigger AOMs. All of the impressive number of Python programs have been written by James Bateman.

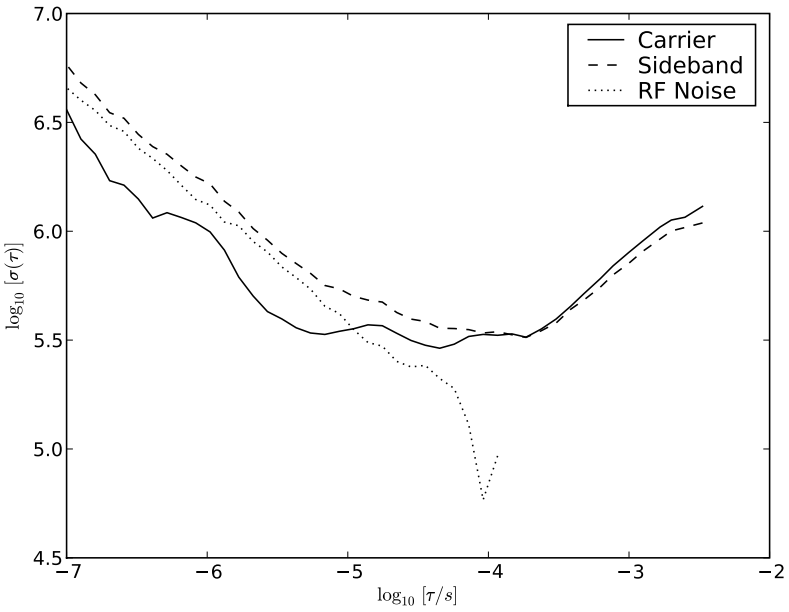

FIGURE 7.6: *Allan variance of one EOM sideband and carrier with the stabilized trapping laser. Graph and data by James Bateman [118].*

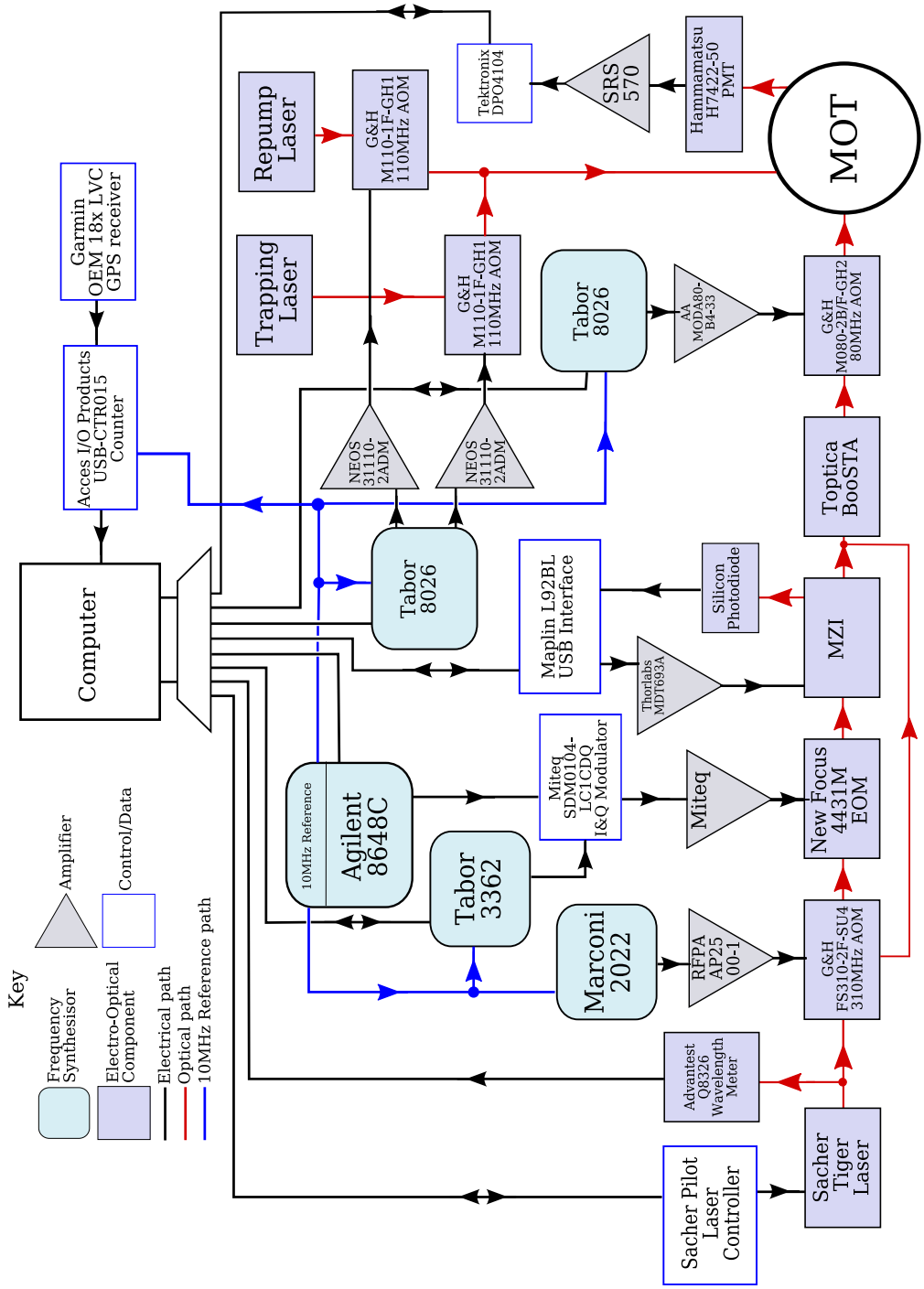

FIGURE 7.7: *Block diagram of computer control system*

7.4 Data Collection

The fluorescence is collected with the lens system outlined in Section 5.6.7 and measured with a photo-multiplier tube (PMT). The PMT is biased with a voltage of around 0.5V from a Hamamatsu C8137-02 PMT voltage controller. The current from the PMT is amplified with a SR570 low noise current amplifier, the voltage output ($0.5\,\mathrm{V}/\mu\mathrm{A}$) of which is monitored using a Tektronix DPO4104 oscilloscope. Each pulse sequence is repeated at a rate of 10 Hz and averaged by the Tektronix oscilloscope for 3 seconds to reduce high frequency detector and amplifier noise. The Tektronix oscilloscope can record up to 10 megasamples and the data is collected by the computer via HTTP over ethernet. After the trapping and repump beams have been extinguished the trapping beam is pulsed to optically pump the atoms into the $F = 2$ ground state ('prepare' pulse) which takes around $500\,\mu$s. The manipulation laser then commences its pulse sequence, details of which depend upon the experiment. After the manipulation pulse, the trapping beam is pulsed to measure the population transfered back into the $F = 2$ ground state ('read' pulse). The difference in populations between the $F = 2$ and $F = 3$ ground states is calculated by fitting an exponential decay curve to the prepare and read pulses. The exponential is fitted by an overall amplitude factor and decay constant. The amplitudes for each pulse are then tabulated against the relevant experimental parameters (e.g. manipulation pulse length). The data may be filtered to remove data points in which the MOT cloud was poorly formed by the MOT lasers unlocking; this is done by 'grading' the MOT brightness as the cloud forms. Any such filtering is noted in Chapter 8.

7.5 Practical Aspects of Raman Transitions

The experiments we plan to investigate assume a two-level atom (or a collection of two level states) and so we must control the multilevel transitions in Rb to get the best approximation to the ideal system. As discussed in Section 6.3, the ground states undergo light shifts due to the excited states and the two-photon coupling strengths depend upon the various Raman pathways and beam polarizations. In this section we discuss how these practical issues are resolved.

7.5.1 Quantization Axis

We require a quantization axis to be applied to the MOT cloud in order to achieve Raman transitions. We shall also need to apply a magnetic field to separate the magnetic sub-levels by greater than the two-photon Rabi frequency to avoid populating the $m_{\mathrm{F}} \neq 0$ sub-levels and thus reducing the signal strength. This may be achieved by simply applying a DC magnetic field along the required axis, however this will shift the magnetic field zero point, required for trapping, away from the beam centre and so the atom cloud will again form in a zero magnetic field position. We may turn the trap magnetic field off but the field in the coils will take tens of milliseconds to dissipate ($\rightarrow 0.1\%$ in 100 ms) in which time the atoms will have expanded from the measurement region. We have chosen therefore to apply an AC magnetic field which oscillates at the experimental pulse rate so that the pulses are synchronized with the magnetic field maximum, but at a rate where the field does not change significantly during the Raman pulse. The frequency of the AC magnetic field is high enough that the trapped atoms do not 'see' the quantization field and so do not move from the trap centre. The drive frequency is generated by a Tektronix AFG3102 frequency synthesiser and amplified by an audio amplifier (HQ Power VPA2350MB). Two extra pairs of coils have been placed around the x and y axis MOT windows and the third axis can be controlled with the MOT coils.

7.5.2 Two Photon Transition Rates

To identify regimes in which the two-photon transition rate is greater than the single photon scattering rate, we have plotted these values as functions of wavelength shown in Figure 7.8 (upper graph). Zeeman shifts due to magnetic fields have not been included as they are negligible on wavelength scale, and the single photon scattering rate includes the three significant components in the manipulation laser (assuming equal intensities in the 310 AOM beam and the two EOM sidebands); we have also neglected the broadband ASE scattering rate.

7.5.3 Light-Shifts

As we are detuned from single-photon resonance, the ground states are AC stark shifted and near resonance the light shift of the Raman resonance ($F = 3 \rightarrow F = 2$ transition) changes dramatically as shown in Figure 7.8 (lower graph). Any small variation in intensity or detuning of the Tiger laser near to these resonances will shift the Raman resonance and therefore degrade the Rabi flopping fringe fidelity. The measured light-shifts from the data in Chapter 8 agree with this plot (to within a factor of 2) and any shifts from the ASE are probably cancelled out due to its broadband nature either side of resonance.

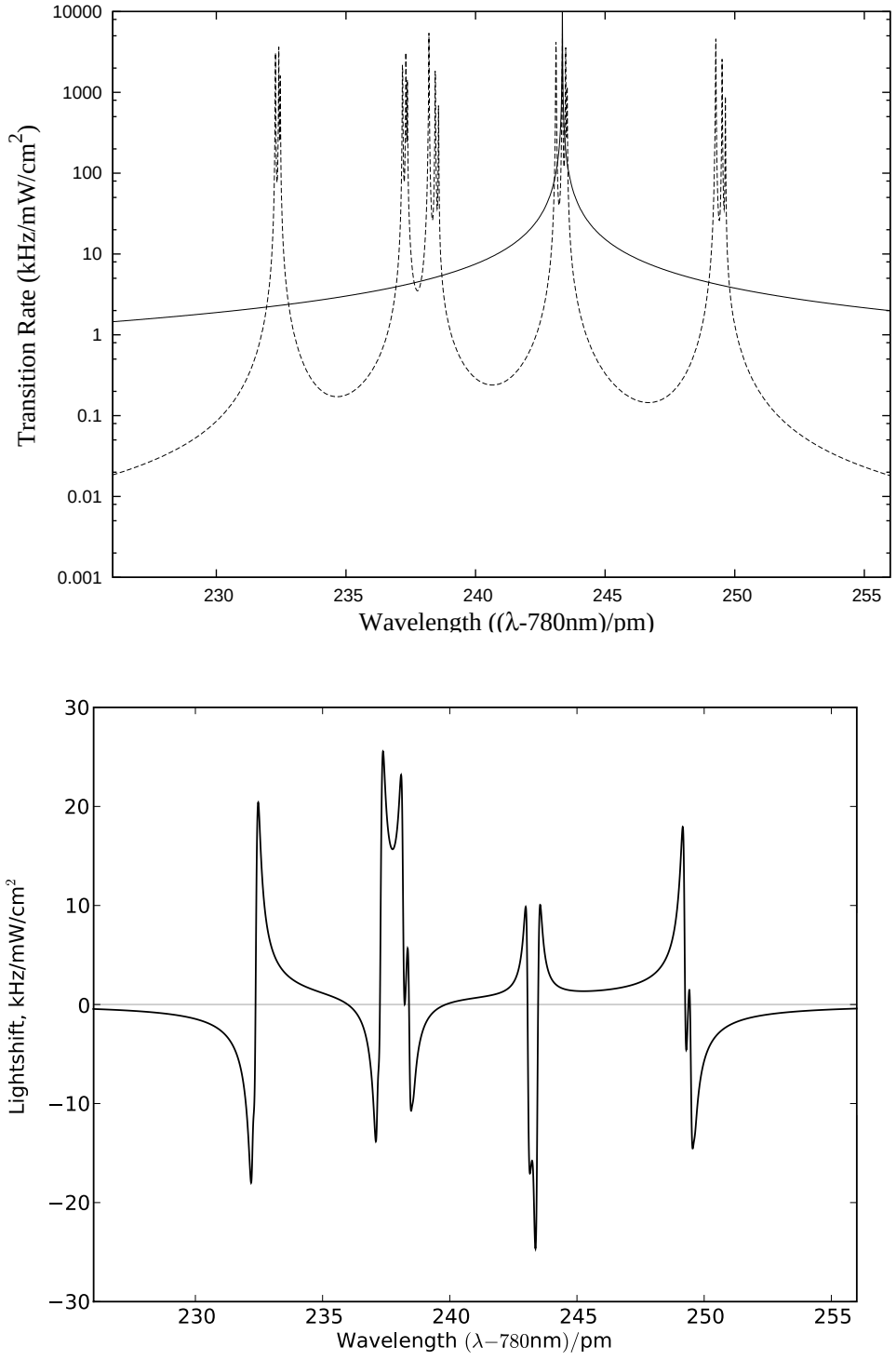

FIGURE 7.8: *Top: Two-photon transition rate (solid line) and single-photon scattering rate (dashed line). Bottom: Light shift of the hyperfine splitting between* ^{85}Rb $F = 2, m_F = 0$ *to* $F = 3, m_F = 0$ *with circularly polarized beams, including the redundant sideband. The x-axis units are the last three digits of the wavelength, 780.xxx* nm. *Lightshift graph by James Bateman*

Chapter 8

Coherence Experiments

The work described in this thesis has all been aimed at the demonstration and investigation of coherent schemes for the cooling and manipulation of atoms. According to our theoretical model, taking into account the decohering effects of spontaneous emission and collisions as described in Chapter 6, using the collision rate estimated in Chapter 5 and the single photon scattering rate determined in Chapter 7, we estimate that for a detuning of 10 GHz we should be able to achieve Rabi flopping frequencies of $2\pi \times 130$ kHz (200mW in 2.2mm $\frac{1}{e^2}$ diameter) with a fringe contrast of nearly 100% (where the contrast is the difference divided by the sum of the maximum and minimum fringe height). In Chapter 7 we also measured the scattering rate from amplified spontaneous emission from the BoosTA and found it to be negligible provided that the emission was filtered by passage through a Rubidium vapour cell. Based upon our knowledge of these sources of decoherence, our model therefore predicts high fidelity Rabi flopping between the ground states.

This chapter describes detailed experimental characterization of the fidelity achievable in practice. Our initial results, perhaps inevitably, failed to demonstrate the predicted fidelity, pointing instead to further sources of disturbance and decoherence that we have been able to identify, characterize and - in most cases - eliminate or reduce. We have thus been able to demonstrate atom interferometry with satisfactory fidelity - a visibility of 42% decaying with a time constant of 3 milliseconds - and, as a result of the experiments

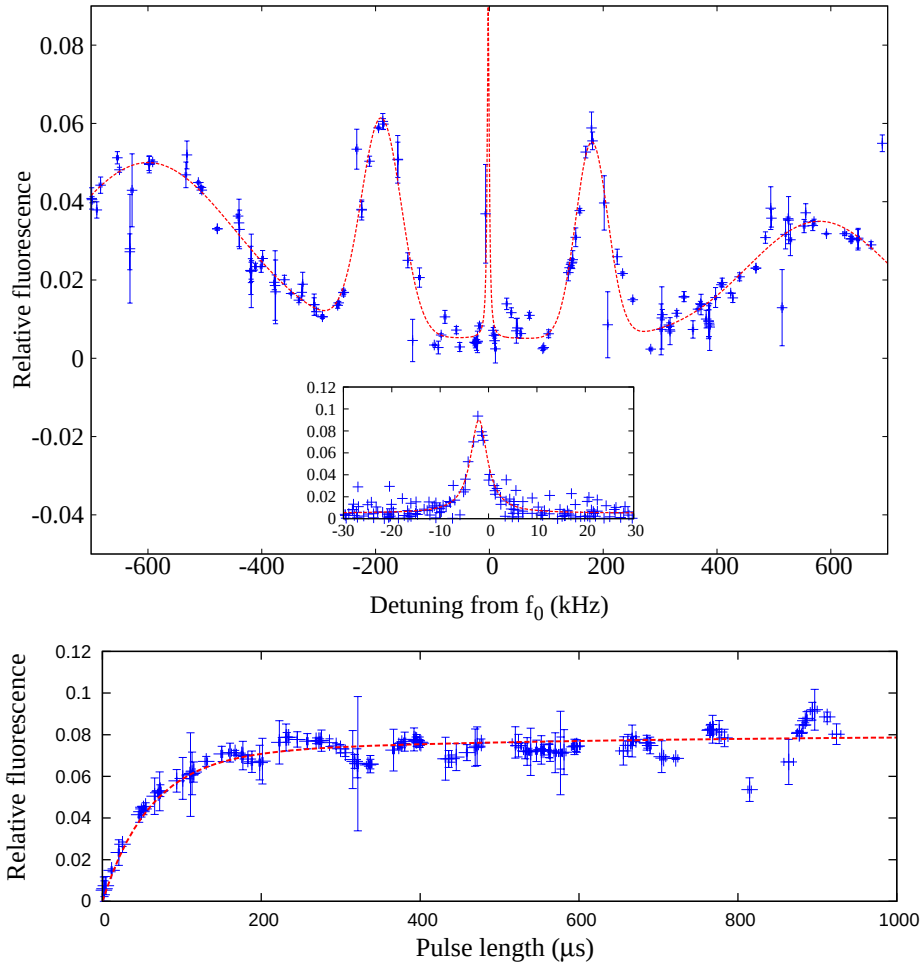

FIGURE 8.1: *Initial data of a spectral scan of the relative detuning of the Raman beams (top). The plot shows the difference in fluorescence between the 'prepare' and 'read' pulses, which is proportional to the population in the $F = 3$ ground state, as a function of the detuning from the unperturbed transition frequency $f_0 = 2,725,732,440\,\mathrm{Hz}$. The red line had been added as an aid to the eye by fitting the central peak by a Lorentzian lineshape and the four other inhomogeneously broadened peaks by Gaussian lineshapes. The bottom graph shows a temporal scan of the pulse length of the Raman beams at the two-photon resonance of the spectral plot (top). The plot shows a trend toward half the expected population with no oscilating Rabi-flopping features (compare with figure 3.2). The Raman beams had $\sigma - \sigma$ polarizations and the Tiger laser was tuned to 780.53 nm.*

described here, we are able to identify the further experimental modifications that will allow truly high fidelity coherent manipulation in the near future.

8.1 Sources of Decoherence

Rabi flopping has become a common tool in quantum information processing as the two state system makes an ideal qubit. These groups, however, use atoms tightly confined in dipole traps [154, 159, 160] or single ions in electromagnetic traps [161, 162, 163].

A similar experiment using free atoms is the gravity measurement at Stanford, USA, using a low density Caesium atomic fountain which allows very long interactions times (hundreds of ms); therefore the Rabi frequency can be much lower than required in our experiment in which the Rabi frequency must be greater than the residual Doppler width ($\sim$300 kHz at 100 μK) to retain adiabaticity during the Raman pulses. As mentioned at the beginning of this chapter we can at most expect a Rabi frequency of $2\pi \times 130$ kHz and so we cannot perform the experiments in Section 6.5 with the current setup, but we may investigate the feasibility of performing coherent interactions in a dense sample of atoms, which extends over several hundred microns.

From the initial data-set of Raman transitions, such as Figure 8.1, which do indeed show sub-natural linewidth features expected with two-photon Raman transitions, but there was no indication of the 'sinc-squared' lineshapes or strong Rabi flopping as predicted for a coherent interaction. In this chapter we identify and assess each model variable and measure their relative effect upon the coherence of the interaction. Below is a short summary of each variable.

- **Single Photon Scatter**

  This variable is increased as the Raman beams are tuned closer to single photon resonance, and also by amplified spontaneous emission from the BoosTA.

- **Collisions**

  Collisions may cause population transfer between states or interrupt the phase of the coherent interaction. They may also be responsible for scattering atoms to outside of the interaction region.

The Raman detuning, dipole matrix element and beam intensity affect the Rabi frequency through the generalized Rabi frequency (units of MHz).

$$\frac{\Omega}{2\pi} = \sqrt{\left(0.197^2 \frac{I^2}{\Delta^2} + \delta^2\right)} \tag{8.1}$$

where I (W m^{-2}) is the intensity of Raman beams , Δ (MHz) is the detuning from single photon resonance and δ (MHz) is the detuning from two-photon resonance. We have used

the two-photon resonance Rabi frequency from Equation 6.32, although the numerical factor ($0.197\,\mathrm{MHz\,m^2\,J^{-1}}$) will change with imperfect polarizations of the Raman beams.

- **Dipole Matrix Elements**

  These parameters represents the coupling between states and therefore the transition strength. They are affected by the polarization of the beams and correspondingly by inhomogeneities of the quantization axis due to magnetic fields.

- **Raman Detuning**

  The detuning and relative phase stability between Raman fields may introduce dephasing to the coherent interaction.

- **Beam Intensity**

  Spatial or temporal variation in the intensity of the Raman beams can change the Rabi flopping frequency and also affect the lightshift of the two-photon resonance.

We begin this chapter with the method of data collection and analysis, and a summary of the important features of the theoretical model. It must be noted that for the proceeding plots the expected Rabi frequency - as calculated with Equation 8.1 - is not quoted on any of the plots as accurate measurement of the Raman beam intensities was not recorded. This is because the highest achievable Rabi frequency is lower than required so the primary experimental focus was on reducing decoherence. Using the various models presented in the next section the intensity calculated from the measured Rabi frequency is within the average power range (100-200mW).

8.2 Data Collection

Figure 8.2 shows a typical Raman pulse sequence; the red lines are the data collected for each plot. We start with a cold, trapped, atomic cloud collected with the trapping and repump beams on. The MOT quadrupole field remains on throughout the pulse sequence as induced currents created during a fast switch-off of the coils may take tens of milliseconds to dissipate, in which time the atoms will have fallen from the trap. Between each Raman pulse sequence the trapping and repump beams are switched on

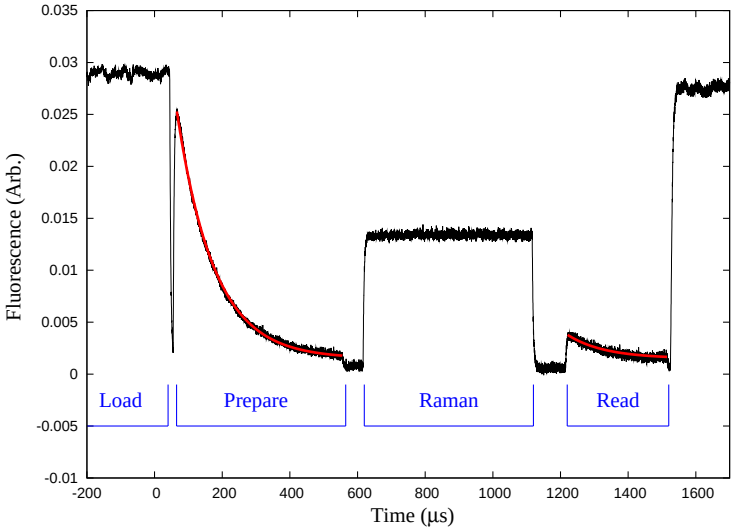

FIGURE 8.2: *Typical pulse sequence. The red line is a fitted exponential of which the height and decay constant are used for the following plots. In this pulse sequence 10% of the population has been transferred and the decay constant is* 110 μs.

for 100 ms to rebuild the cold atomic cloud. The Raman pulse sequence is completed within 2 ms to ensure the majority of atoms remain in the trap region (see Section 5.7.2). Each pulse sequence is repeated at a rate of 10 Hz and averaged over three seconds by the Tektronix DPO4104 oscilloscope. The quantization coils are modulated at 20 Hz which is slow enough that the rate of field change during the pulse is negligible but fast enough so that the trapped atomic cloud does not follow the quantization field. After the trapping and repump beams are extinguished, we apply the trapping beam detuned three linewidths from the $F = 3 \rightarrow F' = 4$ transition to optically pump the atoms into the $F = 2$ ground state. The height and decay constant of the $F = 3$ state fluorescence are recorded. The decay from the $F = 3$ state is quite slow ($1/e \simeq 4000\ \gamma$) due to the closed nature of the transition but this aids in the accuracy of the exponential fitting. The prepare pulse lasts for 500 μs to ensure complete emptying of the $F = 3$ state.

The Raman lasers are then pulsed, the details of the pulses depending upon the individual experiments (See Chapter 6). In the following graphs we apply a top-hat pulse with no chirping or shaped-intensity variations: a simple fractional π pulse. For each Raman pulse we will either vary the length of the pulse or vary the EOM detuning from the resonance frequency ($f_0 = 2,725,732,440$ Hz). After the Raman pulse, the trapping beam is pulsed a second time to measure the repopulation of the $F = 3$ ground state, and yet again the decay is fitted to an exponential and the height and decay constants are

recorded. After each averaged pulse sequence the computer downloads the data, resets the oscilloscope, uploads new waveforms to the Tabor waveform generators, changes the Agilent frequency and re-adjusts the Mach-Zehnder interferometer to remove the carrier.

8.3 Data Analysis

A sufficiently large data-set can take several hours to collect, as each data point takes 10 seconds for the MOT cloud to be formed, waveforms to be uploaded and the MZI to be stabilized. As mentioned earlier, the trapping and repump lasers only remain locked for up to an hour at a time and the Tiger laser drifts by hundreds of MHz over a day. These variations between data-points may cause spurious signals and also hide important weak signals within the noise.

To remove most of the noise, the computer randomly chooses the experimental variable (e.g. frequency or time) from within a specified range so that any slow drifts are converted to stochastic noise. The data are further filtered during analysis by rejecting any points where the MOT cloud brightness (as determined from fluorescence during the prepare pulse) is within a specific range. This ensured that significant numbers of atoms are loaded into the trap to provide an adequate signal to noise ratio, and to remove data sets where the MOT cloud is unformed or weak (due to MOT lasers drifting from lock). This level of filtering is broad and generally only removes 5-30% of points, which are usually due to uncertainty in the fitting of the exponential decay curve to a weak signal (this can be checked against the original data set and scope screen capture). The randomly chosen variables are not equally distributed (as they are random) so one cannot apply a simple averaging to smooth out the data points; instead we use a 2D Gaussian-weighted smoothing algorithm written in Mathematica. The functions for the Gaussian weighting, $\bar{y}$ and corresponding standard deviation, σ_y, are

$$\bar{y} = \frac{\sum_k P_k y_k}{\sum_k P_k} \quad \sigma_y = \sqrt{\frac{\sum_k P_k (y_k - \bar{y})^2}{\sum_k P_k}} \tag{8.2}$$

where

$$P_k = \exp\left[\frac{-(x_k - x_0)^2}{2w^2}\right] \tag{8.3}$$

and

$$w = \frac{\Delta}{2\sqrt{2\ln 2}} \tag{8.4}$$

and y_k is the data-point which is averaged across neighbouring, Gaussian-weighted P_k, data-points separated from y_k (at x_0) by x_k; Δ is the FWHM of the Gaussian-weighting function which is chosen to be smaller than any significant experimental scales (the value of which is noted on the figure). In the following figures, the data points are depicted in blue, the smoothed data by a red line and the standard deviations from the smoothed data by grey bars.

8.4 Dipole Matrix Elements

The coupling between two states is quantified by the dipole matrix elements as discussed in Section 3.2.3. Part of the calculation considers the conservation of angular momentum between the incident photon and the initial and final states. The angular momentum of a photon is defined by the polarization along its direction of motion relative to the quantization axis of the atom. We use co-propagating circularly polarized beams to couple the $m_F = 0$ magnetic sublevels of the two ground states; therefore we must apply a quantization axis parallel to the Raman beams.

Within a MOT, the atoms will be cooled and trapped toward the zero-point of the magnetic field. The atoms will distribute themselves around this zero point but not necessarily symmetrically due to any imbalance of power between counter-propagating beams. Therefore the atoms experience a quantization field plus an inhomogeneous residual magnetic field due to imperfections in the magneto-optical trap configuration. Any field component not along the quantization axis will result in Zeeman shifts of the two-photon resonance (for magnetically sensitive sublevels, $m_F \neq 0$) and reduction in coupling strength due to an imperfectly defined quantization axis.

The distribution of the cold atom cloud and offset from the zero magnetic field point is measured from plots similar to Figure 8.1 with varying field strengths. Each peak is fitted to a Lorentzian ($m_\mathrm{F} = 0$) or Gaussian ($m_\mathrm{F} \neq 0$) lineshape and the maximum and FWHM is recorded. The uncertainty is estimated by the range of values for maximum and FWHM that fit within the uncertainty of the data-points in the plots.

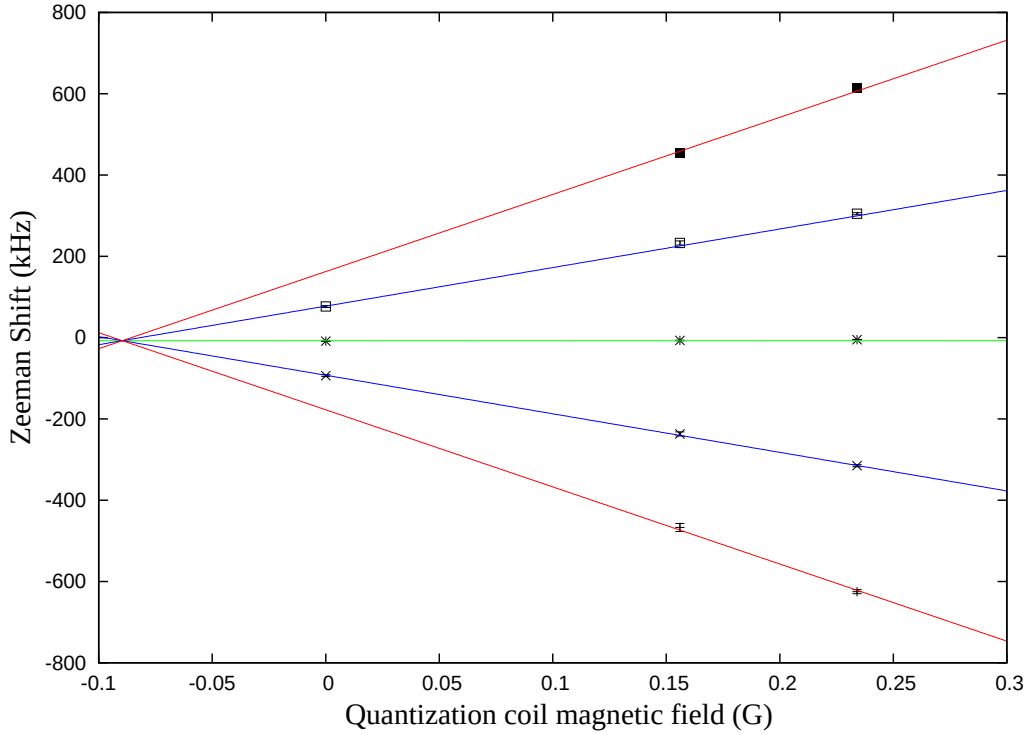

FIGURE 8.3: *Relative Zeeman shifts of the hyperfine magnetic sublevels with varying quantization-field strength. The error bars in the y axis are too small to see on the plot but the coloured fitted lines do pass within the error. The fitted lines correspond to* $\Delta f(kHz) = m_F(0.948 \times mG + 85) + f_{ls}(kHz)$*, where* f_{ls} *is the light shift.*

The Zeeman shift of the non-zero magnetic sublevels has been measured at different quantization field strengths and plotted in Figure 8.3. The solid lines have been fitted to the plot using Equation 3.5 and we see that the atomic cloud does not sit at the zero-field point. The residual Zeeman shift is 85 kHz (taking the lightshifts into account). The gradient of the MOT quadrupole magnetic field is $5\,\mathrm{G\,cm^{-1}}$ in the vertical direction through the MOT coils, and half this value in the horizontal plane; therefore the atom cloud is offset by either 200 μm vertically or 400 μm horizontally. The distribution of the atomic cloud can also be estimated from the inhomogeneously broadened linewidth of the non-zero m_F sublevels in the same manner: we measure the cloud size to be either $160 \pm 32\,\mu$m in the vertical direction or $320 \pm 64\,\mu$m in the horizontal plane. The value for the cloud diameter as measured by fluorescence onto a CCD in Section 5.7.1 is 350 μm so we can infer that the atomic cloud is offset mostly in the horizontal plane.

To verify the statement in Section 6.3.2., that we should expect no Raman transitions with $\pi - \pi$ polarized light, we performed the the same data run as Figure 8.1 but with

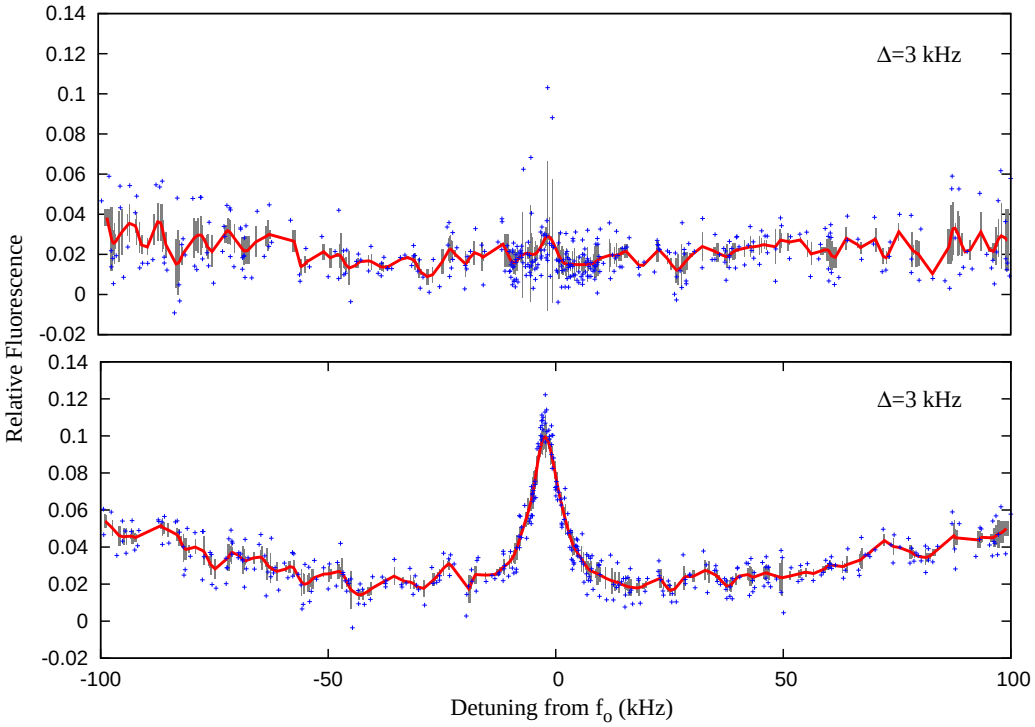

FIGURE 8.4: *The upper plot shows the Raman transition with $\pi - \pi$ polarized Raman beams, whereas the lower plot is with $\sigma - \sigma$ polarizations. The π polarization has a null transition amplitude with a quantization axis along the beam wavevector. The data has been filtered (red line) using the technique outlined in Section 8.3.*

linear polarized beams (top) and circularly polarized beams (bottom). We see no significant features with linear polarization due to the null dipole moments. A quantization axis is required to differentiate between the polarizations of the beams to achieve Raman transitions.

8.5 Single Photon Scatter

Single-photon scatter can cause population transfer between the ground states by excitation to an intermediate upper state, but can also cause dephasing through excitation to an upper state which cannot decay into the opposite ground state. Therefore any single photon scattering, no matter the polarization or specific transition, will result in a decay of coherence. As noted in Section 6.3 the single photon scattering rate is proportional to the square of detuning, $R_{1p} \propto \frac{1}{\Delta^2}$ at large detunings whereas the two-photon Raman resonance varies linearly with detuning, $R_{2p} \propto \frac{1}{\Delta}$. Therefore we may significantly reduce the single-photon decoherence but still retain a considerable Rabi-flopping rate.

What we need to measure is the minimum detuning we can use, as the coherent cooling experiments in Chapter 6 require Rabi frequencies greater than the residual Doppler width of the cold atoms ($\sim 300\,\mathrm{kHz}$).

8.5.1 Dephasing Theoretical Model

We use a numerical solution of the OBEs to calculate the theoretical temporal and spectral curves and therefore dephasing rates. We include a second dephasing term Γ in the coherences to account for collisional-type decoherence that does not cause depopulation. The equations are;

$$\dot{u} = \delta v - \left(\frac{\gamma}{2} + \Gamma\right) u \tag{8.5}$$

$$\dot{v} = -\delta u + \Omega w - \left(\frac{\gamma}{2} + \Gamma\right) v \tag{8.6}$$

$$\dot{w} = -\Omega v + \gamma\left(\frac{1}{2} - w\right) \tag{8.7}$$

where γ is the depopulation *and* dephasing rate. We have also changed the equilibrium population difference (last term in Equation 8.7) from 1 to 1/2 as we expect both ground states to be equally populated in the steady state. The calculated population in the 'excited' ground state (the initially dark state) is given by

$$\rho = \frac{\rho_0}{2}(1 - w) \tag{8.8}$$

where ρ_0 is the maximum population of the $F = 3$ state. The Mathematica code for these theoretical plots is shown in Appendix D.

Accurate fitting of the theoretical plots to the data-sets is complicated by the closely related effects of each decoherence rate. Figure 8.5 shows the effects of each term: the upper two plots are the expected temporal (left) and spectral (right) functions with $\gamma = 0.1\,\Omega$ and $\Gamma = 0$; the bottom two plots have the values $\gamma = 0$ and $\Gamma = 0.1\,\Omega$. The two Rabi flopping plots (left) show little difference between each other, although the upper plot has a slightly increased decay due to the effect of γ on dephasing *and* depopulation. The spectral 'sinc-squared' plots (right) show the greatest difference between decoherence rates as γ causes the relative fluorescence, and therefore population difference, to tend

to a non-zero value at far detunings, whereas Γ causes the population difference to tend to zero at far detuning.

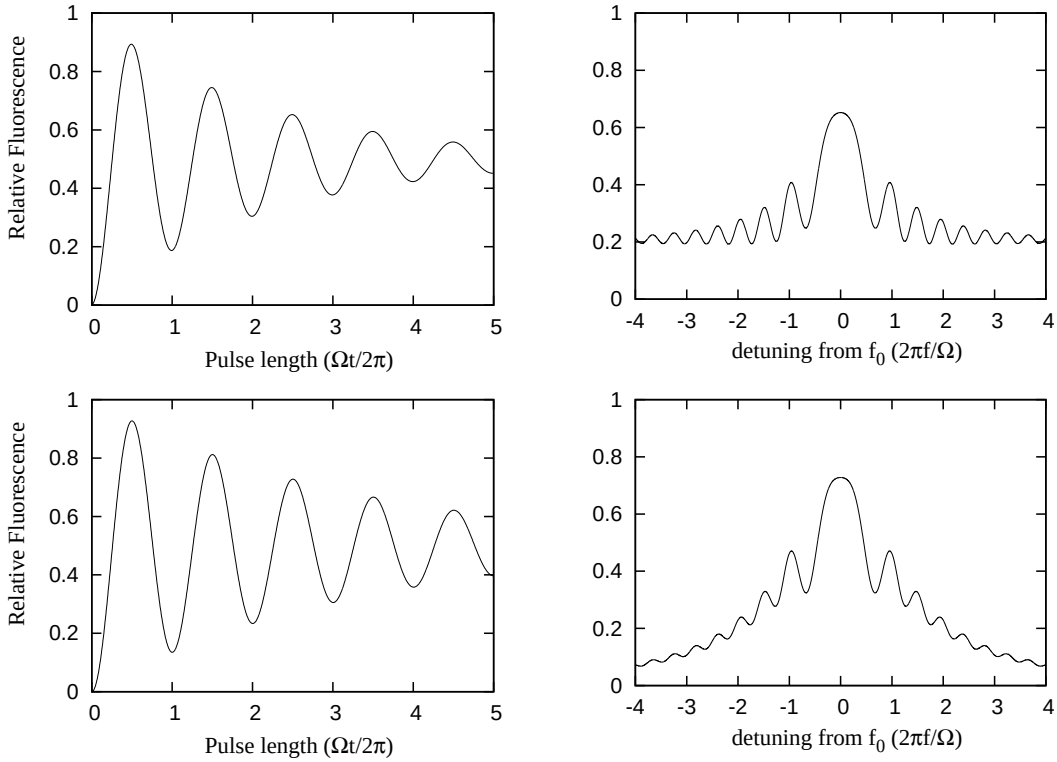

FIGURE 8.5: *Theoretical plots of the relative fluorescence, which is proportional to the population in the $F = 3$ state, as a function of Raman pulse length (left) and detuning from two-photon resonance (right). The upper two plots have $\gamma = 0.1\,\Omega$ and $\Gamma = 0$ (spontaneous emission type dephasing), and the bottom two plots have $\gamma = 0$ and $\Gamma = 0.1\,\Omega$ (collisional type dephasing).*

8.5.2 Dephasing Data

Figure 8.6 shows the measured spectral line shapes and Rabi flopping at various detunings from the single photon resonance of 780.243 nm. At detunings closer to single photon resonance (red) the lineshape tends toward a Lorentzian shape whereas at far detunings (green plot) we see the predicted 'sinc-squared' type shape. Each dataset has been fitted with the OBE model from Section 8.5.1 to the spectral data using the values indicated from the graphs. The single photon scatter γ has been calculated from the scattering rate at each detuning for the measure intensities. The model appear to fit the spectral data well but fails to accurately predict the resulting Rabi flopping. The model

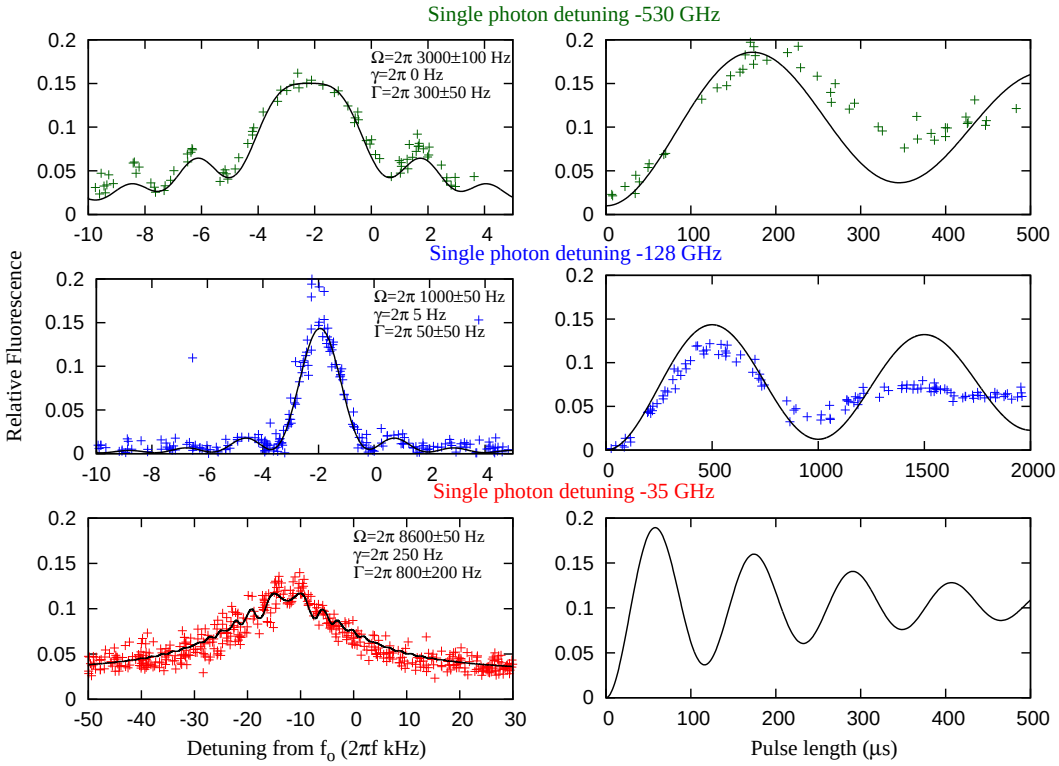

FIGURE 8.6: *Comparison of spectral line shapes and Rabi flopping at various detunings from single photon resonance. The left-hand plots show the spectra at a pulse length of 500 μs, and the right-hand plots show the Rabi flopping at various pulse lengths on resonance (no temporal data was taken for the bottom plot). The black line is calculated by the OBE model from Section 8.5.1 using the values on each graph. The model has been fitted to the spectral data and the single photon scattering γ has been calculated by the scattering rate at each detuning. The model seems to fit well for the spectral plots but there is greater decay in the temporal dataset.)*

does not predict the large amount of coherence decay seen in the measured data and so we must conclude that the model neglects additional significant sources of decoherence.

In all of the data sets collected so far we see that, as shown in Figure 8.7, the rate of decoherence decay does not depend on single photon detuning or absolute intensity. From the lower plot in Figure 8.7 we see a well resolved rising peak and first trough, so we should expect to see many oscillations if the intensity is increased. Unfortunately we barely see any improvement in Rabi flopping contrast, even with greater detuning from single photon resonance and therefore we conclude that the decoherence is due to a factor independent of these variables.

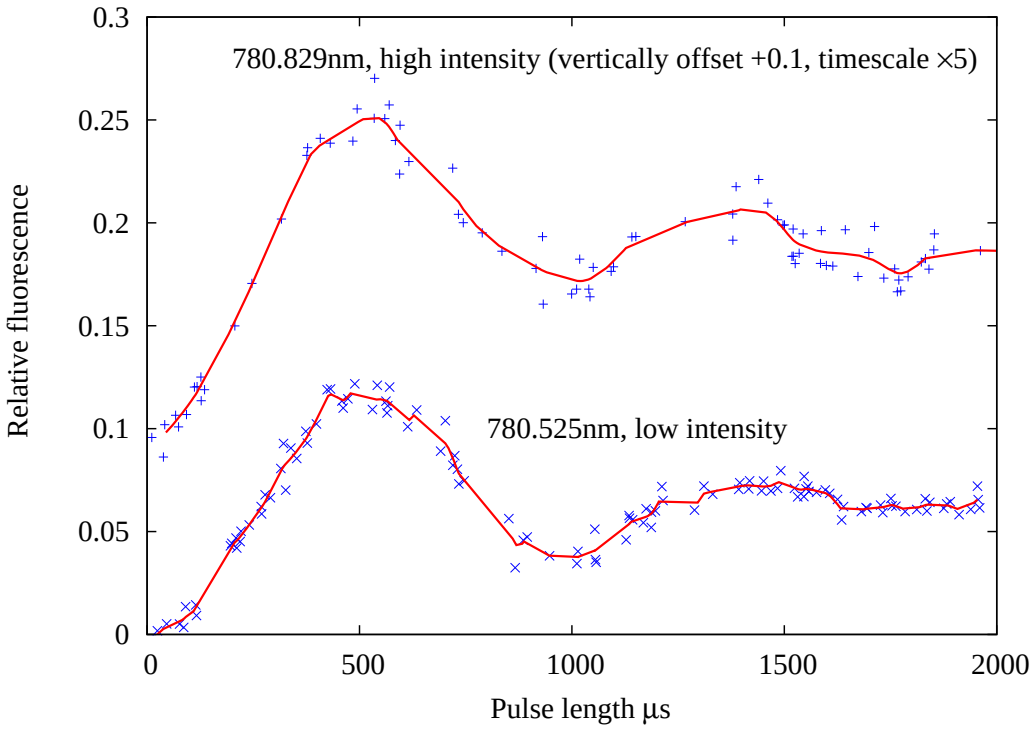

FIGURE 8.7: *Rabi flopping at two different single-photon detunings and intensities. The plot shows that the decay of coherence does not seem to significantly depend upon single photon detuning, nor Raman beam intensity. The data has been filtered (red line) using the technique outlined in Section 8.3 with a FWHM of 30 µs.*

8.6 Collisions

At micro→millikelvin temperatures the atoms do not have enough energy to cause hyperfine-changing collisions between the $5S_{1/2}$ ground states as we have seen in the zero-pulse limit of Figure 7.5. The 'hard sphere' picture of collisions may not apply to cold collisions as the interaction time is quite long due to the slow atomic velocities. Atoms may form short lived molecular states in which the electron *and* nuclear spin interaction must be considered [164, 165]. A large amount of research is available on cold collisions due to their relevance in BEC physics and atomic clocks.

Kokkelmans et al [166] performed a study into the suitability of laser-cooled Rb for an atomic clock reference by calculating the phase shift caused by cold collisions. For the ^{85}Rb $|F = 3, m_F = 0\rangle$ ground state they calculated a collisional rate of 220 mHz for a cloud density of 10^9 atoms per cm^3 and a temperature of 1μK. This is quite large and around two orders of magnitude greater for the $|F = 2, m_F = 0\rangle$ state, although the paper does not mention the reason for this asymmetry. If we use typical parameters of

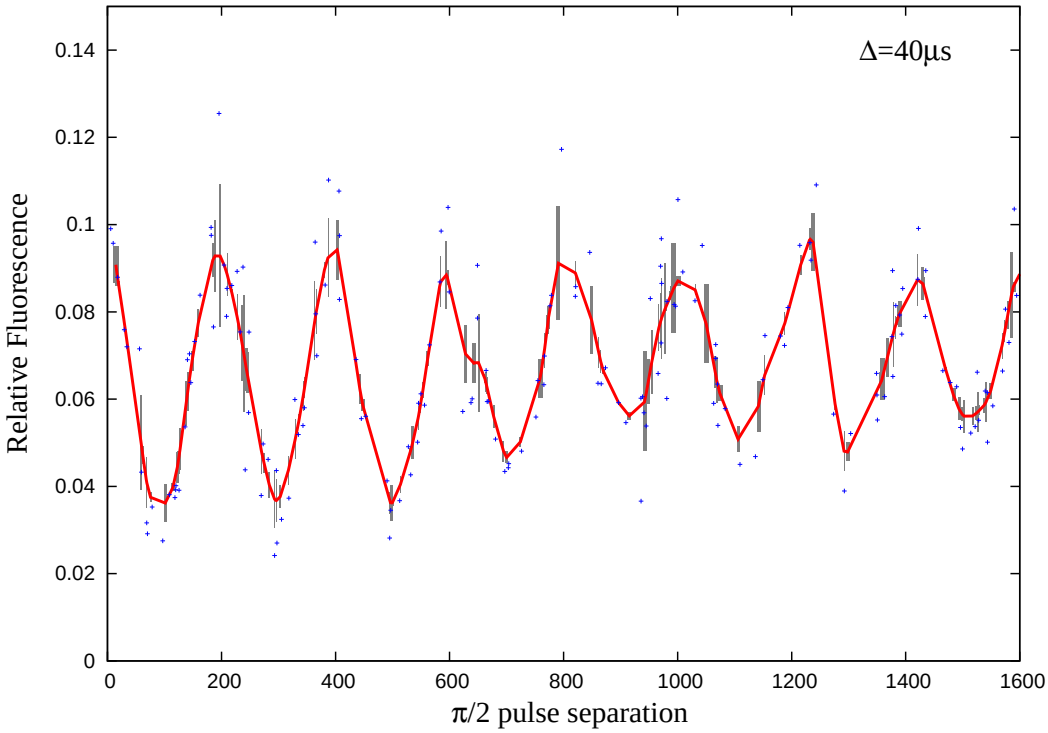

FIGURE 8.8: *Relative fluorescence between the 'prepare' and 'read' pulses between which two $\pi/2$ pulses have been applied with varying delay between them. This is known as Ramsey's method of separated fields. The plot shows that the atomic cloud remains coherent for over a millisecond and so dephasing due to collisions is negligible. The fringes do not go to zero due to imperfect $\pi/2$ pulse areas, and have a contrast of 42%=(max.-min.)/(max.+min.) and a decay constant of 3 milliseconds.*

our system as 10^{11} atoms per cm^3 and 100μK we obtain as collisional rate of 220 Hz which is a significant fraction of the Rabi frequencies we are measuring ($\sim$ 1 kHz).

To separate the effects of dephasing due to the Raman beams themselves from collisional dephasing we use 'Ramsey's method of separated fields' [167] (also known as a Ramsey-Bordé interferometer in the optical regime [148]) in which the Raman beams apply a $\pi/2$ pulse, then allow the atomic superposition to evolve for a variable delay before recombining the interferometer with another $\pi/2$ pulse. As we can achieve a π pulse in $\sim$ 100 μs in which time the atom does not seem to suffer considerable decoherence (as seen in the upper plot in Figure 8.7) we may use this technique to investigate any dephasing effects when there are no Raman beams. Figure 8.8 shows the measured change in population as a function of $\pi/2$ pulse separation. The plot confirms previous measurements that collisions within the MOT are negligible and thus not a source of dephasing. The frequency of the Ramsey fringes is due to the difference in phase between the transition frequency and the frequency difference between the Raman fields: in this

case it is due to the lightshift of the states during the pulse and the null light shift between pulses.

8.7 Beam Intensity and Raman Detuning

Assuming a large single-photon detuning, the main terms in Equation 8.1 are the Raman resonance detuning and the intensity of the Raman beams. As noted in Section 6.3.2, the intensity can affect the Rabi frequency in two ways: temporally by variations during the averaging period, or spatially by the Gaussian beam profile across an extended atom cloud. Each individual atom will undergo Rabi flopping, each starting in the same state, but at slightly different frequencies depending upon the incident field. When the distribution of Rabi frequencies is summed together we see an apparent decay of coherence. This would explain why we see a well resolved initial rise in the Rabi flopping plots as each atom starts in the same state so the variation in frequencies has less of an effect at early times. It was mentioned in Section 8.6 that the decay of coherence appears to be independent of intensity, this is true when considering an absolute value but not a fractional change.

8.7.1 Intensity Variation Theoretical Model

To model the effect of a spatial intensity variation on the measured Rabi flopping, each atom is assumed to oscillate sinusoidally and the frequency of that oscillation depends upon the local beam intensity. Equation 3.25 is adapted to become

$$R(t) = h \sum_{x=0}^{3*d_c} w(x) \times \frac{\Omega^2 \exp^{-x^2/d_{\mathrm{L}}^2}}{\delta^2 + \Omega^2 \exp^{-x^2/d_{\mathrm{L}}^2}} \sin^2\left(\frac{t}{2}\left(\delta^2 + \Omega^2 \exp^{-x^2/d_{\mathrm{L}}^2}\right)\right) \tag{8.9}$$

where $0.5\,d_L$ is the $1/e^2$ diameter of the laser Gaussian cross-section and h is the maximum amplitude of the oscillation. The signal is summed across the MOT cloud with each contribution weighted by the area and Gaussian density distribution, $w(x)$, in which the detection area is separated into concentric rings centered on the MOT cloud which

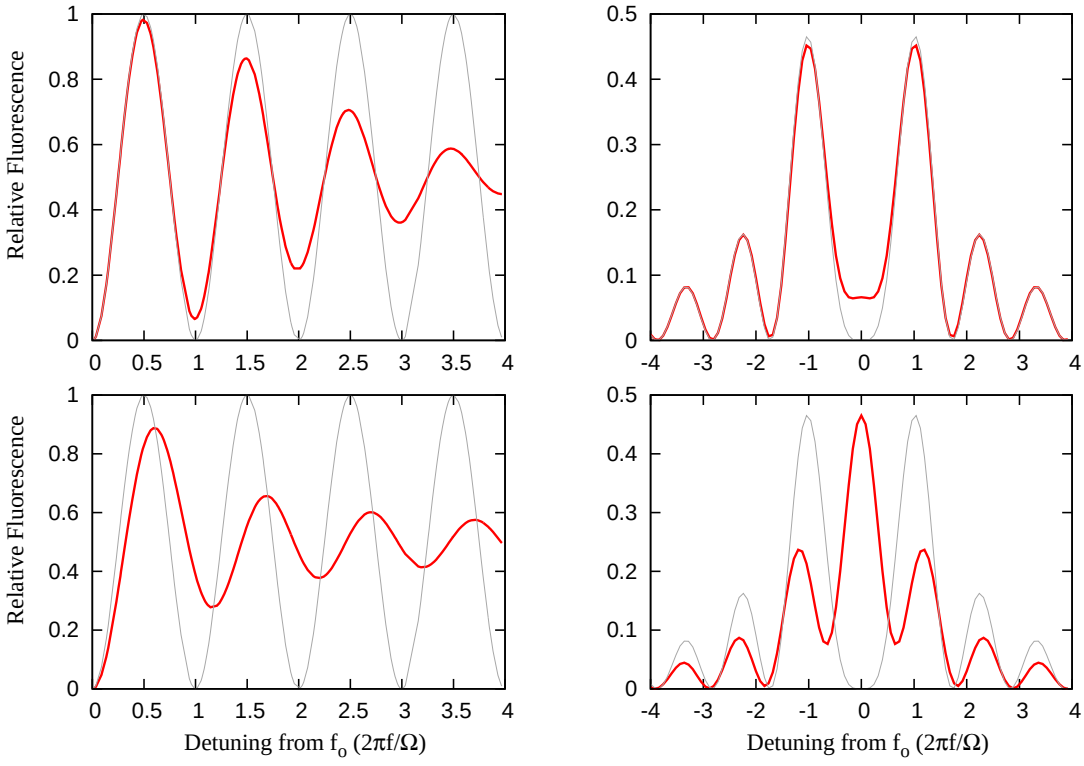

FIGURE 8.9: *Theoretical prediction (red line) for the decay of coherence due to a distribution of Rabi frequencies when averaging over the atomic cloud. The top two plots model the effect of a* 0.2Ω *variation (FWHM) of intensity for all atoms during the averaging period. The left-hand plot shows the variation on resonance over time and the right-hand plot shows the spectrum for a pulse period of* $2\pi/\Omega$*. The lower two plots model the effect of a Gaussian beam profile with a* $1/e^2$ *diameter equal to 3 times the FWHM of the atomic cloud. The grey line shows the expected Rabi flopping with no decay.*

has a FWHM of $\frac{d_c}{2\sqrt{2\ln(2)}}$:

$$w(x) = \frac{\pi((x+\Delta x)^2 - x^2)\exp^{-x^2/2d_c^2}}{9\pi d_c^3\sqrt{(2\pi)}} \tag{8.10}$$

where Δx is the width of each ring (summation step size). In the above equations the signal is summed over a width of $3\,d_c$ as the cloud density is negligible beyond this value. To account for intensity variation over time each value of R(t) is summed over a distribution of Rabi frequencies, Ω, with a normalized Gaussian distribution whose FWHM is equal to the temporal intensity variation. The Python code for this model can be found in Appendix D.

Figure 8.9 shows the expected Rabi flopping with a 0.2Ω variation (FWHM) in intensity (top) and the Rabi flopping for a MOT cloud with Gaussian beam $1/e^2$ diameter 3

times greater the MOT cloud FWHM (bottom). Both plots show significant decay of coherence and the spatial intensity plot also introduces a chirp of the Rabi frequency. The temporal variation in intensity (top) produces less decay of coherence at shorter time periods than a spatial decay (bottom), and this can be seen in the spectral plots (right) in which the off-resonant minimas tend to be closer to zero (although this is not obvious from the plots due to the chirp produced by the spatial variation).

8.7.2 Intensity Variation Data

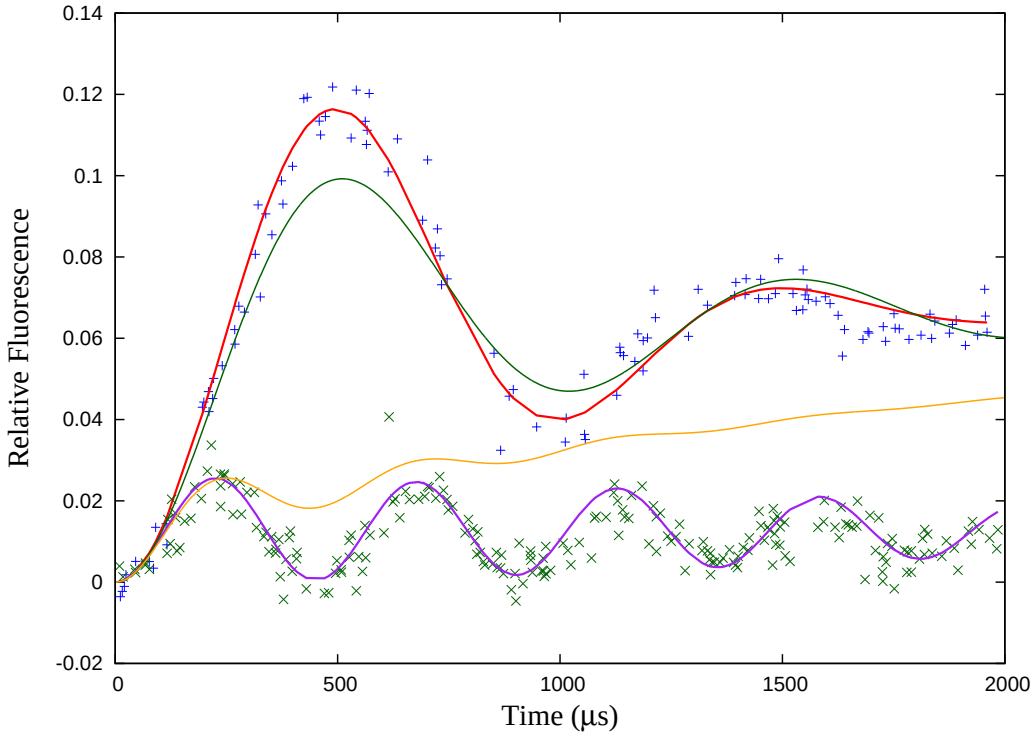

FIGURE 8.10: *Comparison of the optical Bloch model (green and orange lines) and the intensity variation model (red and purple lines) to the data points (blue and green dots) for the decay of coherence of the Rabi flopping. The blue dots are the datapoints for Rabi flopping on resonance and the green dots are the datapoints for the Rabi flopping detuned by -2 kHz from Raman resonance. The height of the modeled plots have been scaled to fit the intensity variation model (h=0.13) which assumes a* 0.5Ω *FWHM temporal intensity variation. The optical Bloch model decay of coherence has been adjusted to give the closest fit on resonance.*

Figure 8.10 shows a fit of both the optical Bloch model with decoherence (green line on resonance and orange line off resonance) and the intensity variation model (red line on resonance and purple line off resonance) with the measured data both on resonance (blue dots) and 2 kHz off resonance (green dots). The off-resonance plot shows the

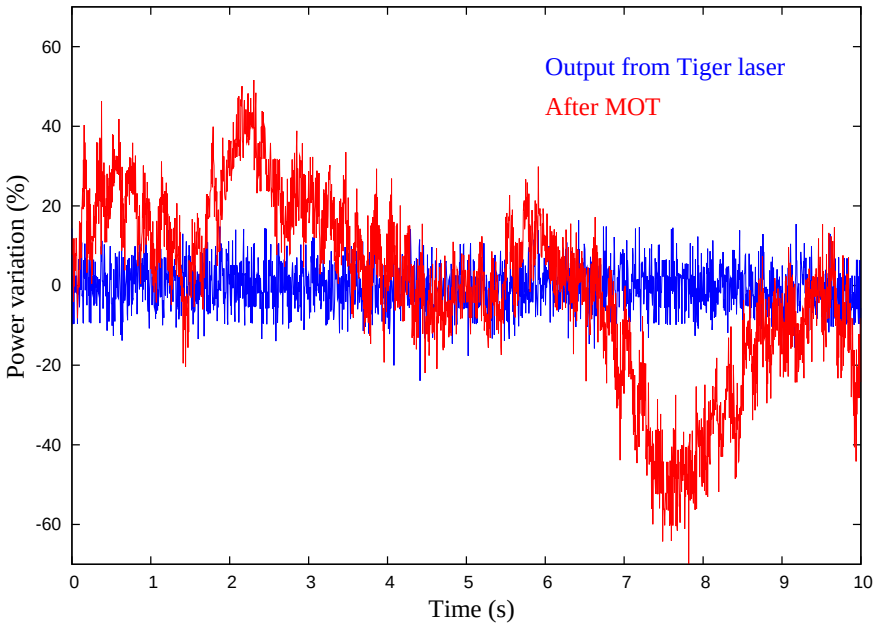

FIGURE 8.11: *Intensity variations in the Raman beam intensity at the Tiger laser output (blue) and after the MOT (chamber). The variations have been normalized and the mean value subtracted. The standard deviation of the red plot is 22%.*

most apparent difference between the two models: in the OBE model (orange) the oscillation quickly decay and the population difference tends toward 1/2 total, whereas the intensity variation model (purple) more accurately predicts the rate of decay. The intensity variation model uses the measured value for the Gaussian beam $1/e^2$ diameter as 2.2 mm and the cloud FWHM as 350 μm. In order to fit to the data the FWHM of the intensity variation over time needed to be 0.5Ω.

Figure 8.11 show the intensity of the Raman beams measured at the output of the Tiger laser and after the Raman beams have passed through the MOT chamber. The plot shows a significant variation of intensity (standard deviation 22%) over seconds which is due to thermal air currents moving the beam as it couples into the optical fibre before the BoosTA. The thermal drifts may also have a greater effect on the relative intensities of the two Raman components as the two-photon Rabi frequency depends upon the product of the individual amplitudes. The increase of coherence in Figure 8.10 by detuning from resonance indicates that the intensity variations have a greater effect than the relative phase stability between Raman fields.

8.8 Discussion

It is evident from the extremely close fit of the theoretical curves in Figure 8.10 (standard deviation of 0.01 on resonance) and the independence of coherence on absolute intensity and detuning in Figure 8.7 that the intensity variations of the Raman beams over time and space are the most significant cause of apparent decoherence. Changes in quantization due to inhomogenous magnetic fields are most probably negligible and the applied quantization magnetic field is several orders of magnitude greater than the residual fields. Single photon scatter can be greatly reduced by detuning far from the D_2 transition and we have seen well resolved 'sinc-squared' type shapes in such regimes. It was estimated in Chapter 5 that collisions within the cold atom cloud are negligible, and in Chapter 7 it was shown that collisions do not transfer populations; these findings were confirmed by the measurements of coherent Ramsey fringes over a millisecond.

In comparison to the experiment at Stanford by Chu et al mentioned at the beginning of this chapter which involves 10^6 Caesium atoms, with a (1D) temperature of 10 nK, which are launched vertically and then fall back due to gravity; hence it is called an atomic fountain [146]. The cold temperatures mean the available interaction time is up to 160 ms, during which time Ramsey-Bordé interferometry is performed with stimulated Raman transitions similar to Section 8.7 Chu et al are interested in the phase difference between the two arms of the interferometer, which is related to the local gravity gradient (see Figure 6.6), and appears in the change in frequency of the Ramsey fringes. Therefore one can tune the Raman beams closer to the single photon resonance ($\Delta = 0.99\,\text{GHz}$) to achieve a Rabi flopping frequency of $\sim 6\,\text{kHz}$ with 2.5cm diameter beams, with total power $\sim 150\,\text{mW}$, interacting with a 5mm diameter MOT cloud. This ensures that there are negligible spatial variations in intensity across the MOT cloud and by stabilizing the Raman beams to less than 0.5% there is a narrow distribution of Rabi frequencies. The single photon scatter which occurs at such close detuning causes the contrast of the Ramsey fringes to be limited to 62%, but as the primary interest is in the frequency of the Ramsey fringes, one can compromise the finge contrast with the increase of Rabi frequency.

The intensity variations over time appear to be have the greatest effect on decoherence and are most likely due to thermal air currents affecting the coupling of the Raman fields into the optical fibre. By making the apparatus more compact and enclosing in a draught-proof enclosure we should be able to reduce beam pointing effects. Further stabilization can be achieved by monitoring the beam intensity before it enters the MOT chamber and feeding the signal back to an AOM to adjust the intensity accordingly [168]. The spatial variation in beam intensity may become a problem if we need to increase the Rabi frequency by narrowing the beams. The resulting decoherence can be tackled by shaping the beam profile to achieve a more uniform intensity profile. The MOT cloud dimensions may also be reduced by increasing the gradient of the quadrupole magnetic field, so we have recently added water cooling to the MOT coils so that the field gradient can be doubled. The MOT size can also be reduced by lowering the background gas pressure so that fewer atoms are trapped, but this will result in a lower signal to noise ratio, which is already close to the useable limit (hence the long averaging times). Another option is using a dipole trap [154] or dark spot trap [169] to compress the atoms into a smaller volume.

It is possible to shape the beam profile into a flat top Gaussian ('Super-Gaussian') or the extreme of a flat-top shape using spatial light modulators [170], phase plates [171], aspheric doublets [172] or micro-lens arrays [173]; although by 'homogenizing' the beam, the intensity is reduced. By improving the intensity characteristics of the Raman beams we should be able to detune closer to resonance so that the Rabi frequency can be increased: a requisite for the coherent cooling experiments in Chapter 7.

Currently the atoms are prepared in the $|F = 2, m_{\mathrm{F}} = 0\rangle$ magnetic-insensitive sublevel by using the trapping laser to optically pump all of the atoms out of the $F = 3$ state. This results in a nearly equal distribution in all of the m_{F} sublevels, therefore we lose 8% of of our potential signal. In Tables A.4 and A.5 there exists a null dipole element for transitions with linear polarizations ($\epsilon = 0$) from $F = i \rightarrow F' = i$, where $i = 2, 3$. Applying both trapping and repump beams - with linear polarizations - perpendicularly to the quantization axis it is possible to optically pump all of the atoms into the $|F = 2, m_{\mathrm{F}} = 0\rangle$, thus improving the signal to noise ratio by a factor of five.

The final but most significant improvement is an overall increase in power of the Raman beams. The experiments in Section 6.5 rely upon using adiabatic rapid passage with velocity sensitive stimulated Raman transitions. To ensure interaction with all atoms in the MOT cloud requires a Rabi flopping frequency greater than the residual Doppler-broadened width of the transition frequencies, which is around 100 kHz. We can already perform atom interferometry, as shown in Figure 8.8 with π pulses but to achieve *adiabatic* rapid passage requires many Rabi oscillations. The intensity of the Raman beams must be increased and can be achieved by replacing the Tiger laser with a more powerful (and reliable) diode laser or a Ti:Sapphire laser or by amplifying both Raman fields with additional BoosTAs.

Chapter 9

Conclusion

We have proposed the use of all-optical methods employing coherent interactions between long-lived ground states which may be used to impart large amounts of momentum via pulsed Raman transitions. The thesis discussed the feasibility of performing coherent interactions with a cold dense sample of free atoms with large (fraction of a mm) spatial dimensions, compared with previous work using tightly focused dipole traps (tens of microns) [154, 159, 160], trapped single atoms and ions [161, 162, 163], or extremely cold (nK) atoms in an atomic fountain [146]. In order to attempt the above studies has required the building of a magneto-optical trap, frequency stabilized trapping lasers and Raman fields which can be controlled in amplitude, relative frequency and phase, and direction.

Theoretical modelling of the coherent interaction within the cold atom cloud predicted high contrast Rabi-flopping fringes; however, initial data showed no sign of coherence. From these results we investigated all known sources of decoherence, such as inhomogeneous magnetic fields which result in an undefined quantization axis affecting two-photon transition probability, single photon scatter, collisional dephasing and variations in the intensity and relative phase of the Raman fields. It was found that magnetic field effects and collisions are negligible, single photon scatter can be greatly reduced at far detuning from resonance and that any relative phase instabilities between the Raman fields is negligible on the experimental timescales (ms).

It was found, both theoretically and experimentally, that variations in the intensity of the Raman beams, both temporally and spatially across the atom cloud, will produce a distribution of Rabi frequencies. When the signal was integrated across the whole atom cloud and averaged for several seconds to achieve a suitable signal to noise ratio, the distribution of Rabi frequencies 'washed out' the fringes and appears as an apparent decay of coherence. Compared with decoherence through phase interruptions and depopulation, the atoms show high coherence at short Raman pulse periods because they all start in the same state from which any variation in Rabi frequency has a smaller effect; correspondingly at longer Raman pulse periods the decay is greatly enhanced. This effect also explains the independence of the coherence decay rate on absolute beam intensity and single-photon detuning (far from resonance) as well as an increase in coherence away from two-photon resonance.

Fortunately, control of the Raman beam intensity is a technical, not fundamental, problem which can be overcome with a few improvements to the setup. Temporal variations can be stabilized by enclosing the Raman beam path in a draught-proof enclosure and by actively stabilizing the intensity via an acousto-optic modulator. Spatial variation of the Raman beams over the MOT cloud can be reduced by increasing the beam size although this would result in an undesirable reduction of the Rabi frequency. Several methods exist which can 'flatten' the beam profile so that the atomic cloud experiences a uniform field [170, 171, 172, 173]. Another option is to reduce the size of the MOT cloud by increasing the MOT magnetic field gradient, using a 'dark spot MOT' [169], or confining in a dipole trap [154]. These techniques may result in a reduced signal to noise ratio which can be improved with better state preparation, as currently the atoms are distributed over several m_{F} sublevels. The atoms may be pumped completely into the $m_{\mathrm{F}} = 0$ sublevel with a linearly polarized beam along the quantization axis and so improve the signal to noise ratio by factor of five. All of the suggested improvements are currently being investigated or implemented.

The most significant improvement, in order to increase the Rabi-flopping rate to frequencies greater than the residual Doppler width of the atom cloud for the coherent cooling experiments, is an increase of power in the Raman beams. This can be achieved by replacing the Tiger laser with a higher power diode laser, or a Ti:Sapphire laser,

or by using additional BoosTA modules to amplify the Raman fields separately. By removing the interference effects we may also be able to detune the Raman beams closer to single-photon resonance to increase the Rabi frequency.

The Ramsey fringes experiment shown in Figure 8.8 demonstrates that it is possible to perform atom interferometry experiments in the current configuration. The Rabi-frequency is not high enough to significantly affect the velocities of the atoms with the coherent cooling techniques outlined in Chapter 7, but we should be able to attempt the vapour cell interferometry experiment described in Chapter 6 and this will give us the chance to experiment with controlling the directions of the Raman beams. Once the Rabi frequency has been increased by using higher power Raman fields we can investigate techniques to impart momentum to the cold atoms efficiently via shaped pulses.

Appendix A

Rubidium Values

A.1 Constants

Various constants are used throughout this thesis and are tabulated here as a quick reference. All values are taken from the 2006 CODATA recommended values [174].

Constant	Symbol	Value	Units
Speed of light (vacuum)	c	299792458	m/s
Planck's constant	$h \equiv 2\pi\hbar$	$6.62606896(33) \times 10^{-31}$	$J\,s$
Electron charge	e	$1.602176487(40) \times 10^{-19}$	C
Boltzmann constant	k_B	$1.38065(4) \times 10^{-23}$	J/K
Bohr magneton	μ_B	$927.400915(23) \times 10^{-26}$	J/T
Permittivity	ϵ_0	$(4\pi \times 10^{-7} c^2)^{-1}$	F/m
Atomic mass unit	u	$1.660538782(83) \times 10^{-27}$	kg

TABLE A.1: *Recommended values for fundamental constants used in this thesis.*

A.2 Hyperfine Splittings

The hyperfine energy splittings are due to spin-orbit momentum coupling to the nuclear moment and are calculated by

$$\Delta\omega_{hfs} = \frac{1}{2\hbar}\left(A_{hfs}K + B_{hfs}\frac{3K(K+1) - 4I(I+1)J(J+1)}{8I(2I-1)J(2J-1)}\right) \tag{A.1}$$

where

$$K = F(F+1) - I(I+1) - J(J+1) \tag{A.2}$$

and J is the spin-nuclear moment, S is the spin moment, I is the nuclear moment and F is the hyperfine moment. A_{hfs} and B_{hfs} are the magnetic dipole and electric quadrupole constants, respectively, which are measured experimentally [50].

A.3 Landé g-factors

The hyperfine Landé g-factor which determines the strength of the magnetic splitting of the hyperfine sub-levels can be approximated by [51];

$$g_F \simeq g_J \frac{F(F+1) - I(I+1) + J(J+1)}{2F(F+1)} \tag{A.3}$$

where

$$g_J \simeq 1 + \frac{J(J+1) + S(S+1) - L(L+1)}{2J(J+1)} \tag{A.4}$$

and L is the orbital moment. The approximations are correct to 0.1% and the nuclear g-factor, g_I is ignored as $g_J \gg g_I$. The hyperfine g-factors for ^{85}Rb are therefore

	$5S_{1/2}$		$5P_{3/2}$			
F	2	3	1	2	3	4
g_F	-1/3	1/3	-1	1/9	7/18	1/2

TABLE A.2: *Rubidium 85 Landé g-factors*

A.4 Detunings from ^{85}Rb $F = 3 \rightarrow F' = 4$

Peak	Transition	Detuning from a (MHz)	Wavelength (nm)
a	^{85}Rb $F3 \rightarrow F'4$	0	780.244
b	^{85}Rb $F3 \rightarrow F'3/4$ X	-60.32	
c	^{85}Rb $F3 \rightarrow F'2/4$ X	-92.02	
d	^{85}Rb $F3 \rightarrow F'3$	-120.64	
e	^{85}Rb $F3 \rightarrow F'2/3$ X	-153.34	
f	^{85}Rb $F3 \rightarrow F'2$	-184.04	
g	^{87}Rb $F2 \rightarrow F'3$	-1126.49	780.247
h	^{87}Rb $F2 \rightarrow F'2/3$ X	-1259.81	
i	^{87}Rb $F2 \rightarrow F'1/3$ X	-1338.28	
j	^{87}Rb $F2 \rightarrow F'2$	-1393.14	
k	^{87}Rb $F2 \rightarrow F'1/2$ X	-1471.61	
l	^{87}Rb $F2 \rightarrow F'1$	-1550.08	
m	^{85}Rb $F2 \rightarrow F'3$	2915.09	780.238
n	^{85}Rb $F2 \rightarrow F'2/3$ X	2883.39	
o	^{85}Rb $F2 \rightarrow F'1/3$ X	2868.71	
p	^{85}Rb $F2 \rightarrow F'2$	2851.69	
q	^{85}Rb $F2 \rightarrow F'1/2$ X	2837.01	
r	^{85}Rb $F2 \rightarrow F'1$	2822.32	
s	^{87}Rb $F1 \rightarrow F'2$	5441.54	780.233
t	^{87}Rb $F1 \rightarrow F'1/2$ X	5363.07	
u	^{87}Rb $F1 \rightarrow F'0/2$ X	5326.96	
v	^{87}Rb $F1 \rightarrow F'1$	5284.6	
w	^{87}Rb $F1 \rightarrow F'0/2$ X	5248.49	
x	^{87}Rb $F1 \rightarrow F'0$	5212.38	

TABLE A.3: *The frequency detunings from ^{85}Rb $F = 3 \rightarrow F' = 4$ (cooling transition). Wavelengths for each ground state are shown for reference. Crossovers are labeled X.*

A.5 Dipole Matrix Elements

The strength of a transition is determined by the dipole matrix element. According to the Wigner-Eckhart theorem [47], the dipole matrix can be reduced into into the various angular momentum components:

$$\langle F' m'_F | q\vec{r}, \epsilon | F m_F \rangle = \langle F' | q\vec{r} | F \rangle (-1)^{F'-1+m_F} \sqrt{(2F+1)} \begin{pmatrix} F' & 1 & F \\ m'_F & -\epsilon & -m_F \end{pmatrix} \quad \text{(A.5)}$$

where $\epsilon = -1, 0, 1$ is the polarization and the array in brackets is the Wigner 3j symbol which can be calculated by programs such as Mathematica (or by hand if one is feeling brave). This equation can be further reduced into fine structure terms.

$$\langle F' | q\vec{r} | F \rangle = \langle J' | q\vec{r} | J \rangle (-1)^{F'+J+1+I} \sqrt{(2F'+1)(2J+1)} \begin{Bmatrix} J & J' & 1 \\ F' & F & I \end{Bmatrix} \quad \text{(A.6)}$$

where the curly brackets denote the Racah 6j Symbol. As noted in Chapter 3, the value $\langle J' | q\vec{r} | J \rangle$ can be measured from the natural decay time τ.

$$\langle J' | q\vec{r} | J \rangle = \sqrt{\frac{3\pi\epsilon_0 \hbar c^3}{\omega_0^3 \tau} \frac{2J'+1}{2J+1}} \quad \text{(A.7)}$$

The experimentally measured value for τ is $26.25 \pm 0.07\,\text{ns}$ [54], for the Rubidium D_2 line $J = 1/2$ and $J' = 3/2$. We find the reduced dipole moment for ^{85}Rb to be

$$\mu_{85} = \langle J' | q\vec{r} | J \rangle = 4.2263\, q a_0 \quad \text{(A.8)}$$

where a_0 is the Bohr radius. The reduced dipole moment for ^{87}Rb only differs by 10ppm due to the isotope shift and so $\mu_{85} \simeq \mu_{87}$. The remaining factors are known as the Clebsch-Gordan coefficients. Therefore the strength of a transition in ^{85}Rb is,

$$\begin{aligned} \langle F', m'_F | q\vec{r}, \epsilon | F, m_F \rangle &= \mu_{85} (-1)^{2F'-1+m_F+J+1+I} \sqrt{(2F+1)(2F'+1)(2J+1)} \\ &\quad \times \begin{pmatrix} F' & 1 & F \\ m'_F & -\epsilon & -m_F \end{pmatrix} \begin{Bmatrix} J & J' & 1 \\ F' & F & I \end{Bmatrix} \end{aligned} \quad \text{(A.9)}$$

The values for the Clebsch-Gordan coefficients for the Rubidium D_2 line are tabulated below.

		$F=3, m_F = m'_F - \epsilon$							
	q	-3	-2	-1	0	1	2	3	$\sum_{m_F} \lvert\mu\rvert^2$
$F'=4$	-1	$\sqrt{\frac{1}{2}}$	$\sqrt{\frac{3}{8}}$	$\sqrt{\frac{15}{56}}$	$\sqrt{\frac{5}{28}}$	$\sqrt{\frac{3}{28}}$	$\sqrt{\frac{3}{56}}$	$\sqrt{\frac{1}{56}}$	3/2
	0	$-\sqrt{\frac{1}{8}}$	$-\sqrt{\frac{3}{14}}$	$-\sqrt{\frac{15}{56}}$	$-\sqrt{\frac{2}{7}}$	$-\sqrt{\frac{15}{56}}$	$-\sqrt{\frac{3}{14}}$	$-\sqrt{\frac{1}{8}}$	
	1	$\sqrt{\frac{1}{56}}$	$\sqrt{\frac{3}{56}}$	$\sqrt{\frac{3}{28}}$	$\sqrt{\frac{5}{28}}$	$\sqrt{\frac{15}{56}}$	$\sqrt{\frac{3}{8}}$	$\sqrt{\frac{1}{2}}$	
$F'=3$	-1		$-\sqrt{\frac{5}{72}}$	$-\sqrt{\frac{25}{216}}$	$-\sqrt{\frac{5}{36}}$	$-\sqrt{\frac{5}{36}}$	$-\sqrt{\frac{25}{216}}$	$-\sqrt{\frac{5}{72}}$	35/54
	0	$-\sqrt{\frac{5}{24}}$	$-\sqrt{\frac{5}{54}}$	$-\sqrt{\frac{5}{216}}$	0	$\sqrt{\frac{5}{216}}$	$\sqrt{\frac{5}{54}}$	$\sqrt{\frac{5}{24}}$	
	1	$\sqrt{\frac{5}{72}}$	$\sqrt{\frac{25}{216}}$	$\sqrt{\frac{5}{36}}$	$\sqrt{\frac{5}{36}}$	$\sqrt{\frac{25}{216}}$	$\sqrt{\frac{5}{72}}$		
$F'=2$	-1			$\sqrt{\frac{1}{189}}$	$\sqrt{\frac{1}{63}}$	$\sqrt{\frac{2}{63}}$	$\sqrt{\frac{10}{189}}$	$\sqrt{\frac{5}{63}}$	5/27
	0		$\sqrt{\frac{5}{189}}$	$\sqrt{\frac{1}{189}}$	$\sqrt{\frac{1}{21}}$	$\sqrt{\frac{8}{189}}$	$\sqrt{\frac{5}{189}}$		
	1	$\sqrt{\frac{5}{63}}$	$\sqrt{\frac{10}{189}}$	$\sqrt{\frac{2}{63}}$	$\sqrt{\frac{1}{63}}$	$\sqrt{\frac{1}{189}}$			

TABLE A.4: *Clebsch-Gordan coefficients for* ^{85}Rb $F = 3$

		$F=2, m_F = m'_F - \epsilon$					
	q	-2	-1	0	1	2	$\sum_{m_F} \lvert\mu\rvert^2$
$F'=3$	-1	$\sqrt{\frac{2}{9}}$	$\sqrt{\frac{4}{27}}$	$\sqrt{\frac{4}{45}}$	$\sqrt{\frac{2}{45}}$	$\sqrt{\frac{2}{135}}$	14/27
	0	$-\sqrt{\frac{2}{27}}$	$-\sqrt{\frac{16}{135}}$	$-\sqrt{\frac{2}{15}}$	$-\sqrt{\frac{6}{135}}$	$-\sqrt{\frac{2}{27}}$	
	1	$\sqrt{\frac{2}{135}}$	$\sqrt{\frac{2}{45}}$	$\sqrt{\frac{4}{45}}$	$\sqrt{\frac{4}{27}}$	$\sqrt{\frac{2}{9}}$	
$F'=2$	-1		$-\sqrt{\frac{7}{54}}$	$-\sqrt{\frac{7}{36}}$	$-\sqrt{\frac{7}{36}}$	$-\sqrt{\frac{7}{54}}$	35/54
	0	$-\sqrt{\frac{7}{27}}$	$-\sqrt{\frac{7}{108}}$	0	$\sqrt{\frac{7}{108}}$	$\sqrt{\frac{7}{27}}$	
	1	$\sqrt{\frac{7}{54}}$	$\sqrt{\frac{7}{36}}$	$\sqrt{\frac{7}{36}}$	$\sqrt{\frac{7}{54}}$		
$F'=1$	-1			$\sqrt{\frac{1}{20}}$	$\sqrt{\frac{3}{20}}$	$\sqrt{\frac{3}{10}}$	1/2
	0		$\sqrt{\frac{3}{20}}$	$\sqrt{\frac{1}{5}}$	$\sqrt{\frac{3}{20}}$		
	1	$\sqrt{\frac{3}{10}}$	$\sqrt{\frac{3}{20}}$	$\sqrt{\frac{1}{20}}$			

TABLE A.5: *Clebsch-Gordan coefficients for* ^{85}Rb $F = 2$

		$F=2, m_F = m'_F - \epsilon$					
	q	-2	-1	0	1	2	$\sum_{m_F} \lvert\mu\rvert^2$
$F'=3$	-1	$\sqrt{\frac{1}{30}}$	$\sqrt{\frac{1}{10}}$	$\sqrt{\frac{1}{5}}$	$\sqrt{\frac{1}{3}}$	$\sqrt{\frac{1}{2}}$	7/6
	0	$-\sqrt{\frac{1}{6}}$	$-\sqrt{\frac{4}{15}}$	$-\sqrt{\frac{3}{10}}$	$-\sqrt{\frac{4}{15}}$	$-\sqrt{\frac{1}{6}}$	
	1	$\sqrt{\frac{1}{2}}$	$\sqrt{\frac{1}{3}}$	$\sqrt{\frac{1}{5}}$	$\sqrt{\frac{1}{10}}$	$\sqrt{\frac{1}{30}}$	
$F'=2$	-1	$\sqrt{\frac{1}{12}}$	$\sqrt{\frac{1}{8}}$	$\sqrt{\frac{1}{8}}$	$\sqrt{\frac{1}{12}}$		5/12
	0	$-\sqrt{\frac{1}{6}}$	$-\sqrt{\frac{1}{24}}$	0	$\sqrt{\frac{1}{24}}$	$\sqrt{\frac{1}{6}}$	
	1		$-\sqrt{\frac{1}{12}}$	$-\sqrt{\frac{1}{8}}$	$-\sqrt{\frac{1}{8}}$	$-\sqrt{\frac{1}{12}}$	
$F'=1$	-1	$\sqrt{\frac{1}{20}}$	$\sqrt{\frac{1}{40}}$	$\sqrt{\frac{1}{120}}$			1/12
	0		$\sqrt{\frac{1}{40}}$	$\sqrt{\frac{1}{30}}$	$\sqrt{\frac{1}{40}}$		
	1			$\sqrt{\frac{1}{120}}$	$\sqrt{\frac{1}{40}}$	$\sqrt{\frac{1}{20}}$	

TABLE A.6: *Clebsch-Gordan coefficients for* ^{87}Rb $F=2$

		$F=1, m_F = m'_F - \epsilon$			
	q	-1	0	1	$\sum_{m_F} \lvert\mu\rvert^2$
$F'=2$	-1	$\sqrt{\frac{1}{24}}$	$\sqrt{\frac{1}{8}}$	$\sqrt{\frac{1}{4}}$	5/12
	0	$-\sqrt{\frac{1}{8}}$	$-\sqrt{\frac{1}{6}}$	$-\sqrt{\frac{1}{8}}$	
	1	$\sqrt{\frac{1}{4}}$	$\sqrt{\frac{1}{8}}$	$\sqrt{\frac{1}{24}}$	
$F'=1$	-1	$\sqrt{\frac{5}{24}}$	$\sqrt{\frac{5}{24}}$		5/12
	0	$-\sqrt{\frac{5}{24}}$	0	$\sqrt{\frac{5}{24}}$	
	1		$-\sqrt{\frac{5}{24}}$	$-\sqrt{\frac{5}{24}}$	
$F'=0$	-1	$\sqrt{\frac{1}{6}}$			1/6
	0		$\sqrt{\frac{1}{6}}$		
	1			$\sqrt{\frac{1}{6}}$	

TABLE A.7: *Clebsch-Gordan coefficients for* ^{87}Rb $F=1$

Appendix B

Pump-Probe Model with Optical Pumping

The saturated absorption model presented in Chapter 3 does not accurately predict the spectrum for Rubidium 85 as it does not take into account the effect of optical pumping. When an atom initially in a specific ground state is excited to an upper level which has the probability of decaying to other ground states, the population in the original ground state is reduced thus decreasing absorption.

To model such behaviour, we treat Rubidium as a 4-level system, so that all of the m_F levels are degenerate and the pump and probe beams are unpolarized. The ground state is labeled $|0\rangle$ and the excited states $|i\rangle$, where i can be 1, 2 or 3. The excited states decay at a rate Γ_i. Each excited state decays at the same rate and the statistical fraction of atoms which decay into state $|0\rangle$ is

$$\Gamma_{i0} = \frac{|\mu_{i0}|^2}{|\mu_{i0}|^2 + |\mu_{ix}|^2}\gamma = \Gamma_i - \Gamma_{ix} \tag{B.1}$$

Where μ_{i0} is the Clebsch-Gordan Coefficient (CGC)[1] for the transition $0 \rightarrow i$ and μ_{ix} is, similarly, the coefficient for loss into other, non-specific, dark states which we label

[1]
$$|\mu_{i0}|^2 = |\mu_{F\rightarrow F'}|^2 = \sum_{q=-1}^{1}\sum_{m_F=-F}^{F} |\langle F', m'_F = m_F + q|\mu, q|F, m_F\rangle|^2 \tag{B.2}$$

where q is the photon polarization; $-1, 0, 1$ for σ^-, π^0 and σ^+ respectively.

$|x\rangle$ (This, in Rb, would be the uncoupled ground state). For a closed transition $\Gamma_{i0} = \gamma$. We have summed the CGCs over all m_F states and polarizations and γ is the natural decay rate. We label the pumping rate,

$$B_{0i} = I_{pump}\frac{2\sigma(\omega, v)}{\hbar\omega_0} \tag{B.3}$$

where I_{pump} is the pump intensity and

$$\sigma(\omega, v) = \frac{\pi e^2\omega_0}{\hbar\epsilon_0 c}|\mu_{i0}|^2\left\{\frac{1}{\pi}\frac{\gamma/2}{(\omega - \omega_{i0} - kv)^2 + \left(\frac{\gamma}{2}\right)^2}\right\} = \sigma_0|\mu_{i0}|^2 L_i(\omega, v) \tag{B.4}$$

The part of Eqn B.4 in curly brackets is the normalised Lorentzian lineshape, $L_i(\omega, v)$, around the resonance frequency ω_{0i}. We take the lifetime of the ground state to be the reciprocal of the transit time, $\Gamma_0 = 1/\tau_{tr}$. In a degenerate two-level system[2] the stimulated absorption and emission pumping rate are equal, $B_{0i} = B_{i0}$.

We would like to find the difference of the ground state populations to the excited states, as previously done in Eqn 3.41:

$$\Delta N = N_0 - N_1 - N_2 - N_3. \tag{B.5}$$

We must first outline the rate equations for each level

$$\begin{aligned}
\frac{dN_0}{dt} &= -N_0(B_{01} + B_{02} + B_{03} + \Gamma_0) + N_1(B_{01} + \Gamma_{10}) \\
&\quad + N_2(B_{02} + \Gamma_{20}) + N_3(B_{03} + \Gamma_{30}) + n^0\Gamma_0 && \text{(B.6)} \\
\frac{dN_1}{dt} &= B_{01}N_0 - N_1(B_{01} + \Gamma_1) && \text{(B.7)} \\
\frac{dN_2}{dt} &= B_{02}N_0 - N_2(B_{02} + \Gamma_2) && \text{(B.8)} \\
\frac{dN_3}{dt} &= B_{03}N_0 - N_3(B_{03} + \Gamma_3) && \text{(B.9)}
\end{aligned}$$

where n^0 is the population of the ground state with no pumping. We have assumed that the excited states all decay before they leave the beams and that $\hbar\omega_{0i}$ is much greater than the thermal energy of the atoms. The steady state solutions ($\frac{dN_0}{dt} = \frac{dN_1}{dt} = \frac{dN_2}{dt} =$

[2]We shall assume that the frequency separation between excited states is much greater than the spectral width of the pumping beam and the scan rate of the laser is much slower than any radiative processes.

$\frac{dN_3}{dt} = 0$) of Eqns B.7, B.8 and B.9 depend only on the individual excited state and the ground state, so that we may substitute them into the steady state solution of Eqn B.6:

$$\begin{aligned} N_0(B_{01} + B_{02} + B_{03} + \Gamma_0) &= \left(\frac{B_{01}N_0}{B_{01} + \Gamma_1}\right)(B_{01} + \Gamma_{10}) \\ &+ \left(\frac{B_{02}N_0}{B_{02} + \Gamma_2}\right)(B_{02} + \Gamma_{20}) \\ &+ \left(\frac{B_{03}N_0}{B_{03} + \Gamma_3}\right)(B_{03} + \Gamma_{30}) \\ &+ \Gamma_0 n^0 \end{aligned} \tag{B.10}$$

We can rearrage Eqn B.10 to find N_0 and divide through by Γ_0 to find

$$N_0 = \frac{n^0}{1 + \left(\frac{\Gamma_{1x}}{\Gamma_0}\right)\left(\frac{1}{1+\Gamma_1/B_{01}}\right) + \left(\frac{\Gamma_{2x}}{\Gamma_0}\right)\left(\frac{1}{1+\Gamma_2/B_{02}}\right) + \left(\frac{\Gamma_{3x}}{\Gamma_0}\right)\left(\frac{1}{1+\Gamma_3/B_{03}}\right)}. \tag{B.11}$$

To find ΔN we can substitute the steady state solutions of Eqns B.7, B.8 and B.9 into Eqn B.5.

$$\Delta N(\omega, v) = N_0\Big(1 - \frac{1}{1 + \Gamma_1/B_{01}} - \frac{1}{1 + \Gamma_2/B_{02}} - \frac{1}{1 + \Gamma_3/B_{03}}\Big). \tag{B.12}$$

We finally come to our result for the population difference in a four-level system by substituting Eqn B.11 into Eqn B.12.

$$\Delta N(\omega, v, \Gamma_0) = \frac{n^0\Big(1 - \frac{1}{1+\Gamma_1/B_{01}} - \frac{1}{1+\Gamma_2/B_{02}} - \frac{1}{1+\Gamma_3/B_{03}}\Big)}{1 + \left(\frac{\Gamma_{1x}}{\Gamma_0}\right)\left(\frac{1}{1+\Gamma_1/B_{01}}\right) + \left(\frac{\Gamma_{2x}}{\Gamma_0}\right)\left(\frac{1}{1+\Gamma_2/B_{02}}\right) + \left(\frac{\Gamma_{3x}}{\Gamma_0}\right)\left(\frac{1}{1+\Gamma_3/B_{03}}\right)} \tag{B.13}$$

This equation does not lead to any further insight of the mechanics of optical pumping but allows us to make quite accurate predictions of the pump-probe spectra.

As derived in Chapter 3. we wish to find the absorption coefficient

$$\alpha(\omega, \Gamma_0) = N_V n^0 \int f_D(v)\Delta N(\omega, v, \Gamma_0)\Big(\sum_i |\mu_{i0}|^2 L_i(\omega, -v)\Big)dv \tag{B.14}$$

where $f_D(v)$ is the Doppler broadening from Eqn 3.12. We have intentionally placed a dependence upon the transit time as this factor can have an effect upon the spectra, as noted in Reference [60]. We treat the beam profile as a top hat shape of diameter d and

describe the transit times by the Maxwell Boltzmann speed distribution

$$g(s) = 4\pi\Big(\frac{M}{2\pi k_B T}\Big)^{3/2} s^2 \exp -\frac{Ms^2}{2k_B T} \tag{B.15}$$

where the speed can be converted to transit time by $s \Rightarrow \phi\Gamma_0$. Our final equation for the pump-probe spectra is

$$\frac{I_{probe}(l)}{I_{probe}(0)} = \exp\Big(- l \int g(\phi\Gamma_0)\alpha(\omega, \phi\Gamma_0) d\Gamma_0 \Big) \tag{B.16}$$

To calculate the spectra for ^{85}Rb and ^{87}Rb for Figure 3.9 the values in Table B.1 were used.

One may notice that the probe intensity used in this model is much weaker than the usual quoted value of the saturation intensity and yet the spectra show strong Lamb dips. This signifies that optical pumping has an important role and that one must use a very weak probe beam in order to not overly affect the populations. We have actually included the effect of the probe beam into Figure 3.9 by splitting the pump parameter B_{0i}

$$B_{0i} = \frac{2\sigma_0}{\hbar\omega_0}|\mu_{i0}|^2\big(I_{pump}L_i(\omega, v) + I_{probe}L_i(\omega, -v)\big) \tag{B.17}$$

We have set the probe intensity to $0.01I_S$. If we increase the probe intensity we see the ^{85}Rb peaks a, b and c increase and peaks d, e and f decrease. This is of course due to further optical pumping but has the effect of matching the model to the experimental results more accurately. This may be due to some probe pumping or back reflections of the strong pump from the vapour cell windows.

To compare the effect of optical pumping with that of saturation, Figure B.1 displays the measured pump-probe spectra to a saturation-only model and saturation *and* optical pumping model for equal experimental parameters. The saturation-only case has very weak Lamb dips of which only the closed transition and related crossover peaks are significant. The optical pumping model closely matches the measured data.

[3]Table B.1. We must equally distribute the natural populations between the two ground states which are normalised by the total number of ground m_F states and the natural abundance. ^{85}Rb F=3 has $2F + 1$ m_F states, so that the natural population is $(0.7217)\frac{7}{7+5}$, where F2 has 5 m_F states and the isotope occurs in 72.17% of natural Rubidium. In Eqn B.4 we are summing over each m_F state to calculate the dipole matrix element, so we are left with the normalization factor n^0.

	Description	Value ^{85}Rb	Value ^{87}Rb	Ref.
n^0	Ground state natural population[3]	$\frac{0.7217}{5+7}$	$\frac{0.2783}{3+5}$	
N_V	Number density	$\simeq 10^{15}$ (Temp dependent, see Ref.)		[46]
l	Vapour cell length	7.5cm		Measured
γ	Natural decay rate	$2\pi \cdot 6.063$MHz		[54]
Γ_i	Total excited state decay rate	γ		
Γ_{10}	Fractional decay of excited state	$\langle F=3\|1\gamma\|F'=4\rangle$	$\langle F=2\|1\gamma\|F'=3\rangle$	Eqn A.9
Γ_{20}	”	$\langle F=3\|0.556\gamma\|F'=3\rangle$	$\langle F=2\|0.5\gamma\|F'=2\rangle$	”
Γ_{30}	”	$\langle F=3\|0.222\gamma\|F'=2\rangle$	$\langle F=2\|0.167\gamma\|F'=1\rangle$	”
μ_{01}	Dipole matrix element	$\langle F'=4\|\sqrt{4.50}\mu_{85}\|F=3\rangle$	$\langle F'=3\|\sqrt{3.50}\mu_{87}\|F=2\rangle$	”
μ_{02}	”	$\langle F'=3\|\sqrt{1.94}\mu_{85}\|F=3\rangle$	$\langle F'=2\|\sqrt{1.25}\mu_{87}\|F=2\rangle$	”
μ_{03}	”	$\langle F'=2\|\sqrt{0.56}\mu_{85}\|F=3\rangle$	$\langle F'=1\|\sqrt{0.25}\mu_{87}\|F=2\rangle$	”
$\mu_{85/87}$	Reduced dipole element	$4.2263\ a_0$		Eqn. A.7
a_0	Bohr radius	0.0529 nm		[174]
M	Atomic mass	85.912 a.m.u	86.909 a.m.u	[175]
T	Temperature	290K		Measured
I_{pump}	Pump intensity	$0.1I_S$		Measured
I_S	Saturation intensity	1.6mWcm^{-2}		Eqn. 3.43
ω_0	Transition frequency	$2\pi \cdot 384.230$ THz		[49]
ω_{01}	”	a	g	Tab. A.3
ω_{02}	”	d	j	”
ω_{03}	”	f	l	”
ϕ	Beam diameter	3mm		Measured

TABLE B.1: *Values used for the optical pumping model in Figure 3.9. ["] means 'same as above'.*

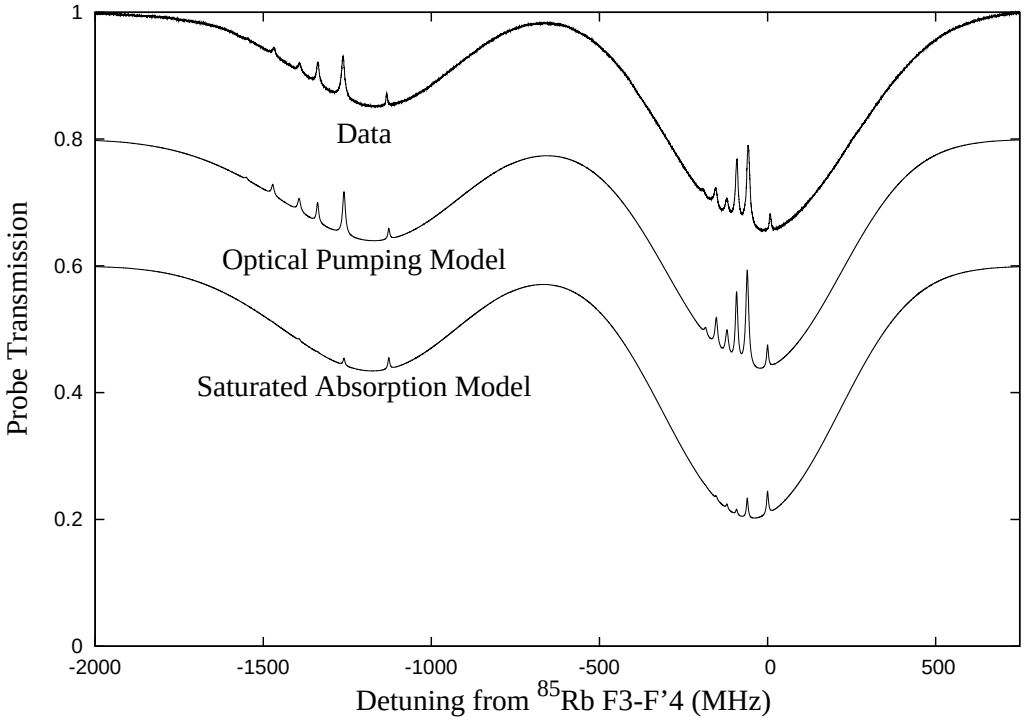

FIGURE B.1: *Comparison of measured spectrum (top) with theoretical models including (middle) and not including (bottom) optical pumping with saturation. The modelled curves have been offset for clarity. The power of the pump beam has been adjusted in the model to achieve the closest agreement of the data and optical pumping model but is not significantly different from the actual intensity (within a factor of 2). The plot signifies the importance of optical pumping in pump probe spectra where saturation is commonly thought to be the main effect.*

Appendix C

Density Matrix Equations

It is difficult to calculate the effects of a light field interacting with an ensemble of atoms with a wavefunction approach as the atoms may decay from a thermal distribution of excited states into a vast number of modes which need to be accounted for with a fully quantized field theory. The more common approach is to calculate the statistical properties of the ensemble with a semiclassical model in which the atom is quantized and the field is classical. This is a standard text-book derivation, so presented here is a brief overview of the important points. We start by adapting the standard wavefunction description of atomic states into a statistical picture with the density operator and then solving the interaction between a two-level atom and a monochromatic laser field.

In the dipole approximation, in which the incident field does not vary significantly across the atomic dimensions, we may describe the state of a multilevel atom as a linear superposition of eigenfunctions for each state weighted by temporal, C_k and a spatial ψ_k amplitudes:

$$\Psi(\vec{r},t) = \sum_k C_k(t)\psi_k(\vec{r})e^{-i\frac{E_k}{\hbar}t} \tag{C.1}$$

The nomenclature is simplified with the Dirac Bra-Ket notation:

$$\Psi(t) = |\Psi\rangle = \sum_k C_k(t)|k\rangle \tag{C.2}$$

where we have neglected any spatial variation of the wavefunction and assume the system to be normalised, $\sum_k C_k(t) = 1$. Therefore a two-level wavefunction is

$$|\Psi\rangle = C_g(t)|g\rangle + C_e(t)|e\rangle \tag{C.3}$$

where $|g\rangle$ and $|e\rangle$ are the ground and excited states, respectively. The time evolution of this system obeys the time dependent Schrödinger equation (TDSE).

$$i\hbar\frac{\mathrm{d}}{\mathrm{dt}}|\Psi\rangle = \mathscr{H}|\Psi\rangle \tag{C.4}$$

where $\hat{\mathscr{H}} = \hat{\mathscr{H}_0} + \hat{\mathscr{H}_I}$ is the Hamiltonian operator which describes the time evolution of the pure (unperturbed) state energies

$$\hat{\mathscr{H}_0} = \begin{pmatrix} E_g & 0 \\ 0 & E_e \end{pmatrix} \tag{C.5}$$

with $E_e \gg E_g$, and the Hamiltonian of the interaction energy

$$\hat{\mathscr{H}_I} = -\hat{\mu}\cdot\mathscr{E}(t) \tag{C.6}$$

where the interacting monochromatic field of amplitude $\mathscr{E}_0$ and frequency ω is

$$\mathscr{E}(t) = \frac{\mathscr{E}_0}{2}\{e^{-i\omega t} + e^{i\omega t}\}. \tag{C.7}$$

The dipole moment operator $\hat{\mu}$ determines the coupling between states $|g\rangle$ and $|e\rangle$ as shown in Section 3.2.3 and Appendix A. We have assumed the polarization of $\mathscr{E}(t)$ has be absorbed into the dipole matrix elements:

$$\langle\Psi|\hat{\mu}|\Psi\rangle = C_e^* C_g\langle e|\mu_{ge}|g\rangle + C_g^* C_e\langle g|\mu_{eg}|e\rangle \tag{C.8}$$

where $\langle g|\mu_{gg}|g\rangle = \langle e|\mu_{ee}|e\rangle = 0$. As $\mu_{ge} = \mu_{eg}$ the dipole moment may also be written as

$$\hat{\mu} = \mu_{ge}\big(|g\rangle\langle e| + |e\rangle\langle g|\big) \tag{C.9}$$

We can think of $|g\rangle\langle e|$ as the lowering operator from $|e\rangle$ to $|g\rangle$ and $|e\rangle\langle g|$ as the raising

operator from $|g\rangle$ to $|e\rangle$. If we expand Equation C.6 in terms of Equations C.7 and C.9 we find

$$\begin{aligned}\hat{\mu}\cdot\mathscr{E}(t) &= \frac{\mathscr{E}_0\mu_{ge}}{2}\big(|g\rangle\langle e| + |e\rangle\langle g|\big)\cdot\left\{e^{-i\omega t} + e^{i\omega t}\right\} \\ &= \frac{\mathscr{E}_0\mu_{ge}}{2}\Big(|g\rangle\langle e|e^{-i\omega t} + |g\rangle\langle e|e^{i\omega t} + |e\rangle\langle g|e^{-i\omega t} + |e\rangle\langle g|e^{i\omega t}\Big) \qquad \text{(C.10)}\end{aligned}$$

The exponential terms $e^{-i\omega t}$ and $e^{i\omega t}$ can be thought of as the absorption and emission of a photon, respectively. We can then see that the first and last terms in the brackets of C.10 are negligible with respect to the other two terms. The term $|g\rangle\langle e|e^{-i\omega t}$ describes the absorption of a photon lowering the state from $|e\rangle$ to $|g\rangle$. As $E_e \gg E_g$ this term is very unlikely to occur, likewise considerations mean we can also neglect $|e\rangle\langle g|e^{i\omega t}$. This is known as the *Rotating Wave Approximation* as we neglect these terms, thus also removing components oscillating at $\omega + \omega_0$ (where $\omega_0 = (E_e - E_g)/\hbar$) which is too fast to have any influence on the transition.

We can now state our interaction Hamiltonian in its final form

$$\mathscr{H}_I = \frac{\hbar}{2}\begin{pmatrix} 0 & \Omega^* e^{i\omega t} \\ \Omega e^{-i\omega t} & 0 \end{pmatrix} \qquad \text{(C.11)}$$

where Ω is the Rabi frequency

$$\Omega = \frac{\mu_{eg}\mathscr{E}_0}{\hbar} \qquad \text{(C.12)}$$

We would like to find the probability of an atom being in a specific state of the system, and to do this we use the density operator. The density operator is defined as the inner product of the wavefunction $\hat{\rho} = |\Psi\rangle\langle\Psi|$ and we may find the projection of the wavefunction onto the basis set of eigenfunctions with the *density matrix*; whose components are

$$\rho_{ik} = C_k^* C_i = \langle i|\hat{\rho}|k\rangle \qquad \text{(C.13)}$$

The populations in the pure states (diagonal components) and the coherences (off-diagonal elements) are defined as

$$\rho = \begin{pmatrix} \rho_{gg} & \rho_{ge} \\ \rho_{eg} & \rho_{ee} \end{pmatrix} \tag{C.14}$$

The equation of motions of the states is described by the Liouville variant of the time dependent Schrödinger equation (TDSE),

$$i\hbar\dot{\rho} = [\mathscr{H}, \rho] \tag{C.15}$$

Substituting ρ and the Hamiltonian into the TDSE[1]

$$\mathscr{H}_0 + \mathscr{H}_I = \begin{pmatrix} E_g & \frac{\hbar\Omega^*}{2}e^{i\omega t} \\ \frac{\hbar\Omega}{2}e^{-i\omega t} & E_e \end{pmatrix} \tag{C.18}$$

results in the rate of change of the state and coherent populations

$$\dot{\rho}_{gg} = \frac{i}{2}\Omega\rho_{ge}e^{-i\omega t} - \frac{i}{2}\Omega^*\rho_{eg}e^{i\omega t} + \gamma\rho_{ee} \tag{C.19}$$

$$\dot{\rho}_{ee} = \frac{i}{2}\Omega^*\rho_{eg}e^{i\omega t} - \frac{i}{2}\Omega\rho_{ge}e^{-i\omega t} - \gamma\rho_{ee} \tag{C.20}$$

$$\dot{\rho}_{ge} = i\rho_{ge}\omega_0 - \frac{i}{2}\Omega^*e^{i\omega t}(\rho_{ee} - \rho_{gg}) - \frac{\gamma}{2}\rho_{ge} \tag{C.21}$$

$$\dot{\rho}_{eg} = -i\rho_{eg}\omega_0 + \frac{i}{2}\Omega e^{-i\omega t}(\rho_{ee} - \rho_{gg}) - \frac{\gamma}{2}\rho_{eg}. \tag{C.22}$$

We have also included the decay terms phenomenologically. γ is the natural decay rate of state $|e\rangle$ and we assume that state $|g\rangle$ is the lowest ground state and does not decay via spontaneous emission. The $\gamma/2$ terms in the coherences are known as the transverse relaxation rates. We can remove the fast rotating terms in the exponentials by transforming into the rotating frame via the following substitutions (know as the

[1] The Matrix algebra result for expanding the TDSE is (shown here for reference)

$$\begin{pmatrix} a & b \\ c & d \end{pmatrix}\begin{pmatrix} e & f \\ g & h \end{pmatrix} - \begin{pmatrix} e & f \\ g & h \end{pmatrix}\begin{pmatrix} a & b \\ c & d \end{pmatrix} \tag{C.16}$$

$$= \begin{pmatrix} bg - fc & f(a-d) + b(h-e) \\ c(e-h) + g(d-a) & cf - gb \end{pmatrix} \tag{C.17}$$

slow variables)

$$\tilde{\rho}_{ge} = \rho_{ge}e^{-i\omega t} \tag{C.23}$$

$$\tilde{\rho}_{eg} = \rho_{eg}e^{i\omega t} \tag{C.24}$$

$$\tilde{\rho}_{gg} = \rho_{gg} \tag{C.25}$$

$$\tilde{\rho}_{ee} = \rho_{ee} \tag{C.26}$$

We have now arrived at the Bloch equations by making the above substitutions

$$\dot{\tilde{\rho}}_{gg} = -\frac{i\Omega}{2}(\tilde{\rho}_{eg} - \tilde{\rho}_{ge}) + \gamma\tilde{\rho}_{ee} \tag{C.27}$$

$$\dot{\tilde{\rho}}_{ee} = \frac{i\Omega}{2}(\tilde{\rho}_{eg} - \tilde{\rho}_{ge}) - \gamma\tilde{\rho}_{ee} = -\dot{\tilde{\rho}}_{gg} \tag{C.28}$$

$$\dot{\tilde{\rho}}_{ge} = -i\tilde{\rho}_{ge}\delta - \frac{i\Omega}{2}(\tilde{\rho}_{ee} - \tilde{\rho}_{gg}) - \frac{\gamma}{2}\tilde{\rho}_{ge} \tag{C.29}$$

$$\dot{\tilde{\rho}}_{eg} = i\tilde{\rho}_{eg}\delta + \frac{i\Omega}{2}(\tilde{\rho}_{ee} - \tilde{\rho}_{gg}) - \frac{\gamma}{2}\tilde{\rho}_{eg} = \dot{\tilde{\rho}}^{*}_{ge} \tag{C.30}$$

where $\delta = \omega - \omega_0$ and assuming $\Omega^* = \Omega$ is real [2] We can find the steady-state values of the populations and coherences by setting the time derivatives to zero:

$$\tilde{\rho}_{ee} = \frac{i\Omega}{2\gamma}(\tilde{\rho}_{eg} - \tilde{\rho}_{ge}) \tag{C.31}$$

$$\tilde{\rho}_{ge} = \frac{i\Omega}{2}\frac{\tilde{\rho}_{gg} - \tilde{\rho}_{ee}}{\gamma/2 + i\delta} = \tilde{\rho}^{*}_{eg}. \tag{C.32}$$

By conserving populations, $\tilde{\rho}_{gg} + \tilde{\rho}_{ee} = 1$, and solving for $\tilde{\rho}_{ee}$ and $\tilde{\rho}_{eg}$,

$$\tilde{\rho}_{ee} = \frac{\Omega^2}{4}\frac{1}{\delta^2 + \frac{1}{4}\gamma^2 + \frac{1}{2}\Omega^2} \tag{C.33}$$

$$\tilde{\rho}_{eg} = \frac{\Omega}{4}\frac{\delta + i\gamma}{\delta^2 + \frac{1}{4}\gamma^2 + \frac{1}{2}\Omega^2} \tag{C.34}$$

It can be shown [99] that the steady state solution of the coherence, Equation C.34, is proportional to the atomic susceptibility, where the real part is the refractive index and the imaginary part is the absorption coefficient.

[2] This is true in the case of a single field acting upon a two state system. When more fields and states are included, the relative phases between the Rabi frequencies become important.

Appendix D

Electronics and Programs

D.0.1 Control Theory

Control theory is a vast and fascinating field that cannot be sufficiently covered in such a short section. We shall merely dip our toes into the basics from which we can understand the fundamental processes in our servo system. The mathematics of control theory has its roots in Laplace transforms and so we start with the formal definition[1],

$$F(s) = \mathcal{L}\{f(t)\} = \int_0^\infty e^{-st} f(t) dt \tag{D.1}$$

where the time-dependent function $f(t)$ is real valued and $t \geq 0$. Here we have transformed some function $f(t)$ which may describe the dynamics of a system into a function of a complex variable $s = \rho + i\omega$. The reason behind applying a Laplace transform is that it converts differential and integral equations into polynomial equations of s. For example;

$$\mathcal{L}\{\frac{d}{dt} f(t)\} = \int_0^\infty \frac{d}{dt} e^{-st} f(t) dt = sF(s) \tag{D.2}$$

Similarly, integration becomes a division by s: $\mathcal{L}\{\int f(t)\} = F(s)/s$.

We can see that a complex system which contains high order differential variables can

[1]We assume the function $f(t \leq 0) = 0$ and that we are dealing with the *unilateral* Laplace transform which refers to $t = 0 \rightarrow \infty$. We can 'transform' this into the Fourier transform by using the *bilateral* form (i.e. integrating between $-\infty$ and ∞) and explicitly using just the complex component of s. If fact, the Laplace transform is a generalized Fourier transform as it takes into account the full complex plane, s

be simply treated as a variable to the nth order of s. The function $F(s)$ can be returned to the time domain by the inverse Laplace transform. The most common example is the low pass RC filter, where the first-order temporal response is

$$RC\frac{d}{dt}v_{out}(t) = v_{in}(t) - v_{out}(t). \tag{D.3}$$

Performing the Laplace transform we find,

$$\frac{s}{\omega_0}V_{out}(s) = V_{in}(s) - V_{out}(s) \tag{D.4}$$

where $1/RC = \omega_0 = 2\pi f_0$ is the cut-off frequency of the filter. Rearranging we get,

$$G(s) = \frac{V_{out}}{V_{in}} = \frac{1}{1 + s/\omega_0} \tag{D.5}$$

The gain of the filter $G(s)$ is also called the 'control law' which is applied to the input signal. To explicitly show the filter's frequency response we use the substitution $s = i\omega$,

$$|G(i\omega)| = \frac{1}{\sqrt{1 + \omega^2/\omega_0^2}} \tag{D.6}$$

$$\phi = \arg G(i\omega) = \tan^{-1}\frac{\omega}{\omega_0} \tag{D.7}$$

where ϕ is the phase.

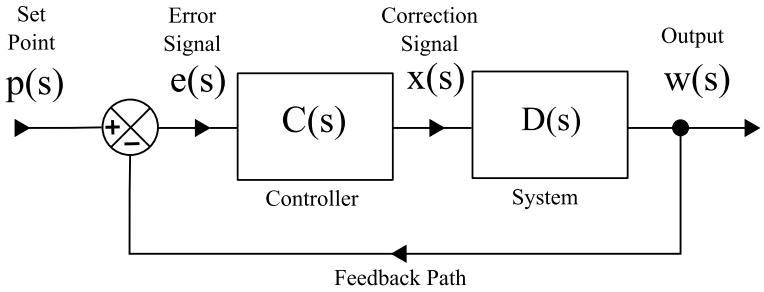

FIGURE D.1: *Block diagram of a basic control system featuring a feedback loop.*

The above example describes the 'open-loop gain' of a system. To understand the effect of feedback in controlling a system,we consider taking a portion of the output and feeding it back into the input, thus 'closing the loop'. Block diagrams come in as extremely useful when describing complicated process paths. Figure D.1 shows a simple feedback system. The output, $w(s)$, of a system $D(s)$ is compared with a 'set point'

$p(s)$, the difference is called the 'error' $e(s) = p(s) - w(s)$. The error signal is passed through some control element $C(s)$ (such as an amplifier), the output of which $x(s)$ is passed back to the system under control. Without knowledge of the specifics of the system or controller, we can multiply the gain of each to obtain the overall open-loop gain, $L_{open}(s) = D(s)C(s)$. The effect on the output is $w(s) = L_{open}(s)e(s)$. Expanding the function for $e(s)$ and solving for $w(s)$, we find the closed-loop dynamics,

$$w(s) = \frac{D(s)C(s)}{1 + D(s)C(s)} p(s) = L_{closed}(s)p(s) \tag{D.8}$$

One must now decide upon the characteristics of control element $C(s)$ so as to reduce the error $e(s)$ and stabilize the system dynamics $D(s)$. This is a very simplified schematic of real systems. The beauty of using block diagrams and Laplace transformation is that one can keep adding in 'blocks' to represent the real setup (See Figure D.2 for the block diagram of the laser stabilization).

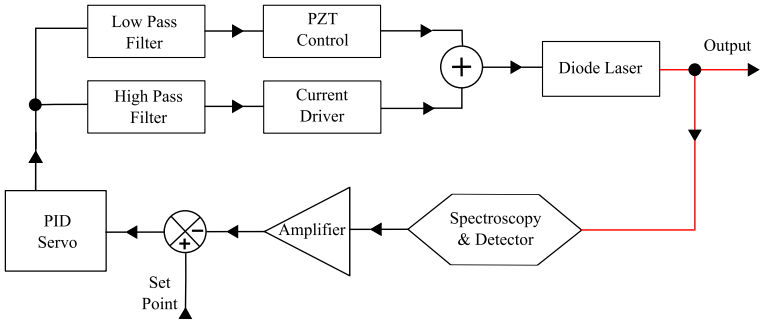

FIGURE D.2: *Block diagram of the Laser stabilization setup. The red line indicates the laser beam path whereas the black line represents the electrical path. The PZT and current controllers convert the electrical correction signal into frequency correction of the laser. The laser block represents the system dynamics of the laser itself, such as linewidth, intensity noise and phase noise. The spectroscopy block converts the frequency signal back into an electrical signal characteristic of the FMS lineshape.*

D.1 Grating Peizo-Transducer Circuit

The piezo driver is based around the datasheet circuit diagram for the XR8038 frequency synthesizer chip (unfortunately no longer manufactured). The modulation frequency is set by C2 and VR4 (front panel potentiometer) according to $f = 1/2\pi C2 \cdot VR4$. VR5 (PCB trimmer) adjusts the duty cycle. Pin 9 outputs a square wave which is used for

triggering. Pin 3 outputs a triangle wave, the amplitude of which is controlled by VR2. In order to achieve the largest ramp amplitude with ±15 V supplies, OUT1 and OUT2 are referenced to the negative rail and not ground. IC2 and IC3 are output buffers and provide a DC offset to the ramp. There are two outputs to provide piezo control to two lasers (Trapping and Repump). Not shown on the schematic are the low frequency error signals from the PID circuit (see section 1.3). These are buffered and summed into IC2 and IC3. Another circuit change is a two-pole 1kHz low pass filter added at the output to filter low frequency pickup on the PZT. This addition noticeably reduced the noise on the Raman pulse data.

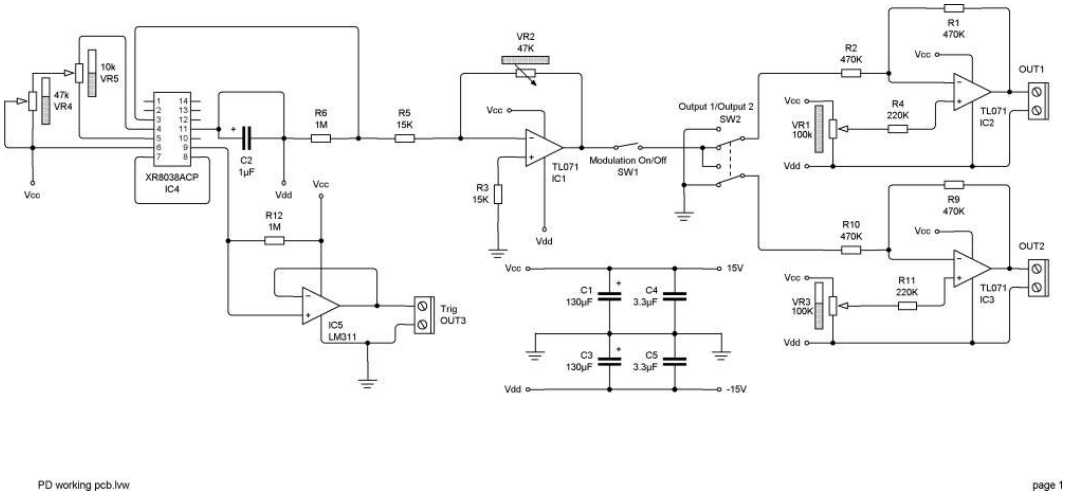

FIGURE D.3: *Piezo driver schematic*

D.2 RF Modulation Circuit

The modulation circuit is mainly based on 'Minicircuits' [176] components (Figure D.4). The choice of modulation frequency was due to the separation between the resonance line and the nearest crossover so as not to overlap sidebands and distort the feature. The range of 12-30MHz was chosen. To cover this range, the modulation frequency was supplied by two voltage controlled oscillators (VCOs, POS-25 & POS-50). The normal operating frequency is around 20MHz using POS-25.

The output of the VCO is passed through a power splitter to separate and decouple the diode modulation and mixer reference. To ensure the correct signal strength each path

is amplified, but this was found to be unnecessary and both amplifiers were subsequently bypassed. The laser drive current is modulated with a Bias-Tee (PBTC-1-G).

A phase shifter is commonly used to adjust the phase of the local oscillator input of the mixer to correct the shape of the FM signal. In the MHz range this can be as simple as increasing the length of the BNC cable between the VCO and Mixer, this is allowed for with BNC connectors on the rear of the PCB. Practically, we found it easier to tune the modulation frequency to account for the phase difference.

The RF spectroscopy signal is mixed with the local oscillator reference using a SBL-3 mixer. The output goes through a low-pass filter to remove the high-frequency components. The design of the circuit board takes account of good RF practice by having a large copper 'pour' area as a ground plane, no co-propagating signal lines close together and capacitive decoupling of the power line at each component. The circuit is then housed in a RF shielded 19" rack plug-in unit. Possible improvements include minimizing the components by removing the unused VCO and amplifiers. The spectroscopy signal may also benefit from a bandpass filter to remove excess noise onto the circuit. As with the PID circuit discussed in the next section, the power supply should have regulation on the PCB.

D.3 PID Circuit

Figure D.5 shows the detailed schematic for the PID servo circuit. The power supply is a regulated DC linear supply with ±15V output. This is connected to the PCB with a filter 9-way D connector. The supply is further filtered with Murata BNX002-01 DC filters. Each operational amplifier (op-amp) has 100 nF power line decoupling capacitors. An improvement to this design would be the addition of voltage regulators at the power supply inputs and 10 μF tantalum capacitors at each op-amp power terminal.

The spectroscopy signal at the input BNC connector is passed through a low-pass filter with a pole at 330 kHz. The differentiator input is picked off here to avoid large output jumps if the set points is altered during lock. The first op-amp acts as a buffer and may be used to amplify the signal. The signal voltage is then compared against a set-point

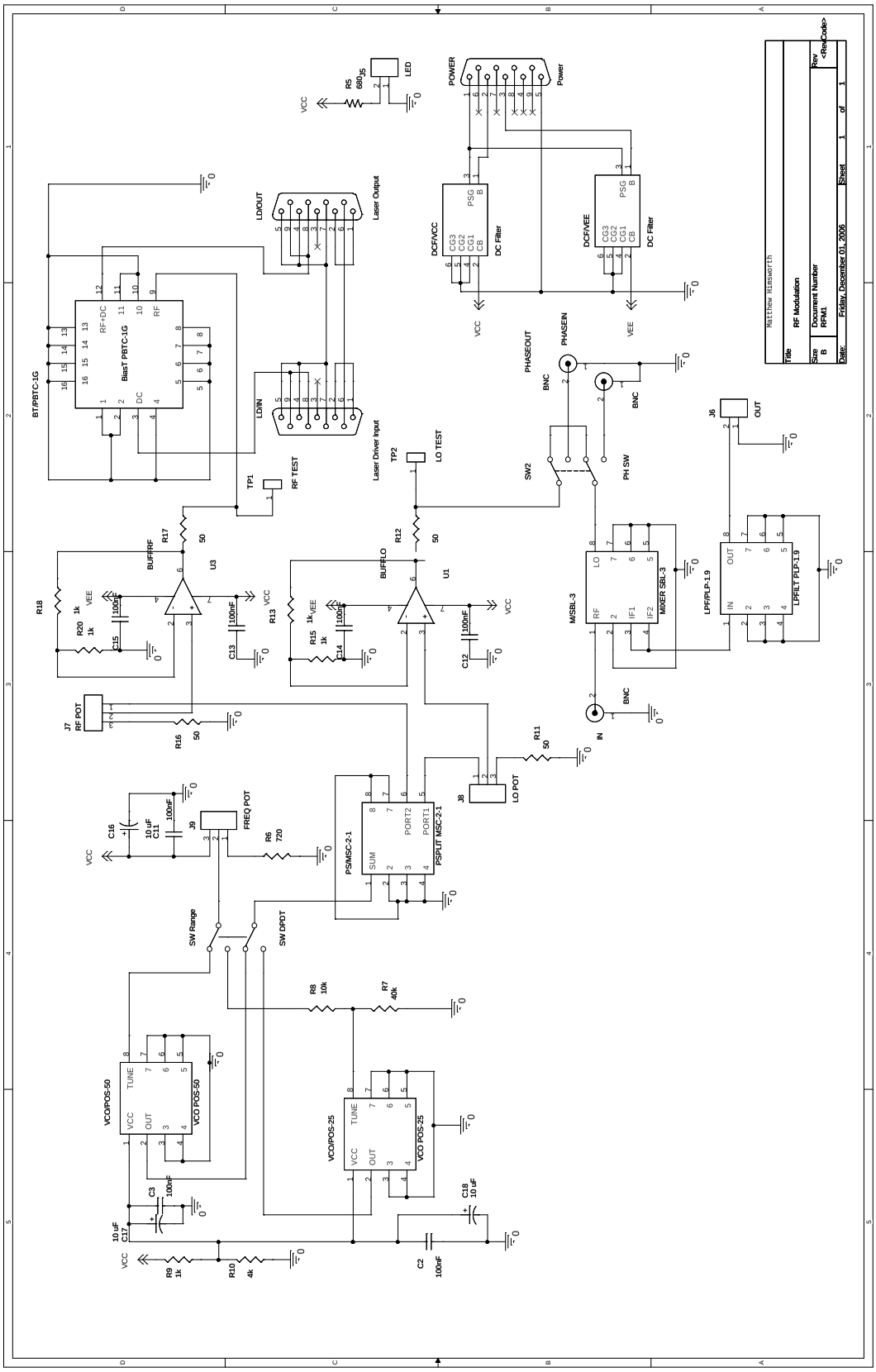

FIGURE D.4: *RF modulation schematic*

voltage with the unitary gain amplifier, OP2, and thus creates the error signal. Another improvement would be to regulate this set-point voltage as any noise would appear as a signal offset. This may be achieved with a voltage regulator or Zener Diode.

The error signal is then fed to the proportional and integral amplifiers and a monitor. The monitor output in this circuit is quite noisy, perhaps due to poor power supply regulation, pickup or set-point error, and must be improved. The proportional control is a standard op-amp amplifier with a maximum gain of 2. The integrator has a time constant of 1.4-15 seconds, although optimum laser stability is at the highest gain (i.e. 1.4 second integration). R14 is a drain resistor to reduce the integral gain at low frequencies to avoid 'wind-up'. J2 resets the integrator when the lock is off.

The differentiator has a variable time constant from 31 ms-20 μs (31 Hz-50 kHz). The high frequency gain is rolled off with R15 and C10 to prevent phase inversion. Practically, the differentiator is normally not used as it does not appear to improve the lock and so must be reconsidered in subsequent designs. The P, I and D controls are summed together with OP7, and the relative gains are set with resistors R17, R18, R19 and R21. The summation output is limited to $\pm$0.7V by diodes D1 and D2 to prevent damage to the laser diode. Resistor R25 is mandatory to avoid shorting the output of OP7 through the diodes. OP8 acts as a buffer and inverter to corrects the polarity of the error signal to the control element. The circuit output was originally taken after OP7, but a frequency divider was added later to separate the low frequency signal for the PZT control and the high frequency signal for the laser drive current. This was added with a piece of 'veroboard' and so must be properly included in new designs. The output may also benefit from a buffer to avoid impedance matching problems.

Overall, the circuit works well as confirmed by the stability results at the end of Chapter 4. For optimum long-term (several hours) stability the lasers need to be encased in a box to prevent drafts as large frequency jumps cannot be handled by the circuit. This is probably due to the voltage limits of the PZT controller. A high voltage ($\simeq$200V) amplifier for the PZT should improve the response.

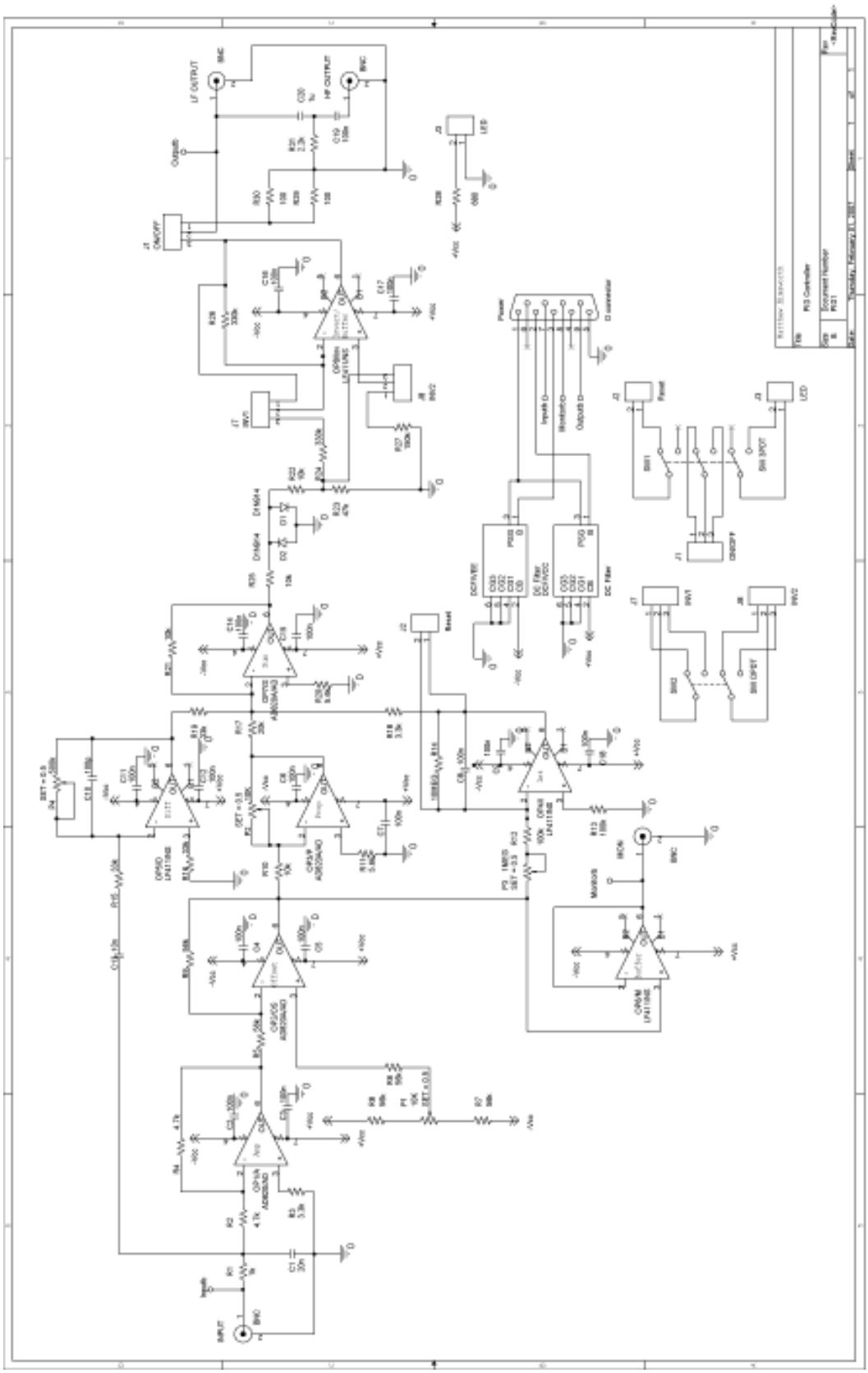

FIGURE D.5: *PID schematic*

D.4 Numerical solutions to the OBEs

In Chapter 8, the data for the spectral and temporal plots of the ground state populations were fitted to a model generated from a numerical solution of the optical Bloch equations in Chapter 6. The numerical solution was achieved in Mathematica using the **NDSolve** function. Below is the code copied straight from Mathematica with added annotations. The first plot generates the temporal curve, the second generates the spectral curve. These are separated because the addition of a second variable (frequency) produces errors in the spectral plot. There is an added decay term, γ, which deals with transverse decay of the coherences, but does not depopulate.

```
x = 1000000 (* This is a pre-factor to cut down the number of iterations that NDSolve can handle *)
\[CapitalOmega] = 2*\[Pi]*1250/x (* Rabi frequency - resonant - in Hertz *)
\[Delta] = -2*\[Pi]*2400/x (* Detuning for the temporal plot  in Hertz *)
\[CapitalGamma] = 2*\[Pi]*150/x (* Longitudinal decay term (depopulation, i.e. single photons  in Hertz*)
\[Gamma] = 2*\[Pi]*220/x (* Transverse decay term (pure dephasing, i.e. collisions)  in Hertz *)
T = 0.001*x (* Temporal plot length in seconds *)
F1 = -2*\[Pi]*10000/x  (* minimum frequency from resonance in spectral plot in Hertz *)
F2 = 2*\[Pi]*6000/x (* maximum frequency from resonance in spectral plot in Hertz *)
F0 = -2*\[Pi]*1800/x (* resonance frequency in spectral plot in Hertz *)
p=0.165 (* maximum population of state *)
data = Import["C:\\rabinoase.csv"]; (* Import temporal data *)
obv = NDSolve[{D[u[t],
     t] == \[Delta]*v[t] - (\[CapitalGamma]/2 + \[Gamma])*u[t],
   D[v[t], t] == -\[Delta]*u[t] + \[CapitalOmega]*
      w[t] - (\[CapitalGamma]/2 + \[Gamma])*v[t],
   D[w[t], t] == -\[CapitalOmega]*v[t] + \[CapitalGamma]*(1 - w[t]),
   v[0] == 0, u[0] == 0, w[0] == 1}, {u, v, w}, {t, 0, T}]
A = Plot[Evaluate[{p*0.5*(1 - w[t])} /. %], {t, 0, T},
   PlotRange -> {-1, 1}, PlotStyle -> RGBColor[1, 0, 0]]; (*Evaluate find the output of NDSolve,
                                                            here we convert to state population *)
B = ListPlot[{data}, Joined -> {False, True},
   PlotRange -> {0.0, 0.04}];
Show[A, B, Frame -> True,
 FrameLabel -> {"Time (\[Mu]s)", "Population"}]
sinc = Import["C:\\sinc2.csv"]; (* Import spectral data *)
sincd = ListPlot[sinc, PlotRange -> {0, 0.2}];
obv = NDSolve[{D[u[f, t],
     t] == (f - F0)*v[f, t] - (\[CapitalGamma]/2 + \[Gamma])*u[f, t],
   D[v[f, t],
     t] == -(f - F0)*u[f, t] + \[CapitalOmega]*
      w[f, t] - (\[CapitalGamma]/2 + \[Gamma])*v[f, t],
   D[w[f, t],
     t] == -\[CapitalOmega]*
      v[f, t] + \[CapitalGamma]*(0.5 - w[f, t]), v[f, 0] == 0,
   u[f, 0] == 0, w[f, 0] == 1}, {u, v, w}, {f, F1, F2}, {t, 0, T}]
sincm = Plot[
   Evaluate[{p*(-0.5*(w[(2*\[Pi]*(f))/1000, 500*10^-6*x] -
          1))} /. %], {f, -10, 5}, PlotRange -> {0.0, 0.2}];
Show[sincm, sincd]
```

D.5 Python Code for the Intensity Variation Model

This model splits the cloud into concentric rings in which the atoms are assume to all experience the same Rabi frequency. Each ring is weighted by its area and the Gaussian distribution of atom number. The resulting signal is then summed over the entire cloud and also over a Gaussian distribution of Rabi frequencies which model an intensity variation over time. The model does not take into account the expansion of the cloud or single photon scatter.

```
from scipy import *
from numpy import *
figure(1)
clf()
h=1.0 #maximum population transfer
P=1000000. #unit denominator, i.e. 1000=milli
R=2000./P # radius of area to sum over, must be greater than cloud size
N=100 # number of steps
cl=(0.5*350/P)/2.35 # 0.5 times cloud diameter (FWHM) divided by P then
#divided by 2.35 (2ln(2))
la=(0.5*0.6*100050/P)/2.35  # 0.5 times laser beam diameter (FWHM)
#divided by P then divided by 2.35 (2ln(2))
lint=0.2+0.000000000001 # fraction variation in time of the total beam intensity
#the small factor is required to avoid a divide by zero error
rint=1.5 #range of intensities to average over for temporal variations
g=5. # number of samples for time intensity variation
f=-2*pi*000. # Raman frequency offset
B=2*pi*2000. # Raman frequency
T=2000.0/P # total time
dat=zeros((N,3))
for i in range(N):
    dat[i,0]=i*(N/100) # time stamp
    dat[i,2]=((B/(sqrt(f**2+B**2)))*sin(0.5*dat[i,0]*sqrt(f**2+B**2)))**2
    # Rabi flopping without decay
    var=zeros((2*g,2)) # variation in time
    for u in range(-g,g,1):
        W=B+(u/g)*(rint*lint*B) # variation of rabi freq with intensity over time
        rab=zeros((N,3))
        for k in range(N):
            rab[k,0]=k*(R/N) #radius
            rab[k,1]=pi*(((R/N)*(k+1))**2-((R/N)*k)**2)*(exp(-((rab[k,0])**2)/(2*(2*(cl))**2)))...
            ...*(1./((2*(cl)))*sqrt(2*pi)) # area of each loop times cloud density
            rab[k,2]=(((W*exp(-(rab[k,0]**2)/(2*(2*la)**2)))/(sqrt(f**2+(W*exp(-(rab[k,0]**2)/...
            ...(2*(2*la)**2)))**2)))*sin(0.5*dat[i,0]*sqrt(f**2+(W*exp(-(rab[k,0]**2)/(2*(2*la)**2)...
            ...))**2)))**2
        var[u,0]=(exp(-((W-B)**2)/(2*((lint*B/2.35)**2)))) # normalizes int var in time
        var[u,1]=(rab[:,2]*rab[:,1]).sum()/(rab[:,1].sum()) # sum over whole cloud radially
    dat[i,1]=(var[:,0]*var[:,1]).sum()/(var[:,0].sum()) #sum of intensity change in time
plot(P*dat[:,0],h*dat[:,1])
figure(1).show()
```

Bibliography

[1] I. Setija *et al.*, Phys. Rev. Lett. **70**, 2257 (1993).

[2] Z. Lin, K. Shimizu, M. Zhan, F. Shimizu, and H. Takuma, Jpn. J. Appl. Phys. **30**, L1324 (1991).

[3] S. Chu, L. Hollberg, J. Bjorkholm, A. Cable, and A. Ashkin, Phys. Rev. A. **55**, 48 (1985).

[4] C. Fort *et al.*, Eur. Phys. J. D. **3**, 113 (1998).

[5] C. Wallace *et al.*, Phys. Rev. Lett. **69**, 897 (1992).

[6] C. Monroe, W. Swann, H. Robinson, and C. Wieman, Phys. Rev. Lett. **65**, 1571 (1990).

[7] J. Simsarian, L. Orozco, G. Sprouse, and W. Zhao, Phys. Rev. A. **57**, 2448 (1998).

[8] N. Beverini *et al.*, Opt. Lett. **14**, 350 (1989).

[9] T. Kurosu and F. Shimizu, Jpn. J. Appl. Phys. **29**, L2127 (1990).

[10] C. Bradley, J. McClelland, W. Anderson, and R. Celotta, Phys. Rev. A. **61**, 053407 (2000).

[11] T. Loftus, J. Bochinski, R. Shivitz, and T. Mossberg, Phys. Rev. A. **61**, 051401(R) (2000).

[12] F. Bardou, O. Emile, J.-M. Courty, C. I. Westbrook, and A. Aspect, Europhys. Lett. **20**, 681 (1992).

[13] F. Shimizu, K. Shimizu, and H. Takuma, Phys. Rev. A. **39**, 2758 (1989).

[14] D. Wineland, Science **226**, 395 (1984).

[15] D. Weiss, B. Young, and S. Chu, Phys. Rev. Lett. **70**, 2706 (1993).

[16] T. Ido *et al.*, Phys. Rev. Lett. **94**, 153001 (2005).

[17] S. Kuhr *et al.*, Science **293**, 278 (2001).

[18] A. Bauch, Meas. Sci. Technol. **14**, 1159 (2003).

[19] R. Wynands and S. Weyers, Metrologica **42**, S64 (2005).

[20] S. Diddams, J. Bergquist, S. Jefferts, and C. Oates, Science **306**, 1318 (2004).

[21] J. Prestage, R. Tjoelker, and L. Maleki, Phys. Rev. Lett. **74**, 3511 (1995).

[22] M. Fox, *Quantum Optics*, First ed. (Oxford University Press, UK, 2006).

[23] O. Carnal and J. Mlynek, Phys. Rev. Lett. **66**, 2689 (1991).

[24] H. Metcalf and P. van der Staten, *Laser Cooling and Trapping*, First ed. (Springer-Verlag, New York, 1999).

[25] M. Anderson, J. Ensher, M. Matthews, C. Wieman, and E. Cornell, Science **269**, 198 (1995).

[26] R. Krems, Phys. Chem. Chem. Phys. **10**, 4079 (2008).

[27] H. Bethem and G. Meijer, Int. Rev. Phys. Chem. **22**, 73 (2003).

[28] P. Atkins and R. Friedman, *Molecular Quantum Mechanics*, Fourth ed. (Oxford University Press, New York, 2007).

[29] P. Felker and A. Zewail, J. Chem. Phys. **82**, 2961 (1985).

[30] T. Uzer and W. Miller, Phys. Rep. **199**, 73 (1991).

[31] M. Di Rosa, Eur. Phys. J. D. **31**, 395 (2004).

[32] H. Bethlem, G. Berden, and G. Meijer, Phys. Rev. Lett. **83**, 1558 (1999).

[33] M. Anderlini *et al.*, ArXiv e-prints (2008), arXiv:cond-mat/0410565v2 [cond-mat.soft].

[34] R. deCarvalho *et al.*, Eur. Phys. J. D. **7**, 289 (1999).

[35] G. Modugno *et al.*, Science **294**, 1320 (2001).

[36] K. Jones, E. Tiesinga, P. Lett, and P. Julienne, Rev. Mod. Phys. **78**, 483 (2006).

[37] R. Wynar, R. S. Freeland, D. J. Han, C. Ryu, and D. J. Heinzen, Science **287**, 1016 (2000).

[38] T. Köhler, K. Góral, and P. Julienne, Rev. Mod. Phys. **78**, 1311 (2006).

[39] M. Greiner, C. Regal, and D. Jin, Nature **426**, 537 (2003).

[40] J. Hutson and P. Soldán, ArXiv e-prints (2006), arXiv:physics/0607234v1 [physics.chem-ph].

[41] J. Maddi, T. Dinneen, and H. Gould, Phys. Rev. A. **60**, 3882 (1999).

[42] T. Freegarde, G. Daniell, and D. Segal, Phys. Rev. A. **73**, 033409 (2006).

[43] J. Bakos, G. Djotyan, G. Demeter, and Z. Sörlei, Phys. Rev. A. **53**, 2885 (1996).

[44] M. Weitz and T. Hänsch, Europhys. Lett. **49**, 302 (2000).

[45] K. Rosman and P. Taylor, Pure & Appl. Chem. **70**, 217 (1998).

[46] P. Siddons, C. Adams, C. Ge, and I. Hughes, J. Phys. B. **41**, 155004 (2008).

[47] A. Edmunds, *Angular Momentum in Quantum Mechanics*, Fourth ed. (Princeton University Press, Princeton, USA, 1996).

[48] C. Foot, *Atomic Physics*, First ed. (Oxford University Press, Oxford, 2005).

[49] G. Barwood, P. Gill, and W. Rowley, Appl. Phys. B. **53**, 142 (1991).

[50] U. Rapol, A. Krishna, and V. Natarajan, Eur. Phys. J. D. **23**, 185 (2003).

[51] D. Steck, Alkali D line data: ^{85}Rb & ^{87}Rb, Oct 2008, http://george.ph.utexas.edu/ dsteck/alkalidata/.

[52] J. Slater, J. Chem. Phys **41**, 3199 (1964).

[53] R. Loudon, *The Quantum Theory of Light*, First ed. (Oxford Science Publications, Oxford, UK, 1983).

[54] B. Schultz, H. Ming, G. Noble, and W. van Wijngaarden, Eur. Phys. J. D. **48**, 171 (2008).

[55] W. Demtroder, *Laser Spectroscopy: Basic Concepts and Instrumentation*, Third ed. (Springer-Verlag, New York, 2002).

[56] L. Allen and J. Eberly, *Optical resonance and two-level atoms*, pbk. ed. (Wiley, New York, 1987).

[57] R. Thompson, Rep. Prog. Phys. **48**, 531 (1985).

[58] V. Letokhov and V. Chebotayev, *Nonlinear Laser Spectroscopy*, First ed. (Springer-Verlag, Berlin, 1977).

[59] S. Haroche and F. Hartmann, Phys. Rev. A **6**, 1280 (1972).

[60] D. Smith and I. Hughes, Am. J. Phys. **72**, 631 (2004).

[61] S. Nakayama, Jpn. J. Appl. Phys. **24**, 1 (1985).

[62] L. P. Maguire, R. van Bijnen, E. Mese, and R. Scholten, J. Phys. B. **39**, 2709 (2006).

[63] C. E. Wieman and L. Hollberg, Rev. Sci. Inst. **62**, 1 (1991).

[64] G. Barwood, P. Gill, and W. Rowley, J. Mod. Opt. **37**, 749 (1990).

[65] A. Ludlow *et al.*, Opt. Lett. **32**, 641 (2007).

[66] H. Lewandowski, D. Harber, D. Whitaker, and E. Cornell, J. Low Temp. Phys. **132**, 309 (2003).

[67] X. Zhu and D. T. Cassidy, J. Opt. Soc. Am. B. **14**, 1945 (1997).

[68] D. Meschede, *Optics, Light and Lasers*, First ed. (Wiley-VCH, Berlin, 2003).

[69] G. Galbács, App. Spectr. Rev. **41**, 259 (2006).

[70] A. Schawlow and C. Townes, Phys. Rev. **112**, 1940 (1958).

[71] M. Fleming and A. Mooradian, Appl. Phys. Lett. **38**, 511 (1980).

[72] C. H. Henry, IEEE J. Quant. Elec. **QE-18**, 259 (1982).

[73] D. Howe, D. Allan, and J. Barnes, Proc. 35th Ann. Freq. Control. Sym. , A1 (1981).

[74] M. Littman and H. Metcalf, Appl. Opt. **17**, 2224 (1978).

[75] B. Dahmani, L. Hollberg, and R. Drullinger, Opt. Lett. **12**, 876 (1987).

[76] G. Genty, A. Gröhn, H. Talvitie, M. Kaivola, and Ludvigsen, IEEE. J. Quant. Elec. **36**, 1193 (2000).

[77] A. Arnold, J. Wilson, and M. Boshier, Rev. Sci. Inst. **69**, 1236 (1998).

[78] A. Siegman, *Lasers*, First ed. (University Science Books, California, USA, 1981).

[79] N. Bowring, D. Li, and J. Baker, Meas. Sci. Tech. **5**, 1313 (1994).

[80] C. Pearman *et al.*, J. Phys. B. **35**, 5141 (2002).

[81] M. de Labacherlerie, C. Latrasse, P. Kemssu, and P. Cerez, J. Phys. III France **2**, 1557 (1992).

[82] K. Corwin, Z. Lu, C. Hand, R. Epstein, and C. Wieman, Appl. Opt. **37**, 3295 (1998).

[83] T. Petelski, M. Fattori, G. Lamporesi, J. Stuhler, and G. Tino, Eur. Phys. J. D. **22**, 279 (2002).

[84] C. Wieman and T. Hänsch, Phys. Rev. Lett. **36**, 1170 (1976).

[85] T. Hänsch and B. Couillaud, Opt. Comm. **35**, 441 (1980).

[86] D. Bomse, A. Stanton, and J. Silver, Appl. Opt. **31**, 718 (1992).

[87] R. Pound, Rev. Sci. Inst **17**, 490 (1946).

[88] G. Bjorklund, Opt. Lett. **5**, 15 (1980).

[89] R. Drever *et al.*, Appl. Phys. B **31**, 97 (1983).

[90] G. Bjorklund, M. Levenson, W. Lenth, and C. Ortiz, Appl. Phys. B. **32**, 145 (1983).

[91] Cadence Design Systems, www.cadence.com/products/orcad.

[92] T. Ikegami, S. Sudo, and Y. Sakai, *Frequency Stabilization of Semiconductor Laser Diodes*, First ed. (Artech House, Boston, 1995).

[93] D. Elliot, R. Roy, and S. Smith, Phys. Rev. A. **26**, 12 (1982).

[94] D. Allan, Proc. IEEE **54**, 221 (1991).

[95] J. Rutman and F. Walls, Proc. IEEE **79**, 952 (1991).

[96] M. Boshier, D. Berkeland, E. Hinds, and V. Sandoghdar, Opt. Comm. **85**, 355 (1991).

[97] T. Hänsch and A. Schawlow, Opt. Comm. **13**, 68 (1975).

[98] P. Lett *et al.*, J. Opt. Soc. am. B. **6**, 2084 (1989).

[99] J. Weiner and P.-T. Ho, *Light-Matter Interaction: Volume 1*, First ed. (John Wiley & Sons, Inc, New Jersey, 2003).

[100] Y. Castin, H. Wallis, and J. Dalibard, J. Opt. Soc. Am. B. **6**, 2046 (1989).

[101] W. Jones, Eur. J. Phys. **1**, 85 (1980).

[102] A. Ashkin and J. Gordon, Opt. Lett. **8**, 511 (1983).

[103] D. Pritchard, E. Raab, V. Bagnato, C. Wieman, and R. Watts, Phys. Rev. Lett. **57**, 310 (1986).

[104] E. Raab, M. Prentiss, A. Cable, S. Chu, and D. Pritchard, Phys. Rev. Lett. **59**, 2631 (1987).

[105] W. Ertmer, R. Blatt, J. Hall, and M. Zhu, Phys. Rev. Lett. **54**, 996 (1985).

[106] A. Migdall, J. Prodan, W. Phillips, T. Bergeman, and H. Metcalf, Phys. Rev. Lett. **54**, 2597 (1985).

[107] J. Arlt, O. Maragó, S. Webster, S. Hopkins, and C. Foot, Opt. Comm. **157**, 303 (1998).

[108] J. Reichel, W. Hänsel, and T. Hänsch, Phys. Rev. Lett. **83**, 3398 (1999).

[109] P. Lett, R. Watts, C. Westbrook, and W. Phillips, Phys. Rev. Lett. **61**, 169 (1988).

[110] S. Chu, Rev. Mod. Phys. **70**, 685 (1998).

[111] D. Sesko, C. Fan, and C. Wieman, J. Opt. Soc. Am. B. **5**, 1225 (1988).

[112] J. Dalibard and C. Cohen-Tannoudji, J. Opt. Soc. Am. B. **6**, 2023 (1989).

[113] P. Ungar, D. Weiss, E. Riss, and S. Chu, J. Opt. Soc. Am. B **6**, 2058 (1989).

[114] J. Lawall *et al.*, Phys. Rev. Lett. **75**, 4194 (1995).

[115] M. Kasevich and S. Chu, Phys. Rev. Lett. **69**, 1741 (1992).

[116] F. Dalfovo, S. Giorgini, L. Pitaevskii, and S. Stringari, Rev. Mod. Phys. **71**, 463 (1999).

[117] S. Patel, *A Chirped, Pulsed Laser System and Magneto-Optical Trap for Rubidium*, PhD thesis, University of Southampton, Southampton UK, 2008.

[118] J. Bateman, *Novel schemes for the optical manipulation of atoms and molecules*, PhD thesis, University of Southampton, Southampton UK, 2008.

[119] C. Klempt *et al.*, Phys. Rev. A. **73**, 013410 (2006).

[120] B. Anderson and M. Kasevich, Phys. Rev. A. **63**, 023404 (2001).

[121] T. Walker, D. Sesko, and C. Wieman, Phys. Rev. Lett. **64**, 408 (1990).

[122] G. Demeter, G. Djotyan, and J. Bakos, J. Opt. Soc. Am. B. **15**, 16 (1998).

[123] S. Lecomte, E. Fretel, G. Gaetano, and P. Thomann, Appl. Opt. **39**, 1426 (2000).

[124] D. Sesko, T. Walker, and C. Wieman, J. Opt. Soc. Am. B. **65**, 1571 (1990).

[125] A. Arnold and P. Manson, J. Opt. Soc. Am. B. **17**, 497 (2000).

[126] A. Steane, M. Chowdhury, and C. Foot, J. Opt. Soc. Am. B. **9**, 2142 (1992).

[127] D. Meacher, D. Boiron, H. Metcalf, C. Salomon, and G. Grynberg, Phys. Rev. A. **50**, R1992 (1994).

[128] R. Feynman, F. Vernon, Jr, and R. Hellwarth, J. Appl. Phys. **28**, 49 (1957).

[129] D. Goswami, Phys. Rep. **374**, 385 (2003).

[130] M. Weitz, B. Young, and S. Chu, Phys. Rev. Lett. **73**, 2563 (1994).

[131] M. Weitz, B. Young, and S. Chu, Phys. Rev. A. **50**, 2438 (1994).

[132] N. Vitatov, T. Halfmann, B. Shore, and K. Bergmann, Annu. Rev. Phys. Chem **52**, 763 (2001).

[133] J. Bateman and T. Freegarde, Phys. Rev. A. **76**, 013416 (2007).

[134] I. Dotsenko, *Raman spectroscopy of single atoms*, PhD thesis, Universität Bonn, Bonn, Germany, 2002.

[135] H. Gray, R. Whitley, and C. Stroud Jr., Opt. Lett. **3**, 218 (1978).

[136] C. Cohen-Tannoudji, G. Grynberg, and J. Dupont-Roe, *Atom-Photon Interactions*, Apr 1998 ed. (Wiley-VCH, Berlin, 1998).

[137] Y. Wu, Phys. Rev. A. **54**, 1586 (1996).

[138] S. Autler and C. Townes, Phys. Rev. **100**, 703 (1955).

[139] J. Bakos, Phys. Rep. **31**, 209 (1977).

[140] I. Jyotsna and G. Agarwal, Phys. Rev. A. **52**, 3147 (1995).

[141] G. Alzetta, L. Moi, and G. Orriols, Il Nuovo Cimento B. **52**, 209 (1979).

[142] M. Fleischhauer, A. Imamoglu, and J. Marangos, Rev. Mod. Phys. **77**, 633 (2005).

[143] J. Vanier, Appl. Phys. B. **81**, 421 (2005).

[144] P. Marte, P. Zoller, and J. Hall, Phys. Rev. A. **44**, R4118 (1991).

[145] H. Müller, S.-W. Chiow, S. Herrmann, and S. Chu, Phys. Rev. Lett. **100**, 031101 (2008).

[146] A. Peters, K. Chung, and S. Chu, Metrologia **38**, 25 (2001).

[147] D. Weiss, B. Young, and S. Chu, Appl. Phys. B. **59**, 217 (1994).

[148] A. Cronin, J. Schmiedmayer, and D. Pritchard, ArXiv e-prints (2008), arXiv:0712.3703v1 [quant-ph].

[149] M. Kasevich and S. Chu, Phys. Rev. Lett. **67**, 181 (1991).

[150] J. Bakos *et al.*, Eur. Phys. J. D. **39**, 59 (2006).

[151] A. Goyal, P. Gavrilovic, and H. Po, Appl. Phys. Lett. **71**, 1296 (1997).

[152] H. Wenzel, B. Sumpf, and G. Erbert, Com. Ren. Physique **4**, 649 (2003).

[153] U. Schünemann, H. Engler, R. Grimm, M. Weidermüller, and M. Zielonkowski, Rev. Sci. Inst. **70**, 242 (1999).

[154] I. Dotsenko *et al.*, Appl. Phys. B. **78**, 711 (2004).

[155] D. Weiss, B. Young, and S. Chu, Phys. Rev. Lett. **73**, 2563 (1994).

[156] D. Haubrich, M. Dornseifer, and R. Wynands, Rev. Sci. Inst. **71**, 338 (2000).

[157] Toptica, Application Note: AN-TA-001, *Tapered Semiconductor Lasers Coherently Amplify ECDLs up to 1W.*

[158] H. Berns and R. Wilkes, Real Time Conference, 1999, 11th IEEE NPSS , 480 (1999).

[159] D. Meschede and A. Rauschenbeute, Atomic Physics 19: XIX International Conference on Atomic Physics **770**, 359 (2005).

[160] D. Yavuz *et al.*, ArXiv e-prints (2008), arXiv:quant-ph/0509176v1.

[161] C. Roos *et al.*, Phys. Rev. Lett. **83**, 4713 (1999).

[162] J. Sørensen *et al.*, ArXiv e-prints (2006), arXiv:quant-ph/0608089v2.

[163] C. E. Wieman, D. Pritchard, and D. Wineland, Rev. Mod. Phys. **71**, S253 (1999).

[164] P. Julienne and F. Mies, J. Opt. Soc. Am. B. **6**, 2257 (1989).

[165] J. Weiner, V. Bagnato, S. Zilio, and P. Julienne, Rev. Mod. Phys. **71**, 1 (1999).

[166] S. Kokkelmans, B. Verhaar, K. Gibble, and D. Heinzen, Phys. Rev. A. **56**, R4389 (1997).

[167] N. Ramsey, Phys. Rev. A. **78**, 695 (1950).

[168] F. Seifert, P. Kwee, M. Heurs, B. Willke, and K. Danzmann, Opt. Lett. **31**, 2000 (2006).

[169] W. Ketterle, K. Davis, M. Joffe, A. Martin, and D. Pritchard, Phys. Rev. Lett. **70**, 2253 (1993).

[170] V. Bagnoud and J. Zuegel, Opt. Lett. **29**, 295 (2004).

[171] Diffractive optical elements by Holoeye, http://www.holoeye.com.

[172] J. Hoffnagle and C. Jefferson, Appl. Opt. **30**, 5488 (2000).

[173] F. Wippermann, U.-D. Zeitner, P. D. A. A. Bräuer, and S. Sinzinger, Opt. Expr. **15**, 6218 (2007).

[174] P. Mohr, B. Taylor, and D. Newell, Rev. Mod. Phys. **80**, 633 (2008).

[175] M. Bradley, J. Porto, S. Rainville, J. Thompson, and D. Pritchard, Eur. Phys. J. D. **23**, 185 (2003).

[176] Minicircuits, http://www.minicircuits.com/.